JSCSEN 89(9)1123-1253 (2024)

ISSN 1820-7421(Online)

# Journal of the Serbian Chemical Society



VOLUME 89

NO 9

BELGRADE 2024

Available on line at

www.shd.org.rs/JSCS/

The full search of JSCS is available through

DOAJ DIRECTORY OF OPEN ACCESS JOURNALS

www.doaj.org

The **Journal of the Serbian Chemical Society** (formerly Glasnik Hemijskog društva Beograd), one volume (12 issues) per year, publishes articles from the fields of chemistry. The **Journal** is financially supported by the **Ministry of Education, Science and Technological Development of the Republic of Serbia.**

Articles published in the **Journal** are indexed in **Clarivate Analytics products: Science Citation Index-Expanded™** – accessed *via* **Web of Science®** and **Journal Citation Reports®**.

**Impact Factor** announced on 28 June, 2023: **1.000; 5-year Impact Factor**: **1.100**.

Articles appearing in the **Journal** are also abstracted by: **Scopus, Chemical Abstracts Plus (CAplus℠), Directory of Open Access Journals, Referativnii Zhurnal (VINITI), RSC Analytical Abstracts, EuroPub, Pro Quest** and **Asian Digital Library.**

| | |
|---|---|
| **Publisher:** | **Serbian Chemical Society**, Karnegijeva 4/III, P. O. Box 36, 1120 Belgrade 35, Serbia<br>tel./fax: +381–11–3370–467, E-mails: **Society** – shd@shd.org.rs; **Journal** – jscs@shd.org.rs<br>Home Pages: **Society** – http://www.shd.org.rs/, **Journal** – http://www.shd.org.rs/JSCS/ |
| **Internet Service**: | Contents, Abstracts and full papers (from Vol 64, No. 1, 1999) are available in the electronic form at the Web Site of the **Journal** (http://www.shd.org.rs/JSCS/). |
| **Former Editors:** | **Nikola A. Pušin** (1930–1947), **Aleksandar M. Leko** (1948–1954),<br>**Panta S. Tutundžić** (1955–1961), **Miloš K. Mladenović** (1962–1964),<br>**Đorđe M. Dimitrijević** (1965–1969), **Aleksandar R. Despić** (1969–1975),<br>**Slobodan V. Ribnikar** (1975–1985), **Dragutin M. Dražić** (1986–2006). |
| **Editor-in-Chief:** | BRANISLAV Ž. **NIKOLIĆ**, Serbian Chemical Society (E-mail: jscs-ed@shd.org.rs) |
| **Deputy Editor:** | DUŠAN **SLADIĆ**, Faculty of Chemistry, University of Belgrade |
| **Sub editors:** | |
| *Organic Chemistry* | DEJAN **OPSENICA**, Institute of Chemistry, Technology and Metallurgy, University of Belgrade<br>JÁNOS **CSANÁDI**, Faculty of Science, University of Novi Sad |
| *Biochemistry and Biotechnology* | OLGICA **NEDIĆ**, INEP – Institute for the Application of Nuclear Energy, University of Belgrade |
| *Inorganic Chemistry* | BILJANA **GLIŠIĆ**, Faculty of Science, University of Kragujevac |
| *Theoretical Chemistry* | IVAN **JURANIĆ**, Serbian Chemical Society |
| *Physical Chemistry* | LJILJANA **DAMJANOVIĆ-VASILIĆ**, Faculty of Physical Chemistry, University of Belgrade |
| *Electrochemistry* | SNEŽANA **GOJKOVIĆ**, Faculty of Technology and Metallurgy, University of Belgrade |
| *Analytical Chemistry* | RADA **BAOŠIĆ**, Faculty of Chemistry, University of Belgrade |
| *Polymers* | BRANKO **DUNJIĆ**, Faculty of Technology and Metallurgy, University of Belgrade |
| *Thermodynamics* | MIRJANA **KIJEVČANIN**, Faculty of Technology and Metallurgy, University of Belgrade |
| *Chemical Engineering* | TATJANA **KALUĐEROVIĆ RADOIČIĆ**, Faculty of Technology and Metallurgy, University of Belgrade |
| *Materials* | RADA **PETROVIĆ**, Faculty of Technology and Metallurgy, University of Belgrade |
| *Metallic Materials and Metallurgy* | ANA **KOSTOV**, Mining and Metallurgy Institute Bor, University of Belgrade |
| *Environmental and Geochemistry* | VESNA **ANTIĆ**, Faculty of Agriculture, University of Belgrade |
| *History of and Education in Chemistry* | DRAGICA **TRIVIĆ**, Faculty of Chemistry, University of Belgrade |
| **English Language Editors:** | LYNNE **KATSIKAS**, Serbian Chemical Society<br>VLATKA **VAJS**, Serbian Chemical Society<br>JASMINA **NIKOLIĆ**, Faculty of Technology and Metallurgy, University of Belgrade |
| **Technical Editors:** | VLADIMIR **PANIĆ**, Institute of Chemistry, Technology and Metallurgy, University of Belgrade, MARIO **ZLATOVIĆ**, Faculty of Chemistry, University of Belgrade |
| **Journal Manager & Web Master:** | MARIO **ZLATOVIĆ**, Faculty of Chemistry, University of Belgrade |
| **Office:** | VERA **ĆUŠIĆ**, Serbian Chemical Society |

**Editorial Board**

***From abroad:*** **R. Adžić**, Brookhaven National Laboratory (USA); **A. Casini**, University of Groningen (The Netherlands); **G. Cobb**, Baylor University (USA); **D. Douglas**, University of British Columbia (Canada); **G. Inzelt**, Etvos Lorand University (Hungary); **J. Kenny**, University of Perugia (Italy); **Ya. I. Korenman**, Voronezh Academy of Technology (Russian Federation); **M. D. Lechner**, University of Osnabrueck (Germany); **S. Macura**, Mayo Clinic (USA); **M. Spiteller**, INFU, Technical University Dortmund (Germany); **M. Stratakis**, University of Crete (Grecce); **M. Swart**, University de Girona (Cataluna, Spain); **G. Vunjak-Novaković**, Columbia University (USA); **P. Worsfold**, University of Plymouth (UK); **J. Zagal**, Universidad de Santiago de Chile (Chile).

***From Serbia:*** **B. Abramović**, **V. Antić**, **R. Baošić**, **V. Beškoski**, **J. Csanadi**, **Lj. Damjanović-Vasilić**, **A. Dekanski**, **V. Dondur**, **B. Dunjić**, **M. Đuran**, **B. Glišić**, **S. Gojković**, **I. Gutman**, **B. Jovančićević**, **I. Juranić**, **T. Kaluđerović Radoičić**, **L. Katsikas**, **M. Kijevčanin**, **A. Kostov**, **V. Leovac**, **S. Milonjić**, **V.B. Mišković-Stanković**, **O. Nedić**, **B. Nikolić**, **J. Nikolić**, **D. Opsenica**, **V. Panić**, **M. Petkovska**, **R. Petrović**, **I. Popović**, **B. Radak**, **S. Ražić**, **D. Sladić**, **S. Sovilj**, **S. Šerbanović**, **B. Šolaja**, **Ž. Tešić**, **D. Trivić**, **V. Vajs, M. Zlatović**.

**Subscription:** The annual subscription rate is **150.00 €** including postage (surface mail) and handling. For Society members from abroad rate is **50.00 €**. For the proforma invoice with the instruction for bank payment contact the Society Office (E-mail: shd@shd.org.rs) or see JSCS Web Site: http://www.shd.org.rs/JSCS/, option Subscription.

**Godišnja pretplata:** Za članove SHD: **2.500,00 RSD**, za penzionere i studente: **1000,00 RSD**, a za ostale: **3.500,00 RSD**:za organizacije i ustanove: **16.000,00 RSD**. Uplate se vrše na tekući račun Društva: **205-13815-62**, poziv na broj **320**, sa naznakom "pretplata za JSCS".

**Nota:** Radovi čiji su svi autori članovi SHD prioritetno se publikuju.

Odlukom Odbora za hemiju Republičkog fonda za nauku Srbije, br. 66788/1 od 22.11.1990. godine, koja je kasnije potvrđena odlukom Saveta Fonda, časopis je uvršten u kategoriju međunarodnih časopisa (**M-23**). Takođe, aktom Ministarstva za nauku i tehnologiju Republike Srbije, 413-00-247/2000-01 od 15.06.2000. godine, ovaj časopis je proglašen za publikaciju od posebnog interesa za nauku. **Impact Factor** časopisa objavljen 28. juna 2023. godine je **1,000**, a petogodišnji **Impact Factor 1,100**.

Journal of the Serbian Chemical Society
JSCS-info@shd.org.rs • www.shd.org.rs/JSCS

*J. Serb. Chem. Soc.* Vol. 89, No. 9 (2024)

CONTENTS*



Published by the Serbian Chemical Society
Karnegijeva 4/III, P.O. Box 36, 11120 Belgrade, Serbia
Printed by the Faculty of Technology and Metallurgy
Karnegijeva 4, P.O. Box 35-03, 11120 Belgrade, Serbia

* For colored figures in this issue please see electronic version at the Journal Home Page: http://www.shd.org.rs/JSCS/

Journal of the Serbian Chemical Society
JSCS@tmf.bg.ac.rs • www.shd.org.rs/JSCS
*J. Serb. Chem. Soc.* *89* (9) 1123–1131 (2024)
*JSCS–5776*
*Original scientific paper*
Published 7 September 2024

# Synthesis of methyl 3,4-anhydro-6-bromo-2-*O*-*tert*-butyldimethylsilyl-6-deoxy-*α*-D-allopyranoside from *α*-D-glucose

ĐORĐE GLIŠIN, OLGA JOVANOVIĆ, GORDANA STOJANOVIĆ#, ALEKSANDRA ŽIVKOVIĆ, DRAGAN STOJANOVIĆ, MARINA PAVLOVIĆ and BILJANA ARSIĆ#*

*Department of Chemistry, Faculty of Sciences and Mathematics, University of Niš, Višegradska 33, 18000 Niš, Serbia*

(Received 31 August 2023, revised 8 January, accepted 24 April 2024)

*Abstract*: Some of simple carbohydrates and their derivatives are used for the clinical treatment of various diseases. Epoxide derivatives, which can be obtained by the intramolecular elimination of water from two vicinal hydroxyl groups, are stable, but sufficiently reactive compounds very often used as intermediaries in various syntheses. Synthesis of epoxide derivative, methyl 3,4-anhydro-6-bromo-2-*O*-*tert*-butyldimethylsilyl-6-deoxy-*α*-D-allopyranoside from *α*-D-glucose was achieved in high yields in the minimal number of synthetic steps. Anhydrous glucose was used as a starting material which was transformed into methyl *α*-D-glucopyranoside using dry, gaseous hydrogen chloride. Thus obtained derivative was treated with benzaldehyde in the presence of zinc chloride as Lewis acid giving methyl (*R*)-4,6-*O*-benzylidene-*α*-D-glucopyranoside. The obtained compound was treated with *N*-bromosuccinimide (NBS) in dichloromethane in the presence of barium carbonate giving methyl 4-*O*-benzoyl-6-bromo-6-deoxy-*α*-D-glucopyranoside. In the next step, the obtained compound was treated with *tert*-butyldimethylsilyl chloride (TBDMSCl) in pyridine, and methyl 4-*O*-benzoyl-6-bromo-2-*O*-*tert*-butyldimethylsilyl-6-deoxy-*α*-D-glucopyranoside was further mesylated, and the obtained methyl 4-*O*-benzoyl-6-bromo-2-*O*-*tert*-butyldimethylsilyl-6-deoxy-3-*O*-mesyl-*α*-D-glucopyranoside was treated at the end with KOH to give methyl 3,4-anhydro-6-bromo-2-*O*-*tert*-butyldimethylsilyl-6-deoxy-*α*-D-allopyranoside (yield 78 %).

*Keywords*: D-allose derivative; 3,4-epoxide ring; selective silylation; carbohydrates.

## INTRODUCTION

When there are two present OH groups in 1,2- or 1,3-positions in a molecule, their protection can very often be achieved by forming acetals, ketals and

* Corresponding author. E-mail: biljana.arsic@pmf.edu.rs
# Serbian Chemical Society member.
https://doi.org/10.2298/JSC230831049G

ortho esters. This is particularly significant in the synthesis of carbohydrates.[1,2] Some of simple carbohydrates and their derivatives are used for the clinical treatment of various diseases.[3] The most often used procedure for their formation is the treatment of glycol with the excess of aldehyde or ketone in the presence of an acidic catalyst.[4] As acid catalysts gaseous hydrogen chloride can be used, sulphuric and *p*-toluenesulphonic acid (from protic acids), and the most frequently zinc chloride as Lewis acid. Another way is to put anhydrous copper salt which binds water.[5] The third way is to introduce acetals and ketals into the reaction mixture instead of aldehydes themselves and then perform the acid catalysed exchange of acetal groups.[4] It is rarely possible to obtain acetals or ketals from vicinal dihalogenides and glycols under the $S_N2$ mechanism.[6]

Benzylidene acetals are mostly used in the carbohydrate chemistry[1,2] and they can be obtained by the treatment of carbohydrates and benzaldehydes with the acid catalysts, such as hydrogen chloride, sulphuric acid, *p*-toluenesulphonic acid and zinc chloride. Besides, it can be used dimethyl or diethyl-acetals of benzaldehyde in the acid media. The main advantage of this group is that it can be removed by catalytic hydrogenation, and the main disadvantage is that both possible diastereoisomers can be obtained during benzylidation.

The most often used agent for the selective protection of hydroxyl groups is *tert*-butyldimethylsilyl chloride (TBDMSCl). *tert*-Butyldimethylsilyl group[7] is appropriate for the temporary protection of hydroxyl groups because it is stable in the wide region of the reaction conditions, and it can be easily removed by the treatment with acids or fluoride ion, and tailor-made ionic liquids ([dihexaEGim][OMs]/*tert*-amyl alcohol media system).[8] This group is recommended for the selective protection of nucleosides,[9] hexopyranosides[10] and other carbohydrate derivatives.[9]

Epoxides or oxiranes can be obtained by the intramolecular elimination of water from two vicinal hydroxyl groups. They are stable, but sufficiently reactive compounds, very often used as intermediaries in various syntheses.[11] The most frequent way of their synthesis is the treatment of an $\alpha$-hydroxy-sulfonic ester with bases. The first step of the reaction is the formation of alkoxide ion, either by deprotonation of hydroxyl group, or by the hydrolysis of carbonic ester using any base. In the second step, it comes the attack of alkoxide ion on the C-atom to which $-OSO_2R$ group is attached, which is followed by the closure of the epoxide ring, with the inversion of configuration at the electrophilic C-atom. Leaving groups can also be the esters of sulphuric or nitric acids, halides, protonated amino groups, diazonium ions, *etc.*, beside the sulphonic ester.

Two epoxide derivatives in two different decades were synthesized at the Laboratory for Organic Synthesis, Faculty of Sciences and Mathematics, University of Niš, and the synthesis of one of them was published at the end of 1980s.[12] Therefore, the novelty in this research is the synthesis of the second

epoxide derivative methyl 3,4-anhydro-6-bromo-2-*O*-*tert*-butyldimethylsilyl-6--deoxy-*α*-D-allopyranoside (Fig. 1) from *α*-D-glucose, where it was obtained in similar yields to the previously published epoxide derivative[12]. It can be an intermediary in the synthesis of biologically active compounds. To the best of our knowledge, two new compounds not previously reported were synthesised in this work: methyl 4-*O*-benzoyl-6-bromo-2-*O*-*tert*-butyldimethylsilyl-6-deoxy-3-*O*--mesyl-*α*-D-glucopyranoside and methyl 3,4-anhydro-6-bromo-2-*O*-*tert*-butyldimethylsilyl-6-deoxy-*α*-D-allopyranoside.

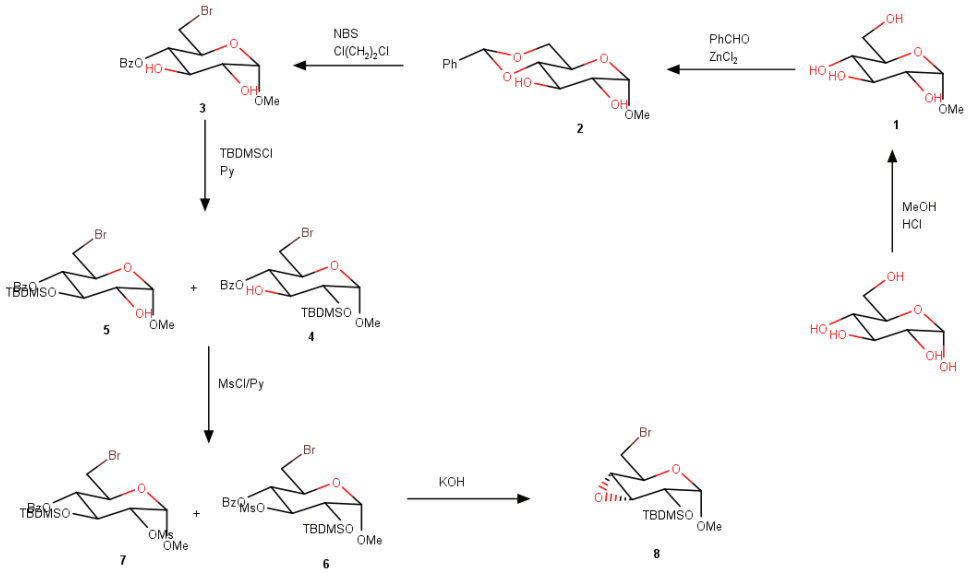


Fig. 1. Synthesis of methyl 3,4-anhydro-6-bromo-2-*O*-*tert*-butyldimethylsilyl-6-deoxy-*α*-D--allopyranoside (**8**) from *α*-D-glucose.

## EXPERIMENTAL

### *Apparatus*

The NMR analyses were performed on a Bruker AC-250 instrument with the standard Bruker software. All analyses were carried out using regular 5 mm NMR tubes.

### *Reagents*

All chemicals used for syntheses were of the analytical reagent grade. The solutions were prepared for NMR analyses in $CDCl_3$ (Merck, Germany), purity 99.8 %. The chemical shifts are referred to tetramethylsilane (TMS, $\delta_H = 0.00$ ppm) in $CDCl_3$.

### *Synthetic procedures*

*Methyl α-D-glucopyranoside (1)*. Methyl *α*-D-glucopyranoside (**1**) was synthesized from *α*-D-glucose using Fisher glycosidation method with methanolic HCl, where the formation of the thermodynamically favoured pyranoside was achieved with a prolonged reaction time and refluxing.[13] In total, it was obtained 25.1 g methyl *α*-D-glucopyranoside (**1**), starting from 50 g

(0.2775 mol) *α*-D-glucose. The yield was 46.58 %. M.p. 164–165 °C. The melting point was in accordance with the previously reported data.[14]

*Methyl (*R*)-4,6-*O*-benzylidene-α-D-glucopyranoside (2)*. Methyl (*R*)-4,6-*O*-benzylidene--*α*-D-glucopyranoside (**2**) was synthesised using the procedure reported by Hall,[15] starting from 16.5 g (0.121 mol) anhydrous $ZnCl_2$, 25 mL (0.2462 mol) benzaldehyde ($\rho$ = 1.045 g/mL) and 16.5 g (0.0851 mol) powdered methyl *α*-D-glucopyranoside (**1**). The crude product was recrystallized with the optimal quantity of hot ethanol 14.15 g methyl (*R*)-4,6-*O*-benzylidene-*α*-D-glucopyranoside (**2**, yield 59 %), were obtained, m.p. 165 °C. The reported melting point was in accordance with the previously published. [15-17]

*Methyl 4-O-benzoyl-6-bromo-6-deoxy-α-D-glucopyranoside (3)*. Methyl 4-*O*-benzoyl-6--bromo-6-deoxy-*α*-D-glucopyranoside (**3**) was prepared according to the modified Hanessian's procedure[18] starting from 0.910 g (3.22 mmol) methyl (*R*)-4,6-*O*-benzylidene-*α*-D-glucopyranoside (**2**), 0.364 g (1.84 mmol) $BaCO_3$ and 0.6825 g (3.83 mmol) *N*-bromosuccinimide (NBS) and using dichloromethane as a solvent, instead of 1,1,2,2-tetrachloroethane. The obtained crystals had m.p. 121–122 °C, which is in accordance with the previously published value.[18] The obtained substance was chromatographed on a silica-gel column using the eluent chloroform:methanol = 15:1, and pure methyl 4-*O*-benzoyl-6-bromo-6-deoxy-*α*-D-glucopyranoside (**3**) was obtained with the mass 0.73 g, yield 65.68 %.

*Methyl 4-O-benzoyl-6-bromo-2-O-tert-butyldimethylsilyl-6-deoxy-α-D-glucopyranoside (4) and methyl 4-O-benzoyl-6-bromo-3-O-tert-butyldimethylsilyl-6-deoxy-α-D-glucopyranoside (5)*. The synthesis of compounds **4** and **5** started from 0.73 g (2.02 mmol) methyl 4-*O*-benzoyl-6--bromo-6-deoxy-*α*-D-glucopyranoside (**3**) and pyridine. They were put in round bottomed flask and stirred by hand until the complete dissolution of the carbohydrate derivative. The flask with the solution was left to cool down at 0 °C, and then 0.448 g (2.97 mmol) of TBDMSCl was added into the previously dissolved substance and cooled at 0 °C. The reaction mixture was left at room temperature for 8 days and followed using TLC with the mobile phase chloroform:methanol = 15:1. The reaction was terminated by the evaporation of pyridine on vacuum evaporator using ethanol. The oil thus obtained was eluted on silica gel column with the mixture chloroform:methanol = 40:1. In this way three reaction products were separated: methyl 4-*O*-benzoyl-6-bromo-2-*O*-tert-butyldimethylsilyl-6-deoxy-*α*-D-glucopyranoside (**4**, 150 mg, 15.42 %; $^1$H-NMR spectrum along with the assignment is available in the Supplementary material to this paper, Fig. S-1), methyl 4-*O*-benzoyl-6-bromo-3-*O*-tert-butyldimethylsilyl-6-deoxy-*α*-D-glucopyranoside (**5**, 180 mg, 18.51 %) and methyl 4-*O*-benzoyl-6--bromo-6-deoxy-2,3-di-*O*-*tert*-butyldimethylsilyl-*α*-D-glucopyranoside (50 mg, 4.1 %).

*Methyl 4-O-benzoyl-6-bromo-2-O-tert-butyldimethylsilyl-6-deoxy-3-O-mesyl-α-D-glucopyranoside (6)*. 150 mg (0.32 mmol) of methyl 4-*O*-benzoyl-6-bromo-2-*O*-*tert*-butyldimethylsilyl-6-deoxy-*α*-D-glucopyranoside (**4**) was placed in round bottomed flask (100 mL) and dissolved in pyridine, and then cooled in ice bath to 0 °C, and then 0.06 mL (0.7752 mmol) methanesulfonyl chloride ($\rho$ = 1.48 g/mL) was added. The obtained mixture was left at 0 °C for 24 h. The reaction was monitored using TLC and terminated by the addition of a small quantity of water. Pyridine from the reaction mixture was removed by the co-evaporation with ethanol, and obtained oil was put on the silica gel column and eluted using chloroform. The mass of the obtained substance **6** was 60 mg (34.36 %). $^1$H-NMR spectrum and the assignments are available in the supplementary material (Fig. S-2).

*Methyl 4-O-benzoyl-6-bromo-3-O-tert-butyldimethylsilyl-6-deoxy-2-O-mesyl-α-D-glucopyranoside (7)*. 180 mg (0.38 mmol) methyl 4-*O*-benzoyl-6-bromo-3-*O*-*tert*-butyldimethylsilyl-6-deoxy-*α*-D-glucopyranoside (**5**) was put in the round bottom flask (100 mL) and dis-

solved in pyridine, then cooled in ice bath to 0 °C and methanesulfonyl chloride (0.06 mL, 0.7752 mmol) was added. The obtained mixture was left at 0 °C for 24 h. The reaction was monitored using TLC and interrupted by the addition of small quantity of water. Pyridine was removed from the reaction mixture by co-evaporation with ethanol, and the obtained oil was put on silica gel column and eluted using chloroform. The mass of the obtained substance **5** was 80 mg (38.18 %).

*Methyl 3,4-anhydro-6-bromo-2*-O-tert-*butyldimethylsilyl-6-deoxy*-α-*D-allopyranoside (**8**)*. Methyl 4-*O*-benzoyl-6-bromo-3-*O-tert*-butyldimethylsilyl-6-deoxy-2-*O*-mesyl-*α*-D-glucopyranoside (**7**) was put in the round bottomed flask (100 mL), and the same operation was performed for methyl 4-*O*-benzoyl-6-bromo-2-*O-tert*-butyldimethylsilyl-6-deoxy-3-*O*-mesyl-*α*-D-glucopyranoside (**6**). Ethanol was added to both flasks, in the quantity to dissolve the substance, and into thus obtained solutions 0.06 g (1.0693 mmol) KOH was added. The reaction was heated for 15 min at 70 °C which is enough time for the reaction to proceed quantitatively; it was monitored using TLC and chloroform as the mobile phase. Only one of those two makes epoxide, and it is the compound methyl 4-*O*-benzoyl-6-bromo-2-*O-tert*-butyldimethylsilyl-6--deoxy-3-*O*-mesyl-*α*-D-glucopyranoside (**6**), because it possesses good leaving group in the position 3, and the proof for it is TLC and the recorded $^1$H-NMR spectrum (Supplementary material, Fig. S-3). The mass of the obtained epoxide (methyl 3,4-anhydro-6-bromo-2-*O-tert*--butyldimethylsilyl-6-deoxy-*α*-D-allopyranoside, **8**) is 30 mg (yield 78 %).

## RESULTS AND DISCUSSION

The anhydrous glucose was used as a starting material which was transformed into methyl *α*-D-glucopyranoside (**1**) using dry, gaseous HCl. Reaction was performed in a such a way that 50 g anhydrous glucose was refluxed for 72 h giving after cooling pure crystalline methyl *α*-D-glucopyranoside (**1**, m.p. 164 °C, Fig. 1). Yield of the first harvest was 16.5 g. The filtrate was evaporated to half volume after the filtering of crystals and left to stay in the fridge overnight. The obtained crystals were filtered and dried; 8.6 g methyl *α*-D-glucopyranoside (**1**) was obtained in the second harvest. Total yield of this reaction was 46.58 %.

Thus obtained methyl *α*-D-glucopyranoside (**1**) was treated with benzaldehyde in the presence of $ZnCl_2$, as a Lewis acid giving methyl (*R*)-4,6-*O*-benzylidene-*α*-D-glucopyranoside (**2**, Fig. 1). The procedure was performed according to the instructions from Hall's method,[15] according to which it was firstly formed the complex between anhydrous $ZnCl_2$ and benzaldehyde, and then methyl *α*-D--glucopyranoside was added. The yields were different in this reaction and depended obviously on the purity of benzaldehyde, the presence of moisture in obtained methyl *α*-D-glucopyranoside, the heating and the presence of moisture in $ZnCl_2$. Therefore, to get yields around 65 % it is necessary each component to be maximally clean and dry.

The obtained methyl (*R*)-4,6-*O*-benzylidene-*α*-D-glucopyranoside (**2**) was treated with *N*-bromosuccinimide (NBS) in dichloromethane in the presence of $BaCO_3$.[19] This reaction is very useful and important because the inactive benzylidene acetal in the position 6 was replaced by Br group in one step, which is easily reduced in the necessary $CH_3$ group, and the alkaline labile benzoyl group

remained in the position 4. Using the alkaline hydrolysis of benzoyl group obtained alkoxide ion easily closes epoxide of *allo*-configuration taking out *trans*-3-*O*-mesyl group. The reaction was performed in such a way that 0.91 g (3.22 mmol) methyl (*R*)-4,6-*O*-benzylidene-*α*-D-glucopyranoside (**2**) was treated with 0.6825 g freshly prepared NBS in 35 mL dichloromethane previously dried through $Al_2O_3$ column. $BaCO_3$ was also added into the reaction (0.364 g, 1.84 mmol). The mixture was refluxed with stirring for 2.5 h and followed the changes using TLC. After the completion of the reaction, the insoluble $BaCO_3$ was filtered off and separated and after the evaporation of the solvent the oil was obtained. After the silica-gel chromatography methyl 4-*O*-benzoyl-6-bromo-6--deoxy-*α*-D-glucopyranoside (**3**) was obtained as a solid, yield 65.68 % (Fig. 1). Its melting point was in good agreement with the reported values.[18]

In the next step, the obtained compound was treated with TBDMSCl in pyridine, in a way that the compound was dissolved in pyridine, cooled at 0 °C in ice bath, and then TBDMSCl was added in a ratio 1.4 mol TBDMSCl to 1 mol of the compound. Three products were obtained: methyl 4-*O*-benzoyl-6-bromo-2-*O*--*tert*-butyldimethylsilyl-6-deoxy-*α*-D-glucopyranoside (**4**), methyl 4-*O*-benzoyl--6-bromo-3-*O*-*tert*-butyldimethylsilyl-6-deoxy-*α*-D-glucopyranoside (**5**), and methyl 4-*O*-benzoyl-6-bromo-6-deoxy-2,3-di-*O*-*tert*-butyldimethylsilyl-*α*-D-glucopyranoside (Fig. 1). This mixture of products was separated on silica-gel column using the eluent chloroform:methanol = 40:1.

Both monosilyl derivatives were mesylated. To the cooled pyridine solution of silyl derivatives, mesyl chloride was added in a ratio 2.4 mol mesyl chloride to 1 mol silyl substrate. The reaction mixture was left at 0 °C for 24 h, and then upon the completion of the reaction, which flow was monitored using TLC, the obtained products (**6** and **7**) were isolated and separated on a silica gel column using chloroform as an eluent.

The structure of these two compounds was not checked because in the next step by the treatment with the base, the compound having TBDMS in position 3, cannot close the epoxide upon the attack of the alkoxide ion in position 4, and only the hydrolysis of benzoyl group takes place. Another compound having OMs group in the position 3 after hydrolysis closes into the 3,4-epoxide ring with *allo*-configuration (**8**, Fig. 1). This compound was characterized using $^1$H-NMR which spectrum is available in the Supplementary material (Fig. S-3). The simulated $^1$H-NMR spectrum of the same compound using NMRium[20] is also available in the Supplementary material (Fig. S-4), which was useful during the assignment process.

Earlier, based on *in vivo* studies, epoxides were considered to possess toxicity and poor pharmacokinetics.[21] However, the recent studies on compounds, such as fosfomycin (an antibiotic for the treatment especially of lower urinary tract infections), carfilzomib (an anti-cancer medication), fumagillin (an antimicrobial

agent) and TNP-470 (an anti-cancer candidate), clearly showed the role of the epoxide moiety in drug potency.[22] The obtained epoxide derivative can be used, therefore, as an intermediary in the syntheses of biologically active molecules.

## CONCLUSION

Epoxide derivatives are stable, but sufficiently reactive compounds to be used as intermediaries in syntheses. The synthesis of the epoxide derivative (methyl 3,4-anhydro-6-bromo-2-*O*-*tert*-butyldimethylsilyl-6-deoxy-*α*-D-allopyranoside) from a cheap starting material (*α*-D-glucose) was achieved in a high yield and the by minimal number of synthetic steps.

## SUPPLEMENTARY MATERIAL

Additional data and information are available electronically at the pages of journal website: https://www.shd-pub.org.rs/index.php/JSCS/article/view/12572, or from the corresponding author on request.

*Acknowledgements.* Authors want to thank all undergraduate students at Department of Chemistry, Faculty of Sciences and Mathematics, University of Niš, Niš, Republic of Serbia, for their help on the synthesis, and also graduated students who took final work in organic synthesis at Department of Chemistry, Faculty of Sciences and Mathematics, University of Niš, Niš, Republic of Serbia, and performed minor contributions to the synthesis. Special thanks to prof. dr Janoš Čanadi from University of Novi Sad, Republic of Serbia, who recorded the NMR spectra.

## ИЗВОД

## СИНТЕЗА МЕТИЛ 3,4-АНХИДРО-6-БРОМО-2-*O*-*ТЕРЦ*-БУТИЛДИМЕТИЛСИЛИЛ-6-ДЕОКСИ-*α*-D-АЛОПИРАНОЗИДА ИЗ *α*-D-ГЛУКОЗЕ

ЂОРЂЕ ГЛИШИН, ОЛГА ЈОВАНОВИЋ, ГОРДАНА СТОЈАНОВИЋ, АЛЕКСАНДРА ЖИВКОВИЋ, ДРАГАН СТОЈАНОВИЋ, МАРИНА ПАВЛОВИЋ и БИЉАНА АРСИЋ

*Департман за хемију, Природно–математички факултет, Универзитет у Нишу, Вишеградска 33, 18000 Ниш*

Неки једноставни угљени хидрати и њихови деривати се користе клинички у третману различитих болести. Епоксидни деривати, који се могу добити интрамолекулском елиминацијом воде из две вициналне хидроксилне групе су стабилна, али довољно реактивна једињења која се често користе као интермедијери у различитим синтезама. Синтеза епоксидног деривата, метил 3,4-анхидро-6-бромо-2-*O*-*терц*-бутилдиметилсилил-6-деокси-*α*-D-алопиранозида из *α*-D-глукозе је остварена у високом приносу у минималном броју синтетичких корака. Анхидрована глукоза је коришћена као полазни материјал који је трансформисан у метил-*α*-D-глукопиранозид коришћењем сувог, гасовитог хлороводоника. Тако добијени дериват је третиран са бензалдехидом у присуству цинк хлорида као Луисове киселине дајући метил-(*R*)-4,6-*O*-бензилиден-*α*-D-глукопиранозид. Добијено једињење је третирано са *N*-бромсукцинимидом (NBS) у дихлорметану у присуству баријум-карбоната дајући метил-4-*O*-бензоил-6-бромо-6-деокси-*α*-D-глукопиранозид. У следећој фази добијено једињење је третирано са *терц*-бутилдиметилсилил-хлоридом (TBDMSCl) у пиридину, и метил 4-*O*-бензоил-6-бромо-2-*O*-*терц*-бутилдиметилсилил-6-деокси-*α*-D-глукопиранозид је даље мезилован, и добијени метил-4-*O*-бензоил-6-бромо-2-*O*-*терц*-бутилдиметилсилил-6-деокси-3-*O*-мезил-*α*-D-глукопиранозид

је третиран са KOH на крају, дајући метил-3,4-анхидро-6-бромо-2-*O*-*трец*-бутилдиметилсилил-6-деокси-*α*-D-алопиранозид (принос 78 %).

(Примљено 31. августа 2023, ревидирано 8. јануара, прихваћено 24. априла 2024)

REFERENCES


1. S. A. Barkes, E. J. Bourne, *Adv. Carbohydr. Chem.* **7** (1952) 137 (https://doi.org/10.1016/S0096-5332(08)60084-3)
2. A. N. De Belder, *Adv. Carbohydr. Chem.* **20** (1965) 219 (https://doi.org/10.1016/S0096-5332(08)60300-8)
3. N. Mishra, V. K. Tiwari, R. R. Schmidt, in *Synthesis and Application*, V. Kumar Tiwari, Ed., Elsevier Inc., Amsterdam, 2020, pp. 1–69 (https://doi.org/10.1016/B978-0-12-816675-8.00001-4)
4. C. Piantadosi, C. E. Anderson, E. A. Brecht, C. L. Yarbro, *J. Am. Chem. Soc.* **80** (1958) 6613 (https://doi.org/10.1021/ja01557a040)
5. S. Penjarla, S. R. Prasad, D. S. Reddy, S. Banerjee, S. Penta, Y. S. Sanghvi, *Nucleosides Nucleotides Nucleic Acids* **37** (2018) 232 (https://doi.org/10.1080/15257770.2018.1460480)
6. J. S. Brimacombe, A. B. Foster, B. D. Jones, J. J. Willard, *J. Chem. Soc., C* (1967) 2404 (https://doi.org/10.1039/J39670002404)
7. E. J. Corey, A.Venkateswarlu, *J. Am. Chem. Soc.* **94** (1972) 6190 (https://doi.org/10.1021/ja00772a043)
8. V. H. Jadhav, S. B. Lee, H.-J. Jeong, S. T. Lim, M.-H. Sohn, D.W. Kim, *Tetrahedron Lett.* **53** (2012) 2051 (https://doi.org/10.1016/j.tetlet.2012.02.016)
9. K. K. Ogilvie, D. J. Iwacha, *Tetrahedron Lett.* **14** (1973) 317 (https://doi.org/10.1016/S0040-4039(01)95650-3)
10. T. Halmos, R. Montserret, J. Filippi, K. Antonakis, *Carbohydr. Res.* **170** (1987) 57 (https://doi.org/10.1016/0008-6215(87)85005-X)
11. A. Das, A. Bhaumik, T. Pathak, *Carbohydr. Res.* **487** (2020) 107870 (https://doi.org/10.1016/j.carres.2019.107870)
12. Dj. Glišin, O. Jovanović, G. Stojanović, *Zbornik radova Filozofskog fakulteta u Nišu, serija fizika i hemija* **1** (1988) 137 (UDK 542.91:547.455.6) (in Serbian)
13. H. S. El Khadem, *Carbohydrates in Encyclopedia of Physical Science and Technology* (Third ed.), Academic Press, Cambridge, MA, 2003, pp. 369–416 (https://doi.org/10.1016/B0-12-227410-5/00080-6)
14. O. Achmatowicz, R. Bielski, *Carbohydr. Res.* **55** (1977) 165 (https://doi.org/10.1016/S0008-6215(00)84452-3)
15. D. M. Hall, *Carbohydr. Res.* **86** (1980) 158 (https://doi.org/10.1016/S0008-6215(00)84593-0)
16. M. E. Evans, *Carbohydr. Res.* **21** (1972) 473 (https://doi.org/10.1016/S0008-6215(00)84931-9)
17. J. W. Van Cleve, *Carbohydr. Res.* **17** (1971) 461 (https://doi.org/10.1016/S0008-6215(00)82557-4)
18. S. Hanessian, in *General Carbohydrate Method*, R. L. Whistler, J. N. BeMiller, Eds., Academic Press, Cambridge, MA, 1972, pp. 183–189 (https://doi.org/10.1016/B978-0-12-746206-6.50035-7)
19. S. Hanessian, N. R. Plessas, *J. Org. Chem.* **34** (1969) 1035 (https://doi.org/10.1021/jo01256a059)

20. A. M. Castillo, L. Patiny, J. Wist, *J. Magn. Reson.* **209** (2011) 123 (https://doi.org/10.1016/j.jmr.2010.12.008)
21. M. M. Manson, *Br. J. Ind. Med.* **37** (1980) 317 (https://doi.org/10.1136/oem.37.4.317)
22. B. Kaur, P. Singh, *Bioorg. Chem.* **125** (2022) 105862 (https://doi.org/10.1016/j.bioorg.2022.105862).

Journal of the Serbian Chemical Society
JSCS@tmf.bg.ac.rs • www.shd.org.rs/JSCS
*J. Serb. Chem. Soc.* *89* (9) S245–S248 (2024) *Supplementary material*

SUPPLEMENTARY MATERIAL TO

# Synthesis of methyl 3,4-anhydro-6-bromo-2-*O*-*tert*-butyldimethylsilyl-6-deoxy-α-D-allopyranoside from α-D-glucose

ĐORĐE GLIŠIN, OLGA JOVANOVIĆ, GORDANA STOJANOVIĆ, ALEKSANDRA ŽIVKOVIĆ, DRAGAN STOJANOVIĆ, MARINA PAVLOVIĆ AND BILJANA ARSIĆ *

*Department of Chemistry, Faculty of Sciences and Mathematics, University of Niš, Višegradska 33, 18000 Niš, Republic of Serbia.*

*J. Serb. Chem. Soc.* *89* (9) (2024) 1123–1131

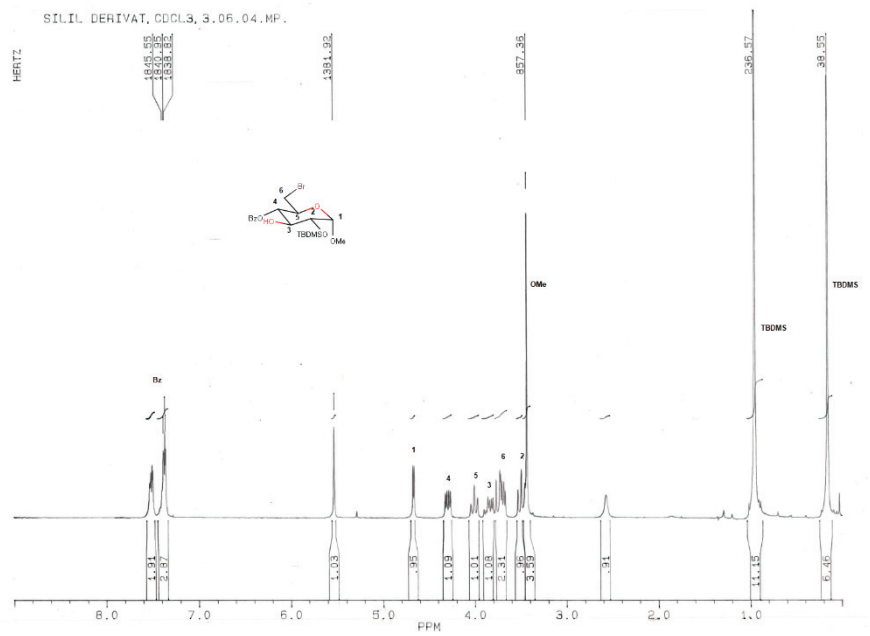


**Figure S-1.** $^1$H NMR spectrum with proton assignments for methyl 4-*O*-benzoyl-6-bromo-2-*O*-*tert*-butyldimethylsilyl-6-deoxy-α-D-glucopyranoside (**4**).

$^1$H NMR (250 MHz, $CDCl_3$): δ 7.36-7.60 (m, 5 H, OBz), 4.65 (d, 1 H, H-1), 4.35 (dd, 1 H, H-4), 3.81 (t, 1 H, H-5), 3.8-3.9 (m, 1 H, H-3), 3.65-3.80 (m, 2 H,

* Corresponding author. E-mail: biljana.arsic@pmf.edu.rs

H-6), 3.50 (m, 1 H, H-2), 3.43 (s, 3 H, OMe), 0.95 (s, 9 H, *tert*-butyl), 0.15 (s, 6 H, dimethylsilyl).

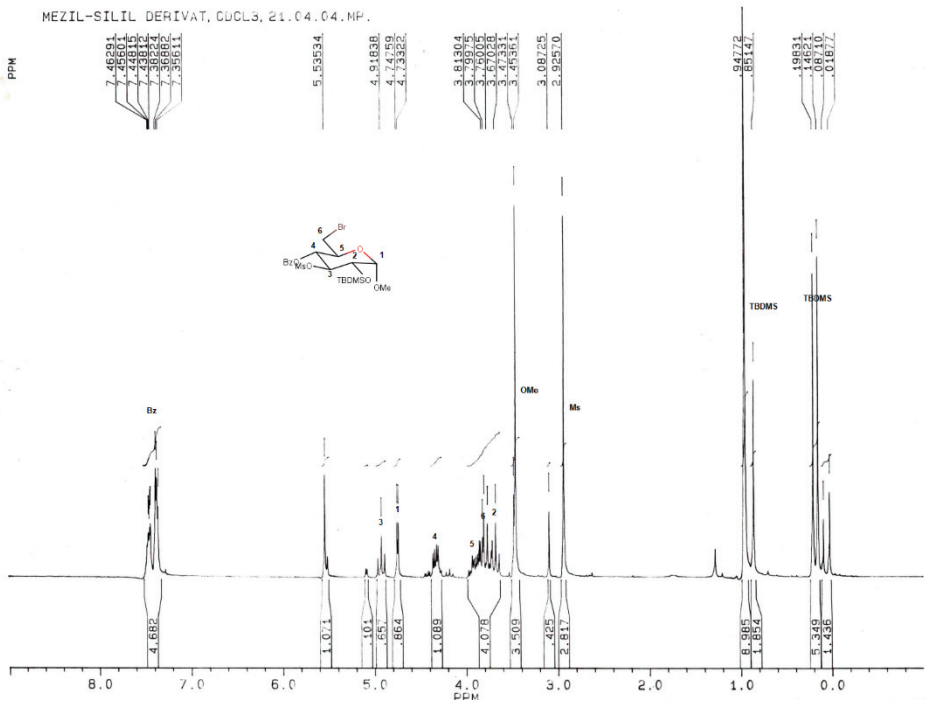


**Figure S-2.** $^1$H NMR spectrum with proton assignments for methyl 4-*O*-benzoyl-6-bromo-2-*O*-*tert*-butyldimethylsilyl-6-deoxy-3-*O*-mesyl-α-D-glucopyranoside (**6**).

$^1$H NMR (250 MHz, $CDCl_3$): δ 7.41 (m, 5 H, OBz), 4.92 (t, 1 H, H-3), 4.74 (d, 1 H, J=3.6 Hz, H-1), 4.2-4.4 (dd, 1 H, H-4), 3.81 (t, 1 H, J=3.3 Hz, H-5), 3.76 (m, 2 H, H-6), 3.67 (dd, 1 H, H-2), 3.46 (s, 3 H, OMe), 2.93 (s, 3 H, OMs), 0.95 (s, 9 H, *tert*-butyl), 0.17 (s, 6 H, dimethylsilyl).

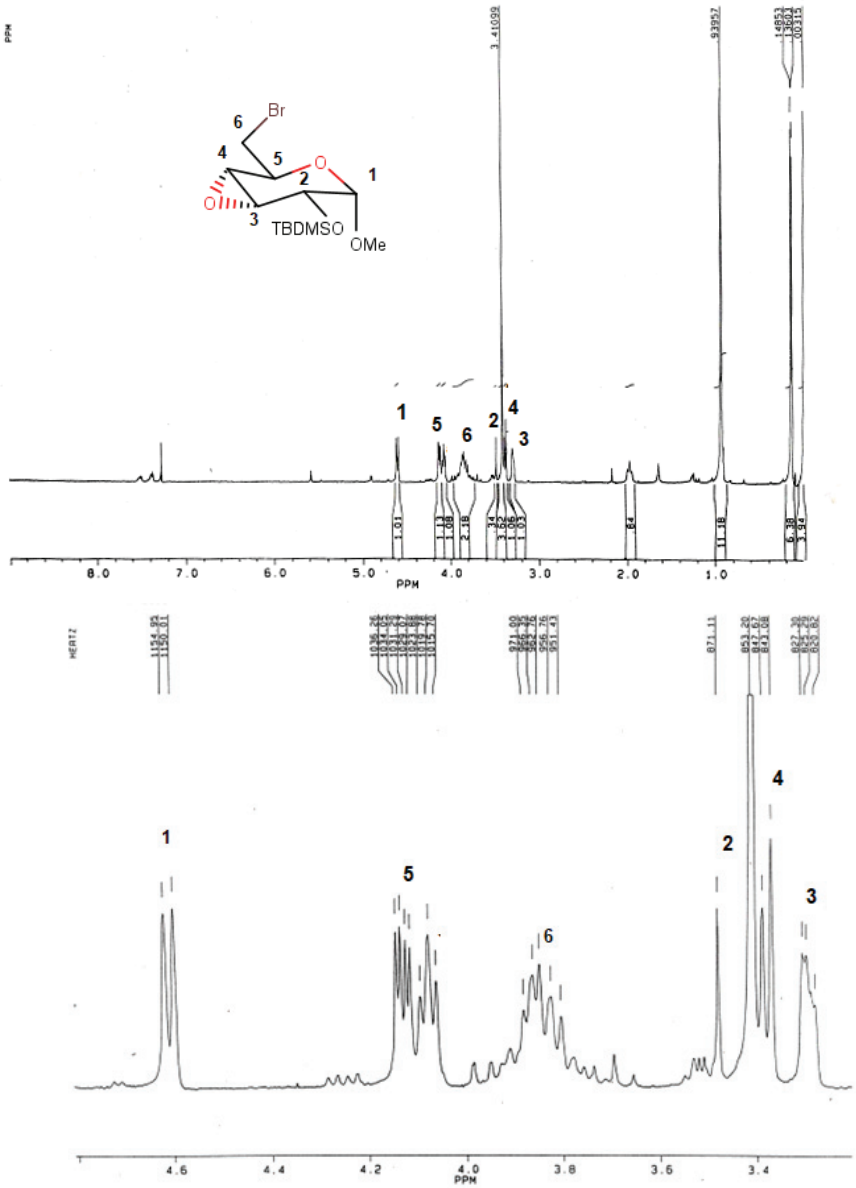


**Figure S-3.** [1]H NMR spectra with proton assignments for methyl 3,4-anhydro-6-bromo-2-*O*-*tert*-butyldimethylsilyl-6-deoxy-α-D-allopyranoside (**8**).

[1]H NMR (250 MHz, $CDCl_3$): δ 4.61 (d, 1 H, H-1), 4.14 (m, 1 H, H-5), 3.85 (m, 2 H, H-6), 3.41 (d, 1 H, H-2), 3.41 (s, 3 H, OMe), 3.38 (m, 1 H, H-4), 3.30 (m, 1 H, H-3), 0.94 (s, 9 H, *tert*-butyl), 0.14 (s, 6 H, dimethylsilyl).

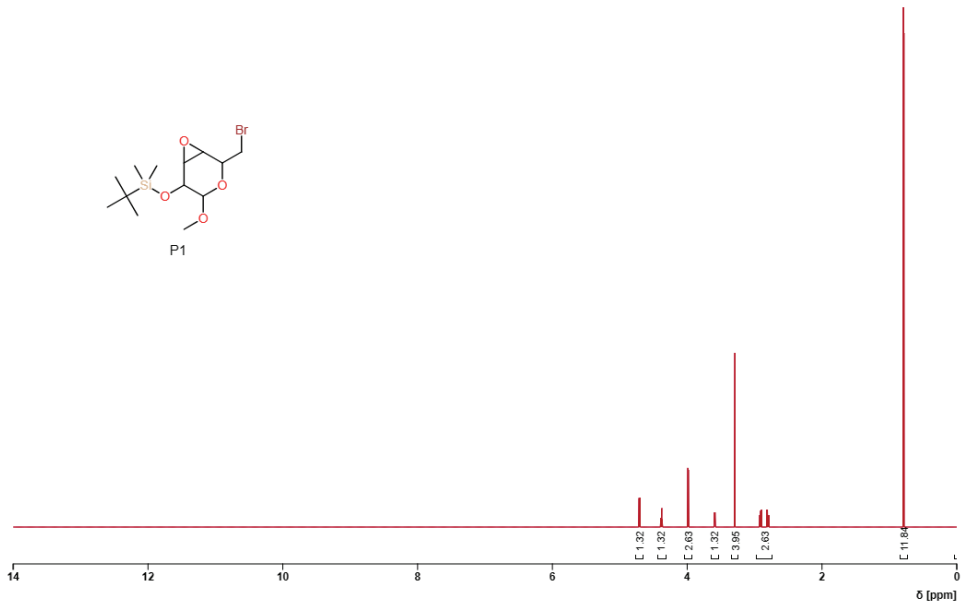


**Figure S-4.** Simulated $^{1}$H NMR spectrum of methyl 3,4-anhydro-6-bromo-2-*O*-*tert*-butyldimethylsilyl-6-deoxy-α-D-allopyranoside (**8**) using NMRium.

Journal of the Serbian Chemical Society
JSCS@tmf.bg.ac.rs • www.shd.org.rs/JSCS
*J. Serb. Chem. Soc.* *89* (9) 1133–1145 (2024)
*JSCS–5777*
*Original scientific paper*
Published 7 September 2024

# Synthesis of novel *N*-substituted benzyl *N*-(1,3-benzothiazol-2-yl) acetamides and their *in vitro* antibacterial activities

HANDAN CAN SAKARYA[1]*, KAMURAN GÖRGÜN[1] and CANSU FILIK IŞCEN[2]

[1]*Eskişehir Osmangazi University, Faculty of Science, Department of Chemistry, 26480, Eskişehir, Turkey and* [2]*Eskişehir Osmangazi University, Faculty of Education, Department of Elementary Education, 26480 Eskişehir, Turkey*

(Received 20 October 2023, revised 19 January, accepted 11 June 2024)

*Abstract*: The novel Schiff bases **3a**–**d** were synthesized by reacting 6-methyl--2-aminobenzothiazole and different substituted benzaldehydes. Afterwards, the obtained Schiff bases were reduced with $NaBH_4$ to form amine compounds **4a**–**d**. In the final step, reaction of the amine with chloroacetyl chloride gave the novel amide derivatives **5a**–**d**. The structures of the all novel synthesized compounds were characterized by FT-IR, $^1$H-NMR, $^{13}$C-NMR, ESI MS, HETCOR, 2D ($^1$H–$^1$H) COSY spectra and elemental analyses. The antimicrobial activities of the novel synthesized compounds, were tested against some Gram-positive and Gram-negative bacterial as well as fungal species and the results were discussed.

*Keywords*: Schiff base; benzothiazole-2-yl-amide; acylation; antibacterial activity; minimum inhibitory concentration.

## INTRODUCTION

Compounds containing the azomethine group (–CH=N–) have been known as Schiff bases. Schiff bases can be prepared by the condensation reaction of a primary amine with an active carbonyl group. Schiff bases contain active azomethine groups (–CH=N–), so they are compounds widely studied. In some studies, Schiff bases have been reported to exhibit various antibacterial, antifungal, herbicidal and clinical activity.[1–3] Heterocyclic compounds are organic compounds that contain at least one heteroatom other than carbon such as sulfur, nitrogen, oxygen and phosphorus, which are within a cyclic carbon structure, noting that these atoms are either outside or inside the ring. Heterocyclic compounds are the most important class of organic compounds as they have excellent activity against many diseases.[4–6] Among these heterocyclic compounds are Schiff bases. For this reason, many heterocyclic Schiff base derivatives have

* Corresponding author. E-mail: hsakarya@ogu.edu.tr
https://doi.org/10.2298/JSC231020059C

been synthesized and reported to show biological activities such as fungicide, antibiotic, pesticide,[7,8] cytotoxic,[9] anticonvulsants,[10] anticancer[11] and antifungal activities.[12]

Benzothiazole derivatives are bicyclic heterocycles which act as a weak base formed in the benzene ring fused with 4- and 5-positions for the thiazole rings and these exhibit wide ranges of chemical activities. Compounds with a thiazole nucleus in their structure have been widely studied because this five-membered aromatic ring containing sulfur and nitrogen atoms plays a vital role in the structure of various drugs, including the antineoplastic agents thiazofurin and dasatinib.[13] Similarly substituted *N*-benzothiazol-2-yl-amides exhibit a wide variety of biological properties such as ubiquitin ligase inhibitors,[14a] antitumor,[14b] anti rotavirus,[14c] the adenosine receptor,[14d–e] and the nuclear hormone receptor.[14e] In particular, some benzothiazoles substituted at the 2-position with a benzoyl amino moiety showed antibacterial, antifungal and antitubercular activity.[14f]

In our present work, we report on: *i*) the synthesis of four novel benzothiazole derivated Schiff bases in varied solvents such as ethanol, methanol, tetrahydrofuran, toluene, acetonitrile and benzene as well as ethyl lactate; *ii*) obtaining novel amine compounds by reduction of Schiff bases, *iii*) synthesis of the corresponding novel amide, *iv*) spectroscopic characterization of the compounds obtained and *v*) the evaluation of their antimicrobial activity. Ethyl lactate is an important monobasic ester. It is a clear to slightly yellow liquid, and is found naturally in small quantities in a wide variety of foods, including wine, chicken, and some fruits. Traditional synthesis methods of Schiff bases have used petroleum-derived solvents such as toluene, which are often toxic. Ethyl lactate is an environmentally benign solvent with effectiveness comparable to petroleum-based solvents. Ethyl lactate has interesting properties such as being a solvent that is non-corrosive, non-carcinogenic, non-teratogenic, biodegradable and does not harm the ozone layer. Moreover, ethyl lactate forms a suitable solution with water for the synthesis of Schiff base. Additionally, this green solvent provides many advantages, such as a catalyst-free protocol, short reaction times, simple operation and processing of products without the need for chromatography.

## EXPERIMENTAL

### *General procedures*

Melting point: Gallenkamp apparatus. IR spectra: Perkin Elmer Precisely Spectrum 100 FT-IR spectrophotometer; in KBr; $\tilde{\nu}$ in $cm^{-1}$. $^{1}$H-NMR, $^{13}$C-NMR, 2D ($^{1}$H–$^{1}$H) COSY and HETCOR spectra: Bruker DPX FT NMR (500 MHz) and (125 MHz) spectrometer; in TMS (DMSO-$d_6$); $\delta$ in ppm relative to $Me_4Si$ as the internal standard, $J$ in Hz. ESI MS: (LS/MS-APCl) AGILENT 1100 MSD spectrometer; at 100 eV; in $m/z$. Elemental analyses: Elementary Analsensysteme GmbH varioMICRO CHNS (Turkish Technical and Scientific Research Council Laboratories, Ankara, Turkey). TLC was performed on pre-coated silica gel plates (Merck 60, $F_{254}$, 0.25 mm). Organic solvents used were at HPLC grade or were purified by the standard procedure. All reagents were of commercial quality or were purified before use.

The spectroscopic data and spectra of the novel synthesized compounds **3a**–**5d** are given in the Supplementary material to this paper.

Bacterial and yeast strains obtained from American Type Culture Collection (ATTC; Rockville, MD, USA), Northern Regional Research Laboratory (NRRL; USDA; Peoria, IL, USA) were employed in this work. They included gram-positive bacteria (*Staphylococcus aureus* ATCC 6538, *Staphylococcus epidermidis* ATCC 12228, *Bacillus subtilis* NRRL-B 4378) and gram-negative bacteria (*Escherichia coli* NRRL-B 3008, *Pseudomonas aeruginosa* NRRL-B 2679). The following 2 fungal strains were also tested: *Candida albicans* NRRL-Y 12983 and *Candida parapsilosis* NRRL-Y 12696.

*Synthetic procedures*

*Method A for the synthesis of* N-*[(2-methylphenyl) methylidene]-6-methyl-1,3-benzothiazol-2-amine (**3a**)*.[9,15] A solution of 2-amino-6-methyl benzothiazole (**1**, 30 mmol) and *O*-methyl benzaldehyde (**2a**, 28.7 mmol) in ethanol (100 µl) were refluxed for 2 h at 75 °C. The mixture was allowed to stand at room temperature overnight and then concentrated. The residue was washed with *n*-hexane (2×100 µl) and filtered off then it was hydrolyzed in water and extracted with ethyl acetate (EtOAc, 4×50 µl). After drying over with anhydrous $Na_2SO_4$ and evaporation, crystalline product (**3a**, 70 %) was obtained and recrystallized from dichloromethane (DCM). Compound **3d** was prepared using the same method described above.

*Method B for the synthesis of* N-*[2-methoxyphenylmethylidene]-6-methyl-1,3-benzothiazol-2-amine (**3b**)*.[9] The solution of 2-amino-6-methyl benzothiazole (**1**, 5 mmol), *O*-methoxy benzaldehyde (**2b**, 6 mmol) and acetic acid (1 µl) in ethanol (25 µl) were heated for 30 min until no starting amine remained. After waiting for a while at room temperature, a precipitate formed, filtered, washed with diethylether, and the resulting product was crystallized in dichloromethane (**3b**, 76 %).

*Modified method C for the synthesis of* N-*[2-hyroxyphenylmethylidene]-6-methyl-1,3-benzothiazol-2-amine (**3c**)*.[16] A mixture of 2-amino-6-methyl benzothiazole (**1**, 5 mmol) the *O*-hydroxy benzaldehyde (**2c**, 6 mmol) in ethyl lactate–water system (3 µl, 70 vol. % ethyl lactate in water) was stirred at room temperature for 4 min. After completion of the reaction, as indicated by TLC, the reaction mixture was left overnight. The formed precipitate was isolated by filtration and washed with water to furnish pure *N*-[(2-hyroxyphenyl)methylidene]-6-methyl-1,3-benzothiazol-2-amine derivatives (**3c**) in excellent yields (90 %), with no need of purification.

*General procedure for the synthesis of* N-*(2-Methylbenzyl)-6-methyl-1,3-benzothiazol-2-amine (**4a**)*.[17,18] *N*-[2-methylphenylmethylidene]-6-methyl-1,3-benzothiazol-2-amine (**3a**, 2.5 g, 9.3 mmol) was dissolved in methanol (75 µl). Then, $NaBH_4$ was added to the stirred solution at room temperature until the solution became colourless. Cold water was added to the solution to precipitate the products. The precipitates were recrystallized from methanol to obtain amine derivative (**4a**, 87 %). Compounds **4b**–**d** were prepared using the same method described above.

*General procedure for the synthesis of 2-chloro*-N-*[6-methyl-1,3-benzothiazol-2-yl]-N-[2-methylbenzyl] acetamide (**5a**)*.[19] Chloracetyl chloride (0.148 µl×10, 1.86 mmol) was added to the novel amine compound (**4a**, 0.50 g, 1.86 mmol) in dry dichloromethane (DCM, 50 µl) in the presence of triethylamine (1 µl, 7.10 mmol). The mixture was then heated to reflux for 2 h and evaporated in vacuo. The residue was hydrolyzed in water (10 ml) and extracted with dichloromethane (5×10 µl). The combined organic layers were dried over anhydrous $MgSO_4$, filtered and evaporated in vacuo. The crystalline was recrystallized from chloroform/dichloro-

methane to obtain (**5a**, 0.48 g, 76 %). Compounds **5b**–**d** were prepared using the same method as described above.

*Biological activity*

The standardized agar well diffusion method was used to determine the activity of the synthesized compounds against sensitive organisms.[20] These organisms were *Staphylococcus aureus*, *Staphylococcus epidermidis* and *Bacillus subtilis* as Gram-positive bacteria, *Escherichia coli* and *Pseudomonas aeruginosa* as Gram-negative bacteria, *Candida parapsilosis* as fungus strains. Mueller–Hinton broth (MHB) is used to determine the susceptibility of bacteria to sulphonamides by the tube dilution method. In this study, the bacterial and yeast cultures were incubated in MHB at 35–37 °C until they were visibly turbid. The density of these cultures was adjusted to a turbidity equivalent to that of the 0.5 McFarland standard with sterile saline. Bacterial and yeast cell suspensions were finally diluted, respectively, to $5\times10^5$ and $10^4$ CFU/µl for use in the assays. Mueller–Hinton agar (MHA) for bacteria and Sabouraud dextrose agar (SDA) for fungi were sterilized in a flask and cooled to 45–50 °C, distributed to the sterilized petri dishes (9 cm). The entire surfaces of the MHA plates and SDA plates were inoculated with the bacteria and fungi by spreading them with a sterile swab dipped into the adjusted suspensions. Six wells, each 6 mm in diameter, were cut out of the agar and 20 µl of the compounds. The inoculated petri dishes were incubated at 37 °C for 24 h. The results were expressed in terms of the diameter of the inhibition zone. Penicillin and chloramphenicol were used as positive controls for bacteria, fluconazole as a positive control for fungi. All assays were performed in duplicate.[21,22]

*Minimum inhibitory concentration (*MIC*)*

*MIC* was determined by the micro dilution method using a 96 well plate according to NCCLS[20] and 100 µl of MHB was placed in each well. Then, the stock solutions of compounds were dissolved in DMSO and transferred into first well, and serial dilutions were performed so that concentrations in the range of 625–5000 µg/ml were obtained. The inoculums were adjusted to contain approximately $10^5$ CFU/ml bacteria and $10^4$ CFU/ml fungi, as described previously. 100 µl of the inoculums was added to all wells and the plates were incubated at 37 °C for 24 h. *MIC* values were detected by adding 20 µl of 0.5 % triphenyl tetrazolium chloride (TTC) aqueous solution. The *MIC* value was taken as the lowest concentration of the compounds that inhibited any visible bacterial and fungi growth, as indicated by TTC staining after incubation.[20] Penicillin, chloramphenicol and fluconazole were used again as the reference antibiotic control.

## RESULTS AND DISCUSSION

### *Synthesis and characterization*

The title compounds **3a**–**5d** were synthesized according to the process described in Fig. 1. The structures of all the compounds **3a**–**5d** were established on the basis of FT-IR, $^1$H-NMR, $^{13}$C-NMR, HETCOR, 2D($^1$H–$^1$H) COSY and MS spectra and elemental analyses. In all compounds, the assignment of individual proton signals in the $^1$H-NMR spectra was based on $J_{HH}$ coupling constant values and confirmed by $^1$H–$^1$H COSY and HETCOR spectra.

The novel Schiff bases **3a**–**d** were synthesized according to the route shown in Fig. 1. Among these compounds, only compound **3c** was synthesized by an alt-

ernative method other than that shown in Fig. 1. To synthesize Schiff base **3c**, various solvents such as ethanol, methanol, tetrahydrofuran, toluene, acetonitrile, benzene and ethyl L-lactate were used. For this purpose, it was aimed to increase the efficiency of the Schiff base, reduce the reaction time and obtain pure product without using purification techniques (Table I). Traditional synthesis methods of Schiff bases use petroleum-derived solvents such as toluene, which are often toxic. However, ethyl lactate is a green solvent and forms a suitable solution with water for the synthesis of Schiff base. In addition, it was observed that Schiff base was formed in high yield when some catalysts, such as scandium (III) triflate, ytterbium (III) triflate, were added to the medium with ethyl L-lactate solvent. For compound **3c**, in addition to the synthesis method of other compounds, we synthesized the Schiff base using ethyl L-lactate as the green solvent. As a result of our experiment on the **3c** compound for trial purposes, Schiff base **3c** was obtained with good yield (Table I, entry 7). Additionally, the reaction was complete within four minutes at room temperature and the imine was pure enough to avoid the necessity for recrystallization or other solvent insensitive isolation or purification procedures.

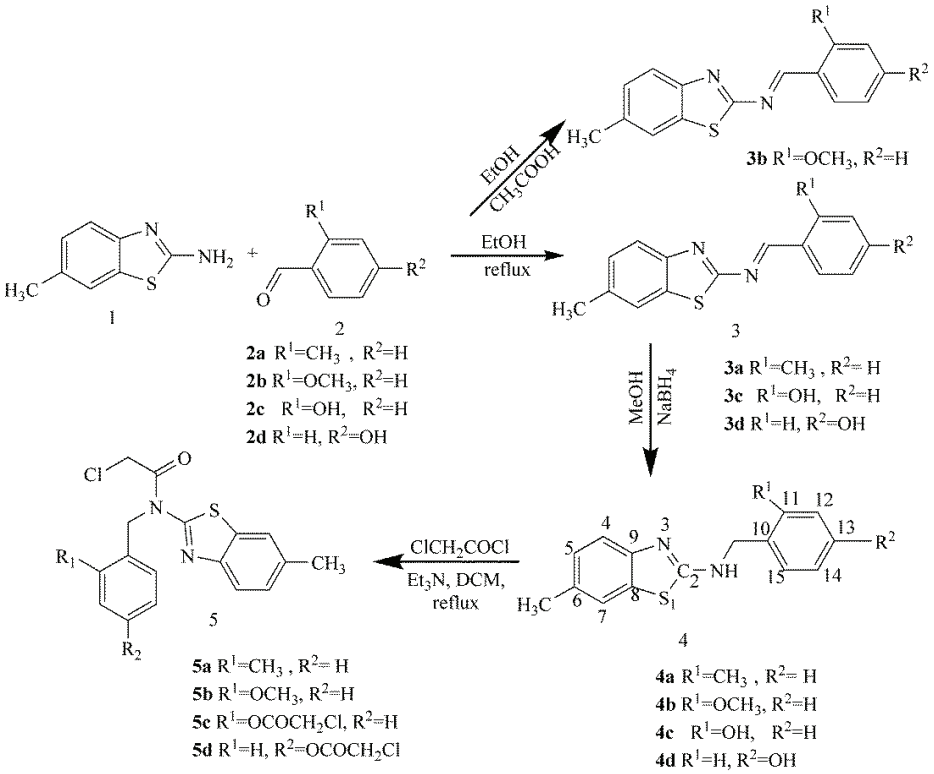


Fig. 1. General scheme of synthetic procedure for compounds **3a**–**5d.**

TABLE I. Reaction conditions for the synthesis of compound **3c**

| No. | Solvent | Time | Yield[a], % |
|---|---|---|---|
| 1 | Acetonitrile | 24 h | 12[b] |
| 2 | Benzene | 24 h | 25[b] |
| 3 | Ethanol | 2 h | 85[b] |
| 4 | Ethyl lactate | 4 min | 95[d] |
| 5 | Methanol | 24 h | c[b] |
| 6 | THF | 24 h | c[b] |
| 7 | Toluene | 24 h | 35[b] |

[a]Isolated yield; [b]all the reactions were carried out at reflux; [c]no reaction; [d]the reaction was carried out at room tempurature

The structures of compounds **3a**–**d** were established from their FTIR, $^1$H--NMR, $^{13}$C-NMR, COSY and HETCOR (also labeled COSY C single bond H) spectra. The FTIR spectra of Schiff bases **3a**–**d** showed a strong band at 1610, 1615, 1620 and 1618 cm$^{-1}$, attributed to azomethine ν(CH=N) (IR spectra of compounds **3a**–**5d** are given in the Supplementary material). The absence of band around 1730 and 3330 cm$^{-1}$ due to carbonyl stretching and $NH_2$ stretching of 2-aminobenzothiazole and aldehyde respectively indicates the condensation of aromatic aldehyde and aromatic amines. $^1$H-NMR spectra also confirmed the proposed stoichiometry and structure of compounds **3a**–**d** ($^1$H-NMR spectra of compounds **3a**–**5d** are given in the Supplementary material). In the $^1$H-NMR spectra of compounds **3a**–**d**, the chemical shift of the aromatic protons was observed within the $\delta$ 6.96–8.12 ppm region of spectrum. The hydroxyl protons for compounds **3c** and **3d** showed as a broad signal within the $\delta$ 10.5–11.5 ppm. The observation of the OH proton of compound **3c** at $\delta$ 11.5 ppm is due to the hydrogen bond of the imine nitrogen, whereas the resonance of the hydroxide proton of compound **3d** was observed at $\delta$ 10.5 ppm due to the absence of hydrogen bond. The imine proton in compounds **3a**–**3d** was observed as a singlet in the range of $\delta$ 9.02–9.45 ppm. Among the novel compounds, the imine proton in compound **3c**, which resonates in the downfield at $\delta$ 9.45 ppm. This is due to the hydrogen bond between the imine nitrogen of the phenyl ortho substituent hydroxide group. However, the imine proton of compound **3d** was observed at $\delta$ 9.02 ppm, which was expressed as the increase of electron density around the imine due to the n→π conjugation effect of hydroxy oxygen. Singlets of benzothiazole substituent methyl protons were observed at $\delta$ 2.45, 2.46, 2.44 and 2.40 ppm for compounds **3a**–**d**, respectively. Two sharp singlets were also observed at $\delta$ 2.65 and 3.96 ppm for methyl protons ($CH_3$–Ar) and methoxy protons (Ar–$OCH_3$) for compound **3a** and **3b**, respectively. The signal for the remaining six protons appeared at 7.14–8.11 ppm, which was assigned to aromatic protons. For compound **3b**, a triplet at 7.14 ppm, doublet at 7.24 ppm and another doublet at 7.83 ppm were assigned for aromatic protons H14, H12 and H4, respectively. In addit-

ion, H5, H13 and H15 protons of the aromatic rings resonate as doublet of doublet at 7.35 ppm, doublet of triplet at 7.66 ppm and doublet of doublet at 8.11 ppm, correspondingly. Similar signals were observed in the $^1$H-NMR spectra of compounds **3a**, **3c** and **3d** (the numbering of the protons of the compound is given in Fig. 1). This assignment was additionally substantiated by $^1$H–$^1$H COSY analysis ($^1$H–$^1$H COSY spectra are given in the Supplementary material). In the $^1$H–$^1$H COSY spectrum of compound **3b**, the two signals in the compound, the doublet of the doublet, are assigned as belonging to the H5 proton and the H13 proton. The H5 proton coupled first to the H4 proton, then to the H7 proton long--range coupling. On the other hand, the H15 proton interacts with both the H14 proton and the H13 proton, giving the signal of the doublet of the doublet. Similarly, the H13 coupled to the H14 proton, the H12 proton, and the H15 proton, giving the triplet of the doublet (Fig. S-6 of the Supplementary material). The HETCOR spectrum compound **3b** clearly showed that there were no hydrogen atoms bonded to C2, C6, C8, C9, C10 and C11 as expected. The correlations between C4 and H4, C7 and H7, C5 and H5 in the benzothiazole ring and C12 and H12, C14 and H14, C15 and H15, C13 and H13 in the phenyl ring were also clearly observed in the HETCOR spectrum (Fig. S-7 of the Supplementary material). The $^{13}$C-NMR spectrum of compounds **3a**–**d** showed 16 signals corresponding to the 16 carbon atoms present in the molecule as shown in Fig. 1. In the $^{13}$C-NMR spectrum, signals belonging to the imine carbon were observed at 164, 161, 166 and 166.5 ppm for compounds **3a**–**d** (Figs. S-12 and S-14 of the Supplementary material). Due to the presence of the carbon–nitrogen π-bond, the signal of the azomethine carbon was observed in the downfield region. The 13 signals observed at 117.88–150.54 ppm were also marked as belonging to aromatic carbons, for compound **3a**. Similar signals were observed in the $^{13}$C-NMR spectra of compounds **3b**–**d.** The ESI mass spectrum of compound **3b** showed a molecular ion peak at *m*/*z* 283.1 ($C_{16}H_{14}N_2SO + H^+$) and fragment ions at *m*/*z* 223.1 ($C_{13}H_7N_2S + H^+$), 165.1 ($C_{12}H_7N + H^+$), Fig. S-8 of the Supplementary material.

Reduction of **3a**–**3d** with $NaBH_4$ in methanol at room temperature occurred easily to give the corresponding amine derivative **4a**–**d** as the only product in good yields 87–93 % (Fig. 1). The structures of **4a**–**d** were clearly assigned as amine compounds by FT-IR, $^1$H-NMR, $^{13}$C-NMR, HETCOR, COSY and ESI MS spectra and elemental analyses. The FT-IR spectral data of the amines **4a**–**d** showed medium intensity absorption bands at 3412, 3430, 3409 and 3434 cm$^{-1}$, respectively, which were attributed to the ν(NH) stretching vibration. This assignment was further supported by the disappearance of the absorption band that was assigned to the azomethine proton. The $^1$H-NMR spectra of the compounds **4a**–**d** revealed a fine triplet peak at $\delta$ 8.25–8.30 ppm for the –NH– group ($^1$H-NMR spectra of compounds **3a**–**5d** are given in the Supplementary mater-

ial). The signals of the methylene protons for the –$CH_2$–NH– group were detected in the region expected in the range of $\delta$ 4.47–4.55 ppm as a doublet. The spectra of **4c** and **4d** show a singlet at $\delta$ 9.75 and $\delta$ 9.30 ppm due to the hydrogen of the hydroxyl group. In the $^1$H-NMR spectrum of compound **4b**, methoxy and methyl protons were observed at $\delta$ 2.31 and 3.83 ppm as singlets. The four doublets at $\delta$ 7.02 and 7.25 ppm indicated the H12 and H4, H5 and H15 protons, respectively. The signals observed at $\delta$ 6.92 and 7.29 ppm as a triplet and at $\delta$ 7.46 ppm as a singlet may be assigned to protons H14, H13 and H7, respectively (Figs. S-21 and S-22 of the Supplementary material). Aromatic protons of compounds **4a**, **4c** and **4d** showed similar characteristics as those discussed in compound **4b**. In the $^{13}$C-NMR spectrum of **4b**, carbon atoms of the phenyl and benzothiazole ring were observed at $\delta$ 111.06, 118.18, 120.62, 121.32, 126.79, 126.96, 128.46, 128.81, 130.44, 130.97, 150.83, 157.32, 166.00 ppm. The methyl, methoxy and methylene carbon atoms were observed at $\delta$ 21.22, 42.89 and 55.82 ppm, respectively (Fig. S-23 of the Supplementary material). Similar signals were observed in the $^{13}$C-NMR spectra of compounds **4a**, **4c** and **4d**. In the HETCOR spectrum of compound **4b**, the signals of aromatic carbon atoms were observed at 111.06, 118.18, 120.62, 121.32, 126.79, 126.96, 128.46, 128.81, 130.44, 130.97, 150.83, 157.32 and 166.00 ppm, respectively (Figs. S-26 and S-27 of the Supplementary material). The mass spectrum of compound **4b** shows a molecular ion peak at *m*/*z* 285.0 (10.2 %) of $M^+ + 1$.

The substituted amine compounds **4a**–**d** were reacted with chloroacetyl chloride in the presence of triethylamine to provide the corresponding amides **5a** and **5b** and esters **5c** and **5d** in good yields 76–82 % (Fig. 1). The structures of compounds **5a**–**d** were established from FTIR, $^1$H-NMR, $^{13}$C-NMR, mass spectra and elemental analyses. The FT-IR spectra of the ester products depicted ν(N–C=O) bands within the range of 1668–1663 cm$^{-1}$ and ν(OC=O) bands at 1775–1762 cm$^{-1}$, which supported the assigned structures **5c** and **5d.** In the FT--IR spectra of the obtained amides **5a** and **5b**, carbonyl amide absorption bands appeared at 1698 and 1683 cm$^{-1}$, respectively. The $^1$H-NMR spectrum of compound **5b** exhibited four doublets at $\delta$ 6.92, 7.08, 7.25 and 7.63 ppm due to H12, H15, H5 and H4 protons, respectively. In addition, H13 proton and H14 proton of the phenyl ring resonated as triplet at 6.87 and 7.29 ppm, correspondingly. The one singlet at 7.81 ppm was assigned for H7 proton (Figs. S-42–S44 of the Supplementary material). Aromatic protons of compounds **5a**, **5c** and **5d** showed similar characteristics to those discussed in compound **5b**. Three sharp singlets were also observed at $\delta$ 2.40, 3.53 and 4.75 ppm for the methyl protons ($CH_3$––benzothiazole), the methoxy protons (Ar–$OCH_3$) and the methylene protons (–$NCH_2$–), respectively. Another singlet at $\delta$ 5.43 ppm was assigned for –N(CO)––$CH_2$Cl group. The triplet originating from the NH protons at $\delta$ 8.22 ppm in compound **4b** was not detected in compound **5b**. In the $^1$H-NMR spectrum of

compounds **5c** and **5d**, unlike compounds **5a** and **5d**, another singlet at $\delta$ 4.80 and 4.76 ppm was assigned to the –N(CO)$CH_2$Cl group. The molecular ion mass of compound **5a** was observed as *m*/*z* 345 in ESI MS. Ion peaks at *m*/*z* 309 and 267 showed that firstly the chlorine atom and then the $CH_2$ClCO– group were ionized from the ionic mass of the molecule (Fig. S-40 of the Supplementary material). The $^{13}$C-NMR spectrum of compounds **5a** and **5b** had a signal at 168 and 167.86 (N–C=O–) as expected, leading us to predict that the product is an amide compound. The $^{13}$C-NMR spectrum of compounds **5c** and **5d** could not be obtained despite many attempts.

*Antimicrobial activity studies*

The antibacterial activity of the twelve novel synthesized compounds **3a**–**5d** was tested against a range of Gram-positive and Gram-negative bacteria and two fungal species in the range of *MIC* values of 625–5000 μg/μl. As shown in Table II, these organisms were *S. aureus*, *S. epidermidis* and *B. subtilis* as Gram-positive bacteria and *E. coli* and *P. aeruginosa* as Gram-negative bacteria, *C. parapsilosis* as fungus strains. Among all compounds tested, **3b**–**d** and **4b** and **4c** showed activity against the bacteria at different *MIC* values (625–5000 μg/μl). However, compounds **3a**, **4a** and 4**b** and **5a**–**c** were not active against the bacteria tested. According to preliminary results, among these compounds, compound **3c** showed activity against Gram-negative bacteria *S. aureus* ATCC 6538, *P. aeruginosa* NRRL-B 2679 with a *MIC* value of 625 μg/μl. Whereas, compounds **3b**–**d** exhibited activity against *C. parabsilosis* NRRL-Y 12696 at a *MIC* of 1250 μg/μl, while compound **4c** showed activity against gram-negative *P. aeruginosa* NRRL-B 2679 and *C. parapsilosis* NRRL-Y 12696 fungus strains with *MIC* values ranging from 2500 to > 50000 μg/μl. Moreover, compounds **3b**–**d** and **4c** showed antifungal activity on *C. parapsilosis* at an inhibition zone of 8 to 14 mm and *MIC* value (1250–2500 μg/μl), but other new compounds such as **3a**, **4a**, **4b** and **5a**–**d** were inactive. According to these results, we could see that among all the compounds, the compound with the ortho substituent hydroxy group, where only the imine group was present, was more active. For example, compound **3c** was slightly more effective compared to compounds **3b** and **3d.** We also found that the scaffold containing the imine group retained antibacterial activity, and the presence of a hydroxy substituent group, especially at the ortho position, increased the activity. Recent reports demonstrated the role of *C. parapsilosis* in the etiopathogenesis of otitis, arthritis, endocarditis, endophtalmitis, meningitis, wound infections, denture stomatitis, reproductive system infections in women, vaginitis, cervicitis and salpingitis.[24] The reason for that different sensitivity between the fungi and bacteria can be found in different transparency of the cell wall.[25] Among the compounds we synthesized, only compounds **3b**–**d** and **4c** showed antifungal activity against *C. parapsilosis* in an inhibition zone of 8–14

mm. This is due to the activity of the imine and amine groups and the substituted electron donating $OCH_3$ and OH in the phenyl ring. Therefore, the biological activity of compounds **3–d** and **4c** depends on the substituted groups. Depending on the substituent groups in the compounds, the activity is OH > $OCH_3$ > $CH_3$. In addition, none of the new compounds synthesized were effecttive on other bacteria and fungi such as *S. epidermidis*, *E. coli*, *B. subtilis* and *C. albicans*.

TABLE II. Antibacterial and antifungal activities of compound **3b**–**4c** as inhibition zone diameters (mm) and *MIC* (μg/μl); P = peniciline G; C = chloramphenicol; F = fluconazole

| Microorganism | **3b** | **3c** | **3d** | **4b** | **4c** | P | C | F |
|---|---|---|---|---|---|---|---|---|
| *S. aureus* ATCC 6538 | – | 625 | – | – | – | 62.5 | 7.8 | – |
| *P. aeuroginosa* NRRL-B 2679 | – | 625 | – | – | 5000< | 62.5 | 62.5 | – |
| *C. parabsilosis* NRRL-Y 12696 | 1250 | 1250 | 1250 | – | 2500 | – | – | 125 |

For the further determination of the antibacterial spectrum of our compounds, the most promising agent **3c** was tested against to commonly used antimicrobial agent (Table III). Among all novel compounds, **3c** showed the highest inhibitory activity against the gram-negative bacteria *S. aureus* and *P. aeruginosa* (*MIC* = 625 μg/μl) compared to the reference drugs (peniciline G: *MIC* = 62.5 μg/μl, chloramphenicol: *MIC* = 7.8 μg/μl, respectively). *S. aureus* bacteria have been reported to be the most common cause of bloodstream, skin and soft tissue, and respiratory tract infections. This pathogen is among those that cause severe infections in patients.[23] *P. aeruginosa* is frequently associated with infections of the urinary and respiratory tract in humans. *P. aeruginosa* infections are also common in patients receiving treatment for severe burns or other traumatic skin damage and in people suffering from cystic fibrosis.[20] Compounds **3b**–**d** revealed the highest *MIC* (1250 μg/μl) against standard *C. parabsilosis*, while the reference compounds peniciline G and chloramphenicol were inactive.

TABLE III. Microbial activity of novel synthesized compounds (**3b**–**5c**); P – peniciline G; C – chloramphenicol; F – fluconazole; inactive = inhibition < 6mm; slightly active = inhibition zone 6–9 mm; moderately active = inhibition zone 9–12 mm and highly active = inhibition zone > 12 mm

| Microorganism | **3b** | **3c** | **3d** | **4a** | **4b** | **4c** | **4d** | **5a** | **5b** | **5c** | P | C | F |
|---|---|---|---|---|---|---|---|---|---|---|---|---|---|
| *S. aureus* ATCC 6538 | – | 10 | – | – | – | – | – | – | – | – | 21 | 24 | – |
| *S. epidermidis* ATCC 12228 | – | – | – | – | – | – | – | – | – | – | 24 | 22 | – |
| *E. coli* NRRL-B 3008 | – | – | – | – | – | – | – | – | – | – | 20 | 26 | – |
| *P. aeruginosa* NRRL-B 2679 | – | 9 | – | – | – | 8 | – | – | – | – | 36 | 32 | – |
| *B. subtilis* NRRL-B 4378 | – | – | – | – | – | – | – | – | – | – | 36 | 30 | – |
| *C. albicans* NRRL-Y 12983 | – | – | – | – | – | – | – | – | – | – | – | – | 22 |
| *C. parapsilosis* NRRL-Y 12696 | 14 | 10 | 10 | – | – | 8 | – | – | – | – | – | – | 25 |

## CONCLUSION

In this study, compound **3c**, one of the novel synthesized Schiff bases, was synthesized in the green solvent ethyl L-lactate medium. This synthesis method has many advantages over the traditional methods used, which are given as follows: the reaction was completed in four minutes and resulted in a 95 % yield, the product formed was not crystalline and required no further purification, the solvent used as a green solvent is not hazardous to the environment, non-corrosive, non-carcinogenic, non-teratogenic and biodegradable, showing an important benefit of our method. In this work, the antimicrobial activity of the novel synthesized was researched. The results showed that some of the novel compounds tested showed significant antimicrobial activity. Microbes that have gained resistance to drug therapy are an increasing public health problem. While there are a few really effective antifungal preparations currently available for the treatment of systemic mycoses, the efficiency of existing drugs is rather limited. The present study has clearly indicated that compound **3c** could be a promising new source of an antibacterial and antifungal agent. The results obtained from ethyl L-lactate synthesis method and activity studies could contribute to the literature.

## SUPPLEMENTARY MATERIAL

Additional data and information are available electronically at the pages of journal website: https://www.shd-pub.org.rs/index.php/JSCS/article/view/12631, or from the corresponding author on request.

*Acknowledgement.* This project has been supported by Eskişehir Osmangazi University Scientific Research Foundation. Project number: 200419032.

## ИЗВОД

## СИНТЕЗА НОВИХ *N*-СУПСТИТУИСАНИХ БЕНЗИЛ *N*-(1,3-БЕНЗОТИАЗОЛ-2-ИЛ)-АЦЕТАМИДА И ЊИХОВА *IN VITRO* АНТИБАКТЕРИЈСКА АКТИВНОСТ

HANDAN CAN SAKARYA[1], KAMURAN GÖRGÜN[1] и CANSU FILIK IŞCEN[2]

[1]*Eskişehir Osmangazi University, Faculty of Science, Department of Chemistry, 26480 Eskişehir, Turkey* и [2]*Eskişehir Osmangazi University, Faculty of Education, Department of Elementary Education, 26480 Eskişehir, Turkey*

Нове Шифове базе **3а**–**д** синтетисане су у реакцији 6-метил-2-аминобензотиазола са различитим супституисаним бензалдехидима. Добијене Шифове базе су редуковане помоћу $NaBH_4$ да би се формирали одговарајући амини **4а**–**д**. У последњем кораку, у реакција амина и хлороацетил-хлорида добијени су нови деривати амида **5а**–**д**. Структуре свих нових синтетизованих једињења су окарактерисане FT-IR, $^1$H-NMR, $^{13}$C-NMR, ESI MS, HETCOR, 2D ($^1$H-$^1$H) COSY спектрима и елементалним анализама. Да би се истражила антимикробна активност нових синтетизованих једињења, они су тестирани против неких Грам-позитивних и Грам-негативних бактеријских и гљивичних врста, а добијени резултати су даље дискутовани.

(Примљено 20. октобра 2023, ревидирано 19. јануара, прихваћено 11. јуна 2024)

REFERENCES


1. H. F. Abd El-halim, M. M. Omar, G. G. Mohamed, *Spectrochim. Acta, A* **78** (2011) 36 (https://doi.org/10.1016/j.saa.2010.06.003)
2. T. B. S. A. Ravoof, K. A. Crouse, M. I. M. Tahir, F. N. F. How, R. Rosli, D. J. Watkins, *Transit. Met. Chem.* **35** (2010) 871 (https://doi.org/10.1007/s11243-010-9406-6)
3. A. Aragón-Muriel, Y. Liscano, Y. Upegui, S. M. Robledo, M. T. Ramírez-Apan, D. Morales-Morales, J. Oñate-Garzón, D. Polo-Cerón, *Antibiotics* **10** (2021) 728 (https://doi.org/10.3390/antibiotics10060728)
4. C. Ramalingan, S. Balasubramanian, S. Kabilan, M. Vasudevan, *Eur. J. Med. Chem.* **39** (2004) 527 (https://doi.org/10.1016/j.ejmech.2004.02.005)
5. G. T. Zitouni, S. Demirayak, A. Ozdemir, Z. A. Kaplancikli, M. T. Yildiz, *Eur*. *J. Med. Chem.* **39** (2004**)** 267 (https://doi.org/10.1016/j.ejmech.2003.11.001)
6. M. A. Neelakantan, S. S. Marriappan, J. Dharmaraja, T. Jeyakumar, K. Muthukumaran, *Spectrochim. Acta, A* **71** ( 2008) 628 (https://doi.org/10.1016/j.saa.2008.01.023)
7. M. T. Tarafder, A. Kasbollah, N. Saravan, K. A. Crouse, A. M. Ali, O. K. Tin, *J. Biochem. Mol. Biol. Biophys.* **6** (2002) 85 (https://doi.org/10.1080/10258140290027207)
8. I. Kucukguzel, S. G. Kucukguzel, S. Rollas, G. O. Sanis, O. Ozdemir, I. Bayrak, T. Altug, J. P. Stables, *Farmaco* **59** (2004) 893 (https://doi.org/10.1016/j.farmac.2004.07.005)
9. P. Vicini, A. Geronikaki, M. Incerti, B. Busonera, G. Poni, C. A. Cabras, P. La Colla, *Bioorg. Med. Chem.* **11** (2003) 4785 (https://doi.org/10.1016/S0968-0896(03)00493-0)
10. R. Pignatello, A. Panico, P. Mazzone, M. R. Pinizzotto, A. Garozzo, P. M. Fumeri, *Eur. J. Med. Chem* **29** (1994) 781 (https://doi.org/10.1016/0223-5234(94)90137-6)
11. S. Samadhiya, A. Halve, *Orient. J. Chem*. **17** (2001) 119
12. G. Mustafa, M. Zia-ur-Rehman, S. H. Sumrra, M. Ashfaq, W. Zafar, M. Ashfaq, *J. Mol. Struct*. **1262** (2022) 133044 (https://doi.org/10.1016/j.molstruc.2022.133044)
13. A. Ayati, S. Emami, A. Asadipour, A. Shafiee, A. Foroumadi, *Eur. J. Med. Chem.* **97** (2015) 699 (https://doi.org/10.1016/j.ejmech.2015.04.015)
14. a) F. Parlati, U. V. Ramesh, R. Singh, D. G. Payan, R. Lowe, G. C. Look, *PCT Int. Appl. WO* 2005037845, 2005p, b) M. Yoshida, I. Hayakawa, N. Hayashi, T. Agatsuma, Y. Oda, F. Tanzawa, S. Iwasaki, K. Koyama, H. Furukawa, S. Kurakata, Y. Sugano, *Bioorg. Med. Chem. Lett*. **15** (2005) 3328 (https://doi.org/10.1016/j.bmcl.2005.05.077) c) T. R. Bailey, D. C. Pevear, *PCT Int. Appl*. 2004078115, 2004p, d) A. Alanine, A. Flohr, A. K. Miller, R. D. Norcross, C. Riemer, *PCT Int. Appl*. WO 2001097786, 2001p; e) S. Kerwin, L. H. Hurley, M. R. De Luca, B. M. Moore, *PCT Int. App*l. WO 9748694, 1997p; f) A. R. Brade, H. B. Khadse, A. S. Bobade, *Indian Drugs* **35** (1998) 554
15. D. Pareek, M. Chaudhary, P. K. Pareek, R. Kant, K. G. Ojha, R. Pareek, S. M. U. Iraqi, A. Pareek, *Chem. Sin.* **3** (2010) 22
16. A. Dandia, A. K. Jain, A. K. Laxkar, *Tetrahedron Lett.* **54** (2013) 3929 (https://doi.org/10.1016/j.tetlet.2013.05.035)
17. J. H. Billman, A. C. Diesing, *J. Org. Chem.* **22** (1957) 1068 (https://doi.org/10.1021/jo01360a019)
18. G. N. Walker, M. A. Klett, *J. Med. Chem.* **9** (1966) 624 (https://doi.org/10.1021/jm00322a049)
19. Y. Davion, G. Guillaumet, J.-M. Léger, C. Jarry, B. Lesur, J.-Y. Mérour, *Heterocycles* **63** (2004) 1093 (https://doi.org/10.3987/com-04-10022)
20. NCCLS, National Committee for Clinical Laboratory Standards, 2008, p. 120
21. F. Savaroglu, S. Ilhan, C. Filik-Iscen, *J. Med. Plants Res.* **5** (2011) 3286

22. F. Savaroglu, C. Filik Iscen, A.P. Oztopcu Vatan, S. Kabadere, S. Ilhan, R. Uyar, *Turk. J. Biol.* **35** (2011) 361 (https://doi.org/10.3906/biy-0906-46)
23. F. R. Deleo, B. A. Diep, M. Otto, *Inf. Dis. Clin. N. Amer.* **23** (2009) 17 (https://doi.org/10.1016/j.idc.2008.10.003)
24. A. Pietrzak, G. Chodorowska, I. Jazienicka, P. Osemlak, B. Wawrzycki, P. Terlecki, J. Mieczkowska, J. Mosiewicz, T. Zubilewicz, F. Szubstarski, W. Krupski, J. Hercogova, J. C. Szepietowski, T. Lotti, *Derma. Ther.* **24** (2011) 587 (https://doi.org/10.1111/j.1529-8019.2012.01410.x)
25. Y. Yang, E. J. Anderson, *J. Appl. Microbiol.* **86** (1999) 211 (https://doi.org/10.1046/j.1365-2672.1999.00652.x).

Journal of the Serbian Chemical Society
JSCS@tmf.bg.ac.rs • www.shd.org.rs/JSCS
*J. Serb. Chem. Soc.* *89* (9) S249–S277 (2024)
*Supplementary material*

SUPPLEMENTARY MATERIAL TO

# Synthesis of novel *N*-substituted benzyl *N*-(1,3-benzothiazol-2-yl) acetamides and their *in vitro* antibacterial activities

HANDAN CAN SAKARYA[1]*, KAMURAN GÖRGÜN[1] and CANSU FILIK IŞCEN[2]

[1]*Eskişehir Osmangazi University, Faculty of Science, Department of Chemistry, 26480, Eskişehir, Turkey and* [2]*Eskişehir Osmangazi University, Faculty of Education, Department of Elementary Education, 26480 Eskişehir, Turkey*

*J. Serb. Chem. Soc.* *89* (9) (2024) 1133–1145

N-[2-Methylphenyl)methylidene]-6-methyl-1,3-benzothiazol-2-amine (3a). Yield: 70%. M.p. 132-133°. FT-IR: 3042, 1610, 1597, 1530, 1505 (Fig.S1). 1H NMR(500 MHz, DMSO-d6, δ) : 2.45 (s, 3H, CH3-Benzothiazole), 2.65 (s, 3H, Ar-CH3), 7.34 (dd, 1H, 4J12,14=1.28 Hz, J11,13=8.23 Hz, H12), 7.38 (d, 1H, J14,15=7.81 Hz, H15), 7.39 (t, 1H, J12,14=8.93 Hz, H13), 7.53 (dt, 1H, 4JH14-H12=1.31 Hz, J13,15=7.42 Hz, H14), 7.83 (s, 1H, H7), 7.84 (d, 1H, J5,4=8.44 Hz, H5), 8.12 (d, 1H, J4,5=7.81 Hz, H4), 9.34 (s, 1H, -CH=N-) (Fig.S2) (The numbering of protons of the compound is given in Fig. 1). 13C NMR(125 MHz, DMSO-d6, δ): 19.07, 21.24, 117.88, 118.67, 121.28, 125.83, 126.45, 126.88, 127.04, 128.68, 130.90, 131.15, 136.48, 138.58, 150.54, 164.16. Anal. Calcd for C16H14N2S: C 72.15, H 5.30, N 10.52, S 12.04 %; found: C 72.00, H 5.35, N 10.54, S 11,96 %.

N-[2-Methoxyphenyl)methylidene]-6-methyl-1,3-benzothiazol-2-amine (3b). Yield: 76%. M.p. 134-136°. FT-IR: 3045, 1615, 1595, 1551 (Fig.S3). 1H NMR(500 MHz, DMSO-d6, δ) : 2.46 (s, 3H, CH3-Benzothiazole), 3.96(s, 3H, Ar-OCH3), 7.14 (t, 1H, J15,14=7.51 Hz, H14), 7.24 (d, 1H, J13,12=8.41 Hz, H12), 7.35 (dd, 1H, 4J5,7=1.34 Hz, J4,5=8.31 Hz, H5), 7.66 (dt, 1H, 4J13,15=1.75 Hz, J12,14=7.24 Hz, H13), 7.83 (d, 1H, J4,5=8.30 Hz, H4), 7.85 (s, 1H, H7), 8.11 (dd, 1H, 4J15,13=1.65 Hz, J15,14=7.76 Hz, H15), 9.30 (s, 1H, -CH=N-)(Fig.S4 and fig. S5). 13C NMR (125 MHz, DMSO-d6, δ): 21.21, 56.53, 112.93, 121.50, 122.35, 122.71, 122.77, 128.03, 128.56, 134.62, 135.43, 136.11, 149.86, 161.08, 161.73, 171.33. ESI-MS m/z= Calculated for (C16H14N2SO + H+) 283.1, observed 283.18 (Fig.S8). Anal. Calcd for C16H14N2SO: C 68.06, H 5.00, N 9.92, S 11.36 %. Found: C 68.20, H 5.20, N 9.98, S 11.35 %.

* Corresponding author. E-mail: hsakarya@ogu.edu.tr

N-[2-hyroxyphenyl)methylidene]-6-methyl-1,3-benzothiazol-2-amine (3c). Yield: 90%. M.p. 137-138°. FT-IR: 3360, 3040, 1620, 1583, 1570, 1545 (Fig.S9). 1H NMR(500 MHz, DMSO-d6, δ): 2.44 (s, 3H, CH3-Benzothiazole); 7.01(d, 1H, J15,13=7.48 Hz H14), 7.04 (d, 1H, J13,12=8.14 Hz, H12), 7.34 (d, 1H, J5,4=8.43 Hz, H4), 7.52 (dt, 1H, 4J13,15=1.27 Hz, J12,14=8.40 Hz, H13), 7.83 (d, 1H, J4,5=8.20 Hz, H5), 7.86 (s, 1H, H7), 7.93 (dd, 1H, 4J15,13=1.21 Hz, J15,14=7.80 Hz, H15), 9.45 (s, 1H, -CH=N-), 11.5 (s, 1H, PhOH)(Fig.S10 and S11). 13C NMR(125 MHz, DMSO-d6, δ): 21.58, 117.41, 120.06, 120.31, 122.40, 122.70, 128.61, 131.66, 134.47, 135.62, 135.98, 149.73, 160.98, 166.04, 169.73 (Fig.S12). Anal. Calcd. for C15H12N2OS: C 67.14, H 4.51, N 10.44, S 11.95 %. Found: C 67.10, H 4.56, N 10.49, S 11,40 %.

N-[4-hydroxyphenyl)methylidene]-6-methyl-1,3-benzothiazol-2-amine (3d). Yield: 72%. M.p. 136-138°. FT-IR: 3350, 3044, 1618, 1585, 1572, 1543. 1H NMR(500 MHz, DMSO-d6, δ): 2.40 (s, 3H, CH3-Benzothiazole), 6.96 (d, 2H, J11,13=8.55 Hz, H12 and H14), 7.30 (d, 1H, J5,4=8.11 Hz, H4), 7.77 (d, 1H, J4,5=8.45 Hz, H5), 7.79 (s, 1H, H7), 7.94 (d, 2H, J12,14=8.56 Hz, H11 and H15), 9.02 (s, 1H, -CH=N-), 10.5 (s, 1H, Ar-OH)(Fig.S13). 13C NMR(125 MHz, DMSO-d6, δ): 21.54, 116.63, 122.27, 122.36, 126.37, 128.34, 133.08, 134.36, 135.07, 149.92, 163.24, 166.49, 171.41(Fig.S14). Anal. Calcd. for C15H12N2OS: C 67.14, H 4.51, N 10.44, S 11.95 %. Found: C 67.02, H 4.54, N 10.40, S 11,45 %.

N-(2-methylbenzyl)-6-Methyl-1,3-benzothiazol-2-amine (4a). Yield: 87%. M.p. 102-103°. FT-IR: 3412, 1605, 1594, 1571. 1H NMR(500 MHz, DMSO-d6, δ): 2.32 (s, 3H, CH3-Benzothiazole), 2.34 (s, 3H, Ar-CH3), 4.55 (d, 2H, JCH2-NH=5.44 Hz, Ar-CH2NH-), 7.03 (dd, 1H, 4J5,7=1.31 Hz, J4,5=8.15 Hz, H5), 7.18 (m, 3H, H12, H-14 and H15), 7.27 (d, 1H, J5,4=8.11 Hz, H4), 7.32 (d, 1H, J12,14=7.29 Hz, H13), 7.47 (s, 1H, H7), 8.25 (t, 1H, JNH-CH2=5.43 Hz, NHCH2-Ar)(Fig.S15). 13C NMR(125 MHz, DMSO-d6, δ): 19.12, 21.22, 45.92, 118.20, 121.35, 126.27, 126.99, 127.61, 128.28, 130.51, 130.98, 136.43, 137.05, 150.81, 165.78 (Fig.S16). ESI-MS m/z= Calculated for (C16H16N2S + H+) 269.1, observed 269.1 (Fig.S19). Anal. Calcd for C16H16N2S: C 71.60, H 6.01, N 10.44, S 11.95 %. Found: C 71.52, H 6.03, N 10.50, S 11.90 %.

N-(2-methoxybenzyl)-6-Methyl-1,3-benzothiazol-2-amine (4b). Yield: 90%. M.p. 125-127°. FT-IR: 3430, 1608, 1567(Fig.S20). 1H NMR(500 MHz, DMSO-d6, δ): 2.31 (s, 3H, CH3-Benzothiazole), 3.83 (s, 3H, Ar-OCH3), 4.53 (d, 2H, JCH2-NH=5.67 Hz, Ar-CH2NH-), 6.92 (t, 1H, J15,13=7.28 Hz, H14), 7.02 (d, 2H, J12,13=J4,5=8.09 Hz, H12 and H4), 7.25 (d, 2H, J4,5 J12,14=7.03 Hz, H5 and H15), 7.29 (t, 1H, J12,14=7.13 Hz H13), 7.46 (s, 1H, H7); 8.22 (t, 1H, JNH-CH2=5.67 Hz, NHCH2-Ar) (Fig.S21 and S22). 13C NMR(125 MHz, DMSO-d6, δ): 21.22, 42.89, 55.82, 111.06, 118.18, 120.62, 121.32, 126.79, 126.96, 128.46, 128.81, 130.44, 130.97, 150.83, 157.32, 166.00 (Fig.S23). ESI-MS m/z=

Calculated for (C16H16N2SO + H+) 285.1, observed 285.1. Anal. Calcd for C16H16N2SO: C 67.58, H 5.67, N 9.85, S 11.28 %. Found: C 67.28, H 4.58, N 9.86, S 10.40 %.

N-(2-hyroxybenzyl)-6-Methyl-1,3-benzothiazol-2-amine (4c). Yield: 90%. M.p. 170-172°. FT-IR: 3525, 3409, 1595, 1570(Fig.S28). 1H NMR(500 MHz, DMSO-d6, δ): 2.32 (s, 3H, CH3-Benzothiazole), 4.47 (d, 2H, JCH2-NH=5.796 Hz, Ar-CH2NH-), 6.74 (dt, 1H, 4J14,12=0.79 Hz J15,13=7.41 Hz, H14), 6.86 (dd, 1H, 4J12,14=0.65 Hz, J13,12=7.64 Hz, H12), 7.06 (dd, 1H, 4J15,13=1.36 Hz, J14,15=8.24 Hz, H15), 7.10 (dt, 1H, 4J13,15=1.61 Hz, J12,14=7.69 Hz, H13), 7.24 (dd, 1H, 4J5,7=1.16 Hz, J4,5=7.53 Hz, H5), 7.26 (d, 1H, J5,4=8.11 Hz, H4), 7.47 (s, 1H, 4J7,5=0.97 Hz, H7), 8.30 (t, 1H, J=5.70 Hz, NHCH2-Ar), 9.75 (br. s, 1H, Ar-OH) (Fig.S29). 13C NMR(125 MHz, DMSO-d6, δ): 21.22, 43.14, 115.85, 118.00, 119.37, 121.41, 125.34, 127.04, 128.69, 129.36, 130.55, 130.81, 150.45, 155.61, 166.29. Anal. Calcd. for C15H14N2OS: C 66.64, H 5.22, N 10.36, S 11.86 %. Found: C 66.60, H 5.21, N 10.33, S 11.84 %.

N-(4-hyroxybenzyl)-6-Methyl-1,3-benzothiazol-2-amine (4d). Yield: 93%. M.p. 168-170°. FT-IR: 3542, 3430, 1591, 1556. 1H NMR(500 MHz, DMSO-d6, δ): 2.46 (s, 3H CH3-Benzothiazole), 4.49 (d, 2H, JCH2-NH=5.20 Hz, Ar-CH2NH-), 6.74 (d, 2H, J11,13=8.43 Hz, H12 and H14), 7.02 (d, 1H, J4,5=7.16 Hz, H5), 7.2 (d, 2H, J12,14=8.41 Hz, H11 and H15), 7.24 (d, 1H, J5,4=6.84 Hz, H4), 8.28 (t, 1H, JNH-CH2=5.44 Hz, NHCH2-Ar), 9.30 (br. s, 1H, Ar-OH) (Fig.S30 and S31). 13C NMR(125 MHz, DMSO-d6, δ): 21.22, 47.39, 115.54, 118.15, 121.32, 16.98, 129.34, 129.49, 130.42, 130.92, 150.86, 156.95, 165.91 (Fig.S32). Anal. Calcd. for C15H14N2OS: C 66.64, H 5.22, N 10.36, S 11.86 %. Found: C 66.61, H 5.18, N 10.31, S 11.82 %.

2-Chloro-N-[6-methyl-1,3-benzothiazol-2-yl]-N-[2-methylbenzyl] acetamide (5a). Yield: 76%. M.p. 188-190°. FT-IR: 1698, 1600, 1509(Fig.S36). 1H NMR(500 MHz, DMSO-d6, δ): 2.49 (s, 6H, CH3-Benzothiazole and Ar-CH3), 4.55 (s, 2H, Ar-CH2N-), 5.50 (s, 2H, N(CO)CH2Cl), 6.76 (d, 1H, J14,15=7.59 Hz, H15), 7.11 (t, 1H, J12,14=7.54 Hz, H13), 7.18 (t, 1H, J15,13=7.36 Hz, H14), 7.24 (d, 1H, J13,12=8.20 Hz, H12), 7.28 (d, 1H, J4,5=8.63 Hz, H5), 7.62 (d, 1H, J5,4=8.27 Hz, H4), 7.84(s, 1H, H7) (Fig.S37). 13C NMR(125 MHz, DMSO-d6, δ): 19.99, 22.30, 44.62, 49.49, 122.16, 122.9, 124.72, 127.64, 128.37, 128.95, 131.69, 133.31, 134.12, 135.15, 135.54, 136.40, 152.03, 168.63 (Fig.S38). ESI-MS m/z= Calculated for (C18H17ClN2SO + H+) 345.1, observed 345.1(Fig.S40). Anal. Calcd for C18H17ClN2SO: C 62.69, H 4.97, N 8.12, S 9.30 %. Found: C 62.48, H 5.006, N 8.339, S 9.265 %.

2-Chloro-N-[6-methyl-1,3-benzothiazol-2-yl]-N-[2-methoxybenzyl]acetamide (5b). Yield: 82%. M.p. 146-149°. FT-IR: 1683, 1605, 1520 (Fig.S41). 1H NMR(500 MHz, DMSO-d6, δ): 2.40 (s, 3H, CH3-Benzothiazole), 3.53 (s, 3H, Ar-OCH3), 4.75 (s, 2H, CH2N), 5.43 (s, 2H,

N(CO)CH2Cl), 6.87 (t, 1H, J12,14=7.35 Hz, H13), 6.92 (d, 1H, J13,12=6.80 Hz, H12), 7.08 (d, 1H, J14,15=8.21 Hz, H15), 7.25 (d, 1H, J4,5=8.94 Hz, H5); 7.29 (t, 1H, J15,13=7.30, H14), 7.63 (d, 1H, J5,4=8.26 Hz, H4), 7.81 (s, 1H, H7) (Fig.S42, fig.S43 and S44 ). 13C NMR(125 MHz, DMSO-d6, δ): 21.48, 43.77, 46.79, 55.98, 61.29, 111.43, 121.02, 121.34, 121.61, 123.94, 126.50, 128.09, 129.16, 133.22, 134.24, 145.99, 157.00, 167.86 (Fig.S45). ESI-MS m/z= Calculated for (C18H17ClN2SO2 + H+) 361.1, observed 361.1(Fig.S48). Anal. Calcd for C18H17ClN2SO2: C 59.91, H 4.75, N 7.76, S 8.89 %. Found: C 59.72, H 4.64, N 7.63, S 8.99 %.

2-[(Chloroacetyl)(6-methyl-1,3-benzothiazol-2-yl)aminomethyl]phenyl chloroacetate (5c). Yield: 78%. M.p. 159-161°. FT-IR: 1775, 1668, 1600, 1505. 1H NMR(500 MHz, DMSO-d6, δ): 2.40 (s, 3H, CH3-Benzothiazole), 4.70 (s, 2H, Ar-CH2N-), 4.80 (s, 2H, O(CO)CH2Cl), 5.50 (s, 2H, N(co)ch2Cl), 7.07 (d, 1H, J14,15=7.69 Hz, H15), 7.10 (d, 1H, J4,5=7.49 Hz, H5), 7.20 (t, 1H, J15,13=7.49 Hz, H14), 7.30 (d, 1H, J13,12=8.03 Hz, H12), 7.40 (t, 1H J12,14=7.89 Hz, H13), 7.65 (d, 1H, J5,4=8.28 Hz, H4), 7.85 (s, 1H, H7). Anal. Calcd. for C19H16Cl2N2O3S: C 53.90, H 3.81, N 6.62, S 7.58 %. Found: C 53.92, H 3.84, N 6.59, S 7.55 %.

4-[(Chloroacetyl)(6-methyl-1,3-benzothiazol-2-yl)aminomethyl]phenyl chloroacetate (5d). Yield: 82%. M.p. 156-158°. FT-IR: 1762, 1663, 1593, 1520. 1H NMR(500 MHz, DMSO-d6, δ): 2.43 (s, 3H, CH3-Benzothiazole), 4.69 (s, 2H, Ar-CH2N), 4.76 (s, 2H, O(CO)CH2Cl), 5.57 (s, 2H,N(co)ch2Cl ), 6.74 (d, 2H, J11,15=7.69 Hz, H12 and H14), 7.10 (d, 2H, J12,14=8.5 Hz, H11 and H15), 7.28 (d, 1H, J4,5=7.35 Hz, H5), 7.69 (d, 1H, J5,4=8.24 Hz, H4), 7.83 (s, 1H, H7), 8.59 (s, 1H, Ar-OH). Anal. Calcd. for C19H16Cl2N2O3S : C 53.90, H 3.81, N 6.62, S 7.58 %. Found: C 53.88, H 3.83, N 6.61, S 7.55 %.

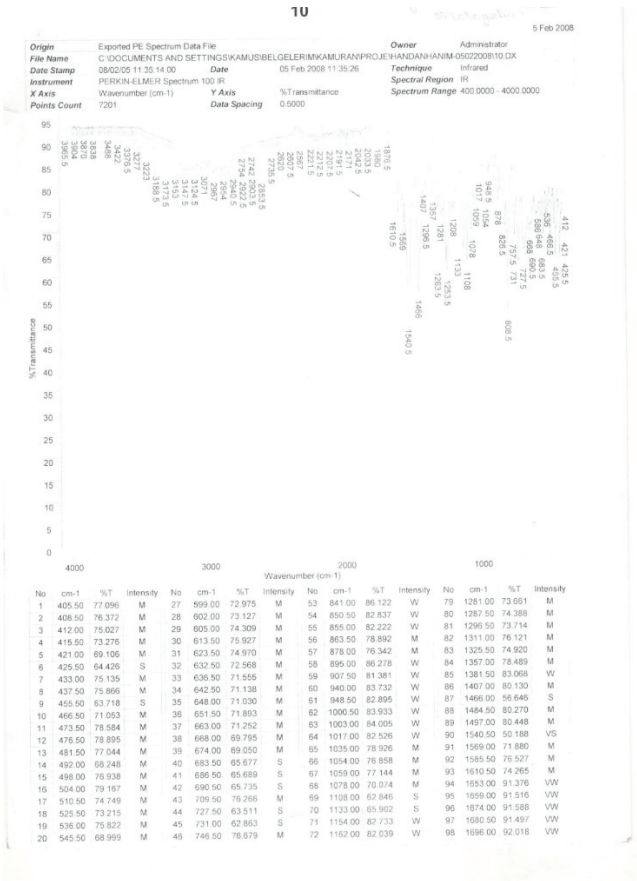


| No | cm-1 | %T | Intensity | No | cm-1 | %T | Intensity | No | cm-1 | %T | Intensity | No | cm-1 | %T | Intensity |
|---|---|---|---|---|---|---|---|---|---|---|---|---|---|---|---|
| 1 | 405.50 | 77.096 | M | 27 | 599.00 | 72.975 | M | 53 | 841.00 | 86.122 | W | 79 | 1281.00 | 73.661 | M |
| 2 | 408.50 | 76.372 | M | 28 | 602.00 | 73.127 | M | 54 | 850.50 | 82.837 | W | 80 | 1287.50 | 74.388 | M |
| 3 | 412.00 | 75.027 | M | 29 | 605.00 | 74.309 | M | 55 | 855.00 | 82.222 | W | 81 | 1296.50 | 73.714 | M |
| 4 | 415.50 | 73.276 | M | 30 | 613.50 | 75.927 | M | 56 | 863.50 | 78.892 | M | 82 | 1311.00 | 76.121 | M |
| 5 | 421.00 | 69.106 | M | 31 | 623.50 | 74.970 | M | 57 | 878.00 | 76.342 | M | 83 | 1325.50 | 74.920 | M |
| 6 | 425.50 | 64.426 | S | 32 | 632.50 | 72.568 | M | 58 | 895.00 | 86.278 | W | 84 | 1357.00 | 78.489 | M |
| 7 | 433.00 | 75.135 | M | 33 | 636.50 | 71.555 | M | 59 | 907.50 | 81.381 | W | 85 | 1381.50 | 83.068 | W |
| 8 | 437.50 | 75.866 | M | 34 | 642.50 | 71.138 | M | 60 | 940.00 | 83.732 | W | 86 | 1407.00 | 80.130 | M |
| 9 | 455.50 | 63.718 | S | 35 | 648.00 | 71.030 | M | 61 | 948.50 | 82.895 | W | 87 | 1466.00 | 56.645 | S |
| 10 | 466.50 | 71.053 | M | 36 | 651.50 | 71.893 | M | 62 | 1000.50 | 83.933 | W | 88 | 1484.50 | 80.270 | M |
| 11 | 473.50 | 78.584 | M | 37 | 663.00 | 71.252 | M | 63 | 1003.00 | 84.005 | W | 89 | 1497.00 | 80.448 | M |
| 12 | 476.50 | 78.895 | M | 38 | 668.00 | 69.795 | M | 64 | 1017.00 | 82.526 | W | 90 | 1540.50 | 50.188 | VS |
| 13 | 481.50 | 77.044 | M | 39 | 674.00 | 69.050 | M | 65 | 1035.00 | 78.926 | M | 91 | 1569.00 | 71.880 | M |
| 14 | 492.00 | 68.248 | M | 40 | 683.50 | 65.677 | S | 66 | 1054.00 | 76.858 | M | 92 | 1585.50 | 76.527 | M |
| 15 | 498.00 | 76.938 | M | 41 | 686.50 | 65.689 | S | 67 | 1059.00 | 77.144 | M | 93 | 1610.50 | 74.265 | M |
| 16 | 504.00 | 79.167 | M | 42 | 690.50 | 65.735 | S | 68 | 1078.00 | 70.074 | M | 94 | 1653.00 | 91.376 | VW |
| 17 | 510.50 | 74.749 | M | 43 | 709.50 | 76.266 | M | 69 | 1108.00 | 62.846 | S | 95 | 1659.00 | 91.516 | VW |
| 18 | 525.50 | 73.215 | M | 44 | 727.50 | 63.511 | S | 70 | 1133.00 | 65.902 | S | 96 | 1674.00 | 91.588 | VW |
| 19 | 536.00 | 75.822 | M | 45 | 731.00 | 62.863 | S | 71 | 1154.00 | 82.733 | W | 97 | 1680.50 | 91.497 | VW |
| 20 | 545.50 | 68.999 | M | 46 | 746.50 | 76.879 | M | 72 | 1162.00 | 82.039 | W | 98 | 1696.00 | 92.018 | VW |

Figure S-1.FT-IR spectrum of N-[2-Methylphenyl)methylidene]-6-methyl-1,3-benzothiazol-2-amine (3a).

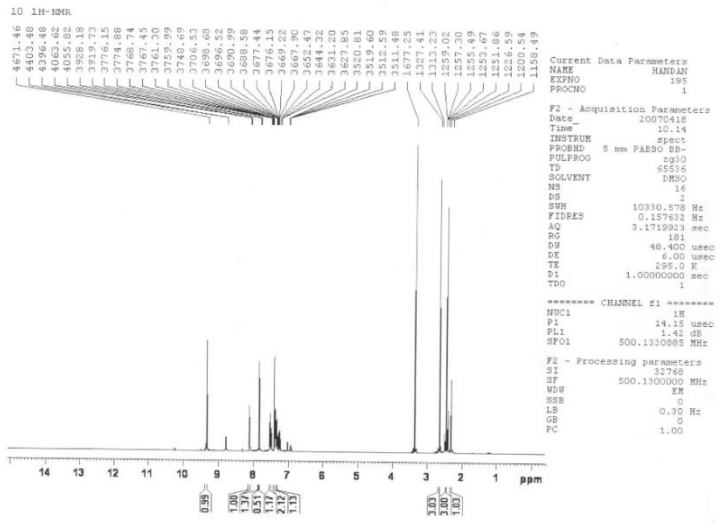

Figure S-2. 1H NMR spectrum of N-[2-Methylphenyl)methylidene]-6-methyl-1,3-benzothiazol-2-amine (3a)

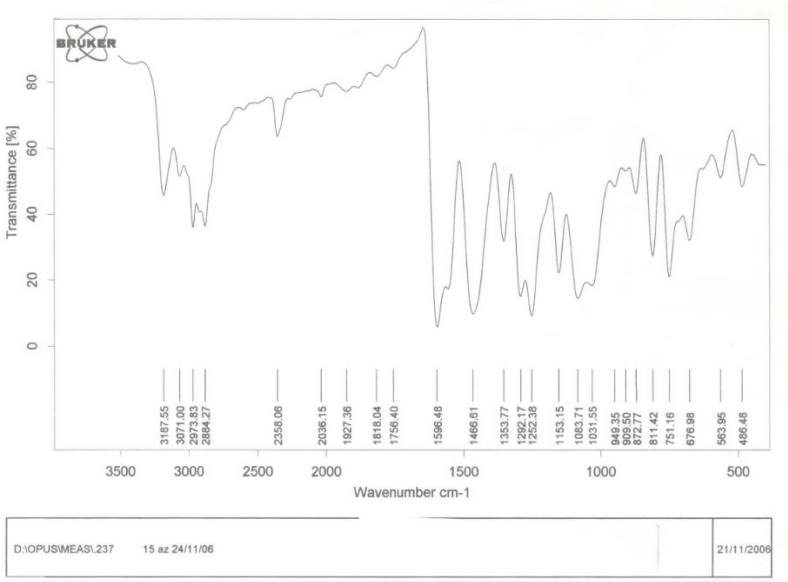


Figure S-3. FT-IR spectrum of N-[2-Methoxyphenyl)methylidene]-6-methyl-1,3-benzothiazol-2-amine (3b)

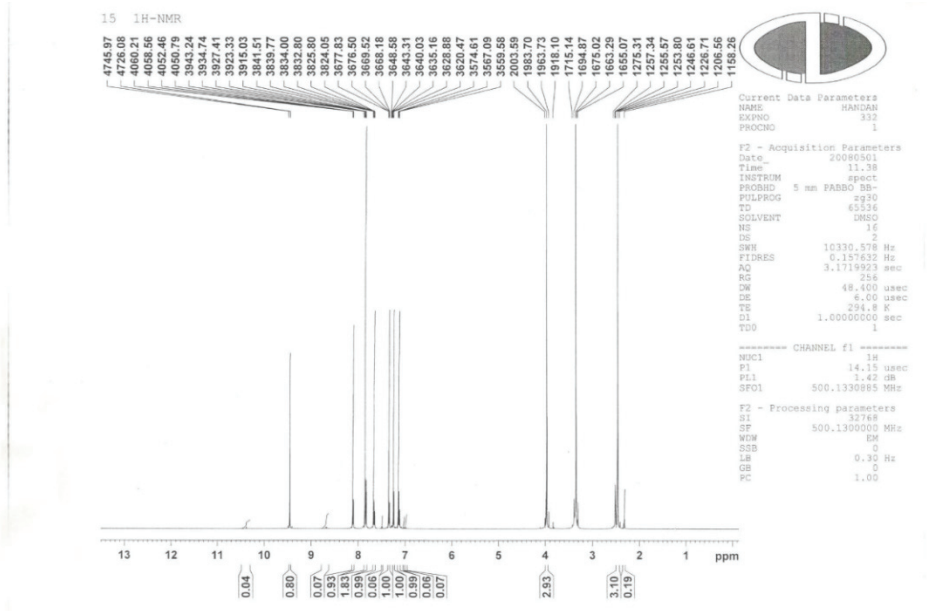


Figure S-4. 1H NMR spectrum of N-[2-Methoxyphenyl)methylidene]-6-methyl-1,3-benzothiazol-2-amine (3b)

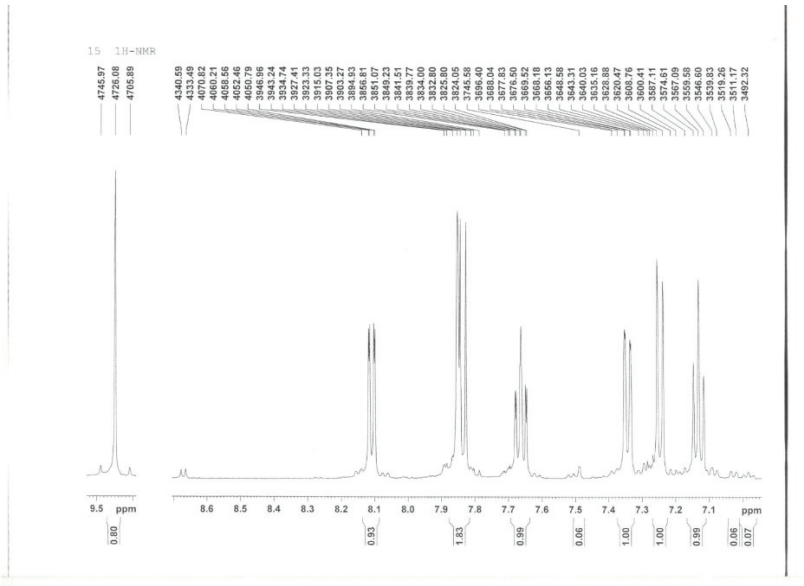


Figure S-5. 1H NMR spectrum of N-[2-Methoxyphenyl)methylidene]-6-methyl-1,3-benzothiazol-2-amine (3b)

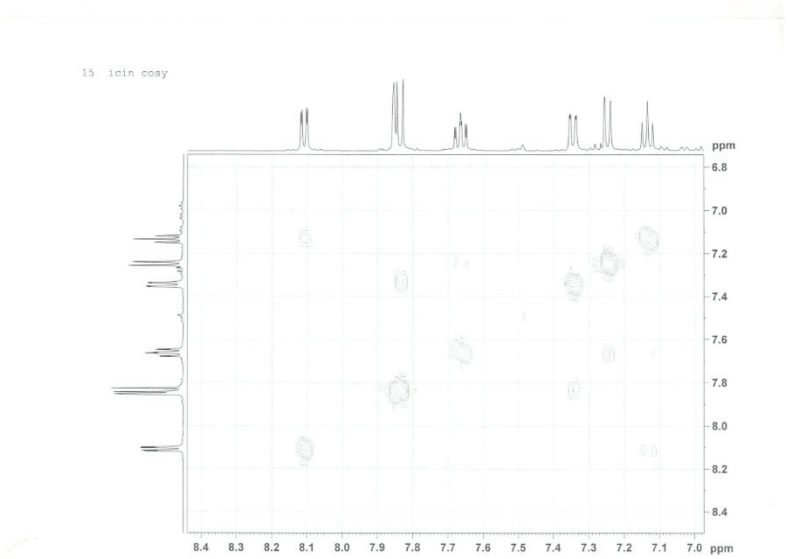


Figure S-6. 1H-1H COSY spectrum of N-[2-Methoxyphenyl)methylidene]-6-methyl-1,3-benzothiazol-2-amine (3b).

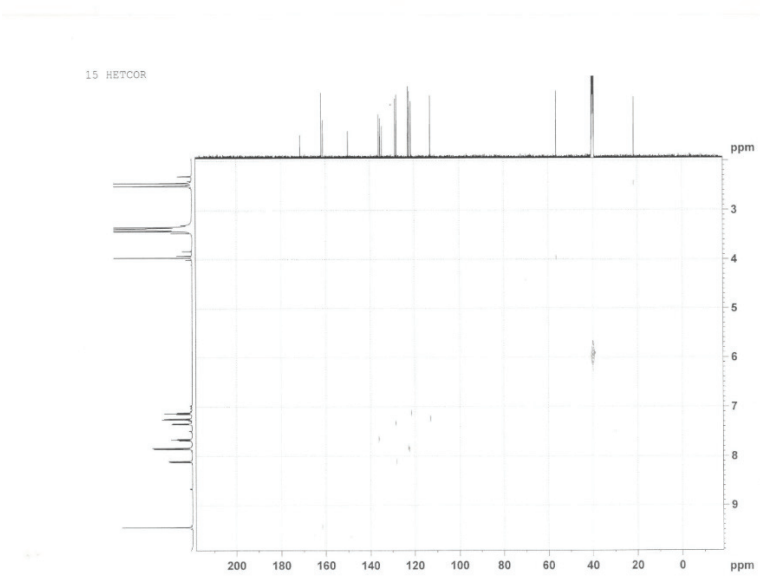


Figure S-7. HETCOR spectrum of N-[2-Methoxyphenyl)methylidene]-6-methyl-1,3-benzothiazol-2-amine (3b)

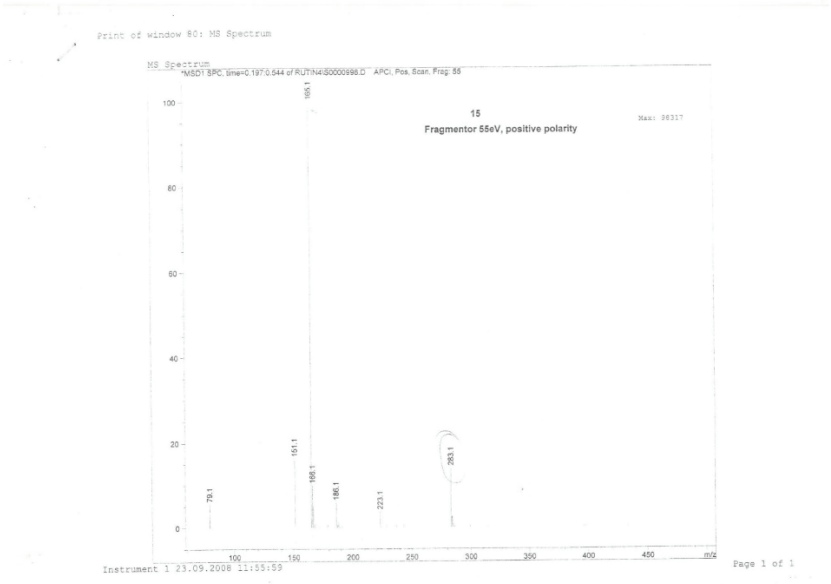


Figure S-8. ESI-MS spectrum of N-[2-Methoxyphenyl)methylidene]-6-methyl-1,3-benzothiazol-2-amine (3b)

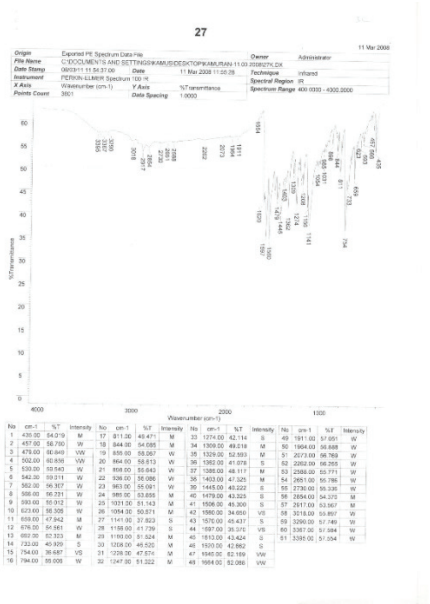


Figure S-9. FT-IR Spectrum of N-[2-hyroxyphenyl)methylidene]-6-methyl-1,3-benzothiazol-2-amine (3c)

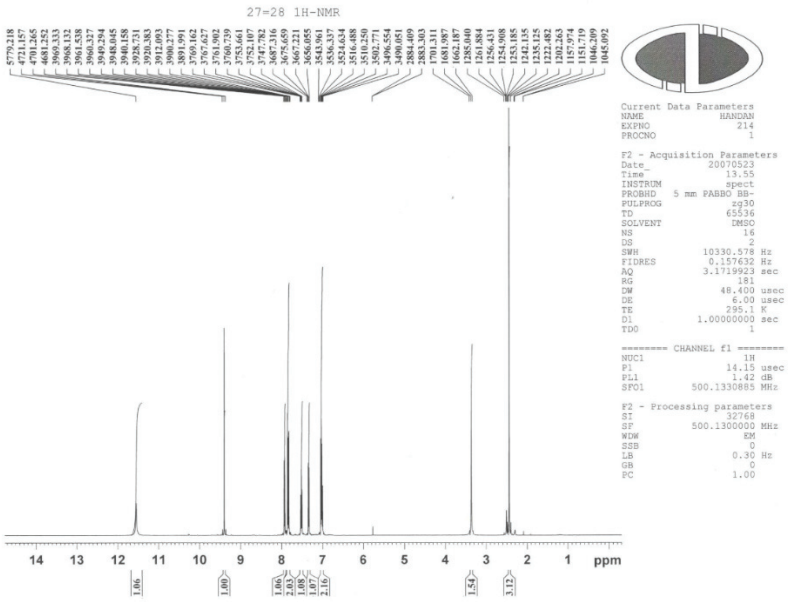


Figure S-10. 1H NMR spectrum of N-[2-hyroxyphenyl)methylidene]-6-methyl-1,3-benzothiazol-2-amine (3c)

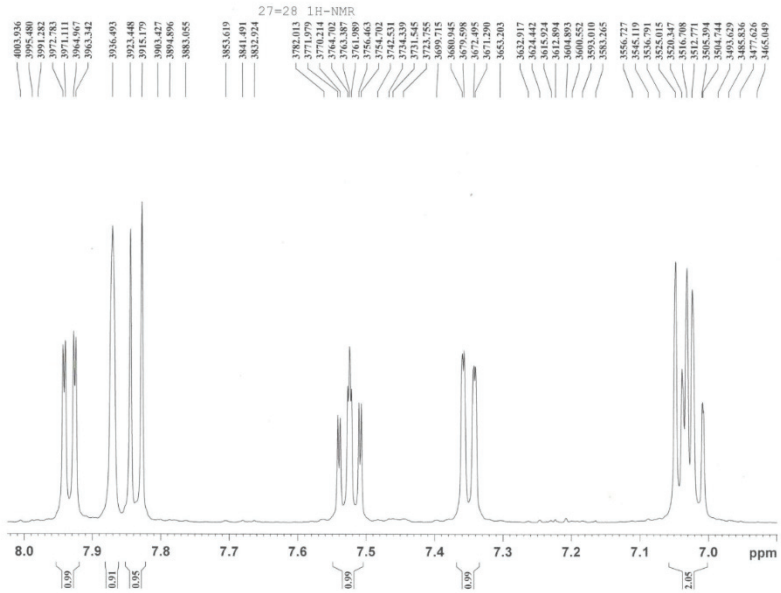


Figure S-11. 1H NMR spectrum of N-[2-hyroxyphenyl)methylidene]-6-methyl-1,3-benzothiazol-2-amine (3c)

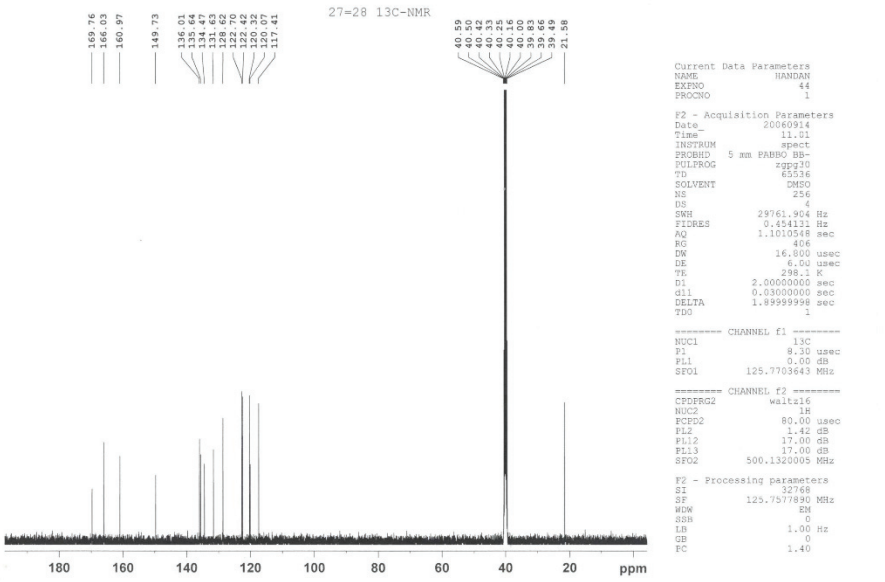


Figure S-12. 13C NMR spectum of N-[2-hyroxyphenyl)methylidene]-6-methyl-1,3-benzothiazol-2-amine (3c).

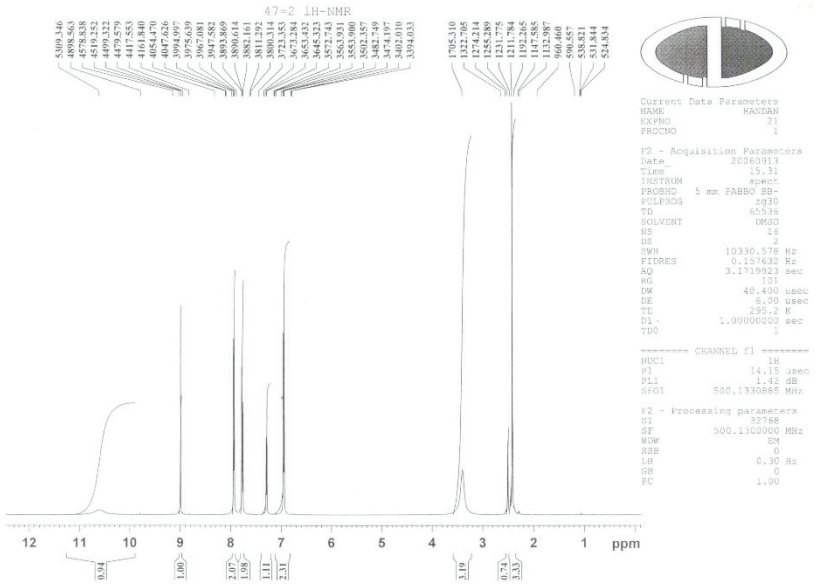


Figure S-13. 1H NMR spectrum of N-[4-hydroxyphenyl)methylidene]-6-methyl-1,3-benzothiazol-2-amine (3d)

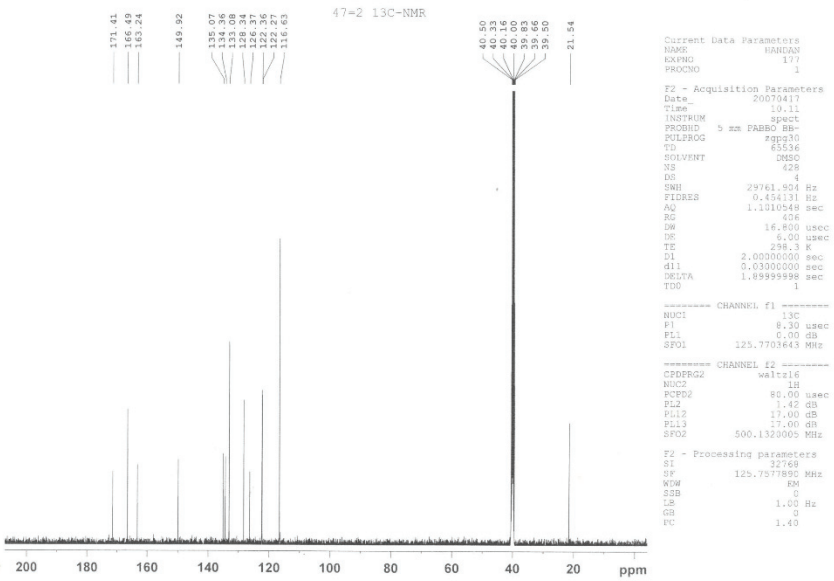


Figure S-14. 13C NMR spectrum of N-[4-hydroxyphenyl)methylidene]-6-methyl-1,3-benzothiazol-2-amine (3d).

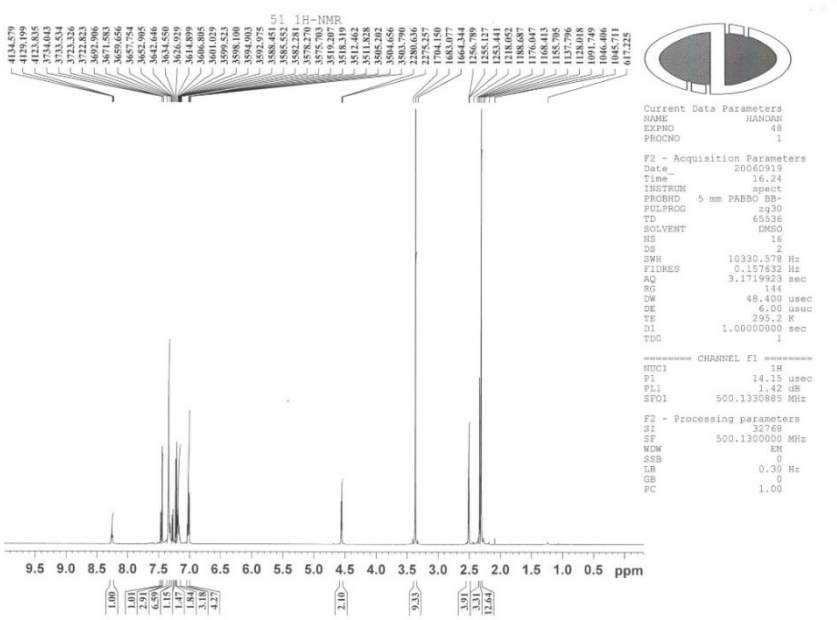


Figure S-15. 1H NMR spectrum of N-(2-methylbenzyl)-6-Methyl-1,3-benzothiazol-2-amine (4a)

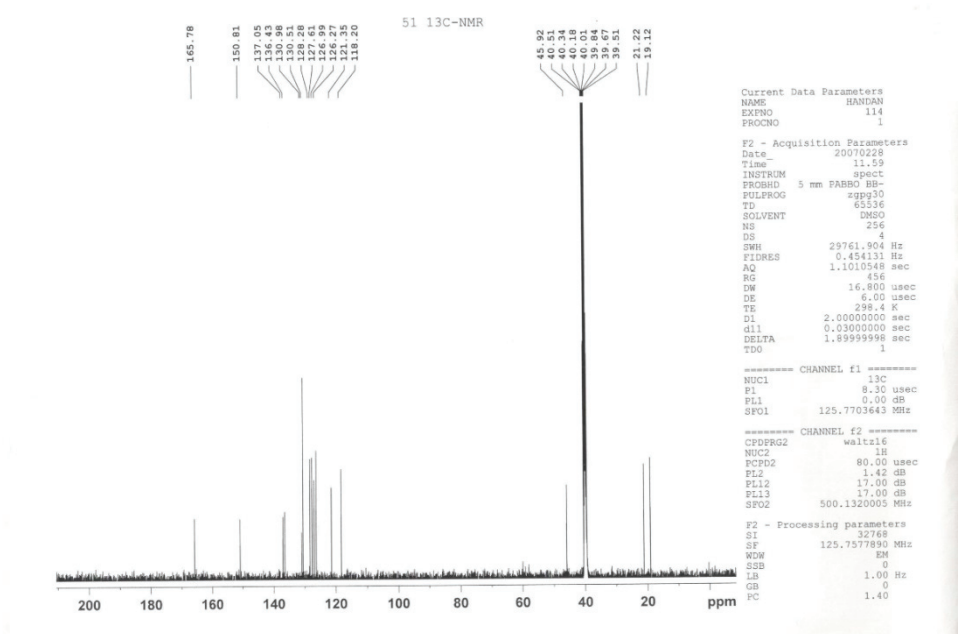


Figure S-16. 13C NMR spectrum of N-(2-methylbenzyl)-6-Methyl-1,3-benzothiazol-2-amine (4a)

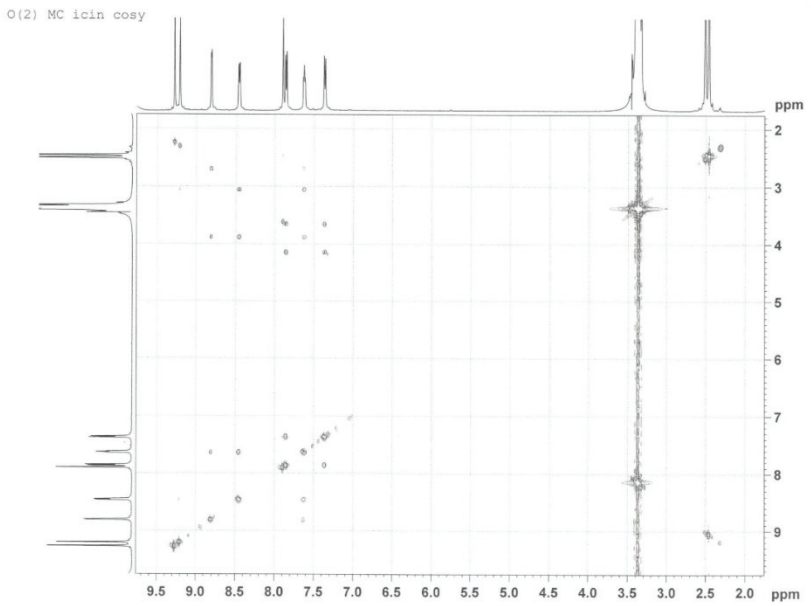


Figure S-17. COSY spectrum of N-(2-methylbenzyl)-6-Methyl-1,3-benzothiazol-2-amine (4a)

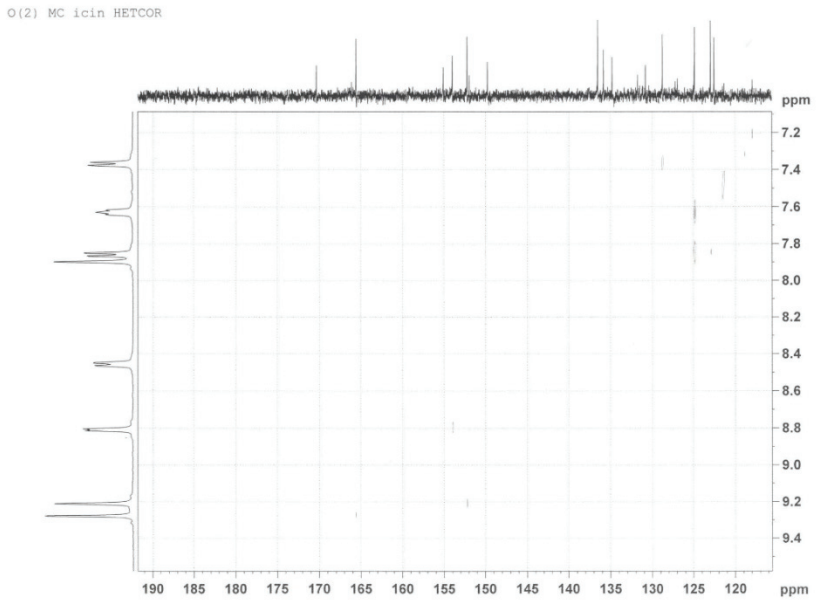


Figure S-18. HETCOR spectrum of N-(2-methylbenzyl)-6-Methyl-1,3-benzothiazol-2-amine (4a)

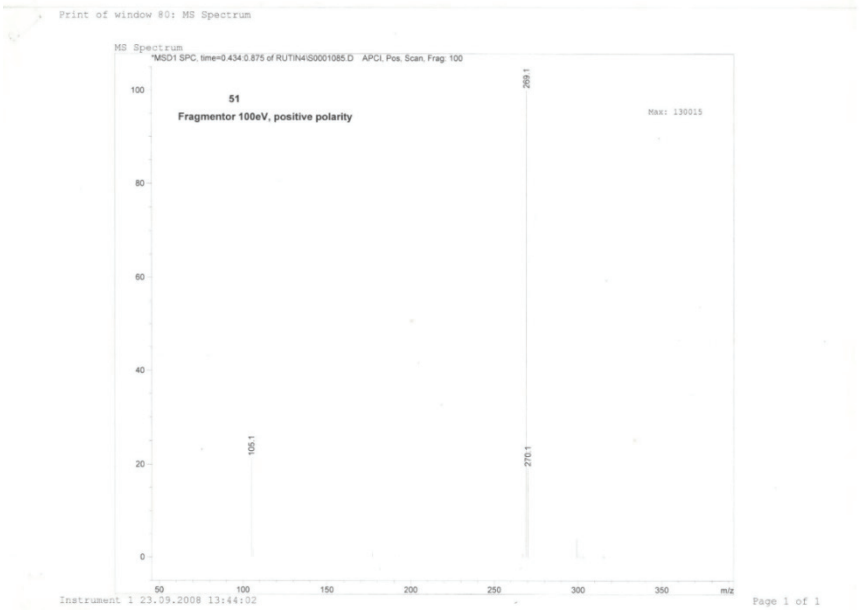


Figure S-19. ESI-MS spectrum of N-(2-methylbenzyl)-6-Methyl-1,3-benzothiazol-2-amine (4a)

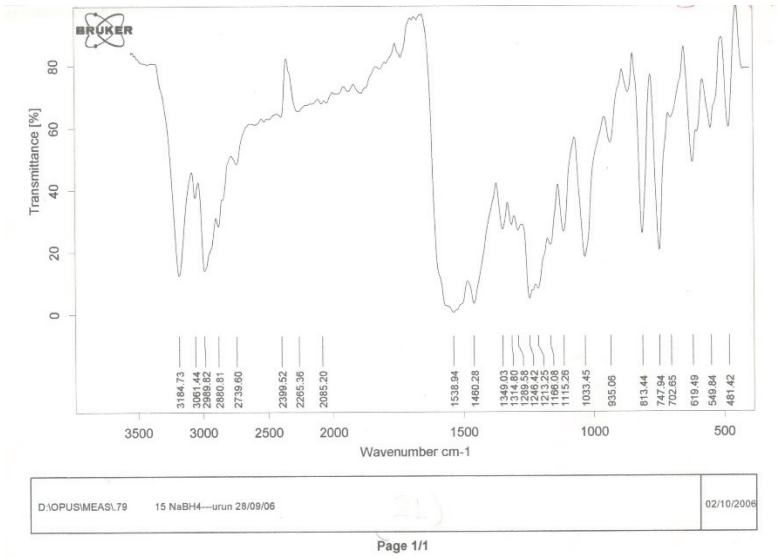


Figure S-20. FT-IR spectrum of N-(2-methoxybenzyl)-6-Methyl-1,3-benzothiazol-2-amine (4b).

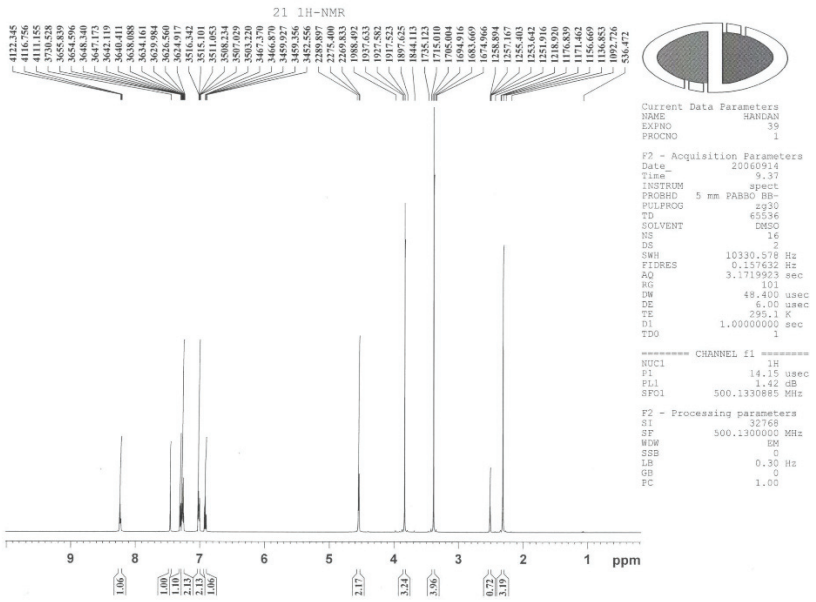


Figure S-21. 1H NMR spectrum of N-(2-methoxybenzyl)-6-Methyl-1,3-benzothiazol-2-amine (4b).

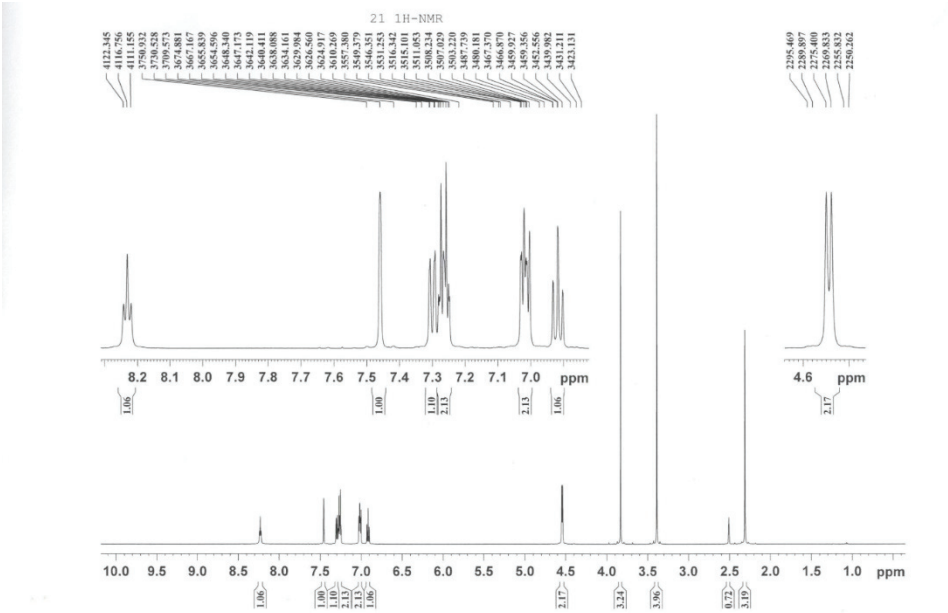


Figure S-22. 1H NMR spectrum of N-(2-methoxybenzyl)-6-Methyl-1,3-benzothiazol-2-amine (4b).

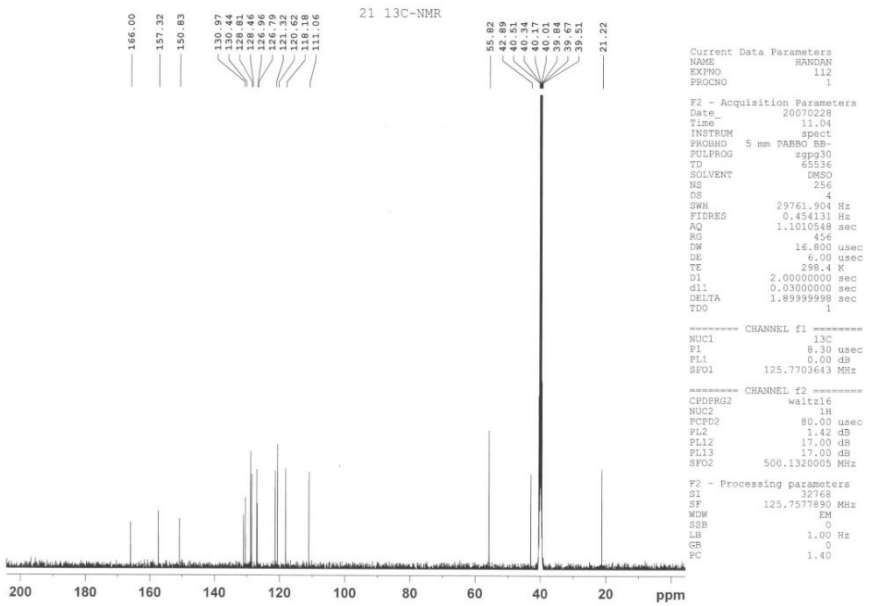


Figure S-23. 13C NMR spectrum of N-(2-methoxybenzyl)-6-Methyl-1,3-benzothiazol-2-amine (4b).

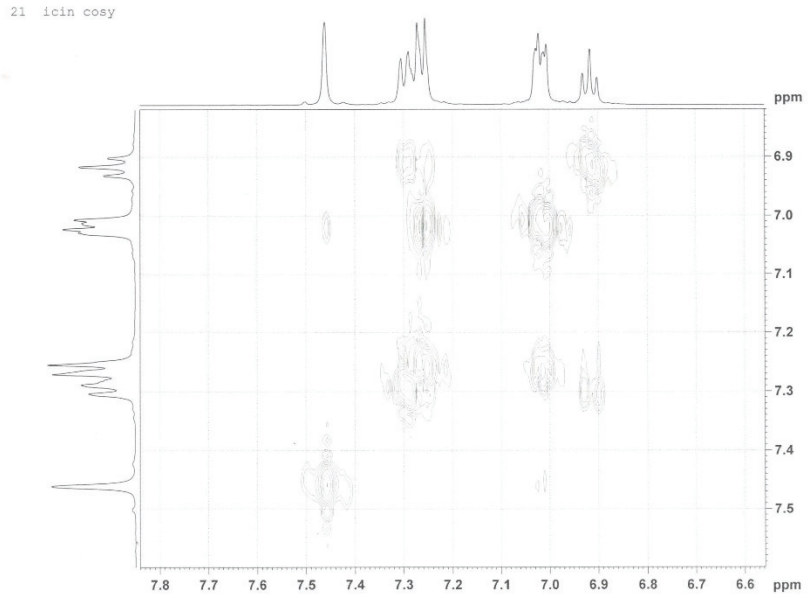


Figure S-24. COSY spectrum of N-(2-methoxybenzyl)-6-Methyl-1,3-benzothiazol-2-amine (4b)

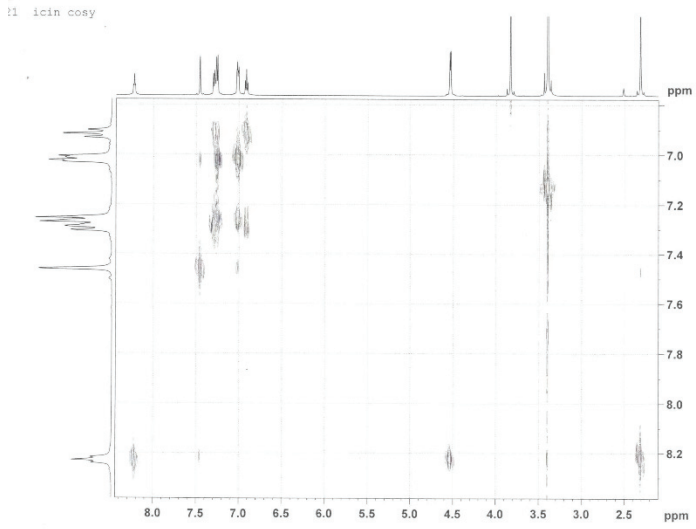


Figure S-25. COSY spectrum of N-(2-methoxybenzyl)-6-Methyl-1,3-benzothiazol-2-amine (4b)

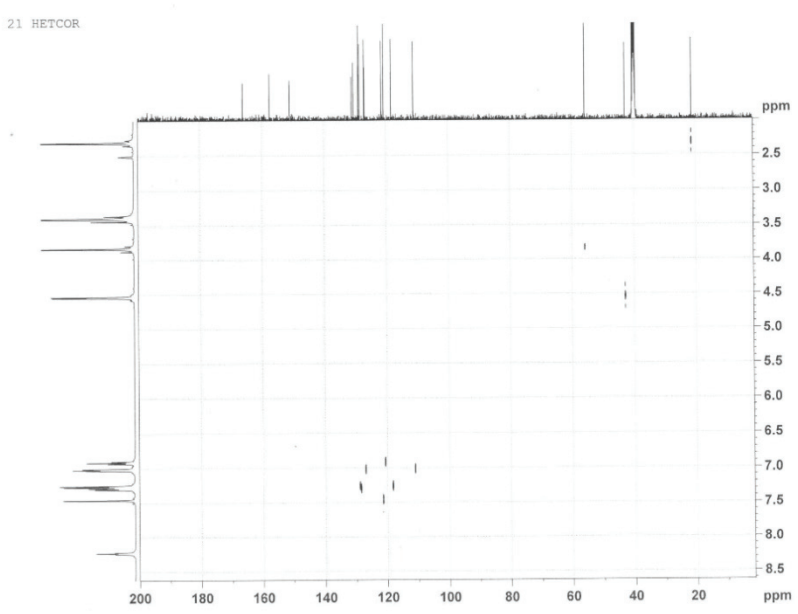


Figure S-26. HETCOR spectrum of N-(2-methoxybenzyl)-6-Methyl-1,3-benzothiazol-2-amine (4b)

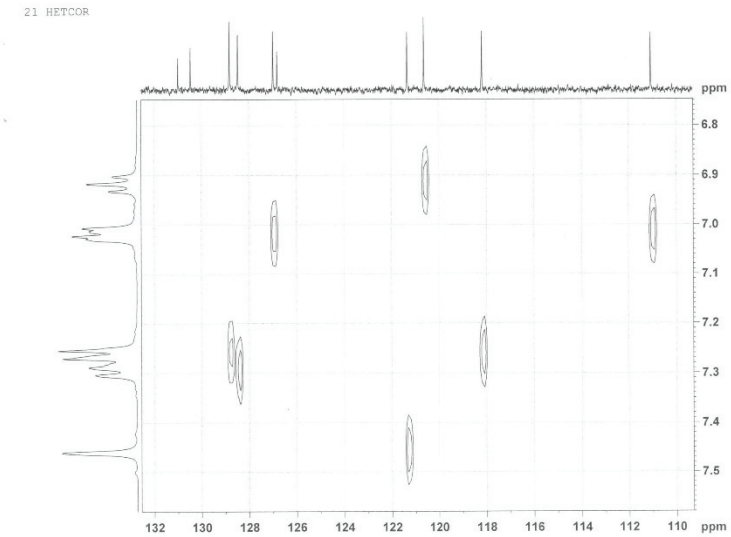


Figure S-27. HETCOR spectrum of N-(2-methoxybenzyl)-6-Methyl-1,3-benzothiazol-2-amine (4b)

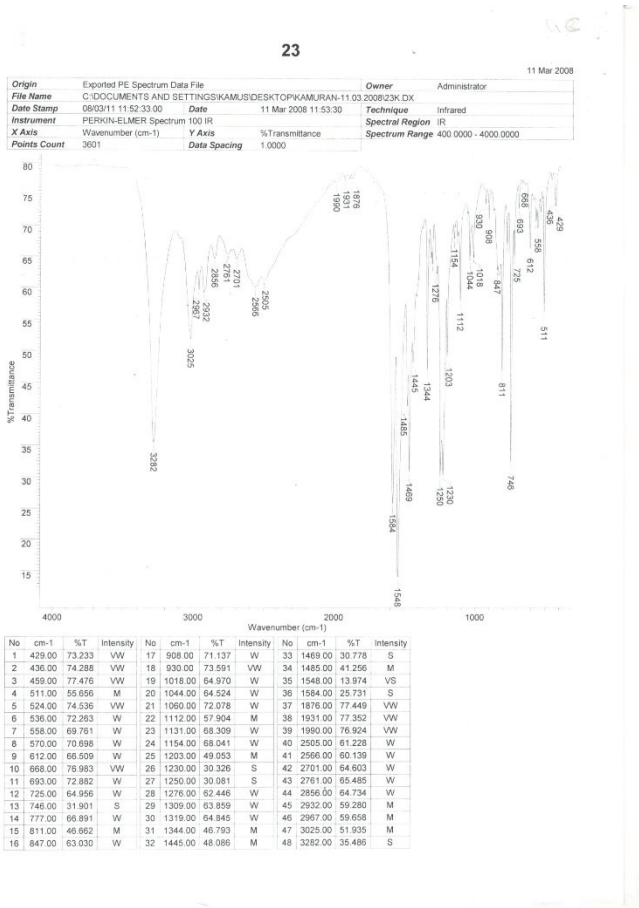


| No | cm-1 | %T | Intensity | No | cm-1 | %T | Intensity | No | cm-1 | %T | Intensity |
|---|---|---|---|---|---|---|---|---|---|---|---|
| 1 | 429.00 | 73.233 | VW | 17 | 908.00 | 71.137 | W | 33 | 1469.00 | 30.778 | S |
| 2 | 436.00 | 74.288 | VW | 18 | 930.00 | 73.591 | VW | 34 | 1485.00 | 41.256 | M |
| 3 | 459.00 | 77.476 | VW | 19 | 1018.00 | 64.970 | W | 35 | 1548.00 | 13.974 | VS |
| 4 | 511.00 | 55.656 | M | 20 | 1044.00 | 64.524 | W | 36 | 1584.00 | 25.731 | S |
| 5 | 524.00 | 74.536 | VW | 21 | 1060.00 | 72.078 | W | 37 | 1876.00 | 77.449 | VW |
| 6 | 536.00 | 72.263 | W | 22 | 1112.00 | 57.904 | M | 38 | 1931.00 | 77.352 | VW |
| 7 | 558.00 | 69.761 | W | 23 | 1131.00 | 68.309 | W | 39 | 1990.00 | 76.924 | VW |
| 8 | 570.00 | 70.698 | W | 24 | 1154.00 | 68.041 | W | 40 | 2505.00 | 61.228 | W |
| 9 | 612.00 | 66.509 | W | 25 | 1203.00 | 49.053 | M | 41 | 2566.00 | 60.139 | W |
| 10 | 668.00 | 76.983 | VW | 26 | 1230.00 | 30.326 | S | 42 | 2701.00 | 64.603 | W |
| 11 | 693.00 | 72.882 | W | 27 | 1250.00 | 30.081 | S | 43 | 2761.00 | 65.485 | W |
| 12 | 725.00 | 64.956 | W | 28 | 1276.00 | 62.446 | W | 44 | 2856.00 | 64.734 | W |
| 13 | 746.00 | 31.901 | S | 29 | 1309.00 | 63.859 | W | 45 | 2932.00 | 59.280 | M |
| 14 | 777.00 | 66.891 | W | 30 | 1319.00 | 64.845 | W | 46 | 2967.00 | 59.658 | M |
| 15 | 811.00 | 46.662 | M | 31 | 1344.00 | 46.793 | M | 47 | 3025.00 | 51.935 | M |
| 16 | 847.00 | 63.030 | W | 32 | 1445.00 | 48.086 | M | 48 | 3282.00 | 35.486 | S |

Figure S-28. FT-IR spectrum of N-(2-hyroxybenzyl)-6-Methyl-1,3-benzothiazol-2-amine (4c).

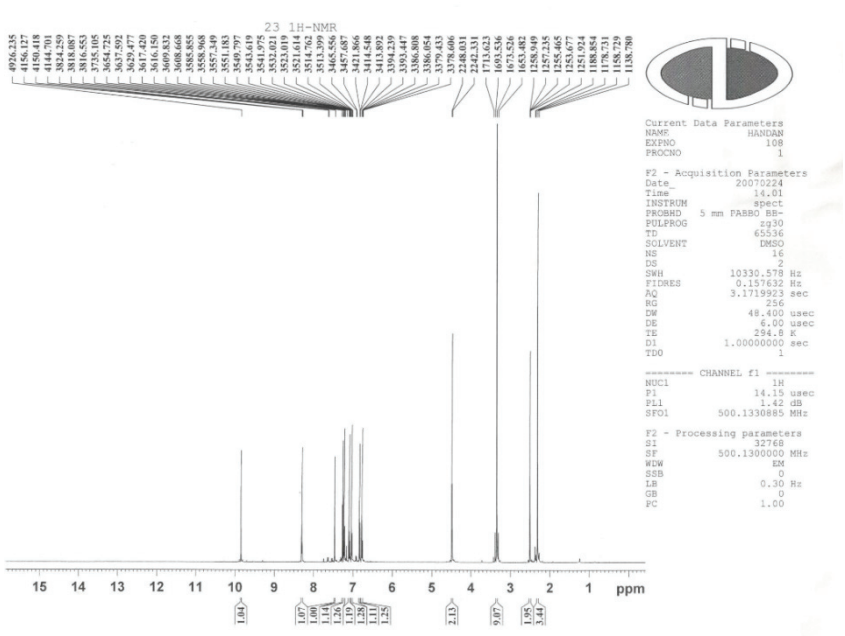


Figure S-29. 1H NMR spectrum of N-(2-hyroxybenzyl)-6-Methyl-1,3-benzothiazol-2-amine (4c).

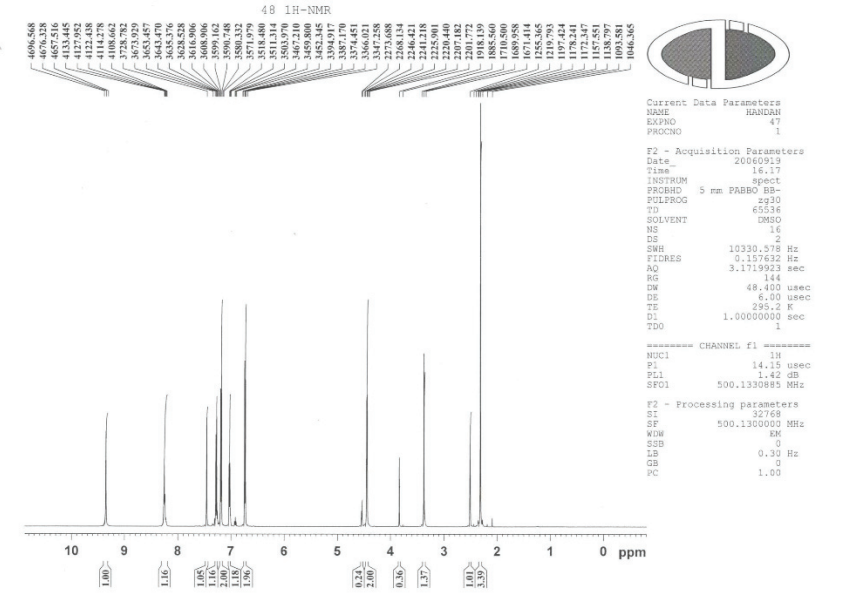


Figure S-30. 1H NMR spectrum of N-(4-hyroxybenzyl)-6-Methyl-1,3-benzothiazol-2-amine (4d).

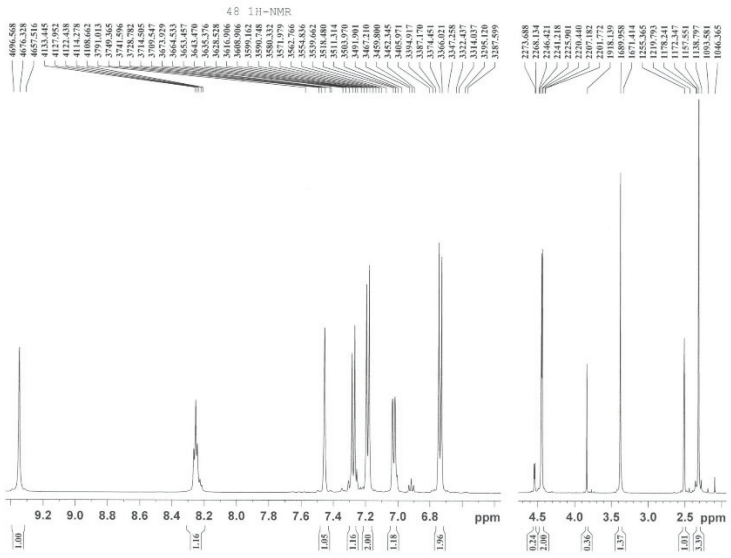


Figure S-31. 1H NMR spectrum of N-(4-hyroxybenzyl)-6-Methyl-1,3-benzothiazol-2-amine (4d).

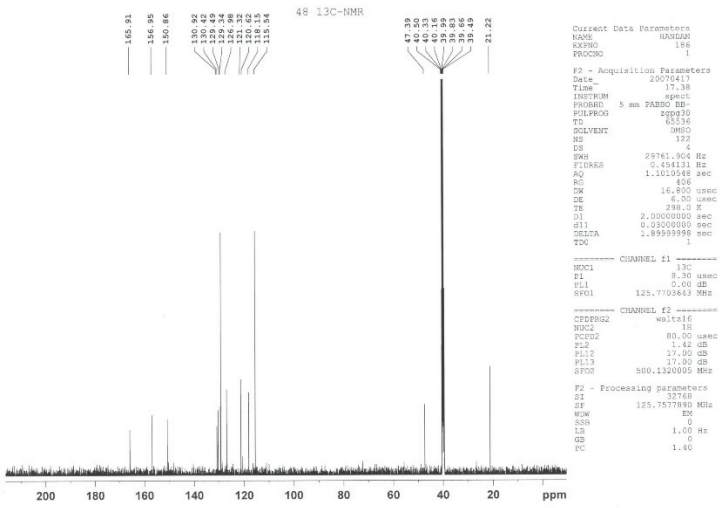


Figure S-32. 13C NMR spectrum of N-(4-hyroxybenzyl)-6-Methyl-1,3-benzothiazol-2-amine (4d).

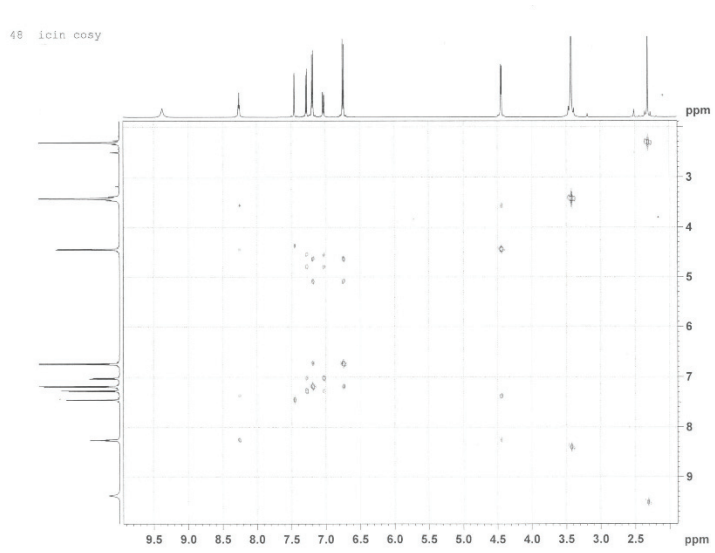


Figure S-33. COSY spectrum of N-(4-hyroxybenzyl)-6-Methyl-1,3-benzothiazol-2-amine (4d).

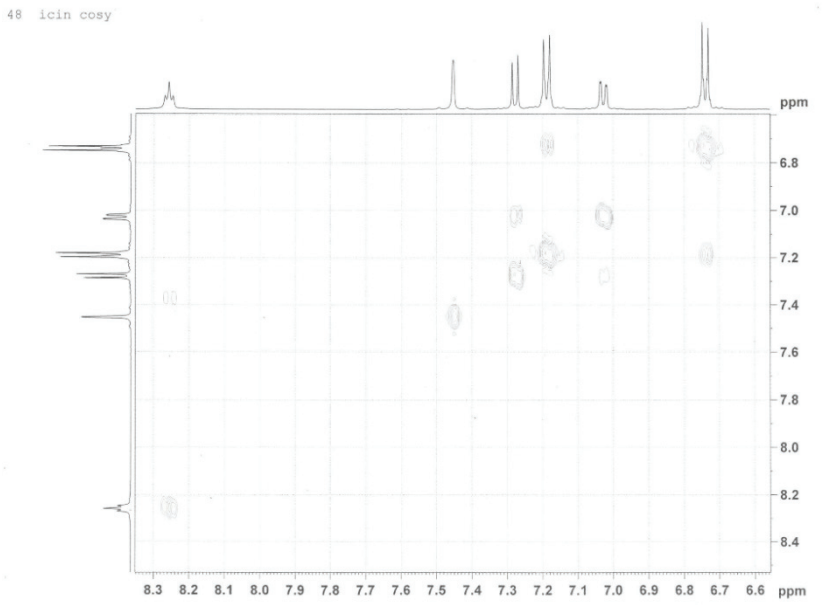


Figure S-34. COSY spectrum of N-(4-hyroxybenzyl)-6-Methyl-1,3-benzothiazol-2-amine (4d).

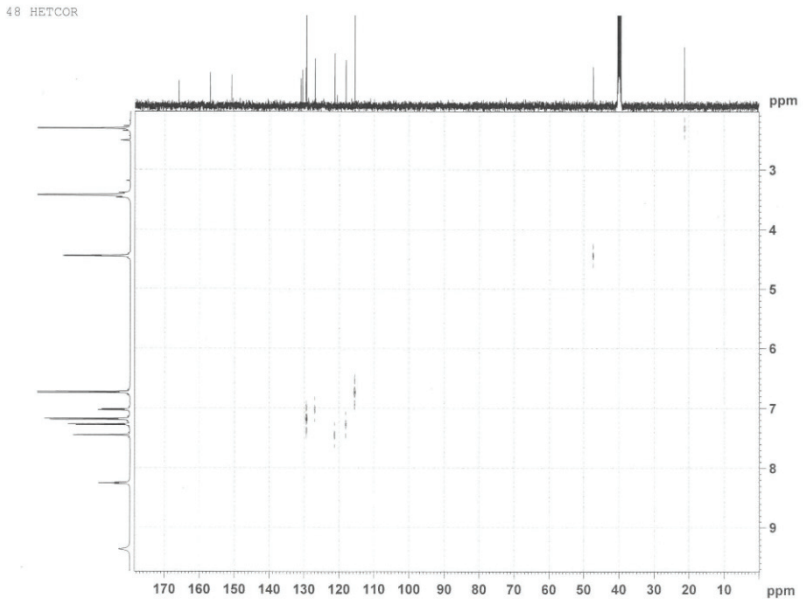


Figure S-35. HETCOR spectrum of N-(4-hyroxybenzyl)-6-Methyl-1,3-benzothiazol-2-amine (4d).

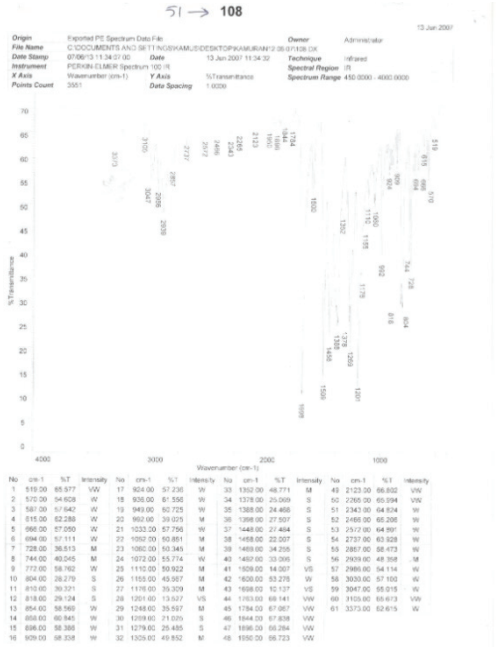


Figure S-36. FT-IR spectrum of 2-Chloro-N-[6-methyl-1,3-benzothiazol-2-yl]-N-[2-methylbenzyl] acetamide (5a).

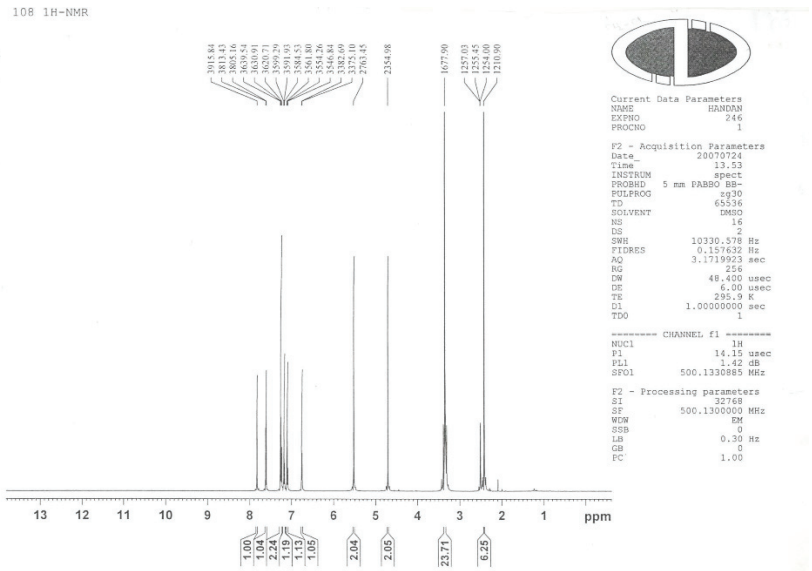


Figure S-37. 1H NMR spectrum of 2-Chloro-N-[6-methyl-1,3-benzothiazol-2-yl]-N-[2-methylbenzyl] acetamide (5a).

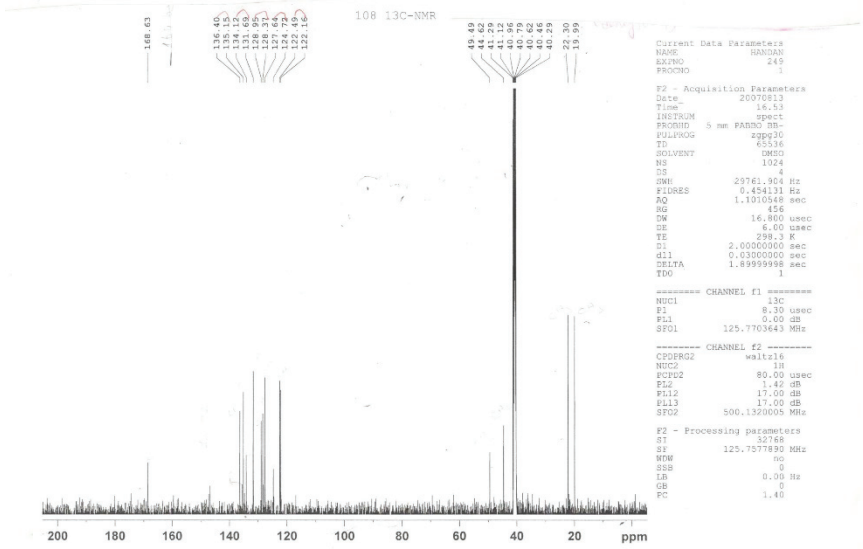


Figure S-38. 13C NMR spectrum of 2-Chloro-N-[6-methyl-1,3-benzothiazol-2-yl]-N-[2-methylbenzyl] acetamide (5a).

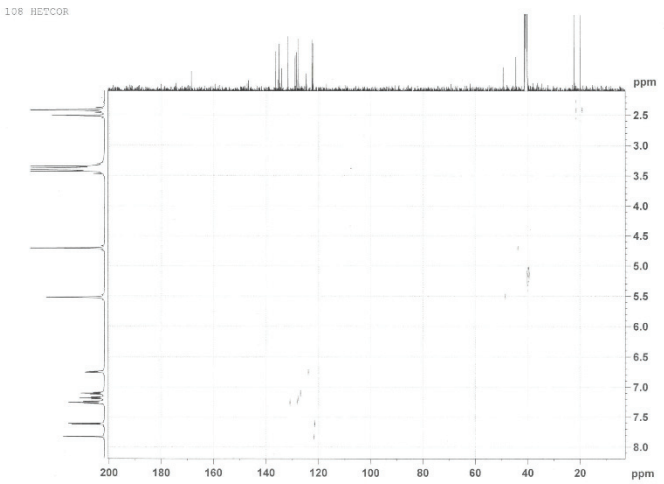


Figure S-39. HETCOR spectrum of 2-Chloro-N-[6-methyl-1,3-benzothiazol-2-yl]-N-[2-methylbenzyl] acetamide (5a).

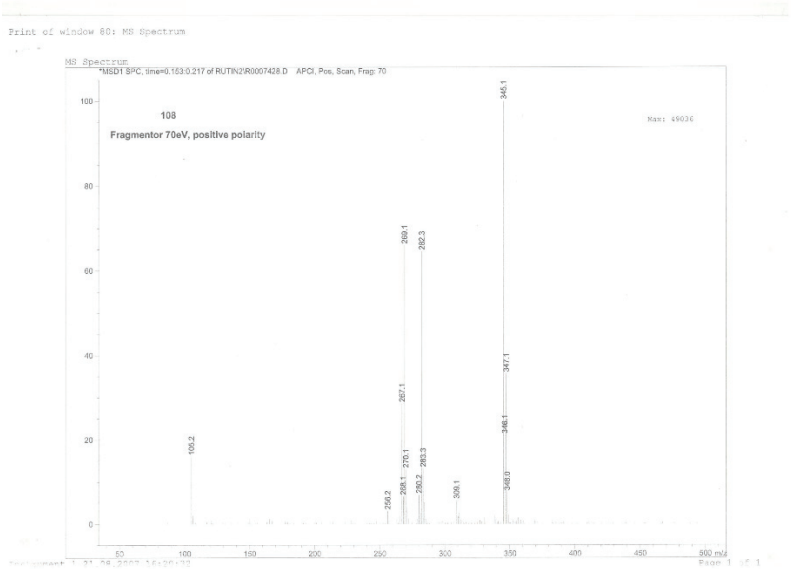


Figure S-40. ESI-MS spectrum of 2-Chloro-N-[6-methyl-1,3-benzothiazol-2-yl]-N-[2-methylbenzyl] acetamide (5a)

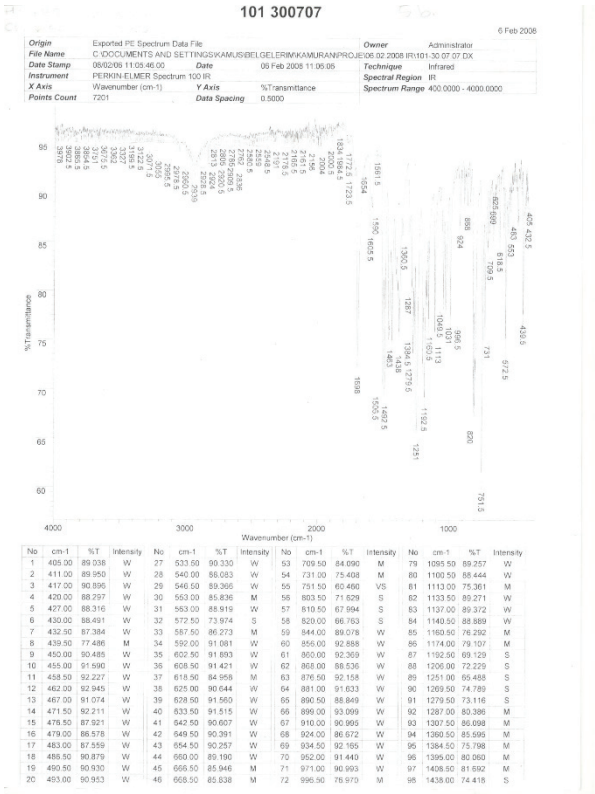


| No | cm-1 | %T | Intensity | No | cm-1 | %T | Intensity | No | cm-1 | %T | Intensity | No | cm-1 | %T | Intensity | No | cm-1 | %T | Intensity |
|---|---|---|---|---|---|---|---|---|---|---|---|---|---|---|---|---|---|---|---|
| 1 | 405.00 | 89.038 | W | 27 | 533.50 | 90.330 | W | 53 | 709.50 | 84.090 | M | 79 | 1095.50 | 89.257 | W |
| 2 | 411.00 | 89.950 | W | 28 | 540.00 | 88.083 | W | 54 | 731.00 | 75.408 | M | 80 | 1100.50 | 88.444 | W |
| 3 | 417.00 | 90.896 | W | 29 | 546.50 | 89.366 | W | 55 | 751.50 | 60.466 | VS | 81 | 1113.00 | 75.361 | M |
| 4 | 420.00 | 88.297 | W | 30 | 553.00 | 85.836 | M | 56 | 803.50 | 71.629 | S | 82 | 1133.50 | 89.221 | W |
| 5 | 427.00 | 88.316 | W | 31 | 563.00 | 88.919 | W | 57 | 810.50 | 67.994 | S | 83 | 1137.00 | 89.372 | W |
| 6 | 430.00 | 88.491 | W | 32 | 572.50 | 73.974 | S | 58 | 820.00 | 66.763 | S | 84 | 1140.50 | 88.889 | W |
| 7 | 432.50 | 87.384 | W | 33 | 587.50 | 86.273 | M | 59 | 844.00 | 89.078 | W | 85 | 1160.50 | 76.292 | M |
| 8 | 439.50 | 77.486 | M | 34 | 592.00 | 91.081 | W | 60 | 856.00 | 92.888 | W | 86 | 1174.00 | 79.107 | M |
| 9 | 450.00 | 90.485 | W | 35 | 602.50 | 91.693 | W | 61 | 860.00 | 92.369 | W | 87 | 1192.50 | 69.129 | S |
| 10 | 455.00 | 91.590 | W | 36 | 608.50 | 91.421 | W | 62 | 868.00 | 88.536 | W | 88 | 1206.00 | 72.229 | S |
| 11 | 458.50 | 92.227 | W | 37 | 618.50 | 84.958 | M | 63 | 876.50 | 92.158 | W | 89 | 1251.00 | 65.488 | S |
| 12 | 462.00 | 92.945 | W | 38 | 625.00 | 90.644 | W | 64 | 881.00 | 91.633 | W | 90 | 1269.50 | 74.789 | S |
| 13 | 467.00 | 91.074 | W | 39 | 628.50 | 91.560 | W | 65 | 890.50 | 88.849 | W | 91 | 1279.50 | 73.116 | S |
| 14 | 471.50 | 92.211 | W | 40 | 633.50 | 91.515 | W | 66 | 899.00 | 93.099 | W | 92 | 1287.00 | 80.386 | M |
| 15 | 479.50 | 87.921 | W | 41 | 642.50 | 90.607 | W | 67 | 910.00 | 90.995 | W | 93 | 1307.50 | 86.098 | M |
| 16 | 479.00 | 86.578 | W | 42 | 649.50 | 90.391 | W | 68 | 924.00 | 86.672 | W | 94 | 1360.50 | 85.595 | M |
| 17 | 483.00 | 87.559 | W | 43 | 654.50 | 90.257 | W | 69 | 934.50 | 92.165 | W | 95 | 1384.50 | 75.798 | M |
| 18 | 486.50 | 90.879 | W | 44 | 660.00 | 89.190 | W | 70 | 952.00 | 91.440 | W | 96 | 1395.00 | 80.060 | M |
| 19 | 490.50 | 90.930 | W | 45 | 666.50 | 85.946 | M | 71 | 971.00 | 90.993 | W | 97 | 1408.50 | 81.692 | M |
| 20 | 493.00 | 90.953 | W | 46 | 668.50 | 85.838 | M | 72 | 996.50 | 76.979 | M | 98 | 1438.00 | 74.418 | S |

Figure S-41. FT-IR spectrum of 2-Chloro-N-[6-methyl-1,3-benzothiazol-2-yl]-N-[2-methoxybenzyl]acetamide (5b).

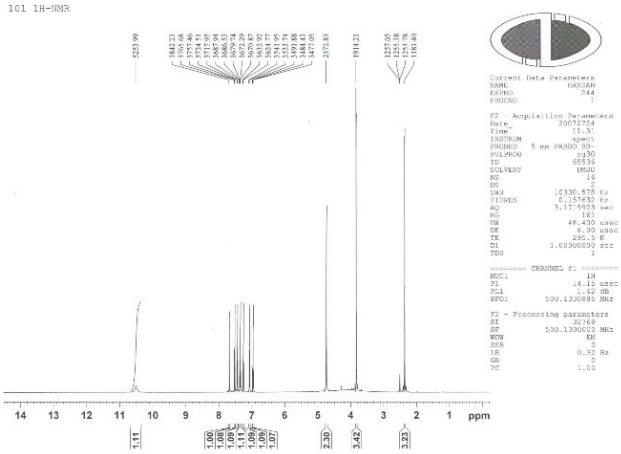


Figure S-42. 1H NMR spectrum of 2-Chloro-N-[6-methyl-1,3-benzothiazol-2-yl]-N-[2-methoxybenzyl]acetamide (5b).

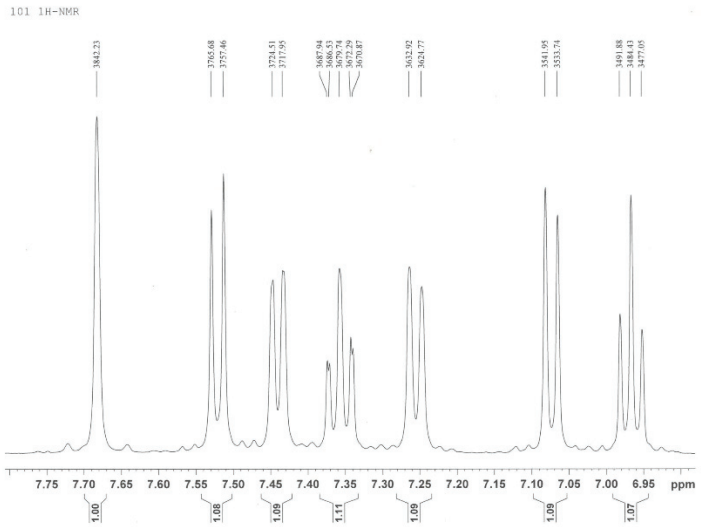


Figure S-43. 1H NMR spectrum of 2-Chloro-N-[6-methyl-1,3-benzothiazol-2-yl]-N-[2-methoxybenzyl]acetamide(5b).

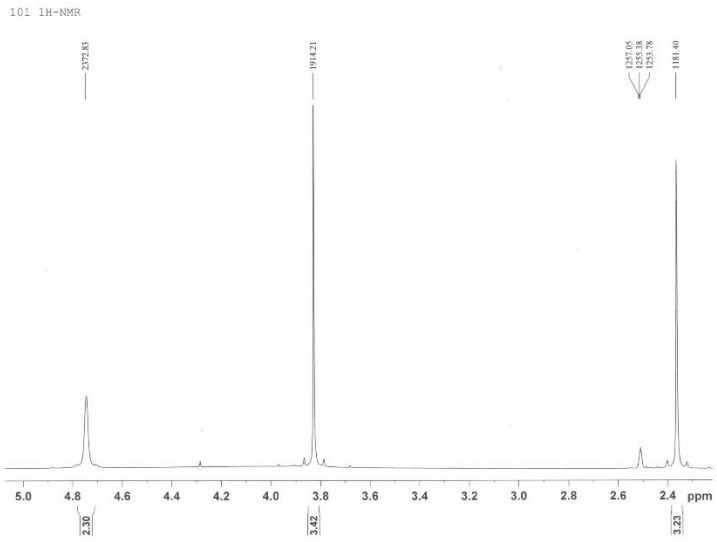


Figure S-44. 1H NMR spectrum of 2-Chloro-N-[6-methyl-1,3-benzothiazol-2-yl]-N-[2-methoxybenzyl]acetamide(5b).

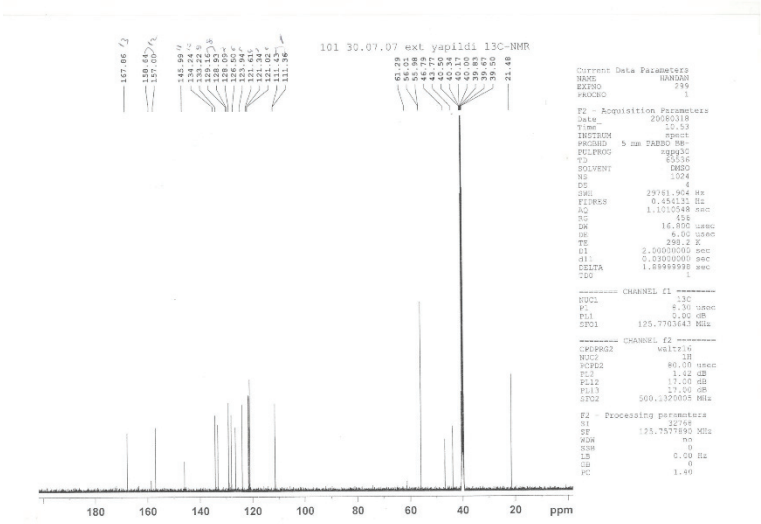


Figure S-45. 13C NMR spectrum of 2-Chloro-N-[6-methyl-1,3-benzothiazol-2-yl]-N-[2-methoxybenzyl]acetamide (5b).

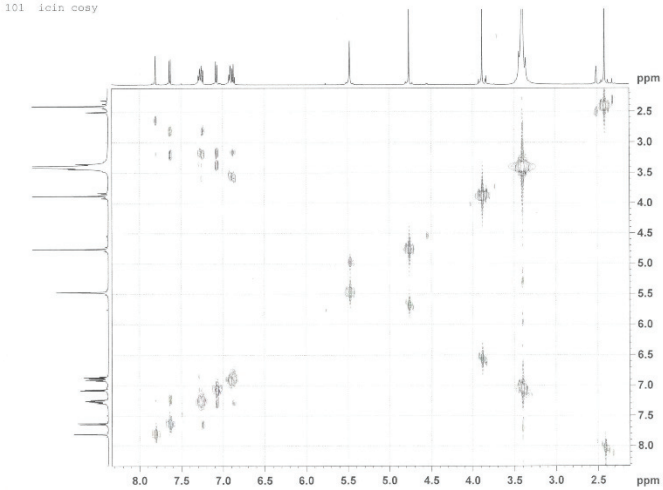


Figure S-46. COSY spectrum of 2-Chloro-N-[6-methyl-1,3-benzothiazol-2-yl]-N-[2-methoxybenzyl]acetamide (5b).

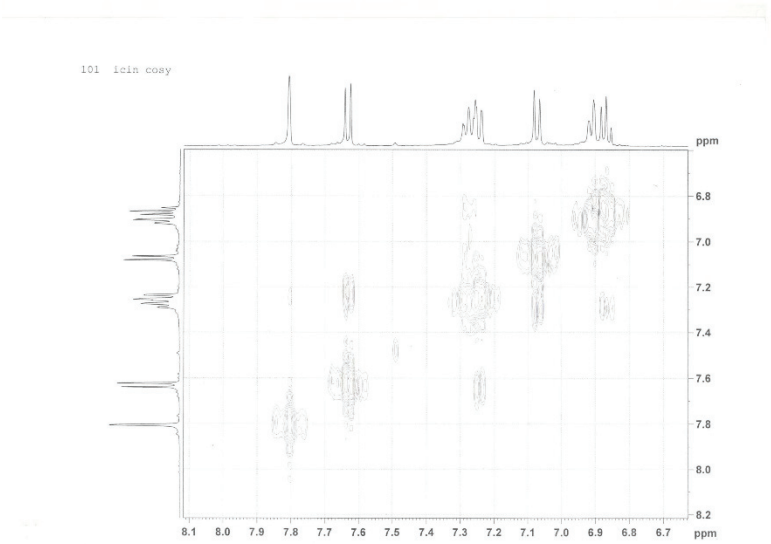


Figure S-47. COSY spectrum of 2-Chloro-N-[6-methyl-1,3-benzothiazol-2-yl]-N-[2-methoxybenzyl]acetamide (5b).

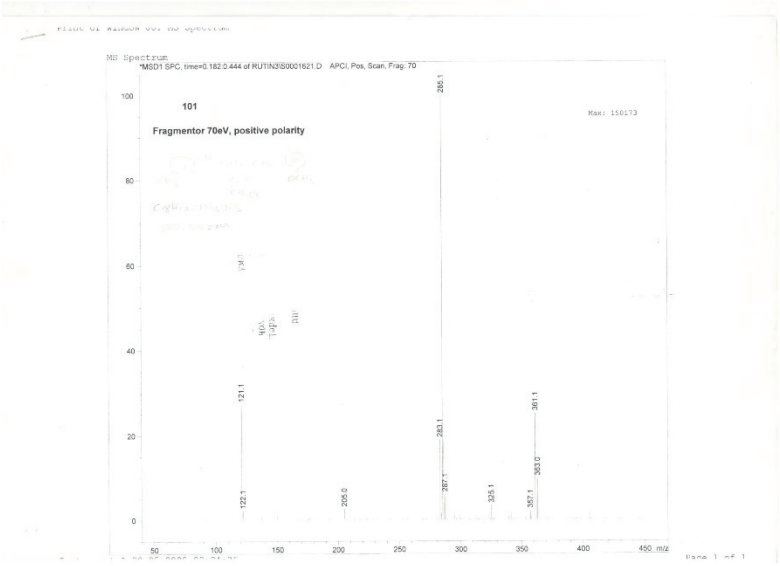


Figure S-48. ESI-MS spectrum of 2-Chloro-N-[6-methyl-1,3-benzothiazol-2-yl]-N-[2-methoxybenzyl]acetamide (5b).

Journal of the Serbian Chemical Society
JSCS-info@shd.org.rs • www.shd.org.rs/JSCS
*J. Serb. Chem. Soc.* *89* (9) 1147–1164 (2024)
*JSCS–5778*
*Original scientific paper*
Published 7 September 2024

# The ethanolic extract of *Eryngium billardierei* F. Delaroche restrains protein glycation in human serum albumin: An *in vitro* study

SANAZ YAVARI[1], AZADEH HEKMAT[1]* and SOROUSH SARDARI[2]

[1]*Department of Biology, Science and Research Branch, Islamic Azad University, Tehran, Iran and* [2]*Drug Design and Bioinformatics Unit, Department of Medical Biotechnology, Biotechnology Research Center, Pasteur Institute of Iran, Tehran 13169-43551, Iran*

(Received 23 July, revised 16 August, accepted 21 November 2023)

*Abstract*: Protein glycation is directly associated with many pathological conditions. This study investigated the potential of *Eryngium billardierei* extract to inhibit the glycation process in human serum albumin (HSA). After preparation of the ethanolic extract of *E. billardierei*, the structural changes of glycated HSA in the absence and presence of different concentrations of *E. billardierei* extract were investigated using circular dichroism (CD), fluorescence spectroscopy and UV–Vis spectroscopy. The results confirmed that *E. billardierei* extract could reduce the formation of advanced glycation end products (AGEs) and Amadori products under *in vitro* glycation conditions and also improve HSA helical structure. In addition, a reduction in the HSA-cross amyloid formation was seen in the thioflavin T assay. The phytochemical analysis disclosed that *E. billardieri* extract is high in flavonoid and phenolic compounds. Accordingly, it could be concluded that the phenolics in *E. billardieri* extract could prevent glucose-induced HSA glycation. This study provides the rationale that *E. billardieri* extract could be implicated in controlling diabetes.

*Keywords*: AGEs; glycation; *Eryngium billardierei* extract; human serum albumin; spectroscopy.

## INTRODUCTION

Fructose, glucose and other reducing sugars are necessary nutrients for the sustenance of human life. However, in the spontaneous non-enzymatic glycation process reducing carbohydrates, especially monosaccharides, bind covalently to the free amino groups of proteins and eventually cause the formation of toxic, heterogeneous, and irreversible advanced glycation end products (AGEs). The glycation of proteins is a main contributing issue to complications of diabetes

*Corresponding author. E-mail: hekmat@ut.ac.ir
https://doi.org/10.2298/JSC230725091Y

mellitus.[1,2] Furthermore, AGE accumulation contributes to the progression of osteoporosis, and lifestyle-related diseases for example arteriosclerosis.[3] The two main sources of AGEs in the human body are the exogenous AGEs found in highly processed foods and the endogenous AGEs that are generated under oxidative stress and hyperglycemic conditions.[4] Various research have reported glycation of circulatory proteins, such as serum albumins.[5,6] Human serum albumin (HSA), a helical triple-domain structure protein, is a major contributor to oncotic blood pressure that includes 585 amino acids in its single polypeptide chain.[7–9] It has been shown that HSA could be involved in the formation of AGEs potentially.[10]

Recently, numerous compounds have been verified for glycation inhibitory potential *in vitro* and some success has been achieved with a few compounds being effective *in vivo* also. Herbs are known to contain functional components which can hinder glycation stress.[11] Furthermore, in comparison with synthetic substances, natural products have been found to be cheap, relatively non-toxic, and usable in an ingestible form.[12] The *Eryngium* is a plant of the Apiaceae family with 274 species, of which nine are native to Iran. *Eryngium billardierei* is applied considerably as a medicinal plant worldwide for the treatment of diverse ailments. The Persian name of the dominant *E. Billardieri* species is the Boqanq. In folk medicine, several parts of *E. Billardieri* are utilized for a wide range of diseases, such as scorpion bites, urinary infections, sinusitis, rheumatism, inflammatory disorders and wound healing. Previous studies showed that extracts obtained from the aerial and root parts of *E. billardieri* have anti-inflammatory, anti-oxidant, anti-bacterial, and anti-nociceptive effects.[13,14] Recent investigations also indicated the anti-diabetic effect of *E. Billardieri* extracts by improving the insulin resistance index and lipid profile, reducing G6Pase and PEPCK levels,[15] as well as reducing glucose levels and liver enzymes, and increasing the level of HDL to near normal.[16]

Accordingly, although previous studies highlighted the anti-diabetic effect of *E. billardieri in vivo*, research concerning the molecular mechanism of anti-glycation effects of *E. billardierei* on proteins is extremely limited. Hence, this study aims to analyze the anti-glycation potential of *E. billardierei* against glycated HAS, for the first time by employing a multi-spectroscopic approach. The results of this study can offer a platform to utilize *E. billardierei* in the treatment of aggregation-oriented disorders.

## EXPERIMENTAL

### *Materials*

Human serum albumin (> 96 %, lyophilized powder, fatty acid-free), D-glucose, nitro-blue tetrazolium (NBT), thioflavin T (ThT), acrylamide, *bis*-acrylamide, glycine, glycerol, *N′,N′*-tetramethylethylenediamine (TEMED), coomassie brilliant blue, and ethyleneamide-tetraacetic acid (EDTA) were acquired from Sigma Co. (USA). The dialysis tubing (cut off

10,000 MW) and membrane filters (25 mm in diameter, 0.2 μm pore size) were from Whatman (UK). Ethanol, di-sodium hydrogen phosphate ($Na_2HPO_4$), sodium phosphate monobasic ($NaH_2PO_4$) and sodium azide ($NaN_3$) were obtained from Merck Co. (Germany). Plant materials were purchased from a local market in Tehran province (Iran). The voucher specimen (No. IAUH-12161) was confirmed by Avicenna Herbarium, Science and Research Branch, Islamic Azad University (Iran).

*Preparation of ethanolic extract*

The extraction procedure was adapted from previous research.[17] Briefly, the sepal and petal parts of *E. billardieri* were dried in an oven and ground to a fine powder with a mechanical grinder (Retsch, Germany). Afterward, 50 g of plant powder was macerated in 500 mL of ethanol (70 vol. %), covered with aluminum foil and kept in a shaker at room temperature. After 72 h, the extract was filtered through Whatman filter papers. Subsequently centrifuged at 3500 rpm for 20 min. Condensation was conducted by a rotary evaporator (Heidolph, Germany). The supernatant was dried at 37 °C and the obtained semisolid mass was kept at 4 °C for further analyses.

In-vitro *glycation of HSA*

Samples of HSA ($1.5\times10^{-5}$ M) were diluted to 10 mg $mL^{-1}$ in sodium phosphate buffer (50 mM $NaH_2PO_4/Na_2HPO_4$ and 1 mM EDTA at pH 7.4 containing 0.02 % $NaN_3$ (to avoid microbial contamination) in capped vials under sterile conditions, which contained glucose (40 mM), glucose with different concentrations of ethanolic extract of *E. billardierei* (45, 105, 135, 175, 210 and 240 μg $mL^{-1}$), ethanol (70 vol. %) or no additive as a control (N-HSA). Protein concentration was determined spectrophotometrically with an extinction coefficient (*E1%*) of 5.30 at 280 nm[18] using a double-beam spectrophotometer (PG Instruments $T90^+$, UK). All dishes were autoclaved and all solutions were filter-sterilized (0.2 μm). The capped vials were incubated at 37 °C for 21 days and protected from light. This incubation time was selected to provide appropriate time for the completion of the intermediate stage of HSA glycation and production of Amadori products.[10] On completion of incubation, samples were dialyzed against sodium phosphate buffer for 48 h at 4 °C to remove excess amount of glucose.[19,20] After dialysis, all samples were aliquotted and stored at –20 °C for further analyses. The concentration of G-HSA (HSA incubated with glucose) was verified in triplicates by bicinchoninic acid protein (BCA) assay.

*Determination of total phenolic content (*TPC*)*

The *TPC* of *E. billardierei* at different concentrations was estimated utilizing the Folin–Ciocalteu (FC) method, as described earlier.[14] Briefly, 0.5 mL of the extract samples and standard gallic acid (GA) (10, 20, 40, 60, 80, 100 μg $mL^{-1}$) were positioned into the test tubes and mixed for 5 min at room temperature. Afterward, 2.5 mL of FC's reagent was mixed and shaken. After 5 min, 2 mL of sodium carbonate (2 %) was added and allowed to stand at room template for 2 h. The UV–Vis absorption was recorded by spectrophotometer at 760 nm. The blank was performed utilizing a reagent blank with solvent. The experiments were performed in triplicates. The calibration curve was plotted utilizing standard GA. The results were expressed as mg GAE/g dry extract.

*Determination of total flavonoid content (*TFC*)*

The test sample's *TFC* was determined utilizing the aluminum chloride method according to the previous method.[14] Quercetin (20–100 μg $mL^{-1}$) was utilized to make the calibration curve. Briefly, 1.5 mL of the extract with a defined concentration was mixed with 1.5 mL of a

solution of aluminum chloride, 2 %) and afterward 3 mL of potassium acetate (5 %) was added to the mixture. After 40 min incubation, the absorbance was measured at 415 nm. The experiments were performed in triplicates and average values were used. The TFC was expressed as mg QE/g dry weight of extract.

*UV–Vis spectroscopy*

The UV–Vis spectra of ethanolic extract (240 μg mL$^{-1}$), N-HSA (5 μM), G-HSA (5 μM), G-HSA (5 μM) in ethanol solution, and G-HSA with different concentrations of ethanolic extract of *E. billardierei* (45, 105, 135, 175, 210 and 240 μg mL$^{-1}$) were recorded by a double beam spectrophotometer in a wavelength range of 200–700 nm at 37 °C.

*The intrinsic fluorescence measurements*

The intrinsic fluorescence of tryptophan residue of N-HSA (5 μM), G-HSA (5 μM), G--HSA (5 μM) in ethanol solution and G-HSA with different concentrations of ethanolic extract of *E. billardierei* (45, 105, 135, 175, 210 and 240 μg mL$^{-1}$) was monitored *via* a BSFL-102 fluorescence spectrophotometer (BioLAB, Canada) utilizing a 1 cm quartz cell at 37 °C. The excitation wavelength was 285 nm. In all cases, 10 nm emission and excitation slits were utilized. For inner filter influence correction affected by the emission and excitation signals attenuation caused by the quencher absorption, Eq. (1) was applied:[21]

$$F_{\text{corr}} = F_{\text{obs}} \times 10^{(Ab_{\text{ex}} + Ab_{\text{em}})/2} \quad (1)$$

where $Ab_{\text{em}}$, $Ab_{\text{ex}}$, $F_{\text{obs}}$ and $F_{\text{corr}}$ are the mixture absorption at emission as well as excitation wavelengths, the observed fluorescence intensity, besides the corrected fluorescence intensity, respectively.

*AGE Formation analysis*

The emission spectra of N-HSA, G-HSA, G-HSA in ethanol solution and G-HSA in the presence of 45, 105, 135, 175, 210 and 240 μg mL$^{-1}$ of *E. billardierei* extract at 370 nm excitation were acquired using BSFL-102 fluorescence spectrophotometer for the detection of AGE formation. Each point signifies the mean of three independent experiments.

*Circular dichroism analysis*

The secondary structural changes of N-HSA (5 μM), G-HSA (5 μM), G-HSA (5 μM) in ethanol solution and G-HSA in the presence of 175 and 240 μg mL$^{-1}$ *E. billardierei* extract were monitored by model 215 circular dichroism (CD) spectrometer (AVIV, USA) with a scan speed of 20 nm min$^{-1}$. Measurements were recorded at 190–260 nm employing a quartz cell and a path length of 1 mm at 37 °C. Each spectrum was the average of three scans. Using subtracting the proper baseline, each CD spectrum was corrected. The spectrum of the CD buffer alone was subtracted from the spectrum of the sample containing N-HSA. However, since D-glucose exhibited a CD band around 190 nm, the CD curve of G-HSA was corrected by subtracting the spectral contribution of D-glucose-free HSA. The CD curves of G-HSA in the presence of *E. billardierei* extract were also corrected by subtracting the CD spectra of the samples containing glucose and *E. billardierei* extract mixtures. The CD curve of G-HSA in the presence of ethanol was corrected by subtracting the spectral contribution of ethanol and glucose mixtures. The CD spectra deconvolution software (CDNN, version 2.1) was applied to investigate the CD-spectra.

*Determination of Amadori products*

Samples were evaluated for Amadori products based on the NBT reaction with ketoamines. In carbonate buffer (pH 10.35) 0.18 μg mL$^{-1}$ sample of protein was mixed with 0.03

mM NBT reagent and incubated for 1 h at 37 °C. Afterward, absorbance was monitored at 530 nm. Each point signifies the mean of three independent experiments.

*ThT fluorescence analysis*

A stock solution of ThT at 1 mM concentration was prepared in 0.01 M PBS at pH 7.4 and diluted to 0.1 μM. Then 10 μL of ThT was added to the samples (N-HSA (5 μM), G-HSA (5 μM), G-HSA (5 μM) in ethanol solution and G-HSA in the presence of 175 and 240 μg $mL^{-1}$ *E. billardierei* extract) and then incubated for 30 min at 37 °C. Samples were scanned by BSFL-102 fluorescence spectrophotometer using an excitation/emission wavelength of 450/ /490 nm. In all cases, 10 nm emission and excitation slits were utilized. Spectra were corrected concerning the corresponding blank spectra.

*Native-polyacrylamide gel electrophoresis (Native-PAGE) and sodium dodecyl sulfate-polyacrylamide gel electrophoresis (SDS-PAGE)*

To test the effect of *E. billardierei extract* on glycation-induced protein aggregation, Native-PAGE and SDS-PAGE were performed *via* the standard protocol described by Schägger and von Jagow using 10 % acrylamide gel.[22] In native-PAGE electrophoresis, one aliquot of N-HSA, G-HSA, G-HSA in ethanol solution and G-HSA in the presence of 240 μg $mL^{-1}$ extract solution were mixed with an equal volume of sample buffer (glycerol (30 %), 0.25 M Tris–HCl buffer, pH 6.8). Each lane was loaded with 20 mg of samples. Electrophoresis was carried out at 150 V for 110 min. The native proteins were visualized by incubating the gel in acetic acid (10 %) and methanol (40 %) for 25 min, Coomassie blue solution (0.02 % in methanol (30 %) and acetic acid (10 %)) for 25 min, and acetic acid (8 %) on an orbital shaker at room temperature overnight.

In SDS-PAGE electrophoresis, samples were dissolved in sample buffer (glycerol (30 %), 0.25 M Tris-HCl buffer, SDS (3.6 %), pH 6.8), and heated at 85 °C for 10 min. For reducing conditions, 50 mM dithiothreitol (DTT) was added to the sample buffer. Electrophoresis was performed at 80 V for 180 min, in running buffer (50 mM methysulfonic acid, 50 mM tris base, SDS (0.1 %), 1 mM ethylenediaminetetraacetic acid, pH 7.3). The polypeptide bands were visualized by incubating the gel in coomassie blue solution for 25 min and de-stained (ethanol (10 %) and acetic acid (7.5 %)) on an orbital shaker at room temperature overnight.

*Statistical analysis*

The data were recorded as mean ± standard deviation of the mean ($n$ = 3). GraphPad Prism version 8.0 for Windows (GraphPad App, USA) was utilized for the analysis. The data were evaluated for significance utilizing a two-way analysis of variance (ANOVA).

## RESULTS AND DISCUSSION

### *Determination of* TPC *and* TFC *of extract*

Phenolic compounds have a wide range of biochemical activities for instance anti-carcinogenic, anti-oxidant and anti-mutagenic.[14] Furthermore, it has been confirmed that phenolic-rich plant extracts inhibited sugar-induced protein glycation.[23] Fig. 1a displays the *TPC* of *E. billardierei* extract (from sepal and petal parts) with different concentrations and with the values derived from a calibration curve ($y$ = 0.0106$x$ + 0.0544, $R^2$ = 0.99) of GA (10–100 μg $mL^{-1}$). As displayed, total phenolics in the *E. billardierei* extract with the different concentrations varied from 5.01 to 22.15 mg GAE/g dry extract. Additionally, the ana-

lysis of variance confirmed that the content was increased ($P < 0.05$) with the increasing concentration of extract.

Flavonoids are secondary, anti-oxidant, metabolites whose strength is verified by the position and number of free –OH groups. Fig. 1b exhibits the *TFC* of *E. billardierei* extract with various concentrations and quercetin (20–100 μg mL$^{-1}$) was utilized to make the calibration curve. Values were derived from a calibration curve ($y = 0.0070x + 0.0195$, $R^2 = 0.98$). As displayed, *TFC* in *E. billardierei* extract varied from 4.01 to 20.05 mg QE/g DW of the extract. Consequently, the *E. billardierei* extract proved to have significant total flavonoids and phenolics content. Our data were in agreement with those of Daneshzadeh *et al*. who determined the *TPC* and *TFC* of *E. billardierei* extract.[14] However, it should be mentioned that Daneshzadeh *et al*. prepared their extract from both leaves and flowers of *E. billardierei*.

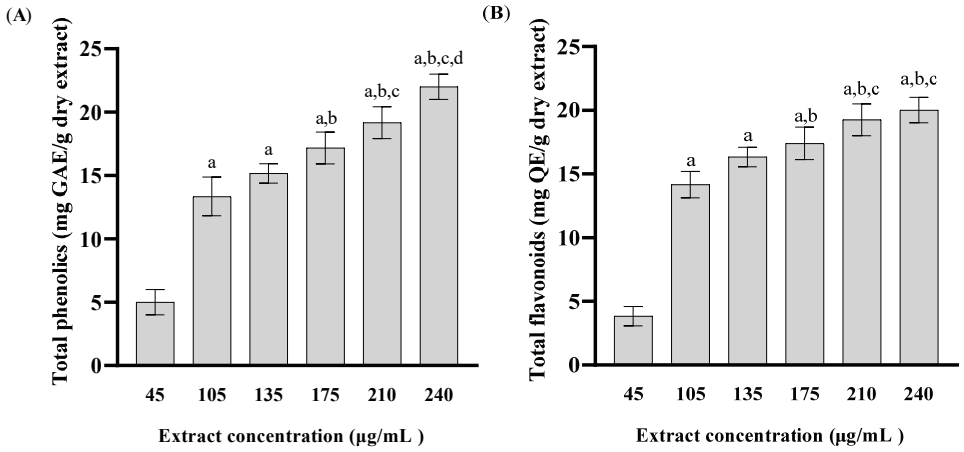


Fig. 1. a) *TPC* and b) *TFC* of *Eryngium billardieri* extract at different concentrations. $P < 0.05$ compared with the [a]45, [b]105, [c]135 and [d]175 μg mL$^{-1}$ of extract.

*UV–Vis spectroscopy results*

The UV–Vis spectroscopy of the ethanolic extraction of *E. billardierei* demonstrated a maximum absorption band ($\lambda_{max}$) at about 266 nm (Fig. 2A). According to the literature, the spectra of phenolic acids and flavonoids have obvious $\lambda_{max}$ at *ca*. 270 or 340 nm.[24] Furthermore, phenolic acids with the benzoic acid carbon framework have their $\lambda_{max}$ in the 200 to 290 nm range.[25] Generally, flavonols in the form of glycosides, exhibit $\lambda_{max}$ in the wavelength range of 260–355 nm.[24] Consequently, the *E. billardierei* extract was found to have remarkable total flavonoids and phenolics content. Additionally, there are no signals in the saponins spectrum (380 to 700 nm),[26] which confirmed the absence of sap-

onins in the *E. billardierei* extract. This observation aligns with *TPC* and *TFC* determination as mentioned earlier.

To supply information on the structural impact of the ethanolic *E. billardieri* extract on G-HSA, the UV–Vis absorption spectra of G-HSA in the absence and presence of different concentrations of *E. billardieri* extract were monitored by applying the mixture of glucose and *E. billardieri* extract at the same concentration as the reference solution. As shown in the inset of Fig. 2B, HSA has two

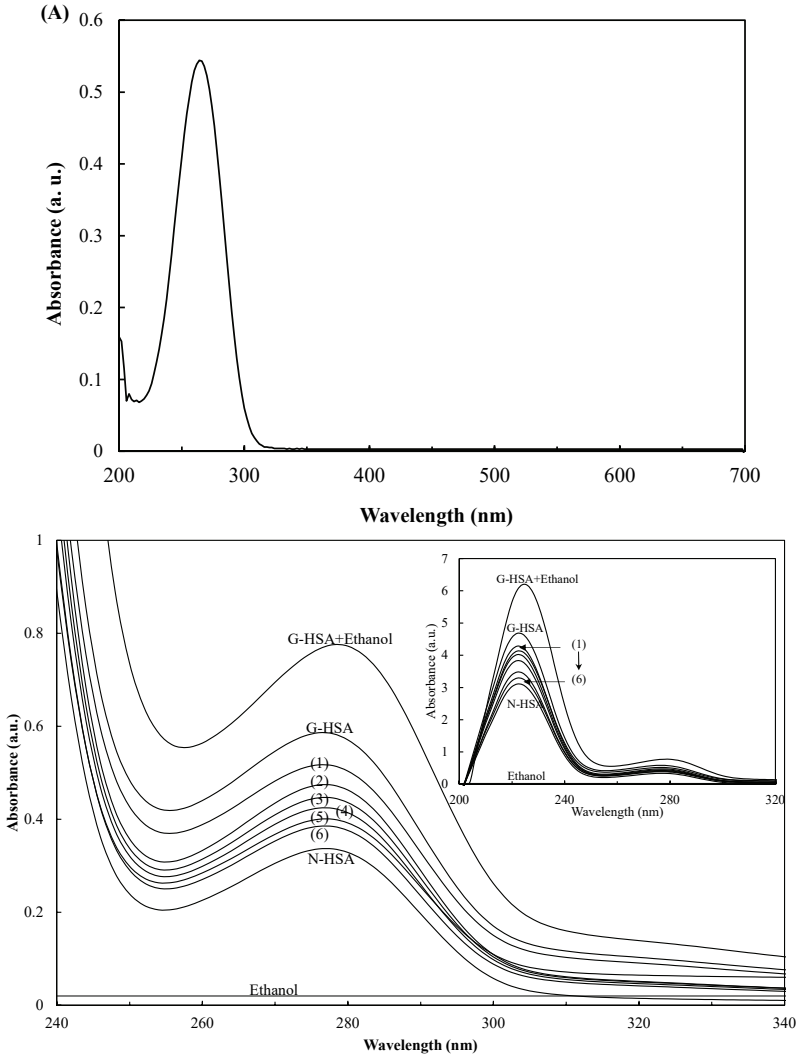


Fig. 2. The UV–Vis spectra of: a) the *E. billardierei* extract and b) N-HSA, G-HSA, G-HSA in ethanolic solution, ethanol and G-HSA in the presence of 45 (1), 105 (2), 135 (3), 175 (4), 210 (5) and 240 (6) μg $mL^{-1}$ of *E. billardierei* extract.

$\lambda_{max}$: *ca*. 230 and 380 nm. The $\lambda_{max}$ at 230 nm belongs to the n→π transition of C=O in the backbone of HSA and it additionally displays the α-helix content in the protein.[27] The $\lambda_{max}$ at *ca*. 280 nm belongs to tryptophan, tyrosine and phenylalanine residues absorption.[28] According to the literature, the absorbance values in the range of 0.2–0.8 are known to offer the highest precision.[29] However, as could be found in Fig. 2B, the UV absorbance values for peptide bonds (*ca*. 230 nm) of HSA are above this range, therefore, the alterations in $\lambda_{max}$ at 280 nm were investigated. The increase in $\lambda_{max}$ (hyperchromicity) at 280 nm for G-HSA was observed (more than two times) with no emergence of a new peak, which could be attributed to alterations in the microenvironment of aromatic amino acids or variation of aromatic amino acids.[19] Similar observations have been reported upon incubation of HSA with glucose.[19,20] This result implies that the unfolding and cross-linking of protein helices during nonenzymatic glycation changes the conformation of HSA.[30] It is well-known that any structural perturbations hamper the normal carrying capacity of HSA.[7]

The solvent employed for the extraction of plants is crucial. The choice of solvent depends on the solvent availability, the nature of the bioactive compounds, the part of a plant to be extracted, and the type of plant. Usually, polar solvents, for instance ethanol and water, are employed in the extraction of polar compounds. Ethanol is nontoxic at low concentrations and is self-preservative at a concentration above 20 %.[31] Additionally, some results suggested that the ethanolic extract of some plants potentially have hypoglycemic effect.[32,33] Consequently, in this investigation we employed the ethanolic extract of *E. billardieri*. Thus, the effects of ethanol on the glycation of HSA were also investigated. The $\lambda_{max}$ at 280 nm for G-HSA incubated in ethanol solution was even higher than G-HSA, which could be attributed to more structural alterations in G-HSA. However, As can be found in this figure the presence of different concentrations of *E. billardieri* extract in G-HSA solutions resulted in a reduction of $\lambda_{max}$ in a dose-dependent manner. It should be noted that *E. billardieri* extract was added to both reference and sample cuvettes, thus, reduction in $\lambda_{max}$ could be a result of the prevention of AGEs formation in HSA *in vitro*.

*Tryptophan (Trp)-fluorescence measurements*

One of the valuable techniques to discover protein–ligand interaction is fluorescence spectroscopy. Generally, the intrinsic fluorescence of HSA is achieved by the lone Trp residue of HSA which is located at position 214 (the $Trp_{214}$ residue) in the hydrophobic cavity of subdomain IIA (Sudlow I).[34] Any variations in polarity around the $Trp_{214}$ residue (fluorophore) could be evaluated by the shift in the fluorescence emission peak ($\lambda_{max,em}$). Thus, the variations in the tertiary structure of G-HSA in the presence of *E. billardieri* extract were determined by fluorescence spectroscopy (Fig. 3). The fluorescence intensity of G-HSA at excit-

ation of 285 nm decreased (about 46 %) with no obvious shift at the $\lambda_{max,em}$, thus it could be assumed that the binding of glucose to HSA is accompanied by fluctuations in the dielectric environment of the indole ring of $Trp_{214}$ residue. Various studies have reported a decrease in the fluorescence intensity of HSA upon glycation.[2,10,35] The fluorescence intensity of G-HSA incubated in ethanol soluteion decreased noticeably, *i.e*., ethanol could induce more fluctuations in the microenvironment of the $Trp_{214}$ residue. However, the presence of *E. billardieri* extracts restored the fluorescence of G-HSA towards native-like in a concentration-dependent manner, suggesting the fact that hydrophobic residues that get exposed upon glycation remain buried in the presence of *E. billardieri* extract.

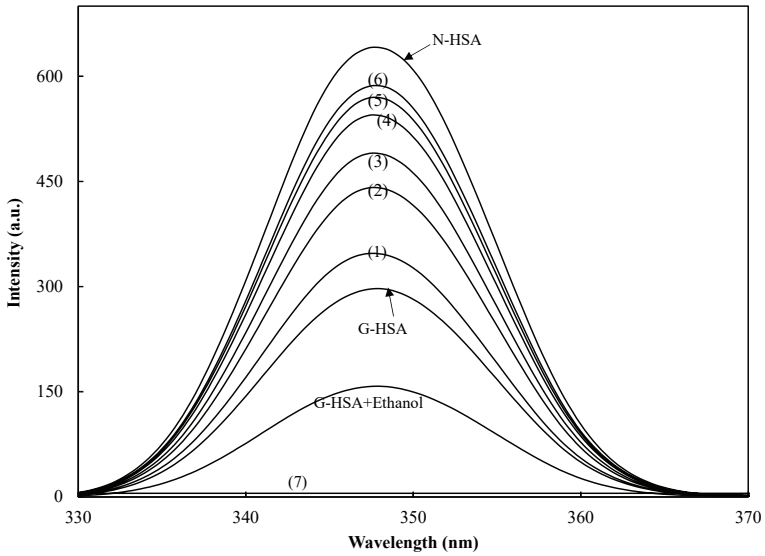


Fig. 3. Fluorescence emission spectra of f N-HSA, G-HSA, G-HSA in ethanolic solution and G-HSA in the presence of 45 (1), 105 (2), 135 (3), 175 (4), 210 (5), and 240 (6) μg $mL^{-1}$ of *E. billardierei* extract and *E. billardierei* extract alone (7).

*AGEs specific fluorescence*

Regularly the specific fluorescence of AGEs is retorted to distinguish AGE formation *in vitro*. The fluorescent AGEs are the heterocyclic aromatic amines having fluorescence at a specific wavelength and giving a characteristic peak. As shown in Fig. 4, N-HSA disclosed an insignificant and weak AGE fluorescence suggesting absence of AGE adduct formation in the native protein. However, there was an obvious enhancement in the AGE-specific fluorescence in G-HSA compared to N-HSA signifying AGE formation in HSA.[19] Surprisingly, a noticeable enhancement in the AGE-specific fluorescence in G-HSA incubated in ethanol compared to G-HSA was observed. Thus, our result revealed that ethanol

could accelerate the formation of AGE products. This observation is in agreement with those of Wu *et al.* who observed the relationship between ethanol concentration and AGE production.[19] Conversely, in the presence of *E. billardieri* extract, there was a reduction (in a concentration-dependent manner) in the fluorescence intensity compared to G-HSA, indicating that *E. billardieri* extract (especially at higher concentrations) could inhibit AGE formation potentially.[6] This observation is in line with other assays suggesting *E. billardieri* extract as a potent anti-glycating agent.

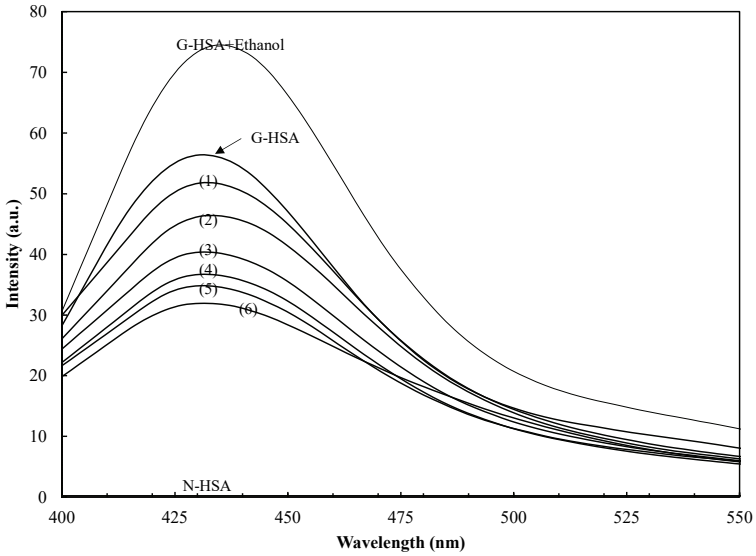


Fig. 4. The fluorescence intensity after excitation at 370 nm of N-HSA, G-HSA, G-HSA in ethanolic solution and G-HSA in the presence of 45 (1), 105 (2), 135 (3), 175 (4), 210 (5) and 240 (6) μg $mL^{-1}$ of extract.

*Determination of Amadori products consuming NBT-reducing activity*

Glycation is a spontaneous reaction between the free amino groups of proteins and aldehyde or ketone groups of reduced sugars upon covalent bond formation.[20] Glycation occurs in three stages: 1) Schiff base production, 2) Amadori product formation and 3) AGE formation. Amadori product is a ketoamine that is made during the glycation process as an important and stable intermediate in the AGEs formation. The formation of Amadori products and AGEs plays a significant role in the pathogenesis of various diseases including diabetes.[10] Amadori products can reduce NBT reagent and subsequently make colored formazan dye with $\lambda_{max}$ at 530 nm. Fig. 5 compares the formation of this dye in G-HSA in the absence and presence of *E. billardieri* extract. According to this figure, the content of Amadori product formation was increased in the G-HSA sample which is

in agreement with the previous observations.[6,10] In the G-HSA incubated in ethanolic solution sample a remarkable increase in Amadori product formation was observed which is in agreement with our AGEs specific fluorescence results. Conversely, the presence of *E. billardieri* extract (175 and 240 μg $mL^{-1}$, the two high concentrations of the extract in which the most changes in G-HSA were observed) caused a significant reduction in the content of Amadori product formation implying that the presence of *E. billardieri* extract resists non-enzymatic glycation of HSA.

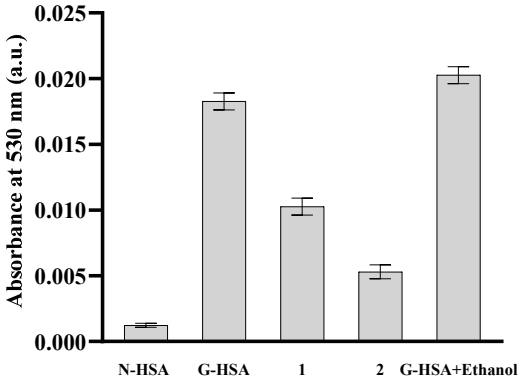


Fig. 5. NBT absorbance at 530 nm of N-HSA, G-HSA, G-HSA in ethanolic solution and G-HSA in the presence of 175 (1) and 240 (2) μg $mL^{-1}$ of *E. billardierei* extract.

*Secondary structure analysis*

Protein glycation could produce protein aggregation directly. Insoluble aggregates can create an amyloid cross-structure, initiating protein stability and structure to be modified.[23] Thus, the modifications in the secondary structure of HSA were monitored by far-UV CD spectroscopy. The far-UV CD spectra of N-HSA demonstrated two double minimums at *ca*. 222 and 208 nm (Fig. 6), which demonstrated the $\pi \rightarrow \pi^*$ transition and the $n \rightarrow \pi^*$ transition of the $\alpha$-helical structure of HSA, respectively.[7] Fig. 6 indicates loss of helical structure as determined by a reduction in the negative ellipticity at 208 and 222 nm in G-HSA compared to the control (N-HSA). As shown in Table I, the ratio of $\alpha$-helix for N-HSA was found to be 57.9 %; however, for G-HSA it was found to be 40.1 %. This result is in agreement with previous studies.[10,19,20] G-HSA incubated in ethanolic solution exhibited a meaningful fall in the $\theta$ values at 208 and 222 nm, and a significant increase in $\beta$-sheet content was also observed. Conversely, in the presence of 175 or 240 μg $mL^{-1}$ *E. billardieri* extract the $\alpha$-helix ratio was found to be 48.4 and 50.3 %, respectively. Generally, protein glycation influences the production of protein aggregation directly. Insoluble aggregates can produce an amyloid cross-structure, making protein stability and structure to be modified. Accordingly, the presence of *E. billardieri* extract resisted secondary

structural alterations and restored the far-UV CD spectra towards native-like in a dose-dependent manner indicating a potent anti-glycation agent.

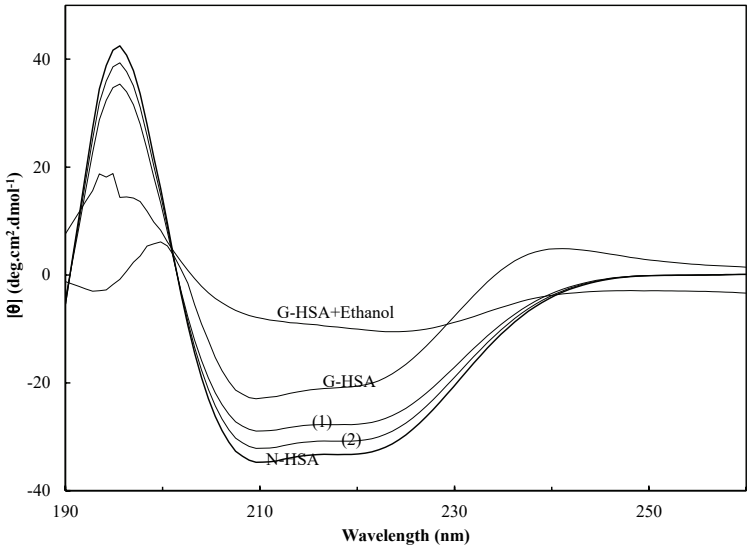


Fig. 6. The CD spectra of N-HSA, G-HSA, G-HSA in ethanolic solution and G-HSA in the presence of 175 (1) and 240 (2) μg $mL^{-1}$ of *E. billardierei* extract.

TABLE I. Content of the secondary structure of HSA and glycated HSA in the absence and presence of the *E. billardierei* extract and ethanol at 37 °C

| Sample | $\alpha$-Helix, % | $\beta$-Sheet, % | Random coil, % |
|---|---|---|---|
| N-HSA | 57.9 | 23.3 | 18.8 |
| G-HSA | 40.1 | 30.1 | 29.8 |
| G-HSA+extract (175 μg $mL^{-1}$) | 48.4 | 24.1 | 27.5 |
| G-HSA+extract (240 μg $mL^{-1}$) | 50.3 | 25.7 | 24.0 |
| G-HSA in ethanolic solution | 21.6 | 43.3 | 35.1 |

*Determination of fibrillar state with ThT*

ThT is a biomarker that interacts with the amyloid fibril structure of proteins making the enhancement of fluorescence intensity in the range of 480–490 nm upon excitation at 450 nm.[6] Accordingly, to determine if *E. billardieri* extract acts as an inhibitor of the amyloid-like aggregates, the fibrillar state with ThT was studied. According to Fig. 7, N-HSA showed minimal fluorescence indicating HSA to be in its native conformation. However, the fluorescence intensity of G-HSA was enhanced compared to N-HSA suggesting that aggregate formation has taken place.[6] The fluorescence intensity of G-HSA incubated in ethanol compared to G-HSA was also enhanced considerably exhibiting an increase in amyloid cross-conformation,[23] *i.e.*, ethanol could induce amyloid-like aggregates

in G-HSA, significantly. This observation is in agreement with our secondary structure analysis. However, G-HSA in the presence of *E. billardieri* extract (175 and 240 μg $mL^{-1}$) displayed decreased ThT fluorescence. Thus, the presence of *E. billardieri* extract could inhibit fibril formation. Hence, it can be expressed that *E. billardieri* extract is a potent mixture that can prevent fibril formation, help protein maintain its native conformation, and prevent several pathological conditions associated with protein aggregation.

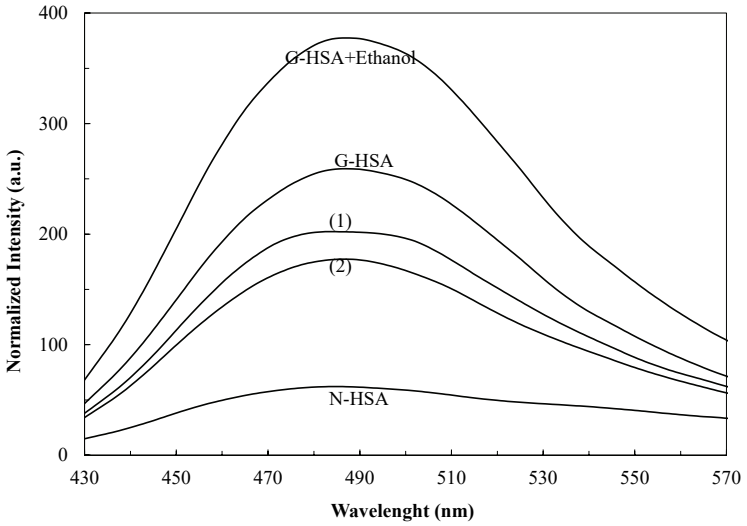


Fig. 7. ThT fluorescence emission spectra of N-HSA, G-HSA, G-HSA in ethanolic solution and G-HSA in the presence of 175 (1) and 240 (2) μg $mL^{-1}$ of *E. billardierei* extract.

*Native-PAGE and SDS-PAGE Electrophoresis*

HSA is a 66 kDa protein with an isoelectric point (p*I*) of 4.7, *i.e.*, the surfaces of HSA carry negative charges at pH > 4.7 and positive charges in solutions at pH < 4.7.[36] Thus, at neutral pH (7.4), HSA has regions that are strongly negatively charged even though it also has positively charged pockets.[7] The attachment of glucose affects the surface charge of HSA which is attributed to the surface amino acids modification.[36] It has been reported that the pI of the G-HSA has a higher acidic value than N-HSA.[37] Fig. 8a exposed that G-HSA revealed a faster anodic migration than N-HSA, indicating that significant glycation had occurred. As observed in Fig. 8a, G-HSA in ethanolic solution revealed a faster anodic migration than G-HSA. However, treatment of G-HSA with 240 μg $mL^{-1}$ of *E. billardierei* extract restored the electrophoretic migration toward N-HSA demonstrating the protective role of *E. billardierei* extract against glucose-mediated glycation.

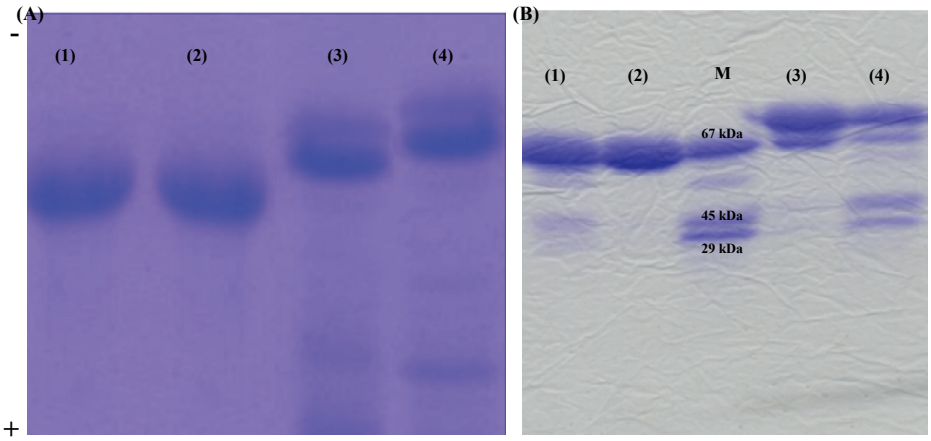


Fig. 8. a) Native-PAGE and b) SDS-PAGE of the effects of *E. billardierei* extract on protein aggregation. Lane 1: N-HSA, lane 2: G-HSA in the presence of 240 μg $mL^{-1}$ of extract, lane 3: G-HSA and lane 4: G-HSA in ethanolic solution. M: molecular mass marker.

It has been accepted that after prolonged glycation, protein could form micelle-like aggregates.[23] The glycation of albumin causes structural changes and an increment in the total molecular weight (*MW*) of the protein. It has been shown that glycation could promote strong conformational changes in protein that affect both tertiary and secondary structures. Hence, glycation could promote amyloid aggregation in protein both reducing the helical content and supporting *β*-cross structure formation that rapidly evolves to the formation of amyloid aggregates.[38] The electrophoretic mobility of N-HSA, G-HSA and *E. billardierei* extract-treated HSA samples was also evaluated on SDS-PAGE. As shown in Fig. 8b, N-HSA displayed a single parental band, while G-HSA presented multiple bands. The other band with lower MW may include the fragments of HSA.[19] Furthermore, the relative mobility of G-HSA and N-HSA was different. G-HSA sample demonstrated reduced mobility compared to N-HSA indicating the attachment of glucose molecules. This observation is in agreement with previous studies in which glycation of HSA by glucose resulted in reduced electrophoretic mobility.[39] G-HSA in ethanolic solution revealed the same relative mobility as the G-HSA sample. Lambrecht *et al.* stated that aqueous ethanol with a concentration of 50 vol. % could result in the formation of disulfide bonds between BSA, notably.[40] Siddique *et al.* exposed that the formation of disulfide bonds played a critical function in the formation of protein aggregates.[41] Feng *et al.* also noted that ethanol could induce disulfide cross-linking and perform a fundamental role in BSA and whey protein isolates aggregate formation.[42] Accordingly, it could be concluded that ethanol-induced disulfide cross-linking plays a crucial role in G-HSA aggregate formation. Treatment of G-HSA with *E. billardierei* extract

restored the electrophoretic migration toward N-HSA demonstrating the protective role of *E. billardierei* extract against glucose-mediated glycation.

Protein glycation directly influences protein aggregation production. Insoluble aggregates can create an amyloid cross-structure, generating protein stability and structure to be changed. In summary, our findings prove that the presence of *E. billardieri* extract decreased Amadori product formation and structural alterations of HSA incubated with glucose. Previous studies verified that phenolic-rich plant extracts prevented sugar-induced protein glycation.[6,43] The phytochemical analysis disclosed that *E. billardieri* extract is high in flavonoid and phenolic compounds. It has been proved that through the glycation process, bioactive constituents such as kaempferol, salicylic acid, carvacrol, gallic acid, rutin and ferulic acid could employ their glycation inhibition impacts by chelating redox-inducing transition metal ions, scavenging free radicals, and neutralizing reactive carbonyl intermediates. Thus, it could be concluded that the phenolics in *E. billardieri* extract could prevent glucose-induced HSA glycation. This favorable effect could aid in lowering the risk of diabetes complications. However, further research is required to verify the actual mechanism of *E. billardieri* extract inhibition and the active chemicals involved in the process.

## CONCLUSION

AGEs are correlated with pathophysiological conditions accordingly making studies, related to protein glycation, of clinical importance. To the best of our knowledge, this research is the first attempt to clarify the effects of *E. billardieri* extract on the structure of HSA from a molecular point of view. The findings of this paper verify that the ethanolic extract of *E. billardieri* could inhibit the pathway of AGE formation by interfering with the glycation of HSA. This study provides insight into the ability of *E. billardieri* extract to prevent the glycation and unfolding of HSA. Hence, although further investigations are warranted to draw firm conclusions, the presence of *E. billardieri* extract in foods could inhibit glycation reactions under hyperglycemia providing protection against pathogenic impacts of AGEs during diabetes.

## И З В О Д

## ЕТАНОЛНИ ЕКСТРАКТ *Eryngium billardierei* F. DELAROCHE СПРЕЧАВА ГЛИКОВАЊЕ ХУМАНОГ СЕРУМСКОГ АЛБУМИНА: СТУДИЈА *IN VITRO*

SANAZ YAVARI[1], AZADEH HEKMAT[1] и SOROUSH SARDARI[2]

[1]*Department of Biology, Science and Research Branch, Islamic Azad University, Tehran, Iran* и [2]*Drug Design and Bioinformatics Unit, Department of Medical Biotechnology, Biotechnology Research Center, Pasteur Institute of Iran, Tehran 13169-43551, Iran*

Гликовање протеина је директно повезано са многим патолошким стањима. У овој студији је испитан потенцијал екстракта *Eryngium billardierei* да инхибира процес гликовања хуманог серумског албумина (HSA). Структурне промене глико-

ваног HSA су испитане у одсуству и присуству различитих концентрација етанолног екстракта *E. Billardierei* користећи методе циркуларног дихроизма, флуоресцентне и UV–Vis спектроскопије. Резултати су показали да екстракт *E. billardierei* може смањити стварање крајњих производа узнапредованог гликовања (AGE) и Амадори производа у *in vitro* условима, као и да повећа удео хеликса у структури HSA. Такође је, применом тиофлавин T теста, утврђено смањење стварања унакрсних амилоидних влакана HSA. Фитохемијска анализа је указала на висок садржај флавоноидних и фенолних једињења у екстракту *E. billardieri*, што упућује на закључак да ова фенолна једињења могу спречити гликовање HSA индуковано глукозом. Резултати ове студије потврђују да се екстракт *E. billardieri* може укључити у контролу дијабетеса.

(Примљено 25. јула, ревидирано 16. августа, прихваћено 21. новембра 2023)

## REFERENCES


1. G. Rabbani, S. N. Ahn, *Int. J. Biol. Macromol.* **123** (2019) 979 (https://doi.org/10.1016/j.ijbiomac.2018.11.053)
2. A. Szkudlarek, A. Sułkowska, M. Maciążek-Jurczyk, M. Chudzik, J. Równicka-Zubik, *Spectrochim. Acta, A* **152** (2016) 645 (https://doi.org/10.1016/j.saa.2015.01.120)
3. W. Ge, J. Jie, J. Yao, W. Li, Y. Cheng, W. Lu, *Mol. Med. Rep.* **25** (2022) 1 (https://doi.org/10.3892/mmr.2022.12656)
4. E. Sharifi-Zahabi, F. H. Sharafabad, H. Abdollahzad, M. Malekahmadi, N. B. Rad, *Adv. Nutr.* **12** (2021) 2157 (https://doi.org/10.1093/advances/nmab072)
5. F. Ahmed, Q. Husain, *Biochimie* **162** (2019) 66 (https://doi.org/10.1016/j.biochi.2019.04.004)
6. A. Shamsi, A. Ahmed, M. S. Khan, F. M. Husain, B. Bano, *Int. J. Biol. Macromol.* **161** (2020) 187 (https://doi.org/10.1016/j.ijbiomac.2020.06.048)
7. A. Hekmat, S. Hatamie, A. A. Saboury, *Inorg. Nano-Met.* (2022) 1 (https://doi.org/10.1080/24701556.2022.2034859)
8. A. Hekmat, R. Bromand Gohar, K. Larijani, *J. Med. Herb.* **10** (2019) 37 (https://jhd.shahrekord.iau.ir/article_673016.html)
9. N. Turković, N. Anđelković, D. Obradović, Z. Vujić, B. Ivković, *J. Serb. Chem. Soc.* **88** (2023) 1 (https://doi.org/10.2298/JSC221212033T)
10. M. Bohlooli, M. Ghaffari-Moghaddam, M. Khajeh, G. Shahraki-Fallah, B. Haghighi--Kekhaiye, N. Sheibani, *J. Photochem. Photobiol., B* **163** (2016) 345 (https://doi.org/10.1016/j.jphotobiol.2016.09.004)
11. N. Tran, B. Pham, L. Le, *Biology* **9** (2020) 252 (https://doi.org/10.3390/biology9090252)
12. S. Sarmah, A. S. Roy, *Int. J. Biol. Macromol.* **195** (2022) 565 (https://doi.org/10.1016/j.ijbiomac.2021.12.041)
13. N. Roshanravan, P. Asgharian, H. Dariushnejad, N. M. Alamdari, B. Mansoori, A. Mohammadi, S. Alipour, M. Barati, A. Ghavami, V. Ghorbanzadeh, *Adv. Pharm. Bull.* **8** (2018) 667 (https://doi.org/10.15171/apb.2018.075)
14. M. S. Daneshzadeh, H. Abbaspour, L. Amjad, A. M. Nafchi, *J. Food Meas. Charact.* **14** (2020) 708 (https://doi.org/10.1007/s11694-019-00317-y)
15. F. Kheirollahzadeh, E. Eftekhari, M. Ghollasi, P. Behzadi, *Mol. Biol. Rep.* **49** (2022) 3401 (https://doi.org/10.1007/s11033-022-07171-0)

16. S. Khani, M. Abdollahi, Z. Asadi, M. Nazeri, M. A. Nasiri, H. Yusefi, A. Moghadam, H. Heidari, *Res. Pharm. Sci.* **16** (2021) 193 (https://doi.org/10.4103/1735-5362.310526)
17. M. Afshari, A. R. Malayeri, M. Mohammadshahi, *J. Contemp. Med. Sci*. **5** (2019) 77 (https://doi.org/10.22317/jcms.v5i2.568)
18. M. K. Siddiqi, P. Alam, S. K. Chaturvedi, S. Nusrat, M. R. Ajmal, A. S. Abdelhameed, R. H. Khan, *Int. J. Biol. Macromol.* **105** (2017) 292 (https://doi.org/10.1016/j.ijbiomac.2017.07.036)
19. K. Abdullah, A. Arefeen, A. Shamsi, F. A. Alhumaydhi, I. Naseem, *ACS Omega* **6** (2021) 12605 (https://doi.org/10.1021/acsomega.1c00631)
20. F. A. Qais, M. M. Alam, I. Naseem, I. Ahmad, *RSC Adv.* **6** (2016) 65322 (https://doi.org/10.1039/C6RA12321J)
21. N. Gligorijević, V. Šukalović, S. Minić, G. Miljuš, O. Nedić, A. Penezić, *J. Serb. Chem. Soc.* **86** (2021) 795 (https://doi.org/10.2298/JSC210420041G)
22. H. Schägger, G. Von Jagow, *Anal. Biochem.* **166** (1987) 368 (https://doi.org/10.1016/0003-2697(87)90587-2)
23. P. Balyan, M. S. Ola, A. S. Alhomida, A. Ali, *Medicina* **58** (2022) 1816 (https://doi.org/10.3390/medicina58121816)
24. M. Jarzębski, P. Siejak, W. Smułek, F. Fathordoobady, Y. Guo, J. Pawlicz, T. Trzeciak, P. Ł. Kowalczewski, D. D. Kitts, A. Singh, *Molecules* **25** (2020) 2696 (https://doi.org/10.3390/molecules25112696)
25. R. J. Robbins, *J. Agric. Food Chem.* **51** (2003) 2866 (https://doi.org/10.1021/jf026182t)
26. M. Hadidi, A. Garvín, R. Ibarz, A. Ibarz, *LWT* **154** (2022) 112809 (https://doi.org/10.1016/j.lwt.2021.112809)
27. N. Na, D.-Q. Zhao, H. Li, N. Jiang, J.-Y. Wen, H.-Y. Liu, *Molecules* **21** (2015) 54 (https://doi.org/10.3390/molecules21010054)
28. Y. Wang, X. Wang, J. Wang, Y. Zhao, W. He, Z. Guo, *Inorg. Chem.* **50** (2011) 12661 (https://doi.org/10.1021/ic201712e)
29. S. Ahmad, U. Shahab, M. H. Baig, M. S. Khan, M. S. Khan, A. Srivastava, M. Saeed, Moinuddin, *PLOS One* **8** (2013) e72128 (https://doi.org/10.1371/journal.pone.0072128)
30. L. Li, Q. Song, X. Zhang, Y. Yan, X. Wang, *Molecules* **27** (2022) 8793 (https://doi.org/10.3390/molecules27248793)
31. A. R. Abubakar, M. Haque, *J. Pharm. Bioallied Sci.* **12** (2020) 1 (https://doi.org/10.4103%2Fjpbs.JPBS_175_19)
32. L. Gebremeskel, K. Beshir Tuem, T. Teklu, *Diabetes, Diabetes Metab. Syndr. Obes.* (2020) 1481 (https://doi.org/10.2147/DMSO.S246996)
33. M. A. Gad-Elkareem, E. H. Abdelgadir, O. M. Badawy, A. Kadri, *PeerJ* **7** (2019) e6441 (https://peerj.com/articles/6441)
34. N. Amani, M. Reza Saberi, J. Khan Chamani, *Protein Pept. Lett.* **18** (2011) 935 (https://doi.org/10.2174/092986611796011473)
35. A. Ahmed, A. Shamsi, M. S. Khan, F. M. Husain, B. Bano, *Int. J. Biol. Macromol.* **113** (2018) 269 (https://doi.org/10.1016/j.ijbiomac.2018.02.137)
36. N. He, R. Wang, Y. He, X. Dang, *Sci. China Chem.* **55** (2012) 1788 (https://doi.org/10.1007/s11426-012-4604-z)
37. S. S. Rohiwal, Z. Ellederova, A. P. Tiwari, M. Alqarni, S. T. Elazab, G. E.-S. Batiha, S. H. Pawar, N. D. Thorat, *RSC Adv.* **11** (2021) 4308 (https://doi.org/10.1039/D0RA09301G)

38. I. Sirangelo, C. Iannuzzi, *Int. J. Mol. Sci.* **22** (2021) 6609 (https://doi.org/10.3390/ijms22126609)
39. K. Abdullah, F. A. Qais, I. Ahmad, H. Hasan, I. Naseem, *Int. J. Biol. Macromol.* **120** (2018) 1734 (https://doi.org/10.1016/j.ijbiomac.2018.09.176)
40. M. A. Lambrecht, I. Rombouts, J. A. Delcour, *Food Hydrocoll.* **57** (2016) 122 (https://doi.org/10.1016/j.foodhyd.2016.01.018)
41. M. A. B. Siddique, P. Maresca, G. Pataro, G. Ferrari, *Food Res. Int.* **99** (2017) 419 (https://doi.org/10.1016/j.foodres.2017.06.003)
42. Y. Feng, X. Ma, B. Kong, Q. Chen, Q. Liu, *Food Hydrocoll.* **111** (2021) 106379 (https://doi.org/10.1016/j.foodhyd.2020.106379)
43. P. G. Dorsey, P. Greenspan, *J. Med. Food* **17** (2014) 447 (https://doi.org/10.1089/jmf.2013.0075).

Journal of the Serbian Chemical Society
JSCS-info@shd.org.rs • www.shd.org.rs/JSCS
*J. Serb. Chem. Soc.* *89* (9) 1165–1176 (2024)
*JSCS–5779*
*Original scientific paper*
Published 7 September 2024

# A DFT study of the chemical bonding properties, aromaticity indexes and molecular docking study of some phenylureas herbicides

SOUHILA LAIB[1,2]*, SAAD BOUCHEKIOUA[2,3] and RAFIK MENACER[3]

[1]*Département de Médecine, Faculté de Médecine, Université de Batna2, Batna, Algérie,* [2]*Laboratoire de Chimie des Matériaux et des Vivants: Activité & Réactivité (LCMVAR), Université de Batna1, Batna, Algérie and* [3]*Centre de Recherche en Sciences Pharmaceutiques CRSP, Nouvelle Ville, Zone d'activité ZAM, Constantine, Algérie*

(Received 12 July, revised 31 August, accepted 29 October 2023)

*Abstract*: Herbicides have imposed disastrous consequences towards the environment and human health. This practice urges scientists to investigate the physical, chemical and biological properties of these substances to avoid the use of the most harmful pesticides. For this purpose, the molecular structure and chemical bonding properties of phenylurea herbicides namely: fenuron (**L1**), monuron (**L2**), diuron (**L3**) and chlorotoluron (**L4**), were calculated in water, using density functional theory (DFT). The energy decomposition analysis (EDA) and the extended transition state natural orbitals for chemical valence (ETS-NOCV) reveal the dominant ionic character in carbon–nitrogen bond between dimethylurea fragment and benzene ring. Besides, the interaction of these herbicides with the human serum albumin (HSA) was undertaken by molecular modeling. The calculation of *HOMA* and *FLU* indexes indicate that the electronic delocalization is stronger in diuron than the other compounds, mainly caused by the two chloro substituents effects on benzene. Good correlations are found between the calculated parameters such as structural parameters, Mulliken atomic charge, topological and bonding properties and aromaticity indexes. The Vinardo molecular docking results suggest that the binding energies of the complexes formed between HSA target and investigated compounds have the following order: **L3** (–27.57 kJ/mol) < **L2** (–25.56 kJ/mol) < < **L4** (–24.94 kJ/mol) < **L1** (–24.10 kJ/mol), which confirmed that the Fenuron is the less harmful option between the studied herbicides especially against HSA.

*Keywords*: Mulliken atomic charge; chlorotoluron; HSA; electronic delocalization; dimethylurea.

* Corresponding author. E-mail: s.laib@univ-batna2.com
https://doi.org/10.2298/JSC230712085L

## INTRODUCTION

Pesticides are substances or mixtures of substances mainly used in agriculture or public health protection programs to protect plants from pests, weeds, or diseases, and humans from vector-borne diseases, such as malaria, dengue fever and schistosomiasis.[1] The application of herbicides on agricultural soils is a well-established and effective practice to control weed growth. They represent about 50 % of the demand for agricultural chemicals; their prolonged use involves the risk of their retention in crops and soils.[2] In genetically engineered plants herbicides metabolism provide efficient and eco-friendly means for enhancement of detoxification of harmful substances.[3] Xenobiotics such as aromatic, pesticides and hydrocarbons are usually synthesized for industrial and agricultural purposes.[4]

Most pesticides are inhibitors of cholinesterases, enzymes, which are critical in neurobiology, toxicology and pharmacology.[5] Recently, phenylurea herbicides have received particular attention because of their high biotoxicity.[6]

Phenylurea herbicides are mostly *N*-dimethyl derivatives bearing various substituents on aromatic ring.[7] The dimethylurea fragment in these molecules is rigid because of the delocalized electrons.[8]

Electronic structure and energetics properties of phenylurea herbicides may become experimentally complicated. Theoretically, phenylurea herbicides have been evaluated in various media by several investigators.[8,10–13] However, to the best of our knowledge, Fenuron, Monuron, Diuron and Chlorotoluron chemical bonding properties and aromaticity indexes have not been analyzed yet.

Understanding the processes of interaction between HSA protein and diuron herbicides is critical for determining the potential risks of these compounds to humans. However, no study detailing the mechanism of interaction of these herbicides with HSA has been published except for diuron.[9] In the first part of our study, the main objective is to reveal the nature of the bond between dimethylurea fragment and the benzene ring of the four phenylurea herbicides using the energy decomposition analysis (EDA) and the extended transition state natural orbitals for chemical valence (ETS-NOCV). QTAIM analysis based on Barder's atoms in the molecule theory is carried out to confirm the presence of the hydrogen bonding between atoms. Also, we have computed the indices of aromaticity based on the measure of electronic delocalization in aromatic molecules. The second part is focused on the molecular docking of the same pesticide molecules with HSA.

## EXPERIMENTAL

### *DFT calculations*

All the geometries optimizations were performed using density functional theory (DFT) and quantum calculation program Gaussian09[14] employing B3LYP/6-31G++(d,p) basis set[15-17] in water. The bonding interactions have been analyzed by means of Morokuma-type energy

decomposition analysis (decomposition of the bonding energy into the Pauli exchange repulsion, total steric interaction and orbital interaction terms)[18] developed by Ziegler and Rauk for DFT methods; incorporated in ADF.[19] ETS-NOCV[20] analyses were performed using the ADF program package. EDA-NOCV calculations were carried out at the GGA-PBE/TZP level. QTAIM analysis was carried out by employing the DGrid/Basin program[21] and Chemcraft 1.4 program[22] was used for the representation of critical points. For these compounds, we compute the indices of aromaticity, the harmonic oscillator model of aromaticity (*HOMA*) index[23,24] and the aromatic fluctuation index (*FLU*).[25]

*Molecular docking study*

To study how the selected herbicides interact with HSA,[9] the related protein was taken from the Protein Data bank (http://www.rcsb.org/pdb): HSA complexed with myristic acid and the R-(+) enantiomer of warfarin (PDB ID: 1H9Z).[26] The crystal structure of HSA has three homologous $\alpha$-helix domains: I (residues 1–195), II (residues 196–383), and III (residues 384–585). Within these domains, there is a further subdivision into A and B subdomains. Notably, domains IIA and IIIA stand out as they possess distinct molecular binding sites, often referred to as active binding site I and active binding site II, respectively. These active binding sites (Sudlow's sites) are characterized by hydrophobic cavities and play a pivotal role in HSA's ability to interact with various molecules, making it a crucial protein in the bloodstream for transporting drugs and other ligands throughout the body. [27]

The protein was freed from ligands (myristic acid and the R-(+) enantiomer of warfarin) by Discovery Studio 3.5 Visualizer.[28] Then polar hydrogen atoms and Kollman charges were added to the protein using the AutoDockTools4.[29] The molecular docking of each studied structure was performed by Vinardo[30] as implemented in GNINA 1.0 code[31] in the following Box Center (BC) and the box dimension (BD): (PDB: 1H9Z; BC: $X = 22.97$, $Y = 8.71$, $Z = 12.87$; BD: $X = 10$, $Y = 10$, $Z = 10$) this box is related to the active Sudlow's sites of interaction.[26] Vinardo was chosen as a scoring function because it has more power of ranking than AutoDock Vina scoring.[30,32] The GNINA code is based on smina[33] and AutoDock Vina.[34]

## RESULTS AND DISCUSSION

### *DFT study*

Four models of phenylurea herbicides, namely fenuron (**L1**), monuron (**L2**), diuron (**L3**) and chlorotoluron (**L4**), were optimized in water and in the ground state (Fig. 1).

### *Mulliken atomic charges analysis*

Mulliken atomic charge results are crucial in quantum chemical calculations, as atomic charges affect molecular polarizability, dipole moment, and electronic structural features of molecular systems.[35]

The existence of positive charges on the carbon ($C_3$) atom of the ring in all systems and negative charges on nitrogen N(–H) atoms indicate the existence of a carbon–nitrogen ionic bond. In compound **L3**, it is observed that the positive charge of the carbon ($C_3$) atom (+0.168 e) of the ring is higher than in other compounds. We can also see that the charge of the nitrogen atom N(–H) of this compound is more negative (–0.630 e) compared to other compounds (see Table

I). This finding leads to the conclusion that the ionic bond is stronger in **L3** than in the other compounds, caused by substituents effects of the electron density of dichlorobenzene.

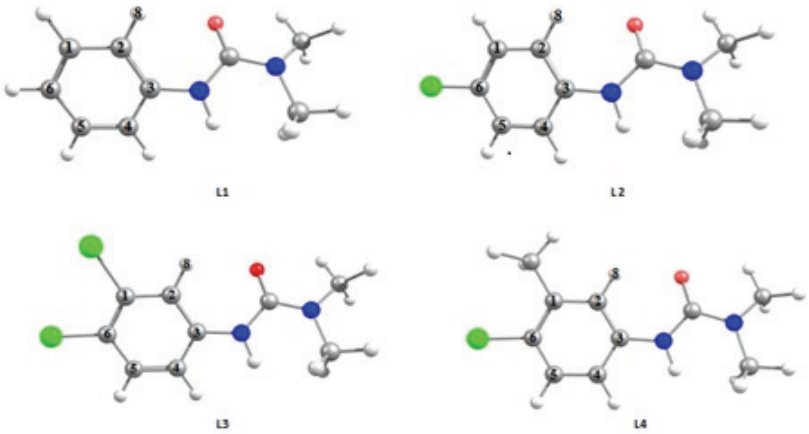


Fig. 1. Molecular structures of four phenylureas herbicides.

TABLE I. Mulliken atomic charges

| Position | L1 | L2 | L3 | L4 |
|---|---|---|---|---|
| $C_3$(Ring) | 0.161 | 0.158 | 0.168 | 0.155 |
| $C_2$(Ring) | –0.102 | –0.085 | –0.080 | –0.089 |
| C(CO) | 0.544 | 0.544 | 0.546 | 0.544 |
| N(–H) | –0.637 | –0.634 | –0.630 | –0.636 |
| $H_8$ | 0.146 | 0.162 | 0.170 | 0.157 |
| H(–N) | 0.343 | 0.347 | 0.350 | 0.346 |
| O | –0.426 | –0.423 | –0.421 | –0.424 |
| Cl | – | 0.087 | 0.259 | 0.106 |

The intramolecular hydrogen bonds (IHB) are also analyzed, with positives charges on the hydrogens atoms, negatives charges on the nitrogen (N) atom, on the oxygen (O) atom and on the carbon ($C_2$) atom of ring in all systems studied. Thus, the third compound presents higher positive charges on the hydrogen atoms (0.170 and 0.350 e, respectively), higher negatives charges on the carbon ($C_2$) atom, on the nitrogen atom and on the oxygen atom (–0.080, –0.630 and –0.421 e, respectively). These results could facilitate the charge transfer over the formation of intramolecular hydrogens bonds (C-H...O and N-H…O).[35]

*Energy decomposition analysis*

The binding interactions were investigated using a Morokuma-type energy decomposition described by Ziegler and Rauk. The advantage of this approach is

to estimate the interaction energy between two fragments. The total bond energy $E_{int}$ is the sum of three terms:

$$E_{int} = E_{orb} + E_{elec} + E_{Pauli} = E_{orb+Pauli} + E_{elec} \quad (1)$$

Where $E_{elec}$ is the electrostatic stabilization energy between the two organic fragments. The Pauli repulsion $E_{Pauli}$ comprises the destabilizing interactions between occupied orbitals, the orbital interaction $E_{orb}$ is the interaction energy of the occupied orbitals on one fragment and unoccupied orbitals on another.[36] The binding decomposition energy EDA of carbon–nitrogen was obtained between the dimethylurea fragment and the benzene ring of the four phenylurea herbicides (see Fig. 2) using the ADF code with GGA-PBE/TZP and the ZORA approximation.

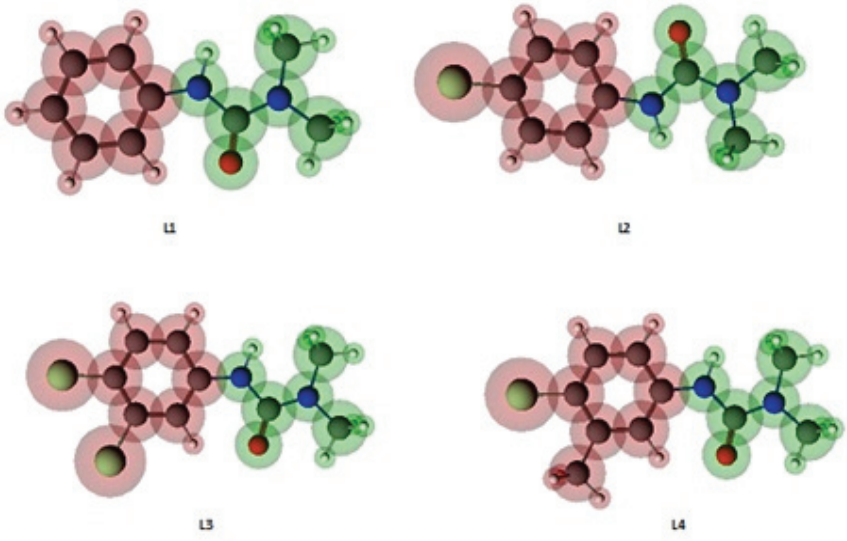


Fig. 2. Energy decomposition fragments related to the four molecules.

As shown in Table II, the total bond energy ($E_{int}$) between dimethylurea fragment and the benzene ring is in the range of ≈ –1180.01 to ≈ –1225.33 kJ mol$^{-1}$. The electrostatic interaction ($E_{elec}$) makes major contributions of compounds, while $E_{pauli}$ + $E_{orb}$ are the smallest component of the interaction energy. These results confirm the existence of a carbon–nitrogen ionic bond between the two fragments and it is relatively stronger in **L3**. Good correlations are found between the nature of this bond and Mulliken atomic charges (Table I).

*ETS-NOCV analysis*

We have employed extended transition state natural orbitals for chemical valence (ETS-NOCV) to study the nature of the bonds of compounds **L1**−**L4**.

TABLE II. Energies (in kJ mol$^{-1}$) of decomposition bonding in the four molecules

| Parameter | **L1** | **L2** | **L3** | **L4** |
|---|---|---|---|---|
| $E_{\text{pauli+orb}}$ | 44.39 | 9.62 | 28.95 | 27.95 |
| $E_{\text{Elec}}$ | –1251.39 | –1223.40 | –1254.20 | –1216.96 |
| $E_{\text{Int}}$ | –1180.01 | –1213.78 | –1223.40 | –1188.67 |
| % Covalent | 0 | 0 | 0 | 0 |
| % Ionic | 100 | 100 | 100 | 100 |

The ETS-NOCV results are summarized in Table III. The major contribution to the bonding is through the electrostatic interaction between the two fragments. Consequently, the ETS-NOCV approach produces decomposition energies that increase in the same way as the Energy decomposition analysis of Ziegler–Rauk.

TABLE III. The results of ETS-NOCV analysis of **L1**–**L4** in kJ mol$^{-1}$

| Energy | **L1** | **L2** | **L3** | **L4** |
|---|---|---|---|---|
| $E_{\text{Pauli}}$ | 3570.66 | 3614.56 | 3565.19 | 3582.34 |
| $E_{\text{orb}}$ | –3110.39 | –3154.74 | –3098.25 | –3119.17 |
| $E_{\text{elec}}$ | –1012.11 | –1019.22 | –1020.90 | –1012.11 |
| $E_{\text{int}}$ | –619.23 | –623.42 | –615.47 | –612.96 |

*QTAIM analysis*

In recent years, the quantum theory of atoms in molecules (QTAIM) has been extensively used for study of the hydrogen bond (HB).[37,38] Popelier[39,40] proposed the following criteria for strength of HB:

For weak HB, $\nabla^2\rho(r) > 0$ and $H(r) > 0$, for HB of medium strength, $\nabla^2\rho(r) > 0$ and $H(r) < 0$, and for strong HB, $\nabla^2\rho(r) < 0$ and $H(r) < 0$.

According to this analysis, we found one critical point of the oxygen–hydrogen bond between hydrogen atom ($H_8$) of the ring and oxygen atom (O) of dimethylurea fragment in all systems analyzed (see Table IV and Fig. 3). This result confirms the existence of an intramolecular hydrogen bond (C–H···O). It can be observed also that the N–H···O hydrogen bond is not to be considered in this analysis. This is verified by the values of Mulliken atomic charges, when the carbon atoms ($C_2$) of a ring have higher negative charges than the nitrogen (N) atom (see Table I).

It can be seen also from Table IV that the maximum total electronic density $\rho(r)$ and its corresponding Laplacian $\nabla^2\rho(r)$ at bond critical point of intramolecular hydrogen bond are positives in all compounds, and the values of $-G/V$ are greater than unit of covalent nature ($\nabla^2\rho(r) < 0$) of IHB ($0.5 < -G/V < 1$).[41] These results show that the IHB (C–H···O) has noncovalent nature ($\nabla^2\rho(r) > 0$) and it is higher in **L3** than those of **L1**, **L2** and **L4**. The latter of which correlated to the electronegativity of the dichloro-atom substituted in **L3**.

The strength of the hydrogen bond is described by geometrical parameters (HB lengths and angle).[42]

TABLE IV. Structural parameters (HB lengths in Å and angle in °) and topological properties (a.u) of bond critical point (BCP) of intramolecular H-bonds of **L1**–**L4** at DFT levels

| Parameter | **L1** | **L2** | **L3** | **L4** |
|---|---|---|---|---|
| $d_{C\text{-}H}$ | 1.079 | 1.079 | 1.078 | 1.078 |
| $d_{H\cdots O}$ | 2.173 | 2.154 | 2.147 | 2.162 |
| ∠C–H···O | 120.7 | 120.7 | 120.5 | 120.2 |
| $\rho_{BCP}(r)$ | 0.014 | 0.016 | 0.018 | 0.011 |
| $\nabla^2\rho_{BCP}(r)$ | 0.055 | 0.063 | 0.070 | 0.042 |
| $H_{BCP}(r)$ | 0.002 | 0.002 | 0.002 | 0.0017 |
| $-G/V_{BCP}$ | 1.197 | 1.163 | 1.141 | 1.234 |

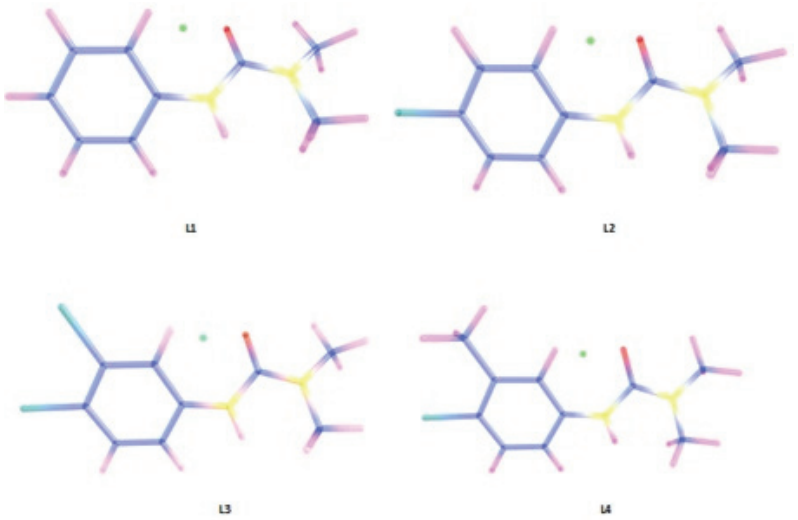


Fig. 3. Molecule graph of **L1**–**L4**.

The correlation between these parameters and ρ(r) are inverse to each other, *i.e.*, decrease in H···O distance corresponds to increase in the electron density. Thus, the short value of O···H distance in **L3** is (2.147 Å) shows strong HB and is observed for C–H···O interaction with high stability. For angles, if HB is stronger, thus the X–H···Y angle is closer to 180°, it was stated that for very strong HBs, the X–H···Y angle range is 175–180°, for strong it is 130–180°, while for weak it is 90–180°.[43] In our analysis, we have found a weak HB in four compounds with small C–H···O angle range (120.2–120.7°).

*Measures of aromaticity indexes*

In this part, we have analyzed the variation of aromaticity in the studied molecules. The concept of aromaticity is of central importance for the interpret-

ation of molecular structure, stability, reactivity and magnetic properties of many compounds, and remains still unquestionable.[44,45] The origin of the aromatic properties is the cyclic delocalized distribution of π-electrons, for this reason recently many new ways to quantify the aromaticity based on the measure of electron delocalization in aromatic molecules have been devised.[46] Among the most common structure-based indices of aromaticity are the harmonic oscillator model of aromaticity (*HOMA*)[23, 24] index and the electron *FLU*ctuation index (*FLU*).[25]

The values of the *HOMA* and *FLU* aromaticity indexes of the four molecules are shown in Table V. The values of the *HOMA* aromaticity index indicate that **L3** has the highest value. This result showed that the electronic delocalization is stronger in **L3**, compared to other compounds, caused by substituents effects of dichlorobenzene.

Aromaticity indexes analyses are in a good agreement with structural parameters, topological and bonding properties, which confirm that the electronic delocalization is strong in **L3**.

TABLE V. Aromaticity indices of the ring for the four molecules

| Index | **L1** | **L2** | **L3** | **L4** |
|---|---|---|---|---|
| *HOMA* | 0.956 | 0.950 | 0.957 | 0.946 |
| *FLU* | 1.007 | 1.013 | 1.011 | 1.013 |

*Molecular docking simulation*

HSA is the most abundant protein component in human plasma,[47] it is the primary transporter that in*FLU*ences *in vivo* molecules absorption, metabolism, excretion and particularly distribution.[48] The distribution of a pesticide *in vivo* could have dangerous toxic[9] consequences, hence this molecular docking study searches for the less harmful pesticide among fenuron (**L1**), monuron (**L2**), diuron (**L3**) and chlorotoluron (**L4**). The four studied molecular structures were docked to HSA (PDB ID:1H9Z) using GNINA 1.0 and the best Vinardo scores were obtained. The best poses associated to the lowest binding energies were selected as the binding mode (Table VI). The Vinardo binding energies of the generated complexes pursue the following trend HSA-**L3** (–27.57 kJ/mol) < < HSA-**L2** (–25.56 kJ/mol) < HSA-**L4** (–24.94 kJ/mol) < HSA-**L1** (–24.10 kJ/mol). These results suggested that the studied pesticides could interact with HSA using hydrogen, hydrophobic and van der Waals interactions. Diuron interacts by hydrogen bonding with the residue Ser-202 (2.88 Å).[49] Monuron establishes one hydrogen bond with the residue Trp-214 (2.72 Å).[47,49,50] Finally, chlorotoluron and fenuron form no hydrogen bond. These findings suggest that the use of fenuron is the less harmful option between the studied pesticides especially against HSA. Diuron is the least stable and the most harmful among the studied compounds.

TABLE VI. Molecular Docking Results: Vinardo Scores, 2D interaction residues and the hydrogen bonding surface

| Target/top compound (Vinardo binding energy) | 2D interaction residues | Hydrogen bonding surface |
|---|---|---|
| 1H9Z/L3 (–27.57 kJ mol$^{-1}$) | 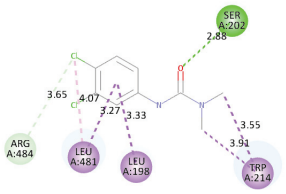 | 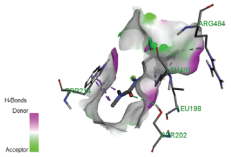 |
| 1H9Z/L2 (–25.56 kJ mol$^{-1}$) | 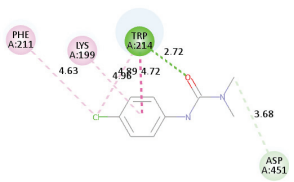 | 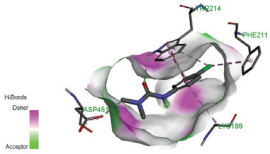 |
| 1H9Z/L4 (–24.94 kJ mol$^{-1}$) | 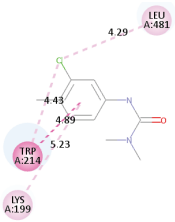 | 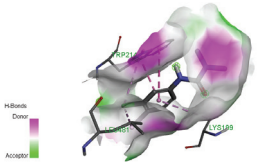 |
| 1H9Z/L1 (–24.10 kJ mol$^{-1}$) | 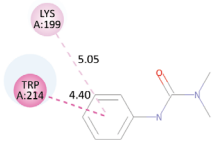 | 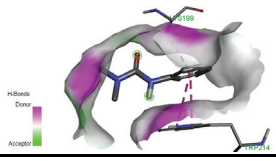 |

## CONCLUSION

The DFT study of the energy decomposition analysis (EDA) and the extended transition state natural orbitals for chemical valence (ETS-NOCV) reveal a strong ionic bonding of carbon–nitrogen in all compounds.

The quantum theory of atoms in molecules confirms the existence of intramolecular hydrogen bonds (C–H···O) in all compounds. This result is verified by the values of Mulliken atomic charges and of the geometrical parameters (HB lengths and angle, respectively), ($d_{C–H}$ between 1.078 and 1.079 Å, $d_{H···O}$ between 2,147 and 2,173 Å and ∠C-H···O between 120.2 and 120.7°).

The dichlorobenzene ligand in **L3** increases electron delocalization, this is shown by the *HOMA* and *FLU* values of this compound (*HOMA* = 0.957 and *FLU* = 1.011).

The molecular docking results suggest that the compound **L3** is the most stable and the most harmful compound among the studied pesticides. In contrast,

**L1** is the least harmful compound. Thus, the Vinardo binding energies follow the trend: **L3** (–27.57 kJ/mol) < **L2** (–25.56 kJ/mol) < **L4** (–24.94 kJ/mol) < **L1** (–24.10 kJ/mol). The use of fenuron is the less harmful option between the studied pesticides especially against HSA.

*Acknowledgements*. S. Laib. acknowledges the financial support of the Algerian Ministry of Higher Education and Scientific Research and the DGRSDT and the Algerian Ministry of Higher Education and Scientific Research for PRFU Project (D01N01UN050220220003). The authors are particularly grateful to Pharmaceutical Sciences Research Center (CRSP), Constantine, Algeria, for computing resources.

ИЗВОД

## DFT СТУДИЈА ОСОБИНА ХЕМИЈСКОГ ВЕЗИВАЊА, ИНДЕКСА АРОМАТИЧНОСТИ И СТУДИЈА МОЛЕКУЛСКОГ ДОКОВАЊА НЕКИХ ХЕРБИЦИДА НА БАЗИ ФЕНИЛУРЕА

SOUHILA LAIB[1,2], SAAD BOUCHEKIOUA[2,3] и RAFIK MENACER[3]

*[1] Département de Médecine, Faculté de Médecine, Université de Batna2, Batna, Algérie, [2]Laboratoire de Chimie des Matériaux et des Vivants: Activité & Réactivité (LCMVAR), Université de Batna-1, Batna, 05000, Algérie и [3]Centre de Recherche en Sciences Pharmaceutiques CRSP, Nouvelle Ville, Zone d'activité ZAM, Constantine, Algérie*

Хербициди узрокују катастрофалне последице за животну околину и здравље људи. То подстиче научнике да истраже физичке, хемијске и биолошке особине ових супстанци, како би се избегла употреба најштетнијих пестицида. У ту сврху су молекулске структуре и особине хемијског везивања фенилуреанских хербицида, наиме фенурона (**Л1**), монурона (**Л2**), диурона (**Л3**) и хлоротолурона (**Л4**), израчунате за водени раствор, користећи теорију функционала густине (DFT). Анализа разлагања енергије (EDA) и природних орбитала за проширено прелазно стање за хемијске валенце (ETS-NOCV) показују доминантно јонски карактер у вези угљеник–азот између диметилуреинског фрагмента и бензеновог прстена. Поред тога, молекулским моделовањем је испитана интеракција ових хербицида са албумином хуманог серума (HSA). Израчунавање *HOMA* и *FLU* индекса указује да је делокализација електрона јача у диурону него у другим једињењима, што је углавном узроковано ефектом два хлоро супституента на бензену. Нађена је добра корелација међу израчунатим параметрима као што су структурни параметри, Маликенова наелектрисања атома, тополошке и везивне особине и индекси ароматичности. Винардови резултати молекулског доковања сугеришу да енергије везивања у комплексима између HSA мете и испитиваних једињења има следећи редослед: **Л3** (–27,57 kJ/mol) < **Л2** (–25,56 kJ/mol) < **Л4** (–24,94 kJ/mol) < **Л1** (–24,10 kJ/mol), што потврђује да је фенурон мање штетна опција међу испитиваним хербицидима, посебно према HSA.

(Примљено 12. јула, ревидирано 31. августа, прихваћено 29. октобра 2023)

## REFERENCES

1. P. N. Stamati, S. Maipas, C. Kotampasi, P. Stamatis, L. Hens, *Front. Public Health* **4** (2016) 1 **(**https://doi.org/10.3389/fpubh.2016.00148)
2. H. Mountacer, L. Tajeddine, M. Sarakha, *Herbicides and Environment*, Intech, Rijeka, 2011 (ISBN 978-953-307-476-4)

3. R. Kebeish, E. Azab, C. Peterhaensel, R. El-Basheer, *Environ. Sci. Pollut. Res. Int.* **21** (2014) 8224 (https://doi.org/10.1007/s11356-014-2710-5)
4. J. Jinhoon, K. Sanjida, M. Youngkook, S. Sooim, O.R. Lee, *Appl. Biol. Chem*. **63** (2020) 1 (https://doi.org/10.1186/s13765-020-00498-x)
5. T. Vrabelj, M. Finšgar, *Biosensors* **12** (2022) 263 (https://doi.org/10.3390/bios12050263)
6. F. J. Benitez, C. Garcia, J. L. Acero, F. J. Real, *World Acad. Sci. Eng. Technol.* **34** (2009) 673 (https://doi.org/10.5281/zenodo.1078350)
7. A. Bautista, J. J. Aaron, M. C. Mahedero and A. Muñoz de la Peña, *Analysis* **27** (1999) 857 (https://doi.org/10.1051/analusis:1999154)
8. V. Mile, I. Harsányi, K. Kovács, T. Földes, E. Takács, L. Wojnárovits, *Radiat. Phys. Chem.* **132** (2017) 16 (https://doi.org/10.1016/j.radphyschem.2016.11.003)
9. H. Chen, H. Rao, J. Yang, Y. Qiao, J. Yao, *J. Environ. Sci. Health*., *B* **51** (2016) 154 (https://doi.org/10.1080/03601234.2015.1108800)
10. K. Haruna, S. Veena, Y. Kumar, S. A. Sheena Mary, P. R. Thomas, M. S. Roxy, A. A. Al-Saadi, *Heliyon* **5** (2019) E01987 (https://doi.org/10.1016/j.heliyon.2019.e01987)
11. L. Humberto, M. Huizar, *J. Chem.* (2015) 751527 (https://doi.org/10.1155/2015/751527)
12. F. Zhang, B. Liu, G. Liu, Y. Zhang, J. Wang, S. Wang, *Sci. Rep.* **8** (2018) 3131 (https://doi.org/10.1038/s41598-018-21394-x)
13. A. A. Buglak, A. V. Zherdev, H.-T. Lei, B. B. Dzantiev, *Plos One* **14** (2019) e0214879 (https://doi.org/10.1371/journal.pone.0214879)
14. *Gaussian 09*, Gaussian Inc, Wallingford, CT, 2009
15. A. D. Becke, *J. Chem. Phys*. **98** (1933) 5648 (https://doi.org/10.1063/1.464913)
16. A. D. Becke, *Phys. Rev*., *A* **38** (1988) 3098 (https://doi.org/10.1103/PhysRevA.38.3098)
17. C. Lee, W. Yang, and R. G. Parr, *Physical Review*. B **37** (1988) 785 (https://doi.org/10.1103/PhysRevB.37.785)
18. F. M. Bickelhaupt, E. J. Baerends, *Reviews in computational chemistry*, K. B. Lipkowitz, D. B. Boyd, Eds., Wiley-VCH, New York, 2000, pp. 1–86 (https://doi.org/10.1002/9780470125922.ch1)
19. T. Ziegler, A. Rauk, *Inorg. Chem*. **18** (1979) 1558 (https://doi.org/10.1021/ic50196a034)
20. K. B. Wiberg, *Tetrahedron* **24** (1968) 1083 (https://doi.org/10.1016/0040-4020(68)88057-3)
21. M. Kohout, *Program DGrid, version 4.3*, 2008
22. *Chemcraft, Release 1.4* (http://www.chemcraftprog.com)
23. J. Kruszewski, T. M. Krygowski, *Tetrahedron Lett*. **13** (1972) 3839 (https://doi.org/10.1016/S0040-4039(01)94175-9)
24. T. M. Krygowski, *J. Chem. Inf. Comp. Sci*. **33** (1993) 70 (https://doi.org/10.1021/ci00011a011)
25. E. Matito, M. Duran, M. Sola, *J. Chem. Phys*. **122** (2005) (https://doi.org/10.1063/1.1824895)
26. I. Petitpas, A. A. Bhattacharya, S. Twine, M. East, S. Curry, *J. Biol. Chem*. **276** (2001) 22804 (https://doi.org/10.1074/jbc.M100575200)
27. G. Sudlow, D. J. Birkett, *Mol. Pharmacol*. **12** (1976) 1052
28. *Dassault Systèmes BIOVIA, Discovery Studio Modeling Environment, release 2017*, Dassault Systèmes, San Diego, CA, 2017
29. G. M. Morris, R. Huey, W. Lindstrom, M. F. Sanner, R. K. Belew, D. S. Goodsell, A. J. Olson, *J. Comput. Chem*. **30** (2009) 2785 (https://doi.org/10.1002/jcc.21256)

30. R. Quiroga, M. A. Villarreal, *Plos One* **11**(2016) e0155183 (https://doi.org/10.1371/journal.pone.0155183)
31. T. Andrew, Mc. Nutt, P. Francoeur, R. Aggarwal, T. Masuda, R. Meli, M. Ragoza, J. Sunseri, D. R. Koes, *J. Cheminform.* **13** (2021) (https://doi.org/10.1186/s13321-021-00522-2)
32. T. Gaillard, *J. Chem. Inf. Model*. (2018) (https://doi.org/10.1021/acs.jcim.8b00312)
33. D. R. Koes, M. P. Baumgartner, C. J. Camacho, *J. Chem. Inf. Model*. **53** (2013) 1893 (https://doi.org/10.1021/ci300604z)
34. O. Trott, A. J. Olson, *J. Comput. Chem*. **31** (2010) 455 (https://doi.org/10.1002/jcc.21334)
35. N. Kerru, L. Gummidi, S. V. H. S. Bhaskaruni, S. N. Maddila, P. Singh, B. S. Jonnalagadda, *Sci. Rep.* **9** (2019) 1 (https://doi.org/10.1038/s41598-019-55793-5)
36. P. Su, Z. Chen, W. Wu, *Chem. Phys. Lett.* **635** (2015) 250 (https://doi.org/10.1016/j.cplett.2015.06.078)
37. K. Shyan, A. Nowroozi, *Struct. Chem.* **27** (2016) 1769 (https://doi.org/10.1007/s11224-016-0796-8)
38. S. J. Grabowski, *Mol. Struct*. **553** (2000) 151 (https://doi.org/10.1016/S0022-2860(00)00576-7)
39. E. D. Glendening, A. E. Reed, J. E. Carpenter, F. Weinhold, *NBO, version 3.1*
40. S. J. Grabowski, *Phys. Chem*. **102** (2006) 131 (https://doi.org/10.1039/B417200K)
41. S. Emamian, S. F. Tayyari, *J. Chem. Sci*. **125** (2013) 939 (https://doi.org/10.1007/s12039-013-0466-y)
42. G. Mahmoudzadeh, *Int. J. New. Chem*. **8** (2021) 277 (https://doi.org/10.22034/ijnc.2020.122797.1101)
43. J. D. Pedelacq, S. Cabantous, T. Tran, T. C. Terwilliger, G. S. Waldo, *Nat. Biotechnol*. **24** (2006) 79 (https://doi.org/10.1038/nbt1172)
44. P. V. R. Schleyer, *Chem. Rev*. **101** (2001) 1115 (https://doi.org/10.1021/cr0103221)
45. M. K. Cyrañski, Z. Czarnocki, G. Häfelinger, A. R. Katritzky, *Tetrahedron* **56** (2000) 1783 (https://doi.org/10.1016/S0040-4020(99)00979-5)
46. J. Poater, M. Duran, M. Solà, B. Silvi, *Chem. Rev*. **105** (2005) 3911 (https://doi.org/10.1021/cr030085x)
47. Y. Chen, Y. Zhou, Mo. Chen, B. Xie, J. Yang, J. Chen, Z. Sun, *Food Chem.* **258** (2018) 393 (https://doi.org/10.1016/j.foodchem.2018.02.105)
48. H. Xia, Q. Sun, N. Gan, P. Ai, H. Li, Y. Li, *RSC Adv*. **13** (2023) 8281 (https://doi.org/10.1039/d2ra07377c)
49. H. Zhang, R. Cai, C. Chen, L. Gao, P. Ding, L. Dai, B. Chi, *Int. J. Mol. Sci*. **24** (2023) 13281 (https://doi.org/10.3390/ijms241713281)
50. A. Mahboob, *Molecules* **28** (2023) 5942 (https://doi.org/10.3390/molecules28165942).

Journal of the Serbian Chemical Society
JSCS@tmf.bg.ac.rs • www.shd.org.rs/JSCS

*J. Serb. Chem. Soc.* *89* (9) 1177–1190 (2024)
*JSCS–5780*

*Original scientific paper*
Published 8 September 2024

# Study of the adsorption process between the phenolic compound catechin and the dietary fiber zymosan A: The influence of pH and concentration

PETRA MATIĆ*, DANIELA KENJERIĆ, LIDIJA ŠOHER and LIDIJA JAKOBEK

*Josip Juraj Strossmayer University of Osijek, Faculty of Food Technology Osijek, Franje Kuhača 18, HR 31000 Osijek, Croatia*

(Received 1 December 2023, revised 5 June, accepted 15 June 2024)

*Abstract*: Polyphenolic compounds have shown various beneficial effects on human health as well as certain bioactivities such as interactions with dietary fiber. Factors that can influence their interactions with dietary fibers include the pH value, the polyphenolic compound concentration and compound stability. The aim of this work was to study the interactions between the polyphenolic compound catechin and the dietary fiber zymosan A from yeast through investigation of the adsorption process. The catechin stability and the influence of concentration and pH value on interactions were investigated. Catechin showed the lowest stability at pH 7.0 with degradation ratio from 6 to 15 %. The lowest adsorption capacity was at pH 7.0, then higher in water and the highest at pH 1.5. A Dubinin–Radushkevich adsorption model fit to the data and FTIR analysis indicates the presence of physical interactions between catechin and zymosan A. This study can contribute to better understanding of interactions of polyphenols and dietary fiber for possible design of functional food, or to increase bioaccessibility of polyphenols.

*Keywords*: catechin; zymosan A; adsorption; interactions; stability; bioavailability.

## INTRODUCTION

Polyphenols are a large group of secondary plant metabolites. Based on their chemical structure, polyphenols can be classified as phenolic acids, flavonoids, stilbens and lignans. Flavonoids can be further divided to flavonols, flavones, isoflavones, flavanones, anthocyanidins and flavanols.[1] Polyphenols have shown many potentially positive bioactivities, but since their role is not completely understood they are still intensively studied.[2] Catechins are polyphenols that belong to the flavan-3-ols group. They can be found in different products such as tea, wine, fruits and cocoa products.[3] Recently, tea catechins have been studied

* Corresponding author. E-mail: petra.matic@ptfos.hr
https://doi.org/10.2298/JSC231130060M

due to its potentially beneficial effects on human health[4], but they have shown low absorption and poor bioaccessibility in the digestive tract.[4] One of the reasons for their poor bioaccessibility can be instability in the digestive tract which depends on pH, temperature and the presence of other substances.[5] Such environmental conditions can lead to the epimerization and oxidation of catechins.[5,6] Oxidation reactions occur in the upper small intestine. The degradation of catechins is also directly correlated to pH value.[6] Indeed, catechins are very unstable in alkaline solutions.[7] To better understand the potential beneficial effects of catechins, their behavior, stability/instability, degradation rate, or degradation products in the digestive system should be further studied. Besides environmental conditions of the gastrointestinal tract, catechins can be affected by interactions with dietary fibers. Dietary fibers have the potential to bond to polyphenols, as well as catechins, protect them from environmental conditions and "carry" them to the lower parts of the digestive tract,[8] where they can be released and show potential bioeffects. Those interactions still need additional studies. One of the insoluble dietary fibers from *Saccharomyces cerevisiae* is zymosan or *β*-(1,3)--glucan.[9] By itself, zymosan has shown several different biological activities related to inflammatory and immune responses, to protecting and delivering drugs, or to the adsorption of toxins[10–13] which have enabled its use in functional food and dietary supplement development.[9] The knowledge of its interactions with phenolic compounds, such as catechins might help to understand possible design of functional food.[14] To the best of our knowledge, the adsorption between catechin and zymosan has not been studied before. The most common and simple method for the study of the interactions between catechins and dietary fiber is the analysis of adsorption data[15,16] in which various adsorption isotherms can be applied in order to obtain information about the interactions.[17,18]

The aim of this work was to study the stability of catechin in different solvents (water, solutions of pH 1.5 and 7.0) and the interactions between catechin and the dietary fiber zymosan A, likewise in different solvents (water, solutions of pH 1.5 and 7.0). The adsorption was studied with different concentrations of catechin and Langmuir and Dubinin–Radushkevich adsorption isotherm models were used to analyze the data.

## EXPERIMENTAL

### *Chemicals and reagents*

Methanol (HPLC grade) was purchased from J.T. Baker (Deventer, Netherlands). (+)--catechin hydrate (≥ 98 %, C1251) and zymosan A from *Saccharomyces cerevisiae* (Z4250) were purchased from Sigma Aldrich (St. Louis, CA, USA). Sodium carbonate and potassium chloride were purchased from Gram-mol (Zagreb, Croatia), hydrochloric acid (37 %) from Avantor (Arnhem, Netherlands), Folin–Ciocalteu reagents from Merck (Darmstadt, Germany) and sodium hydrogen phosphate dodecahydrate and sodium dihydrogen phosphate dihydrate

from Kemika (Zagreb, Croatia). The solution of pH 1.5 was prepared by using hydrochloric acid–potassium chloride (0.1 M). The buffer of pH 7.0 was a phosphate buffer (0.1 M).

*Validation of Folin–Ciocalteu method for catechin determination*

Separate calibration curves to accurately determine the amounts of catechin after adsorption were prepared for catechin dissolved in each of the three different solvents (water, a solution of pH 1.5 and a solution of pH 7.0). In short, dilutions of catechin were prepared (1, 10, 50, 150, 250, 450, 550 and 700 mg $L^{-1}$) in water, in solutions of pH 1.5 and in solutions of pH 7 from stock solutions of catechin/1000 mg $L^{-1}$ prepared in the same solvents. All dilutions of catechin were measured according to Folin–Ciocalteu procedure. In particular, 30 μL of catechin dilution, 2370 μL of distilled water, 150 μL of Folin–Ciocalteu reagent and 450 μL of $Na_2CO_3$/ /200 g $L^{-1}$ were added in a glass tube. The solution was mixed in a vortex (Grant Bio, Cambridgeshire, England) and incubated at 40 °C for 30 min in an incubator (Memert, IN 30, Schwabach, Germany). The absorbance was measured at 765 nm against a blank solution with a UV–Vis spectrophotometer (Shimadzu, UV-1280, Kyoto, Japan). The linearity, the limit of detection (*LOD*), the limit of quatification (*LOQ*) and the accuracy were determined. The same Folin–Ciocalteu procedure was used to determine the amount of un-adsorbed catechin after the experiment of adsorption with these newly created calibration curves.

*Stability/degradation of catechin in different solvents*

The degradation of catechin in water and in solvents of pH 1.5 and 7.0 was studied. Dilutions of catechin ($\gamma_{initial}$, 50, 100, 150, 200, 250, 300 and 500 mg $L^{-1}$) were prepared in water, solvents of pH 1.5 and 7.0. They were incubated at 37 °C in the incubator for 180 min. The amount of catechin after 180 min was determined with the Folin–Ciocalteu method, representing the amount that was not degraded and remained in the solvent after 180 min ($\gamma_{remaining}$, mg $L^{-1}$). The concentration of degraded catechin was calculated according to the Eq. (1):

$$\gamma_{degraded} = \gamma_{initial} - \gamma_{remaining} \quad (1)$$

The degradation ratio was determined according to Eq. (2):

$$\text{Degradation} = 100\left(\frac{\gamma_{degraded}}{\gamma_{initial}}\right) \quad (2)$$

In addition, dilutions of catechin (100 mg $L^{-1}$) were prepared in water, pH 1.5 and 7.0. Those dilutions were put in the incubator at 37 °C for 180 min. After that, they were filtrated through a PTFE syringe filter 0.2 μm and analyzed with RP-HPLC method to see if there are additional peaks that would be the evidence of the degradation of catechin. RP-HPLC method was performed with 1260 Infinity II HPLC system (Agilent Technology, Santa Clara, CA, USA) with a quaternary pump, a photodiode array (PDA) detector, a vial sampler and Poroshell 120 EC C-18 column (4.6 mm×100 mm, 2.7 mm). The mobile phase A was 0.1 vol. % $H_3PO_4$ and mobile phase B 100 % methanol and following gradient: a gradient 0 min 5 % B, 5 min 25 % B, 14 min 34 % B, 25 min 37 % B, 28 min 80 % B, 30 min 80 % B, 32 min 5 % B min, 34 min 5 % B min. Each sample was injected in 10 μl. The flow rate was set to 0.5 mL $min^{-1}$.

*Adsorption of catechin and zymosan A in different solvents*

The adsorption between catechin and zymosan A was studied at 37 °C, in three different solvents (water, solutions of pH 1.5 and 7.0), with varying concentrations of catechin (50, 100, 150, 200, 250, 300 and 500 mg $L^{-1}$). Stock solutions of catechin were prepared in concentration of 1000 mg $L^{-1}$ in different solvents and appropriate volume was added into tubes to achieve

these concentrations in final volume of 2 mL. Zymosan A was weighed directly into tubes to achieve concentration of 500 mg $L^{-1}$ and appropriate solvents were added (water, solvents of pH 1.5 or 7.0) to reach the final volume of 2 mL. Solutions were put in rotator (Grant-bio PTR--35, Oxon, England) and at 37 °C in the incubator for 180 min, then centrifuged (Eppendorf, Hamburg, Germany) and aliquot of 700 μL was taken. Un-adsorbed catechin $\gamma_e$ (mg $L^{-1}$) was quantified with the Folin–Ciocalteu method using the new calibration curves. The amount of catechin adsorbed onto zymosan A $m_{adsorbed}$ / mg was calculated according to the Eq. (3):

$$m_{adsorbed} = \left(\gamma_{remaining} - \gamma_e\right) V_m \tag{3}$$

where $V_m$ (L) is the total volume of a model solution.

Adsorption capacity $q_e$ (the adsorbed amount of catechin (mg) onto g of zymosan A at specific equilibrium concentration) in water, pH 1.5 and 7.0 was calculated with the following Eq. (4) where $m_a$ (g) is the mass of zymosan A in the solution:

$$q_e = \frac{m_{adsorbed}}{m_a} \tag{4}$$

*Adsorption isotherm models*

The experimentally determined data of $q_e$ (mg $g^{-1}$) (adsorption capacity) and $\gamma_e$ (mg $L^{-1}$) (un-adsorbed catechin) were fitted by non-linear forms of Langmuir and Dubinin–Radushkevich adsorption isotherms (Eqs. (5) and (6)). A value $\gamma_e$ corresponds to a value $c_e$ in the adsorption isotherms. Parameters $K_L$ (L $mg^{-1}$, Langmuir equilibrium constant of adsorption), $q_m$ (mg $g^{-1}$, theoretical maximum adsorption capacity of zymosan A) from the Langmuir isotherm (Eq. (5)), as well as $\beta$ ($mol^2$ $J^{-2}$, Dubinin–Radushkevich constant related to the adsorption capacity) and $q_s$ (mg $g^{-1}$, the theoretical saturation capacity) and $c_s$ (mg $L^{-1}$, the saturation concentration) from the Dubinin–Radushkevich isotherm (Eq. (6)) were determined. Since a theoretical $c_s$ value could be a higher concentration for which our experiment was not designed, suitable $c_s$ values were predetermined according to the largest observed data value for $c_e$ and only the parameters $\beta$ and $q_s$ were obtained from fitting the Dubinin–Radushkevich isotherm. $R$ and $T$ / K in Eq. (6) represent the gas constant (8.314 J $K^{-1}$ $mol^{-1}$) and the absolute temperature, respectively:

$$q_e = \frac{q_m K_L c_e}{1 + K_L c_e} \tag{5}$$

$$q_e = q_s \exp\left(-\beta R^2 T^2 \left(\ln \frac{c_s}{c_e}\right)^2\right) \tag{6}$$

The mean free energy of adsorption, $E$, was calculated according to Eq. (7):

$$E = \frac{1}{\sqrt{2\beta}} \tag{7}$$

*FTIR analysis*

Pure catechin, pure zymosan A and catechin–zymosan A binding samples were recorded in the range of 450–4000 $cm^{-1}$ with scanning resolution of 4 $cm^{-1}$ by FTIR (PerkinElmer UATR, MA, USA). The catechin–zymosan A binding samples were prepared with concentration of 500 mg $L^{-1}$ catechin and 300 mg $L^{-1}$ zymosan A in 10 mL water, then pH 1.5 and pH 7.0. Samples were putted in incubator at 37 °C for 180 min and then filtrated through

vacuum filtration unit with filters (LLG membrane filters MCE, 0.22 μm). Catechin–zymosan A binding samples retained on the filters. Samples were dried and put to FTIR analysis.

*Statistical analysis*

MS Excel (Redmond, Washington, USA) software was used for data analysis. The accuracy of the Folin–Ciocalteu method was determined by performing a regression analysis in MS Excel 2013 using the Data Analysis tool, with a confidence interval of 95 %. All adsorption experiments were conducted in two parallels, each concentration measured three times ($n_{TOTAL}$ = 6). Non-linear regression analysis was performed in the MS Excel tool Solver. The sum of squared errors (*SSE*) was calculated according to the Eq. (8), where $m$ is the number of initial concentrations used in the adsorption experiments, $c_{e,i}$ and $q_{e,i}$ are the means of the measured $c_e$ and $q_e$ values for the $i^{th}$ initial concentration, $f(c_e,a,b)$ is the non-linear model function with generic parameters $a$ and $b$ and $n_i$ is number of data points for the $i^{th}$ initial concentration. The standard error, $S$, of nonlinear regression was calculated according to Eq. (9), where $N$ is the total number of initial concentration cases and $k$ = 1 or 2 is the number of parameters to be determined:

$$SSE = \sum_{i=1}^{m} n_i \left[ q_{e,i} - f\left(c_{e,i}, a, b\right) \right]^2 \quad (8)$$

$$S = \sqrt{\frac{SSE}{N-k}} \quad (9)$$

## RESULTS AND DISCUSSION

### *Validation of Folin–Ciocateu method for catechin determination*

The results for the linearity ($R^2$), limit of detection (*LOD*), limit of quantification (*LOQ*) and accuracy for the catechin determination in different solvents (ultrapure water, pH 1.5 and pH 7.0) are presented in Table I.

TABLE I. Validation parameters (linearity ($R^2$), limit of detection (*LOD*), limit of quantification (*LOQ*), accuracy) of spectrophotometric method for the determination of catechin in different solvent; results are based on two replicate samples of each standard concentration, each measured twice; accuracy was determined by performing a regression analysis with a confidence interval of 95 %, catechin solutions were incubated for 180 min in different solutions to enable degradation and calibration according to the actual presence of catechins in different environments; range: 1–700 mg $L^{-1}$

| Validation parameter | Ultrapure water | pH 1.5 | pH 7.0 |
|---|---|---|---|
| | Calibration curve | | |
| Calibration equation | $y = 0.0011x + 0.0104$ | $y = 0.0011x + 0.0108$ | $y = 0.0012x + 0.0104$ |
| $R^2$ | 0.9994 | 0.9950 | 0.9990 |
| *LOD* / mg $L^{-1}$ | 0.85 | 0.85 | 0.19 |
| *LOQ* / mg $L^{-1}$ | 2.57 | 2.57 | 0.59 |
| | Accuracy | | |
| Slope | 1.0164 | 0.9920 | 1.0411 |
| 95 % Confidence interval | 0.9994–1.0334 | 0.9518–1.0322 | 0.9795–1.0195 |
| Intercept | 0.5018 | 1.3745 | 0.3197 |
| 95 % Confidence interval | –4.9923–5.9958 | –13.4753–16.224 | –6.5074–7.1468 |

Catechin showed linear calibration curves in all solvents ($R^2$ from 0.9950–0.9994), with reasonably low *LOD* and *LOQ*. The method was accurate according to the analysis with 95 % reliability, which rejected the existence of a systematic error (the confidence interval for the slope of the calibration curve includes a value 1 and for the intercept includes a value 0). Validated Folin–Ciocalteu method demonstrated to be suitable for the determination of the concentration of catechin after the adsorption process in water, pH 1.5 and 7.0.

*Degradation of catechin in different solvents*

The degradation of catechin was studied for initial concentrations of catechin 50, 100, 150, 200, 250, 300 and 500 mg $L^{-1}$ which were diluted in water, solvents of pH 1.5 and 7.0. Dilutions were incubated for 180 min and 37 °C. After that period the concentration of catechin was determined with the Folin–Ciocalteu method to see the concentration of remaining non-degraded catechin. Catechin was stable in water and pH 1.5 and it did not degrade (data not shown). An earlier study also reported the stability of catechins from green tea around pH 4.[19] However, catechin did degrade at pH 7.0 (Fig. 1a). The concentrations of

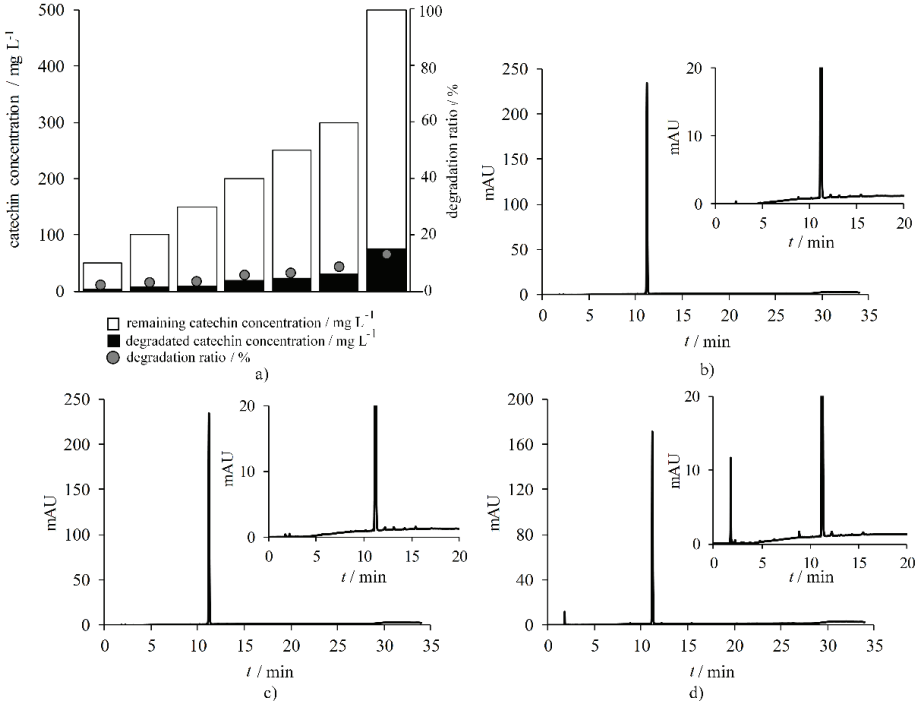


Fig. 1. Degradation of catechin for different initial catechin concentrations (50, 100, 150, 200, 250, 300 and 500 mg/L) at: a) pH 7.0 after 180 min incubation determined with Folin–Ciocalteu method, b) chromatograms of catechin (100 mg $L^{-1}$) at 280 nm, after the incubation for 180 min in ultrapure water and c) pH 1.5 and d) pH 7.0.

remaining catechin after 180 min were lower than the initial concentrations which suggested the degradation of catechin due to elevated pH. The degradation degree was from 6 to 15 %. Furthermore, the degradation percentage increased with the increasing initial concentration of catechin. This agrees with earlier study that reported the degradation of catechin at pH from 5.0 to 9.0.[20] Different factors like pH, temperature, concentration or the presence of other substances can influence the stability of catechin, which can lead to epimerization or degradation of catechin.[5,19,21,22] The degradation (or stability) of catechin in different solvents was investigated with the HPLC method in order to see any additional peaks on chromatograms. The HPLC chromatograms of catechin in different solvents after the incubation for 180 min at 37 °C are shown in Fig. 1. Catechin showed stability in water and at pH 1.5, but less stability at pH 7.0. Additional peaks appeared on the chromatogram at pH 7.0 (Fig. 1d) This agrees with our results obtained with the Folin–Ciocalteu method which indicated that catechin degraded at pH 7 into different products which need further identification. An earlier study found different semiquinones and dimerization products at near-neutral or greater pH.[6] The degradation of catechin can influence the adsorption capacity since the degraded catechin might be calculated into the amount that actually adsorb onto zymosan A. That is why we used the concentration of non-degraded catechin in the calculation of adsorption capacity after the adsorption experiment (Eq. (1)).

*Adsorption of catechin onto zymosan A in different solvents*

The adsorption capacities between catechin and zymosan A in different solvents are shown in Fig. 2. The adsorption capacities in the solvent of pH 7 reported here are values corrected for the degradation of catechin at this pH according to Eqs. (3) and (4). Catechin adsorbed onto zymosan A in amounts from 5 to 61 mg $g^{-1}$ depending on the initial of catechin and the pH of the surrounding. Since the adsorption capacity depends on various factors such as the properties of the adsorbent, the properties of the adsorbate, the properties of the solution, or the type of experiment,[23] it is difficult to compare the results with the literature. The adsorption capacity of standards of polyphenols from tea adsorbed onto oat *β*-glucan in the amount of 156 to 405 mg $g^{-1}$ (at pH 5.80, then polyphenol concentration 0.7 mg $mL^{-1}$, at 50 °C and concentration of buffer 0.10 M),[24] then tea polyphenols at different pH values adsorbed onto *β*-glucan up to 116 mg $g^{-1}$ (at pH 5.56, at 50 °C and concentration of buffer 0.13 M).[25]

Adsorption capacity differed depending on different pH value (Fig. 2). Catechin showed the lowest adsorption capacity in pH 7.0, higher in water and the highest at pH 1.5, depending on the catechin concentration. At different pH, catechin can be present in dissociated or non-dissociated forms. Which chemical forms of catechin exist at certain pH, can be seen in the p$K_a$ value[17] and distri-

bution diagram of species.[26] At pH values lower than p$K_a$, catechin exists mostly in a non-dissociated form, while at pH values above p$K_a$, dissociated form dominates. According to the observed p$K_a$ values for catechin (8.77, 9.97 and 11.99),[26] it appears that catechin exist in non-dissociated form at pH 1.5 and in water (pH 5.47). This might have caused higher amounts of catechin in non-dissociated form to bond to zymosan A at pH 1.5 and as a result show a higher adsorption capacity. At pH 7.0, catechin could be present in both non-dissociated and dissociated forms.

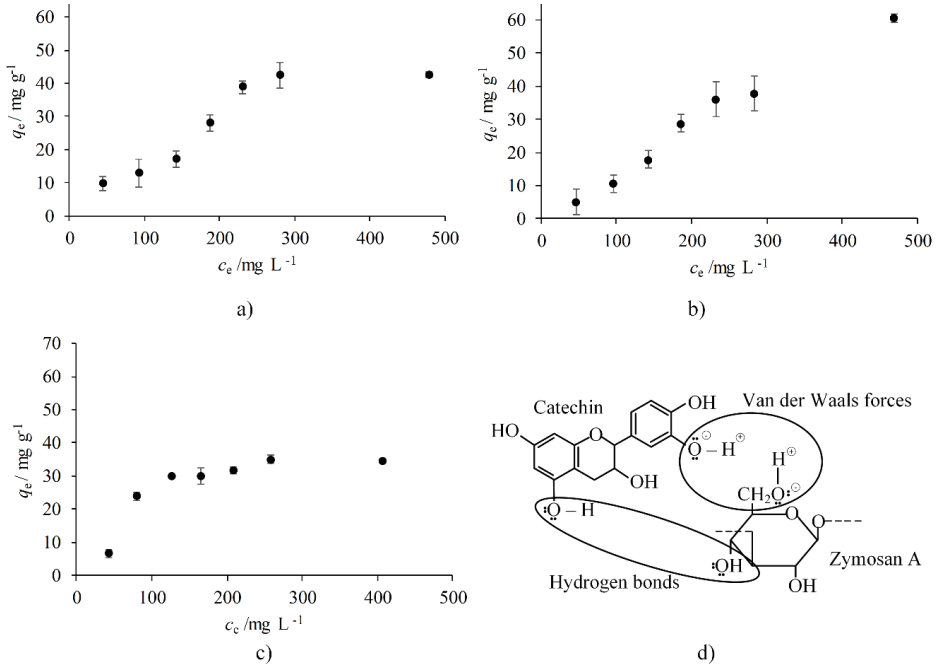


Fig. 2. Adsorption capacities $q_e$ / mg g$^{-1}$ of zymosan A for catechin at different concentrations of catechin: a) adsorption in water; b) pH 1.5; c) pH 7.0; d) possible interactions between catechin and zymosan A.

The ratio of dissociated/non-dissociated form increases with the increase of pH. This could explain the lower adsorption capacity of catechin at pH 7.0. Catechin dissociated and possibly degraded, which affected lower amount of catechin bonded to zymosan A at pH 7.0 and in water. Due to the higher ratio of dissociated/non-dissociated forms with higher pH, some studies have pointed to the less stability of catechin in neutral and alkaline area[27] which agrees with our results. The data after the adsorption process (the amount of catechin adsorbed on zymosan A $q_e$ and unadsorbed catechin concentration $c_e$) are presented as adsorption isotherms (Fig. 2) and adsorption isotherm models were fitted in order to possibly describe the adsorption process.

*Adsorption isotherm models*

The obtained data in the adsorption process ($c_e$ *vs.* $q_e$) can be analyzed with adsorption isotherm equations. The non-linear equations of Langmuir and Dubinin–Radushkevich were fit to the experimental data. Table II summarizes the values of the determined parameters of the isotherm models obtained with least possible error $S$ using the add-in called Solver. The parameters $q_m$ from the Langmuir model and the $q_s$ from the Dubinin–Radushkevich model which represent the predicted apparent maximum adsorption capacities/saturation capacities of zymosan, were from 36 to 65 mg $g^{-1}$ with maximal $S$ error 3. The $R^2$ was between 0.8477 and 0.9697 for both Langmuir and Dubinin–Radushkevich model. Due to error $S$ and $R^2$ both models fit the experimental data well, except Langmuir models for adsorption in water which fit les the experimental data ($R^2$ is 0.8477). The result of Langmuir fit for adsorption at pH 1.5 should be taken with caution, since the equilibrium has not been reached. The $q_m$ and $q_s$ values are in accordance with experimentally determined adsorption capacities (Fig. 2).

TABLE II. Theoretical parameters of Langmuir and Dubinin–Radushkevich adsorption isotherms for different solvent type and 37 °C

| Solvent | Langmuir | | | | Dubinin–Radushkevich | | | |
|---|---|---|---|---|---|---|---|---|
| | $q_m$ / mg $g^{-1}$ | $K_L$ / L $mg^{-1}$ | $S$ | $R^2$ | $q_s$ / mg $g^{-1}$ | $E$ / J $mol^{-1}$ | $S$ | $R^2$ |
| Water | 44 | 0.01 | 3 | 0.8477 | 47 | 2384 | 2 | 0.9326 |
| pH 1.5 | 62 | 0.005 | 3 | 0.9231 | 65 | 2047 | 3 | 0.9638 |
| pH 7.0 | 37 | 0.01 | 2 | 0.9665 | 36 | 2805 | 3 | 0.9697 |

All determined free energies of adsorption ($E$) were lower than 8,000 J $mol^{-1}$, which indicates the presence of physical interactions between catechin and zymosan A, like the formation of H-bonds, hydrophobic interactions or van der Waals forces (Fig. 2d). The bonds between catechin and zymosan A could be through oxygen atoms and OH–groups on the zymosan A molecule and OH--groups on catechin molecule. This agrees with earlier studies.[25,28] It has been shown that the bonds between polyphenols and dietary fiber like $\beta$-glucan can be hydrophobic interactions, hydrogen bonds and van der Waals interactions.[25,29,30] Also, a mechanism of interaction between polyphenols ((–)-epigallocatechin-3--gallate)) and $\beta$-glucan[24] was proposed through oxygen atoms and OH-groups on the $\beta$-glucan molecule and OH-groups on polyphenols. The formation of hydrogen bonds reduces the distance between the aromatic rings of polyphenols and $\beta$--glucans, which enables van der Waals interactions.[24] The OH–groups of catechin on benzene rings might be the main functional groups which bind to zymosan A in the adsorption process (Fig. 2d). It can be suggested that the studied adsorption models reasonably fit the data and these models can be suitable for the

adsorption studies in this work. In an earlier study, the Langmuir model was also suitable for describing the catechin adsorption onto cellulose.[17]

*FTIR spectrum*

FTIR analysis can be used to identify functional groups in the adsorption process.[17] Fig. 3 shows the FTIR spectra of pure catechin and zymosan A and a sample of zymosan A with bonded catehin, all in three different solvents (water, pH 1.5 and 7). Catechin peaks were compared with those found in the literature.[31,32] The catechin molecule poses five OH groups on benzene rings (Fig. 2d). The OH–groups on ring A showed peaks 3276 (O–H group stretching) and 1142 $cm^{-1}$ (C–O–H stretching).[31] The OH–groups on ring B show peaks 1354 $cm^{-1}$

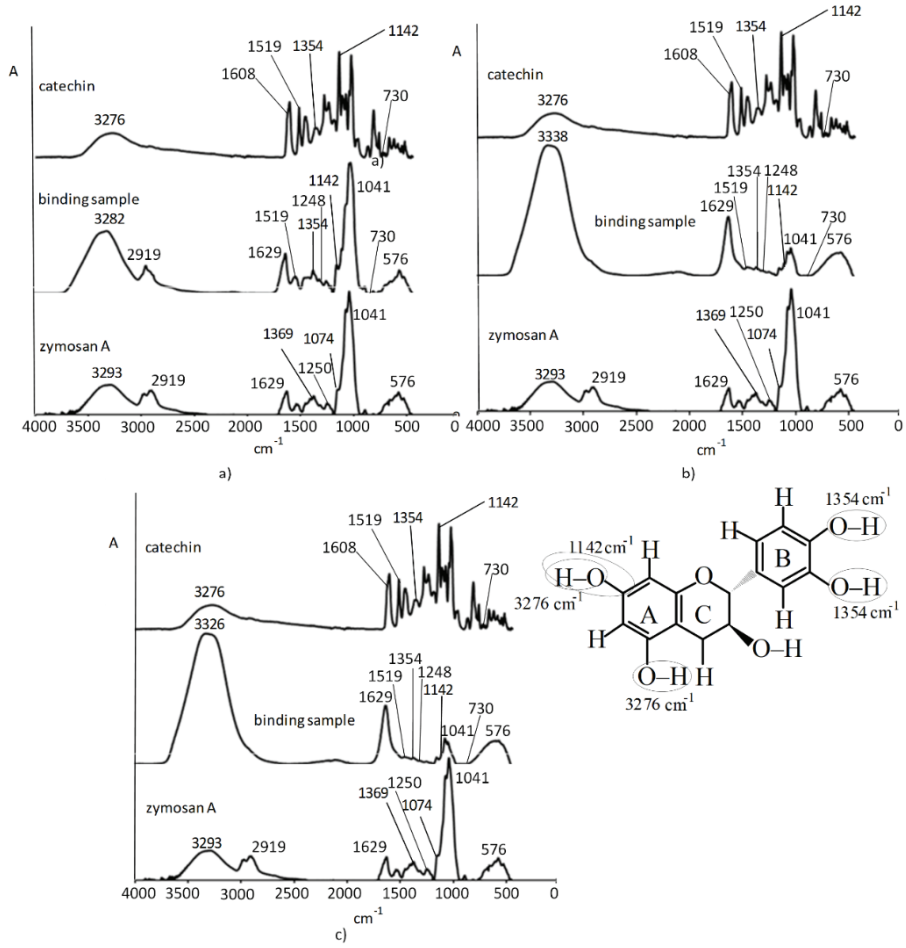


Fig. 3. FTIR spectrum of catechin, catechin–zymosan A binding sample and zymosan A: a) at water; b) at pH 1.5 and c) at pH 7.0.

(O–H in plane bending)[31]. Catechin showed other peaks like 1608 $cm^{-1}$ (ring A deformation), 1519 (ring B deformation) and 730 (C–H out of plane bending).[33]

The FTIR spectra of catechin agree with those published in the literature.[31,32] The pure zymosan A showed characteristic peaks at 3293 (OH stretching groups), 2919 (C–H stretching), 1369 (C–H bond), 1250 ($CH_2OH$ stretch) and 1041 $cm^{-1}$ (C–O–C stretch). The FTIR spectra of zymosan A agree with those published in the literature.[9] Comparing the FTIR spectra of pure zymosan and pure catechin molecule with FTIR spectra of binding samples, the formation of complex can be confirmed.[33] Similar peaks to the peaks for the catechin molecule were observed in the characteristic peaks of catechin–zymosan A binding sample (Fig. 3, 1519, 1354, 1142 and 730 $cm^{-1}$). Furthermore, the peaks of zymosan A were found in all binding samples (1629, 1041 and 576 $cm^{-1}$ in water, pH 1.5 and 7 and additional 2919 $cm^{-1}$ in water). The appearance of catechin and zymosan peaks in the binding samples indicates possible catechin and zymosan A interactions. Differences in the FTIR spectrum for all the binding samples can be seen (Fig. 3). The decrease in intensity of peaks (around 1100–1600 $cm^{-1}$) for binding samples at pH 1.5 and 7 was stronger than for peaks at water. Also, the peak of OH groups of the binding samples at water (3282 $cm^{-1}$) were not so strong and less broad then peaks at pH 1.5 (3338 $cm^{-1}$) and at pH 7.0 (3326 $cm^{-1}$). The decrease in intensity could indicate intermolecular interactions such as hydrogen bonding. In earlier work, disappearance of peaks of hydrogen groups in phospholipid complex of naringenin and naringin PLGA nanosphere complex[33] also indicated such intramolecular bonding. These results have significance for the behavior in the digestive system, for carrying catechins with dietary fibers through the digestive system. Due to the fact that catechin degrade in intestinal tract, one way to improve its bioaccessibility can be the delivery system with dietary fiber[4] like zymosan A. This offers an additional chance for pharmaceutical industry to create some other dietary supplements based on zymosan A and phenolic compounds together. More studies should be carried out before that.

## CONCLUSION

The stability/degradation of catechin and catechin adsorption onto zymosan A in different solvents (water, pH 1.5 and 7.0) was studied. The stability of catechin was pH dependent. After incubation in water, pH 1.5 and 7.0 for 180 min at 37 °C, catechin was stable in water and at pH 1.5. However, it degraded up to 15 % at pH 7.0. HPLC analysis revealed additional peaks of the degradation product. Catechin did adsorb onto zymosan A in water, pH 1.5 and 7.0. The lowest adsorption capacity was found to be at pH 7.0, higher at water and the highest at pH 1.5. Different ratios of non-dissociated/dissociated forms of catechin affected the higher adsorption at pH 1.5 and lower at pH 7.0 and in water. Langmuir and Dubinin–Radushkevich models gave additional information on the

adsorption process. The Dubinin–Radushkevich model indicated the presence of physical interactions between catechin and zymosan A. FTIR analysis showed that catechin could bond on zymosan A through OH–groups on benzene rings of catechin. This study can contribute to better understanding of interactions between catechin and zymosan A and possible design of functional food.

*Acknowledgement*. This research was funded by the Faculty of Food Technology Osijek.

И З В О Д

## ИСПИТИВАЊЕ ПРОЦЕСА АДСОРПЦИЈЕ ПОЛИФЕНОЛНОГ ЈЕДИЊЕЊА КАТЕХИНА И ДИЈЕТЕТСКОГ ВЛАКНА ЗИМОСАН А: УТИЦАЈ pH И КОНЦЕНТРАЦИЈЕ

PETRA MATIĆ[1], DANIELA KENJERIĆ[1], LIDIJA ŠOHER[1] и LIDIJA JAKOBEK[1]

[1]*Josip Juraj Strossmayer University of Osijek, Faculty of Food Technology Osijek, Franje Kuhača 18, HR 31000 Osijek, Croatia*

Полифенолна једињења показују различите ефекте корисне за људско здравље као и одређене биоактивности као што су интеракције са дијететским влакнима. Фактори који утичу на њихове интеракције са дијететским влакнима укључују pH вредност, стабилност полифенолних једињења и концентрацију. Циљ овог рада је испитивање интеракција између полифенолног једињења катехина и дијететског влакна зимосан А из квасца праћењем процеса адсорпције. Испитивана је стабилност катехина и утицај концентрације и pH вредности на интеракције. Катехин је показао најнижу стабилност на pH 7,0 са процентом деградације од 6 до 15 %. Најнижи капацитет адсорпције је постигнут на pH 7,0, затим виши у води и највиши на pH 1,5. Дубинин–Радушкевич адсорпциони модел примењен на добијене податке и FTIR спектроскопска анализа указују на постојање физичких интеракција између катехина и зимосана А. Ово испитивање може допринети бољем разумевању интеракција између полифенола и дијететских влакана за потенцијални дизајн фунционалне хране, као и повећању биодоступности полифенола.

(Примљено 1. децембра 2023, ревидирано 5. јуна, прихваћено 15. јуна 2024)

## REFERENCES

1. F. Truzzi, C. Tibaldi, Y. Zhang, G. Dinelli, E. D'Amen, *Int. J. Mol. Sci.* **2** (2021) 5541 (https://doi.org/10.3390/ijms22115514)
2. L. Jakobek, P. Matić, *Trends Food Sci. Technol*. **83** (2019) 235 (https://doi.org/10.1016/j.tifs.2018.11.024)
3. S. Ho, Y. Y. Thoo, D. J. Young, L. F. Siow, *Food Chem*. **275** (2019) 594 (https://doi.org/10.1016/j.foodchem.2018.09.117)
4. Z. Y. Cai, X. M. Li, J. P. Liang, L. P. Xiang, K. R. Wang, Y. L. Shi, R. Yang, M. Shi, J. H. Ye, J. L. Lu, X. Q. Zheng, Y. R. Liang, *Molecules* **23** (2018) 2346 (https://doi.org/10.3390/molecules23092346)
5. V. K. Ananingshig, A. Sharma, W. Zhou, *Food Res. Int.* **50** (2013), 469 (https://doi.org/10.1016/j.foodres.2011.03.004)
6. A. P. Neilson, A. S. Hopf, B. R. Cooper, M. A. Pereira, J. A. Bomser, M. G. Ferruzzi, *J. Agric. Food Chem.* **55** (2007) 8941 (https://doi.org/10.1021/jf071645m)
7. Q. V. Vuong, C. E. Stathopoulos, M. H. Nguyen, J. B. Golding, P. D. Roach, *Food Rev. Int.* **27** (2011) 227 (https://doi.org/10.1080/87559129.2011.563397)

8. A. E. Quirós-Sauceda, H. Palafox-Carlos, S. G. Sáyago-Ayerdi, J. F. Ayala-Zavala, L. A. Bello-Perez, E. Álvarez-Parrilla, L. A. de la Rosa, F. A. González-Córdova, G. A. González-Aguilar, *Food Funct*. **5** (2014) 1063 (https://doi.org/10.1039/C4FO00073K)
9. G. Venkatachalam, A. Senthilkumar, M. Doble, *ACS Omega* **5** (2020), 15973 (https://doi.org/10.1021/acsomega.0c01243)
10. T. Miura, N. Ohno, N. N. Miura, Y. Adachi, S. Shimada, T. Yadomae, *FEMS Microbiol. Immunol.* **24** (1999) 131 (https://doi.org/10.1111/j.1574-695X.1999.tb01274.x)
11. M. Salgado, S. Rodríguez-Rojo, R. L. Reis, M. José Cocero, A. R. C. Duarte, *J. Supercrit. Fluids* **127** (2017) 158 (https://doi.org/10.1016/j.supflu.2017.04.006)
12. A. Yiannikouris, J. Francois, L. Poughon, C.-G. Dussap, G. Bertin, G. Jeminet, J.-P. Jouany, *J. Agric. Food Chem*. **52** (2004) 3666 (https://doi.org/10.1021/jf035127x)
13. A. Yiannikouris, G. Andre, A. Poughon, J. Francois, C.-G. Dussap, G. Jeminet, G. Bertin, J.-P. Jouany, *Biomacromolecules* **7** (2006) 1147, (https://doi.org/10.1021/bm050968t)
14. T.R. Falcão, C. A. O. Rodrigues, A. A. de Araújo, C. A. A. X. de Medeiros, L. A. L. Soares, M. R. A. Ferreira, R. C. Vasconcelos, R. F. de Araújo Júnior, M. L. D. de Sousa Lopes, G. C. B. Guerra, *BMC Complement Altern. Med*. **19** (2019) 1 (https://doi.org/10.1186/s12906-019-2454-3)
15. P. Matić, Š. Ukić, L. Jakobek, *Chem. Biochem. Eng. Q*. **35** (2021) 177 (https://doi.org/10.15255/CABEQ.2020.1902)
16. A. Siemińska-Kuczer, M. Szymańska-Chargot, A. Zdunek, *Food Chem*. **373** (2022) 131487 (https://doi.org/10.1016/j.foodchem.2021.131487)
17. Y. Liu, D. Yiang, L. Sanguansri, Y. Cai, X. Le, *Food Res. Int.* **112** (2018) 225 (https://doi.org/10.1016/j.foodres.2018.06.044)
18. Y. Liu, D. Yiang, L. Sanguansri, M. A. Augustin, *Food Chem*. **271** (2019) 733 (https://doi.org/10.1016/j.foodchem.2018.08.005)
19. N. Li, L. S. Taylor, M. G. Ferruzzi, L. J. Mauer, *J. Agric. Food Chem*. **60** (2012) 12531 (https://doi.org/10.1021/jf304116s)
20. Y. Narita, K. Inouye, *J. Agric. Food Chem.* **61** (2013) 966 (https://doi.org/10.1021/jf304105w)
21. M. Shi, Y. Nie, X. Q. Zheng, J. L. Lu, Y. R. Liang, J. H. Ye, *Molecules* **21** (2016) 1345 (https://doi.org/10.3390/molecules21101345)
22. Z. Xu, L. Wei, Z. Ge, W. Zhu, *Eur. Food Res. Technol*. **240** (2015) 707 (https://doi.org/10.1007/s00217-014-2375-9)
23. M. L. Soto, A. Moure, H. Domínguez, J. C. Parajó, *J. Food Eng*. **105** (2011) 1 (https://doi.org/10.1016/j.jfoodeng.2011.02.010)
24. R. Gao, H. Liu, Z. Peng, Z. Wu, Y. Wang, G. Zhao, *Food Chem., B* **132** (2012) 1936 (https://doi.org/10.1016/j.foodchem.2011.12.029)
25. Z. Wu, H. Li, J. Ming, G. Zhao, *J. Agric. Food Chem.* **59** (2011) 378 (https://doi.org/10.1021/jf103003q)
26. J. Herrero-Martínez, M. Sanmartin, M. Rosés, E. Bosch, C. Ràfols, *Electrophor.* **26** (2005) 1886 (https://doi.org/10.1002/elps.200410258)
27. T. Raab, D. Barron, F. A. Vera, V. Crespy, M. Oliveira, G. Williamson, *J. Agric. Food Chem*. **58** (2010) 2138 (https://doi.org/10.1021/jf9034095)
28. Y. Gao, R. Yiang, J. Qie, J. Chen, D. Xu, W. Liu, Q. Gao, *Carbohydr. Polym., A* **90** (2012) 1411 (https://doi.org/10.1016/j.carbpol.2012.05.096)
29. H. T. Simonsen, M. S. Nielsen, N. J. Christensen, U. Christensen, T. V. La Cour, M. S. Motawia, B. P. M. Jespersen, S. B. Engelsen, B. L. Møller, *J. Agric. Food Chem*. **57** (2009) 2056 (https://doi.org/10.1021/jf802057v)

30. M. Veverka, T. Dubaj, J. Gallovič, V. Jorík, E. Veverková, M. Mičušík, P. Šimon, *J. Funct. Foods* **8** (2014) 309 (https://doi.org/10.1016/j.jff.2014.03.032)
31. A. M. Mendoza-Wilson, D. Glossman-Mitnik, *J. Mol. Struct*. **761** (2006) 97 (https://doi.org/10.1016/j.theochem.2006.01.001)
32. M. Krysa, M. Szymańska-Chargot, A. Zdunek, *Food Chem*. **393** (2022) 133430 (https://doi.org/10.1016/j.foodchem.2022.133430)
33. A. Semalty, M. Semalty, D. Sing, M. S. M. Rawat, *J. Incl. Phenom. Macrocycl. Chem.* **67** (2010) 253 (https://doi.org/10.1007/s10847-009-9705-8).

Journal of the Serbian Chemical Society
JSCS-info@shd.org.rs • www.shd.org.rs/JSCS
*J. Serb. Chem. Soc.* *89* (9) 1191–1210 (2024)
*JSCS–5781*
*Original scientific paper*
Published 10 September 2024

# Influence of organic/inorganic inhibitors on AISI 304 (1.4301) and AISI 314 (1.4841) steels corrosion kinetics in nitric acid solution

JELENA ŠĆEPANOVIĆ[1], BOJANA ZINDOVIĆ[2], DRAGAN RADONJIĆ[1], MARIJANA R. PANTOVIĆ PAVLOVIĆ[3,4#]* and MIROSLAV M. PAVLOVIĆ[3,4#]

*[1]Faculty of Metallurgy and Technology, University of Montenegro, Cetinjski put, 81000 Podgorica, Montenegro, [2]Institute "SIGURNOST" LLC Podgorica, 81000 Podgorica, Montenegro, [3]Institute of Chemistry, Technology and Metallurgy, National Institute of the Republic of Serbia, Department of Electrochemistry, University of Belgrade, Njegoševa 12, 11000 Belgrade, Serbia and [4]Center of Excellence in Chemistry and Environmental Engineering–ICTM, University of Belgrade, Njegoševa 12, 11000 Belgrade, Serbia*

(Received 14 May, revised 29 May, accepted 23 August 2024)

*Abstract*: This study evaluates the effectiveness of $KMnO_4$, MK3 and 1-butanol inhibitors on corrosion of AISI 314 and AISI 304 stainless steels using linear and potentiodynamic polarization in 0.1 M $HNO_3$. The metrics like corrosion potential ($E_{corr}$), current density ($j_{corr}$) and polarization resistance ($R_p$) influence the inhibitor efficacy. The inhibitors improved electrochemical parameters significantly, indicating strong anti-corrosive properties. 1-Butanol had the strongest effect, enhancing corrosion potential and drastically reducing corrosion current density, demonstrating superior protection. The results indicated that without inhibitors, both steels showed higher corrosion rates and more negative potentials, reflecting their susceptibility to corrosion. The introduction of inhibitors markedly improved these parameters, particularly with 1-butanol, which significantly enhanced the polarization resistance and shifted the corrosion potential towards less negative values. The potentiodynamic results highlighted the dynamic effectiveness of inhibitors, reinforcing their role in mitigating corrosion under varied conditions. The study underscores the importance of selecting the appropriate inhibitors to enhance the durability and longevity of stainless steels in acidic environments, with 1-butanol showing the potential for industrial applications requiring high corrosion resistance. This necessitates comprehensive testing to accurately measure inhibitor capabilities in different conditions.

*Keywords*: austenitic stainless steel; corrosion; inhibitor; linear polarization; potentiodynamic polarization.

* Corresponding author. E-mail: m.pantovic@ihtm.bg.ac.rs
# Serbian Chemical Society member.
https://doi.org/10.2298/JSC240514076S

## INTRODUCTION

Stainless steels are fundamental to a broad spectrum of industries due to their intrinsic corrosion resistance and mechanical robustness.[1,2] These alloys are categorized into various families: austenitic, ferritic, martensitic and duplex. Among these, the austenitic stainless steels like AISI 304 and AISI 314 are renowned for their formability and resistance to a wide range of environmental conditions.[3,4] The selection of stainless steel for specific applications critically depends on its corrosion resistance. Laboratory tests and/or experiential data assist in selecting suitable steel for use under specific conditions. Alongside choosing the right corrosive medium and test conditions such as pH and temperature, the factors like electrode potential and current density significantly influence corrosion rate. For the testing of pitting corrosion, it is crucial to determine the conditions under which pits form, the critical temperature at which they occur and conditions that lead to the cessation of their growth.[5–8]

Austenitic stainless steel is one of the most commonly used materials in various sectors including construction and industries such as chemical and metallurgy, attributed to its excellent weldability, high-temperature resistance and corrosion resistance. The corrosion resistance of austenitic stainless steel, such as AISI 304 (1.4301) and AISI 314 (1.4841), primarily arises from the rapid formation of a passive film, composed of iron and chromium oxides mixed with hydroxides and water. This film forms instantaneously on the steel surface and has been extensively studied using surface analysis techniques. Corrosion remains a pervasive issue today, posing a continuous challenge for engineers aiming to extend the service life of equipment and enhance operational efficiency. However, the losses due to corrosion are not just limited to replacing corroded parts but also result in significant indirect costs such as downtime, product contamination and enduring environmental damage.[9,10] AISI 304 is particularly valued for its performance in diverse atmospheric and corrosive media, though it is susceptible to corrosion under certain acidic conditions.[11] AISI 314 is noted for its high temperature strength and the resistance to oxidation, requiring specific protective measures in harsh environments.[12]

Stainless steel is not stable in many corrosive environments, necessitating the application of protective measures to extend the lifespan of steel installations. Corrosion inhibitors, in very small concentrations, can reduce the corrosion rates to the technologically acceptable levels, making their use increasingly widespread. Moreover, they are often readily available and cost-effective. Inhibitors can be organic or inorganic and they can provide varying types of protection depending on the environmental conditions.[13] The interaction of these steels with their environments, particularly under the influence of various corrosion inhibitors, has been a significant focus of research. The inhibitors play a crucial role by forming a protective film that reduces corrosion rates significantly. Organic inhibitors,

such as imidazolines and their derivatives, as well as inorganic inhibitors, including phosphates and molybdates, have shown varied effectiveness in protecting these steels in acidic and neutral solutions.[14,15] The effectiveness of such inhibitors is often dependent on their ability to adsorb onto the metal surface and block corrosive agents, a phenomenon thoroughly analyzed in recent studies.[16]

Today, stainless steel is one of the most frequently used materials across all industries due to its excellent properties. It is an alloy material consisting of at least 10.5 % chromium and a maximum of 1.2 % carbon. Austenitic steels are used in a variety of areas, from load-bearing structures and architectural applications to kitchen appliances and medical equipment, not only because of their corrosion resistance but also due to their excellent formability, weldability, durability, *etc*. Some austenitic steels with a high content of alloying elements can withstand temperatures up to 1000 °C. The most well-known (basic) austenitic stainless steel is AISI 304 or 18/8, an iron-based alloy containing nominally 18 % Cr and 8.5 % Ni, including small amounts of C, N, Mn and Si.[17] The corrosion resistance of chromium–nickel steels is based on the presence of a sufficient amount of chromium, which facilitates easy passivation of the metal surface through the formation of adsorptive or phase oxide films of trivalent chromium, thereby bringing iron atoms into a passive state. Despite their resistance, stainless chromium–nickel steels can corrode under certain conditions in specific ways. The most common types of corrosion in stainless steels, in electrolyte solutions, include pitting corrosion, intergranular corrosion, contact corrosion and stress corrosion.[18,19]

Various corrosion inhibitors are added depending on the environment to reduce the rate at which the steel layer is damaged. In acidic environments, corrosion inhibitors such as organic compounds containing nitrogen, sulphur and oxygen and their derivatives are most effective, as they create an organic layer on the metal surface. In neutral environments, nitrites, chromates and permanganates are commonly used. The choice of inhibitors depends on several factors, including cost, availability and environmental impacts.[20,21] Schiff bases have emerged as effective organic inhibitors for AISI 304 and AISI 314 stainless steels, characterized by their ability to form complex films on the steel surface. These compounds show promising inhibition performance in both acidic and neutral environments due to their strong adsorption, facilitated by π-electrons and heteroatoms capable of coordinating with metal atoms on the steel surface.[22,23]

Anodic corrosion inhibitors are often oxidizing agents such as nitrates and nitrites, inorganic ions like chromate, permanganate, molybdate, phosphate and metal ions with higher oxidation numbers: $Cu^{+2}$, $Fe^{+3}$ and in some cases hydrogen peroxide and oxygen. Although the redox potentials of nitrates and nitrites are close in value, nitrites are shown to be more effective steel inhibitors. The ability of inhibitors to passivize metal and affect the corrosion process depends on

the size of the exchange current density. If the exchange current density is larger, the overpotential of the electrode reactions is small and vice versa.[24] The use of inorganic anodic inhibitors like nitrates and chromates has been critically reassessed due to their environmental impact, prompting research into safer alternatives.[25]

Potassium permanganate is one of the inhibitors commonly used as a "green" corrosion inhibitor.[24] Economically, it is very important that inhibitors act even at low concentrations. Usually, it is sought that Ni be 80–90 %, corresponding to a retardation factor between 5 and 50, *i.e.*, the inhibitor slows down the corrosion process that many times. The effectiveness of corrosion inhibitors depends on many factors, including the type of metal, metal surface, composition and concentration of the corrosive medium, its pH value and temperature and the type and concentration of the inhibitor. Most inhibitors are specific in their action on a particular metal. An inhibitor effective for a certain type of metal may not act on another type of metal or may even have a negative impact.[23]

Furthermore, the development of environmentally benign corrosion inhibitors, such as green inhibitors derived from natural sources like plant extracts, has accelerated. These inhibitors offer sustainable corrosion protection without the adverse environmental impacts associated with traditional inhibitors.[26,27] Recent studies have further elucidated the corrosion mechanisms and inhibition strategies in AISI 304 and AISI 314 steels. For instance, research by Šćepanović *et al.* highlights novel methodologies in the development and application of corrosion inhibitors.[28] Additionally, the work by Stanić *et al.* and Tomić *et al.* provides insights into the synergistic effects of various inhibitors and their interactions with metal surfaces, showcasing the potential for enhancement of the protective outcomes through innovative approaches and advanced analytical techniques.[29,30]

In the current study, corrosion assessments were performed on AISI 304 and AISI 314 steels, conducted under ambient conditions and utilizing one inorganic and two organic inhibitors, all within a 0.1 M $HNO_3$ solution. This investigation relied on the potentiodynamic polarization and linear polarization methodologies for the evaluation of corrosion behavior. The aim was to deepen the understanding of corrosion processes and inhibitor efficacy for AISI 304 and AISI 314 stainless steels in this manuscript, contributing to the development of more effective corrosion management strategies. By integrating empirical data with theoretical models, the research presented here seeks to provide comprehensive insights into optimizing corrosion inhibition practices to ensure the sustainability and durability of these critical materials in diverse environments.

## EXPERIMENTAL

The experimental phase was conducted in the laboratories of the Faculty of Metallurgy and Technology in Podgorica, in collaboration with the Institute of Ferrous Metallurgy in Nikšić. The steel specimens used in this study were procured from the laboratory facilities of

the Institute of Ferrous Metallurgy in Nikšić. The prepared batches of steel underwent a melting process in a 120 kg capacity induction furnace. Each melting cycle, including the alloying process, lasted approximately 150 min per steel variant. The specimens of AISI 304 and AISI 314 steel were produced according to the standardized procedures outlined in ASTM A743 for corrosion-resistant steel castings. This standard specifies rigorous guidelines for melting, casting and cooling processes to ensure high-quality, homogenous austenitic stainless-steel production. The Institute of Ferrous Metallurgy in Nikšić applied a controlled induction melting and alloying process which adheres to this specification. After melting, the steel was cast into quartz sand molds with a silicate binder based on water glass ("Sigel"), with solidification facilitated by $CO_2$ gas purging to optimize cooling rates and microstructural properties.

The cooling rate was meticulously controlled to promote fine grain structure, enhancing the mechanical properties and corrosion resistance of the steel. This methodically controlled process ensures that the microstructure and grain size of the steel are comparable to comercially available alloys, which is crucial for maintaining the consistency and reliability of our experimental results. Detailed microstructural analysis and comparisons with comercially available AISI 304 and AISI 314 steel variants will be provided to confirm the homogeneity and quality of the manufactured specimens. Subsequent to verification of the chemical composition *via* a quantometer, the molten steel was cast into molds that had been previously prepared. Details regarding the chemical composition of the obtained steel specimens are documented in Table I.

TABLE I. Chemical composition of the AISI 314 and AISI 304 steels utilized in this study

| Steel designation | C | Si | Mn | P | S | Cr | Ni | Al | Cu | Mo |
|---|---|---|---|---|---|---|---|---|---|---|
| AISI 314 | 0.22 | 1.57 | 1.03 | 0.019 | 0.012 | 19.01 | 17.20 | 0.06 | 0.14 | 0.48 |
| AISI 304 | 0.05 | 1.67 | 0.83 | 0.015 | 0.005 | 17.03 | 11.53 | 0.06 | 0.11 | 0.12 |

For the corrosion tests, cylindrical samples with a diameter of 15 mm and a thickness of 5 mm were prepared and utilized as working electrodes. The corrosion tests were conducted using working solutions with specific inhibitor concentrations. The corrosion behavior of AISI 314 and AISI 304 steels was examined in a 0.1 M nitric acid ($HNO_3$) solution. The influence of inhibitors was also studied in the same solution. A freshly prepared solution was used for each experiment, prepared as follows: 0.1 M $HNO_3$, obtained by diluting concentrated 65 % $HNO_3$ with a density of 1.4 g $cm^{-3}$ and a molar mass of 63 g $mol^{-1}$ in distilled water. The inhibitor concentration used was $10^{-4}$ mol $dm^{-3}$. All inhibitors were obtained by dissolving measured amounts of high-purity solid substances in distilled water. Shiff bases were not soluble in distilled water, so their solutions were prepared in 96 % ethanol.

In the experiment, $KMnO_4$ was used as an inorganic inhibitor, while Shiff base MK3, (2*E*)-*N*'-[(1*E*)-1-(2-hydroxyphenyl)ethylidene]-2-[1-(2-hydroxyphenyl)ethylidene]hydrazine-1-thiocarbohydrazide and 1-butanol were used as organic inhibitors. All used chemicals were acquired from Sigma Aldrich.

The obtained steels were initially subjected to electrochemical methods of testing (potentiodynamic polarization and linear polarization) in solutions without the presence of inhibitors. Subsequently, testing was performed in the presence of the selected inhibitors. In order to ensure the reliability and reproducibility of our results, all experiments were conducted in triplicate. This approach allowed us to systematically verify the consistency of our findings across multiple trials. The data presented in this study are the average values derived from these replicates, accompanied by standard deviations to reflect the variability observed. Such

statistical treatment provides a robust basis for evaluating the experimental outcomes and supports the reliability of the conclusions drawn from this research.

## METHODS

### *Electrochemical methods*

Electrochemical measurements were conducted using a stationary working electrode made from steel samples in a three-electrode thermally controlled electrochemical cell. The exposed surface area of the working electrode was 1 $cm^2$, so the current values directly represented the corrosion current density. Two graphite electrodes were used as counter electrodes, positioned opposite each other and opposite the working electrode to create a symmetrical electric field. A saturated calomel electrode (SCE) was used as the reference electrode and was in contact with the working electrode through a Luggin capillary. Before each measurement, the steel electrodes were cleaned with P600, P1500, P3000 grit sandpaper and further mechanically polished with alumina pastes of 1, 0.3 and 0.05 μm, successively. Data were acquired using a Princeton Applied Research potentiostat/galvanostat, model 273.

The steel electrode was immersed in the solution, along with the counter and reference electrodes and linear polarization and potentiodynamic polarization measurements were performed. Linear polarization was conducted on the samples of the tested steels, namely polarization ±20 mV relative to the open circuit potential, with a set potential change rate of 0.1 mV $s^{-1}$, in the specified solutions and using selected inhibitors. Potentiodynamic polarization was performed by continuously changing the potential of the working electrode (1 mV $s^{-1}$) in both the anodic and cathodic direction. At such polarization values, a region of logarithmic dependence of the net current on the potential of the working electrode (sample) is reached, allowing for the construction of correct Tafel slopes in the log($j$)–$E$ coordinate system. The tests were conducted at room temperature, without the introduction of nitrogen, hydrogen or oxygen into the solutions, ensuring that the obtained results corresponded to real systems. The anodic and cathodic polarization curves were obtained for each specimen and the corrosion potentials and corrosion current densities were determined by the Tafel extrapolation and linear polarization methods.

OCP measurements were performed in the aforementioned solutions for 600 s with the data collecting frequency of 2 $s^{-1}$, or until the potential difference (d$E$/d$t$) in the last 5 measurements was smaller than 1 mV $h^{-1}$, whichever comes first.

## RESULTS AND DISCUSSION

### *Linear polarization*

The electrochemical testing of AISI 314 and AISI 304 steels in a 0.1 M $HNO_3$ solution employing both linear and potentiodynamic polarization methods explored the effectiveness of various inhibitors: $KMnO_4$, MK3 and 1-butanol. The measurements included corrosion potential ($E_{corr}$), corrosion current density ($j_{corr}$) and polarization resistance ($R_p$), presented in curves for both methods. For all tested materials, the linear polarization procedure, *i.e.*, polarization ±20 mV with respect to the corrosion potential ($E_{corr}$), with a set potential change rate of 0.1 mV $s^{-1}$, was carried out. The results of the corrosion tests for both AISI 314 and AISI 304 steels in 0.1 M $HNO_3$ solution are presented in Fig. 1.

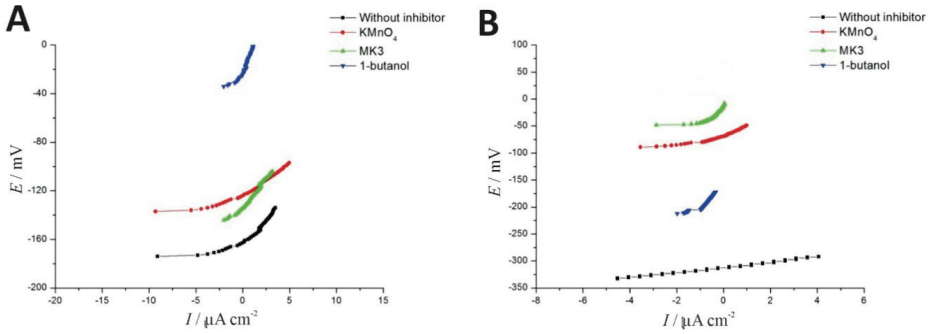


Fig. 1. Potentiodynamic polarization curves for: a) AISI 314 and b) AISI 304 stainless steels in a 0.1 M $HNO_3$ solution.

The results presented in the research show the corrosion potential ($E(j = 0)$), polarization resistance ($R_p$) and the corrosion current density ($j_{corr}$) obtained through linear polarization testing in a 0.1 M $HNO_3$ solution, both with and without the addition of various corrosion inhibitors. The parameters were calculated using Stern–Geary equation. The Stern–Geary equation is given by:

$$I_{corr} = \frac{B}{R_p} \tag{1}$$

where: $I_{corr}$ is the corrosion current density (A $m^{-2}$), $R_p$ is the polarization resistance (Ω), $B$ is the Stern–Geary constant, which depends on the electrochemical kinetics of the corroding metal and is typically calculated from:

$$B = \frac{2.303RT}{nF}\left(\frac{b_a b_c}{b_a + b_c}\right) \tag{2}$$

where $R$ is the universal gas constant (8.314 J $mol^{-1}\cdot K^{-1}$), $T$ is the temperature (K), $n$ is the number of electrons transferred in the corrosion reaction, $F$ is the Faraday constant (96485 C $mol^{-1}$), $b_a$ and $b_c$ re the Tafel slopes for the anodic and cathodic reactions, respectively.

The Stern–Geary constant, $B$, typically ranges between 0.026 and 0.12 V depending on the system and it can also be empirically determined. In our case, it is 0.0217. The parameters offer insights into the anti-corrosive properties conferred by the inhibitors. For AISI 314 without any inhibitor, the corrosion potential was measured at –159 mV, with a polarization resistance of 3.20 kΩ and a corrosion current density of 6.79 μA $cm^{-2}$. These baselines suggest a moderate level of inherent corrosion resistance. The introduction of $KMnO_4$ as an inhibitor improved the corrosion potential to –124 mV, increased the polarization resistance to 5.08 kΩ and reduced the corrosion current density to 4.27 μA $cm^{-2}$, indicating a beneficial effect of this inhibitor. The inhibitor MK3 further enhanced these metrics, showing a corrosion potential of –132 mV, an $R_p$ of 7.78 kΩ and $j_{corr}$ of

2.79 μA cm$^{-2}$. The most substantial improvement was observed with 1-butanol, which altered the corrosion potential dramatically to –5 mV, significantly increased $R_p$ to 21.8 kΩ and lowered $j_{corr}$ to 1.00 μA cm$^{-2}$, underscoring its superior efficacy.

Similarly, AISI 304 steel displayed a baseline corrosion potential of –324 mV, $R_p$ of 6.12 kΩ and $j_{corr}$ of 3.55 μA cm$^{-2}$ without inhibitors. Upon the application of $KMnO_4$, the corrosion potential improved markedly to –67 mV, with $R_p$ increasing to 16.5 kΩ and $j_{corr}$ decreasing to 1.32 μA cm$^{-2}$. The inhibitor MK3 produced even more pronounced effects, optimizing the corrosion potential to –50 mV, elevating $R_p$ to 48.1 kΩ and minimizing $j_{corr}$ to 0.45 μA cm$^{-2}$. 1-Butanol again proved to be the most effective, enhancing the corrosion potential to –155 mV, boosting $R_p$ to 51.6 kΩ and reducing $j_{corr}$ to 0.42 μA cm$^{-2}$. The inhibitors did not only increase the polarization resistance but also shifted the corrosion potential towards less negative values and markedly decreased the corrosion current density. Among the tested inhibitors, 1-butanol emerged as the most effective, demonstrating exceptional enhancement of corrosion resistance parameters across both types of stainless steel. This suggests that careful selection of inhibitors is crucial for the applications where these steels may encounter corrosive environments, particularly in acidic conditions like those simulated with $HNO_3$.

Fig. 1 shows the polarization curves recorded within a low polarization region and corrosion potential and the corrosion current density are determined from these plots. It provides insights into each inhibitor's capacity to mitigate corrosion. For AISI 314, the control condition exhibits a corrosion potential of –159 mV and a current density indicative of significant corrosion activity. The addition of $KMnO_4$ improves the corrosion potential to –124 mV and reduces the current density, suggesting an enhancement in corrosion resistance. MK3 offers further improvement, achieving a more positive potential of –132 mV and a lower current density. The most profound impact is observed with 1-butanol, which shifts the corrosion potential significantly to –25 mV and minimizes the current density, highlighting its superior effectiveness in enhancing corrosion resistance. In the case of AISI 304, the absence of inhibitors results in a highly negative corrosion potential of –324 mV and a moderate current density. The application of $KMnO_4$ improve these parameters to –67 mV, indicating effective corrosion protection. MK3 further enhances these effects, with a potential of –50 mV and a reduced current density. However, 1-butanol demonstrates the greatest efficacy, substantially increasing the potential to –155 mV and achieving the lowest current density among the tested conditions, signifying exceptional corrosion protection. It can be stated that all tested inhibitors significantly improve the corrosion resistance of both AISI 314 and AISI 304 steels. The effectiveness of 1-butanol, in particular, stands out, markedly shifting the corrosion potential towards less negative values and drastically reducing the corrosion current density. The relation

between the graphical and tabular data for both AISI 314 and AISI 304 stainless steels underlines the effectiveness of the corrosion inhibitors tested. Fig. 1 representations align well with the quantitative data, illustrating not only the efficacy of each inhibitor but also highlighting the comparative performance between the two steel types. The results from Fig. 1 underline the substantial improvements in corrosion resistance brought about by the inhibitors, with 1-butanol standing out as the most effective in enhancing the material's durability against corrosive environments. This implies a strong passivation effect, likely due to the formation of a protective barrier on the steel surface, which is crucial for applications where these materials are exposed to corrosive environments. The results underscore the importance of selecting appropriate corrosion inhibitors to enhance the longevity and durability of stainless steels in acidic conditions.

*OCP measurements*

Fig. 2 shows the open circuit potential (OCP) traces over time, illustrating the stabilization effect of corrosion inhibitors $KMnO_4$, MK3 and 1-butanol compared to uninhibited conditions in a 0.1 M $HNO_3$ solution.

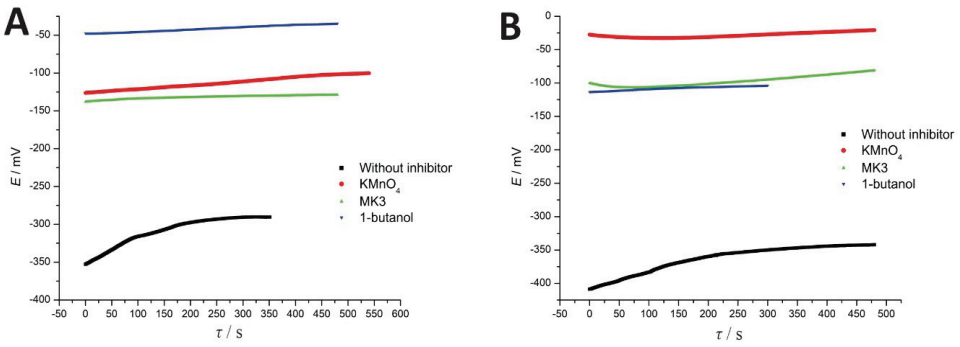


Fig. 2. Open circuit potential (OCP) traces for: a) AISI 314 and b) AISI 304 stainless steels in a 0.1 M $HNO_3$ solution.

The open circuit potential (OCP) traces for AISI 314 and AISI 304 stainless steels in a 0.1 M $HNO_3$ solution are depicted over a 500 s interval. These traces were recorded to evaluate the stability of the electrochemical systems under various conditions, including the application of three different corrosion inhibitors: $KMnO_4$, MK3 and 1-butanol, compared to the uninhibited systems.

For AISI 314, the OCP trace without any inhibitor exhibits a notable downward trend, suggesting a continuous increase in corrosion activity over time. This observation indicates an unstable electrochemical system where the steel surface is actively corroding. Conversely, the introduction of corrosion inhibitors significantly alters this behavior. $KMnO_4$ and MK3 both stabilize the potential after initial fluctuations, with $KMnO_4$ maintaining a relatively constant potential

around –150 mV and MK3 around –100 mV, indicating effective surface passivation and reduced corrosion rates. Notably, 1-butanol shows the most effective inhibition, with the OCP trace remaining stable and closest to zero potential, suggesting minimal corrosion activity and enhanced system stability. Similarly, the OCP traces for AISI 304 reflect comparable trends. The uninhibited condition again shows a progressive decrease in potential, demonstrating the current corrosion. The application of $KMnO_4$ results in a stabilized potential, though it does not achieve the level of stability observed with MK3 or 1-butanol. MK3 provides a stable potential around –100 mV, similar to its effect on AISI 314. In contrast, 1-butanol exhibits superior performance with the most stable and least negative potential among the conditions tested, indicating the robust corrosion protection and the most stable electrochemical system among the configurations tested.

These observations underline the effectiveness of the corrosion inhibitors in stabilizing the electrochemical characteristics of AISI 314 and AISI 304 stainless steels in corrosive environments. The results demonstrate that while all inhibitors improve stability compared to the uninhibited systems, 1-butanol consistently shows the highest efficacy in maintaining near-neutral potentials, thereby providing the best protection against corrosion. This behavior suggests that 1-butanol may form a more comprehensive and protective barrier on the metal surface, which is crucial for applications where these materials are exposed to corrosive conditions.

*Potentiodynamic polarization*

The corrosion parameters are obtained from the polarization curves for AISI 314 and AISI 304 steels, which are presented in Fig. 3.

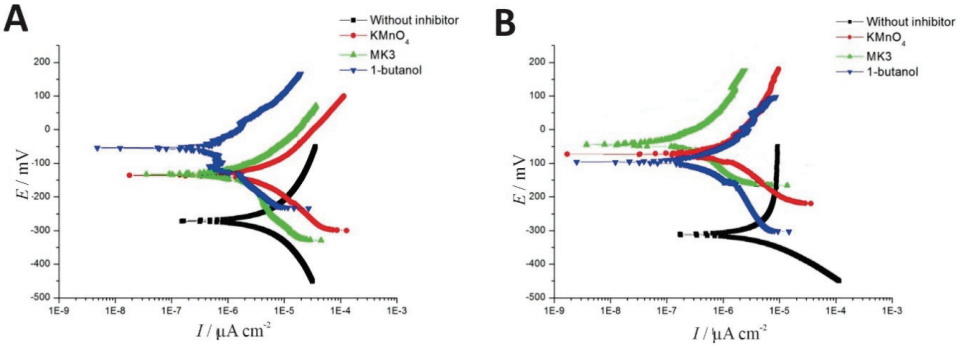


Fig. 3. Detailed potentiodynamic polarization responses of: a) AISI 314 and b) AISI 304 stainless steels.

Detailed insights from potentiodynamic polarization tests conducted on AISI 314 and AISI 304 stainless steels in a 0.1 M $HNO_3$ solution, assessing the effectiveness of various corrosion inhibitors including $KMnO_4$, MK3 and 1-butanol are shown in the forthcoming text. The parameters evaluated in this study include

open circuit potential (OCP), corrosion potential ($E(j = 0)$), anodic Tafel slope ($b_a$), cathodic Tafel slope ($b_c$) and corrosion current density ($j_{corr}$).

For AISI 314, the results indicate a substantial improvement in corrosion resistance upon the application of inhibitors. Without any inhibitor, the steel exhibits an OCP of –290 mV and a corrosion potential of –272 mV, with relatively high Tafel slopes (878 mV dec$^{-1}$ for $b_a$ and –724 mV dec$^{-1}$ for $b_c$) and a corrosion current density of 27.85 μA cm$^{-2}$, suggesting a higher corrosion rate. The introduction of $KMnO_4$ shifts the OCP to –100 mV and the corrosion potential to –136 mV, significantly lowering the Tafel slopes to 183 mV dec$^{-1}$ for $b_a$ and –181 mV dec$^{-1}$ for $b_c$ and reducing the corrosion current density to 6.13 μA cm$^{-2}$. This denotes a significant improvement in corrosion resistance. MK3 further enhances these effects, evidenced by an even lower corrosion current density of 3.49 μA cm$^{-2}$, despite the OCP and $E(j = 0)$ being relatively close (–129 and –133 mV, respectively), with Tafel slopes of 190 mV dec$^{-1}$ for $b_a$ and –328 mV dec$^{-1}$ for $b_c$. The application of 1-butanol shows the most significant enhancement, with the lowest corrosion current density of 0.58 μA cm$^{-2}$ and Tafel slopes of 136 mV dec$^{-1}$ and –174 mV dec$^{-1}$, suggesting highly effective corrosion inhibition.

Similarly, for AISI 304, the use of inhibitors demonstrates a profound effect on corrosion characteristics. The uninhibited condition shows an OCP of –342 mV, a corrosion potential of –324 mV and a higher corrosion rate indicated by a $j_{corr}$ of 8.88 μA cm$^{-2}$. $KMnO_4$ substantially improves the parameters with an OCP of –20 mV and a corrosion potential of –73 mV, along with a reduced $j_{corr}$ of 1.68 μA cm$^{-2}$. MK3, displaying the best results among the inhibitors tested for AISI 304, significantly lowers the corrosion current density to 0.39 μA cm$^{-2}$, with an OCP of –81 mV and a remarkably improved corrosion potential of –27 mV. However, despite 1-butanol reducing the $j_{corr}$ to 1.16 μA cm$^{-2}$, it results in a slightly more negative corrosion potential (–96 mV) compared to $KMnO_4$ and MK3, with an unexpectedly higher OCP of –103 mV. Tafel slopes for different inhibitors for AISI304 are given in Table II.

TABLE II. Tafel slopes for different corrosion inhibitors in 0.1 M $HNO_3$ solution for AISI304

| Inhibitor | $b_a$ / mV dec$^{-1}$ | $b_c$ / mV dec$^{-1}$ |
|---|---|---|
| No inhibitor | 412 | –186 |
| $KMnO_4$ | 321 | –150 |
| MK3 | 263 | –125 |
| 1-Butanol | 243 | –293 |

The collective results from both AISI 314 and AISI 304 stainless steels confirm that the tested inhibitors significantly mitigate corrosion processes in a nitric acid environment. The differences in Tafel slopes and corrosion potentials across different inhibitors reflect the variance in their mechanisms and efficiencies at protecting the steel substrates. Particularly notable is the effectiveness of MK3 and

1-butanol, which does not only lower $j_{corr}$ but also substantially adjust the electrochemical parameters towards more favorable values, thus enhancing the corrosion resistance of both steel types under these challenging conditions.

The presented data emphasize two crucial electrochemical parameters, OCP and $E(j = 0)$. Understanding the differences between these parameters can shed light on the inhibitor's impact on the electrochemical behavior of these steels. OCP is the potential of the electrochemical cell when no external current is applied and it reflects the natural thermodynamic equilibrium state of the electrode in its environment. This measurement is passive and indicates the inherent stability of the metal surface in the solution. $E(j = 0)$, on the other hand, is derived from active polarization tests. It is typically obtained through Tafel extrapolation, where the intersection of the anodic and cathodic Tafel slopes is computed. This value represents the potential at which the net anodic and cathodic currents balance each other out, indicating the potential at which the corrosion rate (current density, $j_{corr}$) is minimal.

For the uninhibited condition for AISI 314, the OCP is at –290 mV, whereas $E(j = 0)$ is slightly more positive at –272 mV. The difference suggests that upon applying an external potential, the electrochemical reactions tend to stabilize at a slightly more noble potential. With inhibitors like $KMnO_4$, MK3 and 1-butanol, the OCP and $E(j = 0)$ values become closer. For example, with 1-butanol, OCP is –34 mV and $E(j = 0)$ is –56 mV, indicating a more effective stabilization of the surface, likely due to the formation of a protective layer that reduces active sites for corrosion. AISI 304 Steel: without inhibitors, the OCP is –342 mV and $E(j = 0)$ is –324 mV. This again indicates a stabilization at a more noble potential when polarization begins. The use of inhibitors reduces the gap between OCP and $E(j = 0)$. Particularly, with MK3, OCP is –81 mV and $E(j = 0)$ is –27 mV. This significant shift towards less negative values indicates a strong inhibition effect, possibly due to the formation of a dense protective film. The difference between OCP and $E(j = 0)$ across different inhibitors and conditions suggests varying degrees of influence by the inhibitors on the electrochemical properties of the steel. A smaller difference typically indicates a more effective inhibition, as the steel's surface characteristics under passive and active conditions become more similar, reflecting a stable and protective inhibitor film. These observations align with corrosion science principles suggesting that effective inhibitors either passivize the metal surface or alter the kinetics of anodic and cathodic reactions to reduce overall corrosion rates. The closer alignment of OCP and $E(j = 0)$ under inhibitor-treated conditions confirms the establishment of a more homogenous and less reactive surface state.

These graphs in Fig. 3 are essential for understanding the electrochemical behavior of AISI 304 and AISI 314 stainless steels under corrosive conditions and evaluating the efficacy of the inhibitors. For AISI 314, the polarization curve

without an inhibitor shows a significantly negative corrosion potential and high current density, indicating a high rate of corrosion susceptibility. The introduction of $KMnO_4$ results in a noticeable shift towards a less negative potential and reduced current density, though it is less effective compared to the other inhibitors. MK3 demonstrates a further improvement, significantly reducing the current density and mildly improving the potential. The most pronounced effect is observed with 1-butanol, which not only shifts the potential towards less negative values but also drastically lowers the current density, suggesting a highly effective inhibition of corrosion. Similarly, the AISI 304 steel exhibits even more dramatic shifts in electrochemical behavior with the application of inhibitors. Without any inhibitor, the steel displays the most negative potential and relatively high current density, indicative of considerable corrosion activity. With $KMnO_4$, the potential is moderately less negative and the current density is notably decreased. MK3 shows a substantial decrease in current density and shifts the potential to less negative values, marking it as highly effective. However, 1-butanol stands out by further reducing the current density significantly, although its impact on shifting the potential is not as pronounced as with MK3.

These observations suggest that the inhibitors tested significantly enhance the corrosion resistance of both AISI 314 and AISI 304 steels in nitric acid environments. The shift in potential towards less negative values and the reduction in $j_{corr}$ across the inhibitors indicate their effectiveness, with 1-butanol and MK3 showing particularly strong performance in reducing the electrochemical signs of corrosion. This implies that these inhibitors likely form protective barriers or passivize the surface, effectively reducing the electrochemical reactions that lead to corrosion. The results highlight the importance of selecting appropriate corrosion inhibitors to extend the service life of stainless steels in corrosive environments.

To address the discrepancies between the $E(j = 0)$ values reported in the manuscript for the linear and potentiodynamic polarization tests, it is important to consider the intrinsic differences in the methodologies and how they interact with the electrochemical properties of AISI 314 and AISI 304 steels in a 0.1 M $HNO_3$ solution. The variations in these values are not indicative of experimental errors or instability in the system, but rather reflect the fundamental differences between the methods and their impacts on the electrode surface. Linear polarization provides a more conservative estimate of the corrosion potential because it involves small perturbations around the open circuit potential. This method is less likely to disrupt the native oxide layer or any inhibitor-induced film on the metal surface, thus providing a value of $E(j = 0)$ that reflects a minimally disturbed state. In linear polarization, $E(j = 0)$ is closer to the real corrosion potential under near-static conditions and thus is likely a better representation of the material's behavior in less aggressive environments. The potentiodynamic polarization involves a dynamic sweep of the potential that can extend well beyond the passive

range into the active corrosion or transpassive regions. This sweep can modify surface conditions, such as through the stripping away of passive layers or the enhanced formation of corrosion products, leading to different apparent $E(j = 0)$ values. In potentiodynamic tests, $E(j = 0)$ is extrapolated from the Tafel slopes, where the intersections represent a theoretical balance between anodic and cathodic currents. This method inherently assumes uniformity in reaction kinetics across the swept range, which might not hold in environments where inhibitor films are forming or being compromised. The findings from both tests are valid within the scope of their respective methodologies. The variance in $E(j = 0)$ values in the tests highlights the importance of selecting the appropriate testing protocol based on the specific service conditions expected for the metal. Furthermore, these results display the complex nature of corrosion processes and the need for multiple approaches to accurately gauge the effectiveness of corrosion inhibitors.

*Protection efficiency*

The protection efficiency, based on the data, is calculated using the Eq. (3):

$$\eta = \frac{j_{\text{corr}} - \left(j_{\text{corr}}\right)_{\text{inh}}}{j_{\text{corr}}} \tag{3}$$

where $j_{\text{corr}}$ is the corrosion current density in the uninhibited solution and $(j_{\text{corr}})_{\text{inh}}$ is in the inhibited solution.

The corrosion inhibition efficiencies derived from linear polarization tests (LP) and potentiodynamic measurements (PD) are summarized in forthcoming paragraphs.

Fig. 4 displays a comparative analysis of corrosion inhibition efficiency for AISI 314 and AISI 304 stainless steels, employing three different inhibitors ($KMnO_4$, MK3, 1-butanol) and utilizing two distinct electrochemical testing methods: linear polarization and potentiodynamic polarization. The bar chart measures the efficiency ($\eta$) in percentage terms, indicating how effectively each inhibitor reduces the corrosion rate compared to an uninhibited system.

For AISI 314, the corrosion rates without any inhibitors serve as a baseline, showing a $j_{\text{corr}}$ of 6.79 μA cm$^{-2}$ for LP and 27.8 μA cm$^{-2}$ for PD. $KMnO_4$ decreases the corrosion rate to 4.27 μA cm$^{-2}$ in LP, achieving 37.1 % efficiency and to 6.13 μA cm$^{-2}$ in PD with a significantly higher efficiency of 77.9 %. This suggests that $KMnO_4$ inhibition mechanism might be more dynamically effective, as captured by the PD method. MK3 provides an even stronger inhibition, reducing the corrosion rate to 2.79 μA cm$^{-2}$ in LP (58.9 % efficiency) and to 3.488 μA cm$^{-2}$ in PD (87.5% efficiency). 1-Butanol exhibits the highest protection, reducing the corrosion rate dramatically to 1.00 μA cm$^{-2}$ in LP (85.3 % efficiency) and to an

impressive 0.58 μA cm$^{-2}$ in PD (97.9 % efficiency), demonstrating its superior efficacy in both static and dynamic conditions.

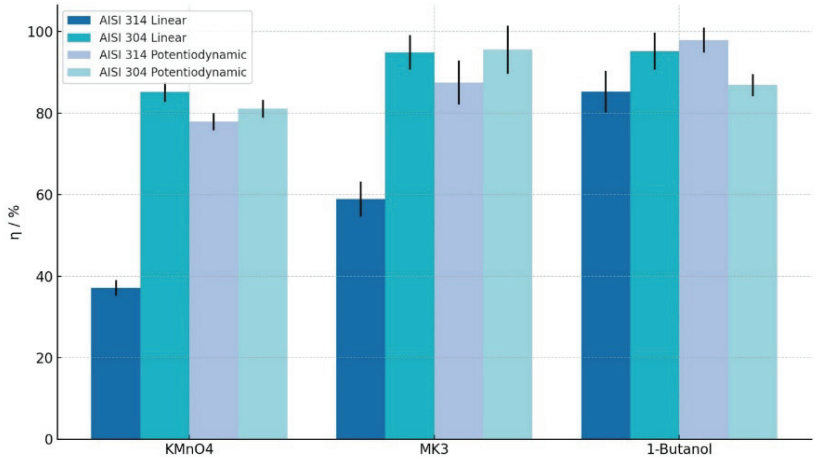


Fig. 4. Overall corrosion inhibition efficiency performance comparison.

Turning to AISI 304, the initial corrosion rates are lower, with 3.55 μA cm$^{-2}$ in LP and 8.88 μA cm$^{-2}$ in PD. With $KMnO_4$, the corrosion rate is reduced to 1.32 μA cm$^{-2}$ in LP, achieving an 85.2 % efficiency and slightly less effectively in PD to 1.68 μA cm$^{-2}$ (81.1 % efficiency). MK3 again performs excellently, lowering the corrosion rate to 0.45 μA cm$^{-2}$ in LP (94.9 % efficiency) and to 0.39 μA cm$^{-2}$ in PD (95.6 % efficiency), showing minimal variation between methods. 1-Butanol also shows strong performance, reducing corrosion to 0.42 μA cm$^{-2}$ in LP (95.2 % efficiency) and to 1.16 μA cm$^{-2}$ in PD (86.9 % efficiency), which suggests a slight decrease in effectiveness under dynamic testing conditions for this inhibitor on AISI 304 compared to AISI 314.

These observations highlight that the choice of the corrosion inhibitor and the method of testing are both crucial in evaluating their effectiveness. 1-Butanol and MK3 consistently show high efficiencies across both types of steel and methods, suggesting their robust performance in various conditions. $KMnO_4$, while generally effective, shows some variability in performance, especially under different testing dynamics. The results emphasize the importance of selecting an inhibitor based on specific environmental conditions and the type of stainless steel, ensuring optimal protection against corrosion. This comprehensive analysis also underscores the value of using multiple testing methods to accurately gauge inhibitor performance across different operational scenarios. Interestingly, the potentiodynamic method tends to show slightly higher efficiencies for AISI 314, particularly noticeable with MK3. This might be due to the dynamic nature of this method, which show more about the protective film formation dynamics, or other

interactive effects at the metal-solution interface that are not as apparent in linear polarization tests.

In the linear polarization tests, AISI 314 steel exhibited a notable shift towards less negative corrosion potentials and a reduction in corrosion current with the application of 1-butanol, highlighting its potent protective capabilities. This shift is indicative of a strong adsorptive interaction between the inhibitor and the steel surface, potentially leading to the formation of a dense molecular barrier that impedes corrosive interactions at the metal–solution interface, as detailed in Fig. 1. For AISI 304 steel, the application of $KMnO_4$ and the Schiff base MK3 resulted in significant improvements in corrosion potential, as shown in Fig. 3. The effectiveness of $KMnO_4$ can be attributed to its ability to oxidize the steel surface, thereby forming a protective oxide layer. In contrast, MK3, being a Schiff base, operates through a different mechanism. Schiff bases are known for their ability to form stable complexes with metal ions due to their conjugated system and the presence of nitrogen and sulphur donor atoms. These complexes can effectively passivize the surface, blocking both the anodic and cathodic sites necessary for corrosion reactions.

Potentiodynamic testing further supported these findings, where 1-butanol demonstrated a substantial reduction in both corrosion rate and potential deviation for both steel types, indicative of its strong protective properties. The corrosion inhibition efficiencies show the varied effectiveness of these inhibitors, highlighting how the structural features and reactive sites of inhibitors like MK3 contribute to their mode of action. $KMnO_4$ typically enhances the formation of an oxide layer, while MK3, through its Schiff base structure, forms chelates with metal ions at the surface, providing a robust shield against corrosion.

## CONCLUSION

The comprehensive analysis of the electrochemical testing conducted on AISI 314 and AISI 304 steels using linear and potentiodynamic polarization methods highlights the significant impact of corrosion inhibitors $KMnO_4$, MK3 and 1-butanol in a 0.1 M $HNO_3$ solution. The investigation employed detailed measurements including corrosion potential ($E_{corr}$), corrosion current density ($j_{corr}$) and polarization resistance ($R_p$), which were crucial for assessing the inhibitors' effectiveness. Based on all the conducted research in this experimental work, the following conclusions can be drawn:

- The linear polarization results for both steel types indicate that without inhibitors, the steels are naturally prone to corrosion in nitric acid environments, as evidenced by their relatively high corrosion current densities and negative corrosion potentials. However, the addition of inhibitors has markedly improved these parameters. $KMnO_4$, while offering moderate improvement, is overshadowed by the more significant enhancements brought about by MK3 and

especially 1-butanol, which did not only reduce the corrosion current density but also dramatically shifted the corrosion potential towards less negative values. For AISI 314, 1-butanol was particularly effective, enhancing the corrosion potential by over 130 mV compared to the uninhibited condition and significantly boosting the polarization resistance.

- Similarly, AISI 304 showed a notable response to the inhibitors. The application of $KMnO_4$ and MK3 resulted in improvement of corrosion potentials and lower corrosion current densities, however, 1-butanol stood out, achieving the most substantial improvement in all parameters measured. This suggests that 1-butanol may be forming a more effective protective barrier on the steel surface, likely through strong adsorptive interactions and possibly the formation of a dense molecular barrier that impedes corrosive reactions.
- The potentiodynamic polarization results further reinforce these findings, showing that the dynamic nature of this method captures the inhibitors' protective mechanisms effectively. The results from both AISI 314 and AISI 304 steels confirm that dynamic conditions may better represent the inhibitors' performance, particularly in how they interact with the steel surfaces by varying electrochemical conditions.
- Schiff base MK3 exhibits very good results and the reason is its chemical structure (C=N bond) and the ability to form a protective monolayer on the steel surface. Changes in the functionality of the group on the terminal aromatic ring led to the changes in the efficiency of inhibition of the corresponding Schiff base compounds. Since synthesized Schiff bases have not been previously used as inhibitors, this experimental work demonstrates their potential application, leaving room for further research and testing on samples of different materials and chemical compositions. Moreover, when analyzing all the obtained results for the efficiency of the inhibitors used in both testing methods (linear and potentiodynamic polarization), 1-butanol has proven to be the most effective inhibitor in the 0.1 M $HNO_3$ solution.
- The consistency between the graphical data and the presented results underscores the efficacy of the testing methods and the reliability of the results. The notable correspondence between the decrease in corrosion rates and the improvement in corrosion potentials across both testing formats highlights the effectiveness of MK3 and 1-butanol in significantly enhancing the corrosion resistance of the steels. The study clearly demonstrates that the selection of an appropriate corrosion inhibitor is crucial for enhancing the durability and longevity of stainless steels in acidic environments. The superior performance of 1-Butanol across both types of stainless steel and both electrochemical testing methods suggests its potential utility in industrial applications where corrosion resistance is paramount. This research does not only provide the valuable insights into the comparative performance of corrosion inhibitors but also highlights the importance of

using multiple testing methods to capture the full range of an inhibitor's protective capabilities in different environmental conditions.

*Acknowledgement.* This work was supported by the Ministry of Science, Technological Development and Innovation of the Republic of Serbia (grant No. 451-03-66/2024-03/200026).

И З В О Д

## УТИЦАЈ ОРГАНСКИХ/НЕОРГАНСКИХ ИНХИБИТОРА НА КИНЕТИКУ КОРОЗИЈЕ ЧЕЛИКА AISI 304 (1.4301) И AISI 314 (1.4841) У РАСТВОРУ АЗОТНЕ КИСЕЛИНЕ

ЈЕЛЕНА ШЋЕПАНОВИЋ[1], БОЈАНА ЗИНДОВИЋ[2], ДРАГАН РАДОЊИЋ[1], МАРИЈАНА Р. ПАНТОВИЋ ПАВЛОВИЋ[3,4] и МИРОСЛАВ М. ПАВЛОВИЋ[3,4]

*[1]Металуршко–технолошки факултет, Универзитет у Црној Гори, Цетињски пут, 81000 Подгорица, Црна Гора, [2]Институт „СИГУРНОСТ“ доо, Подгорица, Црна Гора, [3]Институт за хемију, технологију и металургију, Институт од националног значаја за Републику Србију, Центар за електрохемију, Универзитет у Београду, Његошева 12, 11000 Београд и [4]Центар изузетних вредности за хемију и инжењерство заштите животне средине–ИХТМ, Универзитет у Београду, Његошева 12, 11000 Београд*

Ова студија процењује ефикасност инхибитора $KMnO_4$, МК3 и 1-бутанола на корозију нерђајућих челика AISI 314 и AISI 304, коришћењем линеарне и потенциодинамичке поларизације у 0,1 M $HNO_3$. Корозиони потенцијал ($E_{corr}$), густина струје корозије ($j_{corr}$) и поларизациони отпор ($R_p$) су коришћени за процену ефикасност инхибитора. Инхибитори су значајно побољшали електрохемијске параметре, што указује на јака антикорозивна својства. 1-бутанол је имао најизраженији ефекат, повећавајући корозиони потенцијал и драстично смањујући густину струје корозије, показујући врхунску заштиту. Резултати су показали да без инхибитора, оба челика показују већу брзину корозије и негативније корозионе потенцијале, што одражава њихову подложност корозији. Увођење инхибитора је значајно побољшало ове параметре, посебно 1-бутанола, који је значајно повећао отпорност на поларизацију и померио потенцијал корозије ка мање негативним вредностима. Потенциодинамички резултати су истакли динамичку ефикасност инхибитора, појачавајући њихову улогу у ублажавању корозије у различитим условима. Студија наглашава важност одабира одговарајућих инхибитора за побољшање издржљивости и дуговечности нерђајућег челика у киселим срединама, при чему 1-бутанол показује потенцијал за индустријску примену која захтева високу отпорност на корозију. Ово захтева свеобухватно тестирање за прецизно мерење способности инхибитора у различитим условима.

(Примљено 14. маја, ревидирано 29. маја, прихваћено 23. августа 2024)

REFERENCES

1. W. J. Oh, W. J. Lee, M. S. Kim, J. B. Jeon, D. S. Shim, *Opt. Laser Technol.* **117** (2019) 6 (https://doi.org/10.1016/j.optlastec.2019.04.012)
2. L. A. Arteaga-Hernandez, C. A. Cuao-Moreu, C. E. Gonzalez-Rivera, M. Alvarez-Vera, J. A. Ortega-Saenz, M. A. L. Hernandez-Rodriguez, *Wear* **477** (2021) 203825 (https://doi.org/10.1016/j.wear.2021.203825)

3. K. H. Lo, C. H. Shek, J. K. L. Lai, *Mater. Sci. Eng. R Rep.* **65** (2009) 39 (https://doi.org/10.1016/j.mser.2009.03.001)
4. M. Talha, C. K. Behera, O. P. Sinha, *Mater. Sci. Eng., C* **33** (2013) 3563 (https://doi.org/10.1016/j.msec.2013.06.002)
5. M. H. Ghoncheh, A. Shahriari, N. Birbilis, M. Mohammadi, *Crit. Rev. Solid State Mater. Sci.* **49** (2023) 607 (https://doi.org/10.1080/10408436.2023.2255616)
6. W. Xu, B. Zhang, O. Addison, X. Wang, B. Hou, F. Yu, *Corros. Commun.* **11** (2023) 23 (https://doi.org/10.1016/j.corcom.2023.01.002)
7. K. Morshed-Behbahani, N. Zakerin, *J. Mater. Res. Technol.* **19** (2022) 1120 (https://doi.org/10.1016/j.jmrt.2022.05.094)
8. B. Bobić, B. Jegdić, *Mater. Prot.* **46** (2005) 23–30
9. A. Poursaee, in *Corrosion of Steel in Concrete Structures*, C.S. Poursaee, Ed., Woodhead Publishing, Oxford, 2016, pp. 241–248 (https://doi.org/10.1016/B978-1-78242-381-2.00012-2)
10. Q. Chunxiang, W. Jianyun, W. Ruixing, C. Liang, *Mater. Sci. Eng., C* **29** (2009) 1273 (https://doi.org/10.1016/j.msec.2008.10.025)
11. K. A. Habib, M. S. Damra, J. J. Saura, I. Cervera, J. Bellés, *Int. J. Corros.* **2011** (2011) 824676 (https://doi.org/10.1155/2011/824676)
12. L. Reclaru, L. C. Ardelean, *Mater.* **13** (2020) 13184187 (https://doi.org/10.3390/ma13184187)
13. H. H. Uhlig, R. W. Revie, *Corrosion and corrosion control*, 3rd ed., John Wiley and Sons, Inc., New York, 1985
14. A. A. Al-Amiery, W. N. Isahak, W. K. Al-Azzawi, *Lubricants* **11** (2023) 11040174 (https://doi.org/10.3390/lubricants11040174)
15. M. Corrales Luna, T. Le Manh, R. Cabrera Sierra, J. V Medina Flores, L. Lartundo Rojas, E. M. Arce Estrada, *J. Mol. Liq.* **289** (2019) 111106 (https://doi.org/10.1016/j.molliq.2019.111106)
16. R. Solmaz, A. Salcı, Y. A. Dursun, G. Kardaş, *Colloids Surfaces, A* **674** (2023) 131908 (https://doi.org/10.1016/j.colsurfa.2023.131908)
17. L. Gardner, *Prog. Struct. Eng. Mater.* **7** (2005) 45 (https://doi.org/10.1002/pse.190)
18. *Avesta Sheffield corrosion handbook for stainless steels*, Avesta Sheffield AB and AB Sandvik Steel, Stockholm, 1994, p.p.1–88
19. X. Zhang, Z. Chen, H. Luo, T. Zhou, Y. Zhao, Z. Ling, *Trans. Nonferrous Met. Soc. China* **32** (2022) 377 (https://doi.org/10.1016/S1003-6326(22)65802-3)
20. R. Aslam, M. Mobin, S. Zehra, J. Aslam, *J. Mol. Liq.* **364** (2022) 119992 (https://doi.org/10.1016/j.molliq.2022.119992)
21. R. Salim, E. Ech-chihbi, Y. Fernine, M. Koudad, L. Guo, E. Berdimurodov, M. Azam, Z. Rais, M. Taleb, *J. Mol. Liq.* **393** (2024) 123579 (https://doi.org/10.1016/j.molliq.2023.123579)
22. M. Sharma, S. Singh Yadav, P. Sharma, L. Yadav, M. Zainul Abedeen, H. Singh Kushwaha, R. Gupta, *Inorg. Chem. Commun.* **157** (2023) 111330 (https://doi.org/10.1016/j.inoche.2023.111330)
23. M. Talebian, K. Raeissi, M. Atapour, B. M. Fernández-Pérez, A. Betancor-Abreu, I. Llorente, S. Fajardo, Z. Salarvand, S. Meghdadi, M. Amirnasr, R. M. Souto, *Corros. Sci.* **160** (2019) 108130 (https://doi.org/10.1016/j.corsci.2019.108130)

24. M. Crouse, A. E. Miller, M. G. Pujar, K. L. Vasanth, in *Procedings of Corros. 2002*, paper No. NACE-02410
25. K. Bijapur, V. Molahalli, A. Shetty, A. Toghan, P. De Padova, G. Hegde, *Appl. Sci.* **13** (2023) 131810107 (https://doi.org/10.3390/app131810107)
26. J. R. González-Parra, F. Di Turo, *Sustainability* **16** (2024) 16051868 (https://doi.org/10.3390/su16051868)
27. C. N. Njoku, A. I. Ikeuba, C. C. Anorondu, I. C. Shammah, E. Yakubu, B. N. Elendu, C. S. Enechukwu, I. O. Uduma, P. C. Uzor, *Results Chem.* **7** (2024) 101286 (https://doi.org/10.1016/j.rechem.2023.101286)
28. J. Šćepanović, M. R. Pantović Pavlović, D. Vuksanović, G. M. Šekularac, M. M. Pavlović, *J. Serbian Chem. Soc.* **88** (2023) 1025 (https://doi.org/10.2298/JSC230505031S)
29. P. Stanić, N. Vukićević, V. Cvetković, M. Pavlović, S. Dimitrijević, B. Šmit, M. Živković, *J. Serbian Chem. Soc.* **87** (2022) 1409 (https://doi.org/10.2298/JSC220412071S)
30. M. V. Tomić, V. M. Mićić, R. F. Godec, M. G. Pavlović, D. Vaštag, M. G. Ridošić, M. M. Pavlović, *Int. J. Electrochem. Sci.* **11** (2016) 3339 (https://doi.org/10.20964/101282).

Journal of the Serbian Chemical Society
JSCS@tmf.bg.ac.rs • www.shd.org.rs/JSCS
*J. Serb. Chem. Soc.* *89* (9) 1211–1226 (2024)
*JSCS–5782*
*Original scientific paper*
Published 11 September 2024

# Investigation of the adsorption behaviors of thymol blue, crystal violet and rhodamine B on lichen-derived activated carbon

HÜLYA KOYUNCU[1]* and ALİ RIZA KUL[2]

[1]*Bursa Technical University, Faculty of Engineering and Natural Sciences, Chemical Engineering Department, 16310, Bursa, Turkiye and* [2]*Van Yüzüncü Yıl University, Faculty of Science, Chemistry Department, 65080, Van, Turkiye*

(Received 30 May, revised 10 August, accepted 20 November 2023)

*Abstract*: Since thymol blue (TB), crystal violet (CV) and rhodamine B (RB) are frequently used in various industries, they cause environmental pollution owing to the wastewater treatment process. The current study focused on the removal of TB, CV and RB from aqueous media with lichen-derived activated carbon (LDAC) and comparing their adsorption behavior. The maximum Langmuir adsorption capacity for TB, CV and RB was found to be 400, 213 and 345 mg $g^{-1}$, respectively. The removal (%) of TB, CV and RB was found to be 86.38, 79.02 and 82.73 % at the same conditions, respectively. Experimental data were interpreted with some commonly used kinetic and isotherm models. Calculated activation energies, D-R model energies, enthalpy changes and evaluation of FT-IR, XRD and SEM/EDX images taken before and after dye loading showed that the adsorption of TB, CV and RB on the LDAC are physical processes. The pseudo-second-order kinetic model better described the adsorption behavior of TB, CV and RB on the LDAC. The boundary layer thickness value for all the dyes studied increased with increasing initial dye concentration and temperature, and CV also had a larger boundary layer thickness value than that of TB and RB.

*Keywords:* dye; wastewater remediation; kinetic; thermodynamic.

## INTRODUCTION

Today, water pollution has become a very important problem all over the world. One of the main causes of water pollution is industrialization. For example, it is estimated that approximately 25 % of the pollution of the world's clean waters comes from dyeing and finishing processes in the textile industry. Water consumption for dyeing 1 kg of textile products can vary from approximately 25 to 280 L $kg^{-1}$, and process wastewater can reach 120 L $kg^{-1}$. Many process wastewaters include dyes such as thymol blue (TB), crystal violet (CV)

* Corresponding author. E-mail: hulya.koyuncu@btu.edu.tr
https://doi.org/10.2298/JSC23053089K

and rhodamine B (RB), which are widely used in different industries such as textiles, leather, paints, food, plastic, paper, *etc*.[1] The release of these dyes from industrial wastewater into the environment causes a very serious threat to both human and animal life since they are carcinogenic and non-biodegradable, and even very small amounts can be highly toxic.[2] In addition, due to the complex chemical structures and long half-lives of these dyes, their persistence in the environment poses a serious danger to the ecosystem (Table S-I of the Supplementary material to this paper). TB, CV and RB are toxic dyes. These can affect some organs that play an important role in the vital activities of living things and can cause serious problems when exposed, even in very small amounts.[3–6] Due to the harmful effects of TB, CV and RB, studies are continuing on their removal from water and wastewater. For the removal of dyes from wastewater, there are many different methods, such as adsorption, chemical precipitation, oxidation or ozonation, membrane separation, coagulation or flocculation, biological treatment and photocatalytic degradation.[7–18] Most of these methods are expensive, whereas the adsorption method is cheap and has an easy operating procedure. In addition, high efficiency can be obtained. Since commercial activated carbons are expensive, in recent years, researchers have focused on producing activated carbon from sustainable and cheap alternative sources such as agricultural waste, some plants, and fruit peels. Lichen is a symbiotic partnership in which a fungus (mycobiont) and algae as well as cyanobacteria (photobiont) come together to form a single thallus, with more than 20,000 species found almost everywhere in the world. Although lichens are eco-friendly, sustainable, and low-cost resources, as far as we know, there are very few studies in the literature on the production and use of activated carbon from lichen species.[19,20]

In this study, an innovative approach to use activated carbon synthesized from *Pseudevernia furfuracea* lichen, a common lichen species in the world, to clean water contaminated with toxic dyes such as TB, CV and RB is described. Kinetic, equilibrium and thermodynamic studies were carried out to prove the effectiveness of the innovative adsorbent and demonstrate the adsorption behavior of TB, CV and RB dyes on the LDAC. Important parameters of the adsorption processes, such as initial concentration, temperature, and time, were optimized through batch-type experiments. Additionally, the reusability of the adsorbent was also studied.

## EXPERIMENTAL

### *Materials*

TB (CAS 76-61-9, 1081760025), CV (CAS 548-62-9, 1159400025), and RB (CAS 81--88-9, 1075990025) were purchased from Merck. Some specifications of TB, CV and RB were shown in Table S-I. For the stock solutions of dyes, certain amounts of CV and RB were dissolved in bi-distilled water, and certain amounts of TB were dissolved in 95 % ethanol. The required initial solution concentrations of TB (20, 40, 60, 80, 100 and 120 mg $L^{-1}$), CV (15,

30, 45, 60, 75 and 90 mg $L^{-1}$), and RB (20, 40, 60, 80, 100 and 120 mg $L^{-1}$) used for the adsorption experiments were prepared from the stock solution by diluting with bi-distilled water.

The activated carbon (LDAC) was synthesized in accordance with our previous report.[19] Preparation and characterization ((Brauner–Emmett–Teller (BET), X-ray diffraction (XRD), thermogravimetric analysis (TGA), Fourier transform infrared spectrophotometer (FT-IR) and scanning electron microscope (SEM)) details and the results of the point of zero charge ($pH_{PZC}$) of the lichen *Pseudevernia furfuracea* and LDAC (Fig. S-1 of the Supplementary material) were already given in our previous study.[19] In this study, contact angle measurement of the LDAC was performed with Attension/Theta Lite. The static sessile drop method was carried out with water. The LDAC powders were pressed into a plate with a hydraulic press (Manuel MSE LP/M2S10).

*Adsorption experiments*

500 mL of different initial concentrations of TB, CV and RB dye solutions were mixed with 0.5 g of LDAC and shaken on a shaker (Thermal H11960) for 100 min at different temperatures (298, 308 and 323 K). The pH of the solutions was kept constant at 9.5 in all experiments by adding 0.1 M NaOH and 0.1 M HCl solutions. The samples were centrifuged at 5000 rpm after adsorption, and the filtrates were analyzed by a UV–Vis spectrophotometer (PG Instruments Ltd.). The dye concentrations in the solutions taken at certain times (5, 10, 15, 20, 25, 30, 35, 40, 45, 50, 55, 60, 70, 80, 90 and 100 min) were measured at their highest absorbance wavelengths (TB: 594 nm, CV: 590 nm and RB: 554 nm). All the experiments were carried out in duplicate under the same conditions, and the average of the obtained data was used as the result.

*Equations*

The following were used to calculate the removal percentage (%) and adsorption capacity of the dyes:

$$\text{Removal}(\%) = 100\frac{c_0 - c_t}{c_t} \tag{1}$$

$$q_e = \frac{V(c_0 - c_e)}{m} \tag{2}$$

$c_e$, $c_t$ and $c_0$ (mg $L^{-1}$) represented the equilibrium, any time and the initial concentration of dye, respectively; $m$ (g) represents the mass of the LDAC; and $V$ (L) represents the volume of the solution.

In order to explain the adsorption behaviour of the three dyes on the LDAC and to compare them with each other, kinetic and isotherm modelling studies were carried out with the data obtained from experimental studies, and important thermodynamic parameters such as Gibbs energy ($\Delta G^0$), enthalpy ($\Delta H^0$) and entropy change ($\Delta S^0$) were also calculated. Pseudo--first-order (PFO), pseudo-second-order (PSO) and intra-particle diffusion (IDM) models were used for kinetic modelling. Langmuir, Freundlich and D-R models were applied for isotherm modelling. The linearized versions of these models were given in Table S-II of the Supplementary material.

The adsorption activation energies of TB, CV and RB dyes on the LDAC were calculated using the linearized version of the Arrhenius equation:

$$\ln k = \ln A - \frac{E_a}{RT} \tag{3}$$

In order to determine whether the adsorption of the dyes studied on the LDAC is favourable or not, the separation factor $R_L$ values were calculated from the following equation:

$$R_L = \frac{1}{1 + Kc_0} \tag{4}$$

To determine the heat changes during the adsorption of TB, CV and RB dyes on the LDAC, thermodynamic parameters such as Gibbs energy ($\Delta G^0$), the enthalpy ($\Delta H^0$) and entropy changes ($\Delta S^0$) were calculated by the following equations:

$$\Delta G^0 = -RT \ln K \tag{5}$$

$$K = \frac{q_e}{c_e} \tag{6}$$

$$\ln K = \frac{\Delta S^0}{R} - \frac{\Delta H^0}{RT} \tag{7}$$

Nonlinear regression root mean squared error (*RMSE*) values were calculated to determine which model better fit the experimental data:

$$RMSE = \sqrt{\frac{\sum \left( q_{e,exp} - q_{e,cal} \right)^2}{N}} \tag{8}$$

## RESULTS AND DISCUSSION

### *Characterization of the LDAC before and after TB, CV and RB loading*

To determine the LDAC's wettability, contact angle measurements were conducted by the sessile drop method. A contact angle value of less than 90° will generally indicate that it is very convenient to wet the surface and that the water will spread well over the surface. For contact angle values greater than 90°, surface wetting is generally unfavourable, and the water takes the form of a liquid droplet that minimizes contact with the surface. In fact, our previous study demonstrated the efficacy of this adsorbent in removing methylene blue dye.[19] However, the contact angle value of the LDAC could not be given in that study. In this study, the contact angle of the LDAC was measured as 46.90±4.38° (Fig. S-2 of the Supplementary material), providing additional evidence of the good wettability of the LDAC, which is important in the adsorption process.

It was shown in our previous study that the LDAC had a large BET-specific surface area of 851.24 $m^2\ g^{-1}$.[19] The surface properties of the LDAC before and after TB, CV and RB adsorption were investigated by SEM/EDX (Fig. S-3 of the Supplementary material). When the surface of LDAC was examined, it was seen that it had a granular and porous form (Fig. S-3a). Since these pores in the LDAC structure increased the surface area and the number of active centers, it facilitated the adsorption of the studied dyes in a good way (Fig. S-3b–d). The elemental analysis of the LDAC's surface before and after TB, CV and RB loading was performed by EDX analysis (Fig. S-3e–h). Before the adsorption of TB, CV and

RB, the elemental composition of the LDAC was 82.36 % C, 5.66 % O, 6.87 % Cl and 5.11 % Zn by weight (Fig. S-3e). The zinc and chlorine in the EDX results are due to $ZnCl_2$, used in the chemical activation of activated carbon. Since TB, CV and RB molecules fully occupied all the pores and surface of the LDAC, the elemental composition of the surface (%) changed significantly after TB ($C_{27}H_{30}O_5S$), CV ($C_{25}H_{30}ClN_3$) and RB ($C_{28}H_{31}ClN_2O_3$) adsorption (Fig. S-3f–h).

The FT-IR spectra of the LDAC before and after TB, CV, and RB adsorption were given in Fig. S-4 of the Supplementary material. The low intensity peaks in 2927–2853 $cm^{-1}$ range show asymmetric and symmetrical aliphatic C–H stretching bands (Fig. S-4).[4,19] The broad band stretching between 1550 and 1750 $cm^{-1}$ is likely due to the C=N, C=C and conjugated carbonyl vibrations in the aromatic ring.[7,19] After the adsorption of TB, CV and RB on the LDAC, decreases in peak intensities were observed, indicating that adsorption had taken place, although no significant shift was observed in the peaks.

The XRD patterns of the LDAC before and after TB, CV and RB adsorption were shown in Fig. S-5 of the Supplementary material. As seen in Fig. S-5, there are both sharp peaks and wide peaks in the XRD patterns of the LDAC. Although sharp peaks indicate the presence of crystal structures, broad peaks indicate the presence of amorphous structures. The broad peaks at the $2\theta$ value of around 25 and 43° in the XRD patterns indicate the existence of amorphous carbonaceous structures. The sharp peaks at $2\theta$ 31.5, 34.5 and 36.5° are crystalline carbon structures. It can be said that in the carbonization processes carried out at high temperatures (approximately 800 °C), more crystalline carbon structures such as graphite are formed compared to amorphous structures. In addition, the zinc oxide (from $ZnCl_2$ activation) trapped in the melt by sintering at high temperatures may not have been sufficiently removed by washing processes. The peaks at $2\theta$ 47.4 and 56.4° suggest the presence of ZnO. Also, the peaks at $2\theta$ 62.7 and 67.8° may be due to other impurities. The absence of a significant shift in the peaks after the adsorption of TB, CV and RB dyes can be explained by the fact that the studied dyes do not form chemical bonds that may cause a change in the structure of the active centres on the LDAC surface (Figs. S-4 and S-5). In other words, the adsorption took place by physical mechanisms for all the studied dyes.

*The effect of some parameters on TB, CV and RB adsorptions*

To compare the adsorption capacities, the removal of TB, CV and RB from the aqueous medium by the LDAC was investigated at the same pH (9.5). Since this pH value was greater than the $pH_{pzc}$ value of the LDAC (6.8) and the $pK_a$ values of the dyes (TB, 8.9, CV, 9.4, and RB, 3.7), the electrostatic attraction force between the dyes and the LDAC was increased. Fig. 1a shows how tempe-

rature affects the adsorption of the studied dyes. It is seen that the adsorption capacity ($q_e$) of all dyes studied increases with increasing temperature.

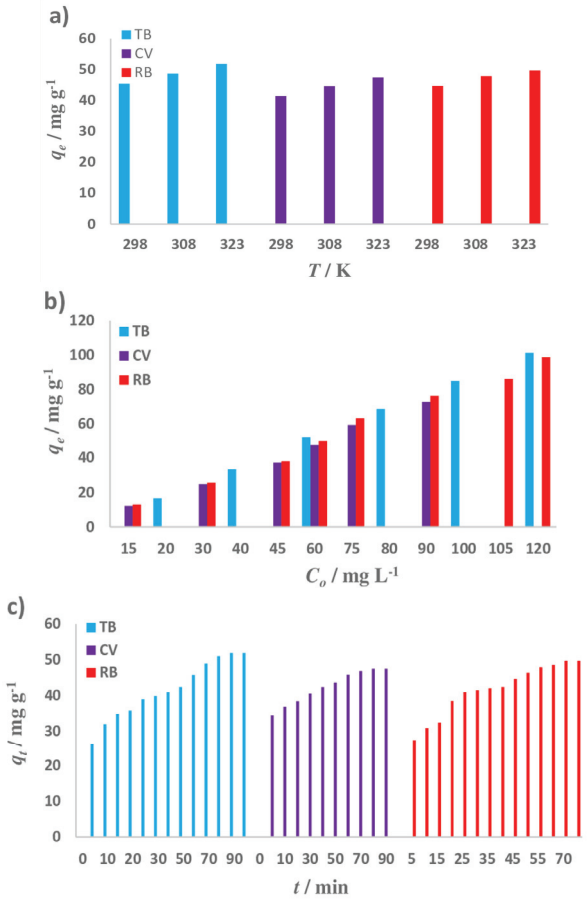


Fig. 1. a) The temperature effects; b) the initial concentration effects; c) the contact time effects on adsorption.

Moreover, the same effect was observed for all initial concentration values. While the $q_e$ values at 298 K were 45.34, 41.41 and 44.67 mg g$^{-1}$ for TB, CV and RB, respectively, these values were 51.83, 47.41 and 49.64 mg g$^{-1}$ at 323 K (60 mg L$^{-1}$ initial dye concentration). With increase of the temperature increases the mobility of the molecules in the solution medium, decreases the solution viscosity and helps the expansion of small pores. In addition, the increase in temperature increases the diffusion rate as the external and internal mass transfer resistances decrease. Thus, the transition of molecules from the liquid phase to the solid phase becomes easier. Fig. 1b shows the effect of initial dye concentration

(TB: 20, 40, 60, 80, 100 and 120 mg $L^{-1}$; CV: 15, 30, 45, 60, 75 and 90 mg $L^{-1}$; RB: 20, 40, 60, 80, 100 and 120 mg $L^{-1}$) on the adsorption capacity ($q_e$). It appears that increasing the initial dye concentrations increases the adsorption capacity by generating a higher driving force of concentration difference that can overcome the solid–liquid mass transfer resistance. $q_e$ increased with increasing initial concentration at three different temperatures (298, 308 and 323 K) for the three dyes. The best results were obtained at 323 K. The contact time, of course, directly affects the cost of the adsorption process. Obtaining the highest adsorption efficiency in a shorter time is advantageous for the process. The ability of LDAC to remove TB, CV and RB from water with high adsorption efficiency in short equilibrium times (90, 80 and 70 min for TB, CV and RB, respectively) shows that this adsorbent can reduce the total process cost of removing dyes from contaminated water.

Fig. 1c shows the effect of contact time on the adsorption capacity. When the change in the bar graphs is examined, it is seen that there is rapid adsorption due to the high solution concentration in the initial times, then the solution concentration decreases and the adsorption rate decreases with the filling of the active centres on the LDAC surface and finally, at the end of a certain time adsorption does not occur that is, the equilibrium state is reached.

*TB, CV, and RB adsorption kinetics*

The adsorption kinetic studies are very important for the modelling and design parameters of the adsorption systems. Three different kinetic models were applied to the experimental data to estimate the adsorption rates and determine the rate-limiting step, thus linear forms of the PFO, PSO and IDM models were used to determine the model parameters (Table I). In addition, nonlinear forms of PFO, PSO and IDM models were applied to the experimental data, and experimental kinetic data were also checked (Fig. 2).

PFO model parameters ($k_1$, $q_e$), correlation coefficient ($R^2$), deviation (%) between calculated $q_e$ and experimental $q_e$ values and *RMSE* values calculated at 323 K temperature, monitored for the three dyes, were given in Table I. The fact that the $R^2$ values were lower, the deviation and *RMSE* values were higher than the other two models examined showed that this model did not fit the experimental data. Furthermore, Fig. 2 proved that the experimental kinetic data did not fit the nonlinear form of the PFO model at all for TB, CV and RB.

PSO model parameters ($k_2$, $q_e$) and the initial adsorption rate ($k_0$), $R^2$, deviations and *RMSE* values calculated for TB, CV and RB were given in Table I. $R^2$ values were greater than 0.99 for all dyes studied. The smaller deviation values indicating good closeness between experimental $q_e$ and calculated $q_e$ were found to be 2.78, 1.52 and 1.97 for TB, CV and RB, respectively. The smaller *RMSE*

values (1.37, 0.81 and 0.62 for TB, CV and RB, respectively) supported the fact that the adsorption of TB, CV, and RB on the LDAC follows the PSO kinetics well. In addition, the rate constant ($k_2$) and the initial adsorption rate ($k_0$) of TB were greater than those of RB and CV, indicating that the affinity of TB molecules for the LDAC is greater than that of CV and RB molecules (Table I). Moreover, Fig. 2 demonstrated that the experimental kinetic data for TB, CV and RB fit well with the nonlinear form of the PSO model. Bakhsh *et al.* reported that the adsorption of thymol blue onto prepared activated carbon from Trachycarpus fortunei seeds obeyed the pseudo-second-order model.[21] Senthilkumaar *et al.* reported that the kinetics of adsorption of crystal violet onto modified activated carbons, prepared from male flowers of coconut trees, were found to be pseudo-second-order with regard to intraparticle diffusion.[22] Wang *et al.* reported that the adsorption of Rhodamine B on biochar samples, prepared from earthworm manure, fitted well with the PSO kinetic model.[23]

TABLE I. PFO, PSO, and IDM model parameters for the adsorption of TB, CV, and RB

| Model | Parameter | TB | CV | RB |
|---|---|---|---|---|
| PFO | $q_{e,exp}$ / mg g$^{-1}$ | 51.83 | 47.41 | 49.64 |
| | $k_1$ / min$^{-1}$ | 0.0364 | 0.0420 | 0.0488 |
| | $q_{e,cal}$ / mg g$^{-1}$ | 32.86 | 19.36 | 32.54 |
| | $R^2$ | 0.8752 | 0.9077 | 0.9276 |
| | Deviation, % | 36.60 | 59.16 | 34.45 |
| | *RMSE* | 17.85 | 27.41 | 16.50 |
| PSO | $k_2$ / g mg$^{-1}$ min$^{-1}$ | 0.00172 | 0.00419 | 0.00213 |
| | $k_0$ / g mg$^{-1}$ min$^{-1}$ | 5.4318 | 10.2774 | 6.3492 |
| | $q_{e,cal}$ / mg g$^{-1}$ | 50.39 | 46.69 | 48.66 |
| | $R^2$ | 0.9915 | 0.9970 | 0.9944 |
| | Deviation, % | 2.78 | 1.52 | 1.97 |
| | *RMSE* | 1.37 | 0.81 | 0.62 |
| IDM | $k_d$ / mg g$^{-1}$ min$^{-1/2}$ | 3.1800 | 1.8903 | 3.5112 |
| | $\theta$ / mg g$^{-1}$ | 21.576 | 30.383 | 20.840 |
| | $R^2$ | 0.9802 | 0.9880 | 0.9577 |
| | $q_{e,cal}$ / mg g$^{-1}$ | 51.74 | 47.29 | 50.22 |
| | Deviation, % | 0.17 | 0.25 | 1.17 |
| | *RMSE* | 0.91 | 0.60 | 1.32 |

IDM model parameters ($k_d$, $\theta$), $R^2$, deviations and *RMSE* values calculated for the three dyes monitoring were given in Table I. The fact that the $q_t$ *vs.* $t^{1/2}$ graphs did not pass through the origin indicated that the mass transfer rate changed in the first and last stages of adsorption. This suggests that intraparticle diffusion is not the only step controlling the rate, and boundary layer effects can also control the rate of adsorption.

The $\theta$ parameter is very important as it relates to the boundary layer thickness. The bigger the $\theta$ value, the larger the boundary layer thickness. The values of

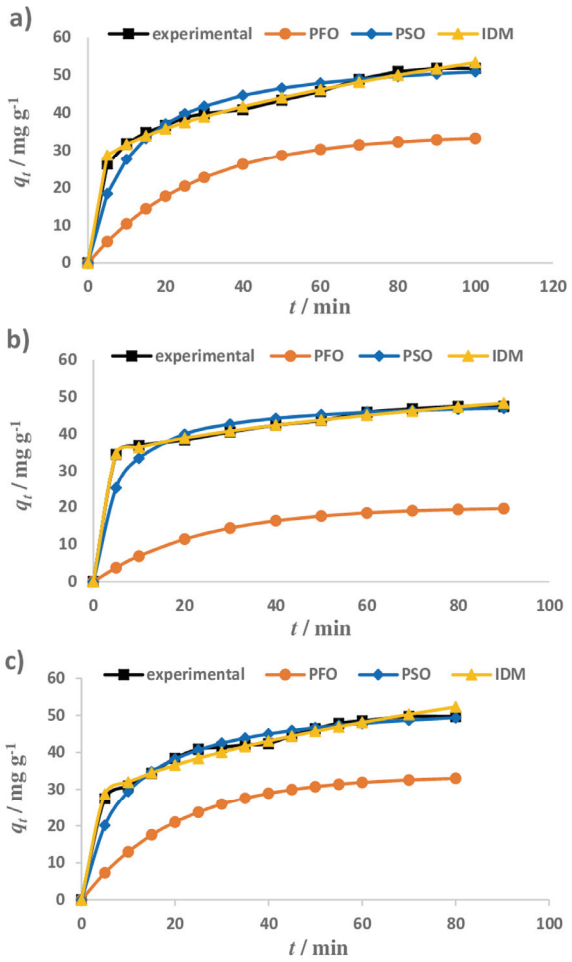


Fig. 2. The kinetic modelling of: a) TB; b) CV; c) RB.

the boundary layer thickness for TB, CV and RB were calculated as 21.576, 30.383 and 20.840 mg g$^{-1}$, respectively (Table I). In addition, the boundary layer thickness values for all studied dyes increased with increasing initial dye concentration and temperature. The greater boundary layer thickness value of CV may explain why the adsorption capacity of CV on LDAC is lower than that of TB and RB. This indicates that intra-particle diffusion was slower at higher temperatures and initial dye concentrations. The rate constants ($k_d$) for TB, CV and RB were found to be 3.1800, 1.8903 and 3.5112 mg g$^{-1}$ min$^{-1/2}$ at 323 K, respectively (Table I). The $R^2$, deviations and *RMSE* values for the IDM model show that the IDM kinetic model is suitable for the studied dyes. The lower deviation and *RMSE* values of TB and CV compared to RB indicate a better fit. As can be

seen from Fig. 2, the nonlinear form of the IDM model is in good agreement with the experimental kinetic data for TB, CV and RB, suggesting that both pore and film diffusion co-control the adsorption kinetics.

*Activation energy*

The activation energy offers an idea about whether the adsorption mechanism is physical or chemical. If the activation energy is less than 40 kJ $mol^{-1}$, it is physical adsorption; if it is greater than 40 kJ $mol^{-1}$, it is chemical adsorption. For the adsorption of TB, CV and RB onto LDAC, the activation energies were calculated using Eq. (3) and the Arrhenius plots (not shown). The activation energies were found to be 45.41, 20.51 and 27.04 kJ $mol^{-1}$ for TB, CV and RB, respectively. Although the activation energy of TB is slightly higher than 40 kJ $mol^{-1}$, the energy value ($E$) determined from the D-R model and the absence of significant shifts in the FT-IR and XRD images suggest that the adsorption is physical. Onen *et al.* reported that the activation energy of TB on mild steel was 6.32 kJ $mol^{-1}$.[24] Laskar and Kumar noted that the value of $E_a$ for crystal violet dye adsorption onto sodium carbonate-modified *Bambusa tulda* was 26.297 kJ $mol^{-1}$.[25] Lee and Zaini reported that the activation energy for the adsorption of RB by magnetic activated carbon was 24.1 and 28.9 kJ $mol^{-1}$ for the PFO and PSO kinetic models, respectively.[26]

*TB, CV and RB adsorption isotherms*

Equilibrium studies are necessary in order to optimize the adsorption process. The equilibrium studies of the adsorption process of TB, CV and RB dyes on LDAC were carried out at 3 different temperatures (298, 308 and 323 K), and the experimental data were adapted to 3 different isotherm models (Langmuir, Freundlich and D-R), and the determined model parameters were presented in Table II.

The maximum Langmuir adsorption capacity ($q_m$) of TB, CV and RB was found to be 400, 212.766 and 344.828 mg $g^{-1}$, respectively (Fig. S-6a of the Supplementary material). The value of $q_m$ for TB is higher than that of CV and RB. The reason for this can be explained by the fact that the initial rate of adsorption ($k_0$) for TB acquired from the PSO model is lower than that of CV and RB. So, TB molecules are adsorbed on the LDAC surface faster. Besides, the smaller boundary layer thickness ($\theta$) of TB allows the molecules to pass easily into the pores of the LDAC (Table I). Kumari *et al.* studied the adsorption of TB dye from wastewater by activated carbons fabricated from plastic waste and reported that the maximum adsorption capacities onto waste polybags (P-ACs), cups (C-ACs),and bottles (B-ACs) were 16.28, 115.4 and 43.93 mg $g^{-1}$, respectively.[27] Senthilkumaar *et al.* reported that the adsorption capacities of CV onto activated carbons (PAAC and SAAC) derived from male flowers of coconut trees

were 60.42 and 85.84 mg $g^{-1}$.[22] Xiao *et al.* found the maximum adsorption capacity of RB onto activated carbon (ASC) was 123.46 mg $g^{-1}$.[28] It can be stated that the maximum adsorption capacity ($q_m$) of TB, CV and RB onto the LDAC obtained in this study is relatively higher than many adsorbent capacities reported by other researchers. In addition, the favourable adsorption of TB, CV and RB on LDAC was demonstrated by the $R_L$ factor being in the range of 0 to 1 (Table II). Similar results regarding the $R_L$ factor of TB, CV and RB on different adsorbents were obtained by the other authors.[22,28,29]

TABLE II. Langmuir, Freundlich and D-R parameters for the adsorption of TB, CV, and RB

| Parameter | TB | CV | RB |
|---|---|---|---|
| | | Langmuir | |
| $q_m$ / mg $g^{-1}$ | 400 | 212.766 | 344.828 |
| $K$ / L $mg^{-1}$ | 0.0183 | 0.0260 | 0.0182 |
| $R^2$ | 0.9991 | 0.9797 | 0.9977 |
| $R_L$ | 0.4766 | 0.3903 | 0.4772 |
| | | Freundlich | |
| $k_f$ | 9.6244 | 4.8018 | 6.7113 |
| $n$ | 1.2384 | 1.0611 | 1.1227 |
| $R^2$ | 0.9976 | 0.9749 | 0.9919 |
| | | D-R | |
| $q_m$ / mg $g^{-1}$ | 0.0383 | 0.0136 | 0.0114 |
| $K'$ / $mol^2$ $kJ^{-2}$ | 0.0081 | 0.0070 | 0.0065 |
| $E$ / kJ $mol^{-1}$ | 7.8567 | 8.4515 | 8.7706 |
| $R^2$ | 0.9850 | 0.9788 | 0.9921 |

The Freundlich model parameters ($k_f$, $n$) and $R^2$ values for the studied dyes were given in Table II. $k_f$ values were determined as 9.6244, 4.8018 and 6.7113 for TB, CV and RB, respectively (Fig. S-6b). If the $k_f$ value is large, the adsorption capacity is also large. By comparing the $k_f$ values for the studied dyes in Table II, it can be said that the adsorption capacity of LDAC is ranked as TB > RB > CV. If the value of $n$ is greater than 1, it is favourable adsorption. $n$ values were found to be greater than 1 for the removal of TB, CV and RB (Table II). Besides, $n > 1$ indicates high affinity between the LDAC and TB, CV and RB and proves that the adsorption occurs in a physical manner and that the adsorption sites on the LDAC are heterogeneous. Other researchers revealed similar results related to the favourable adsorption of TB, CV and RB onto different adsorbents.[27,29,30]

The $R^2$ values for Langmuir, Freundlich, and D-R isotherms were determined to be greater than 0.99 for both TB and RB and greater than 0.97 for CV.

The adaptation of the experimental data to the D-R model was shown in Fig. S-6c and the calculated D-R parameters ($q_m$, $K'$ and $E$) and $R^2$ values were given in Table II. The $E$ value calculated from the D-R model indicates that when $E < 8$

kJ mol$^{-1}$, the adsorption mechanism is physical, when $8 < E < 16$ kJ mol$^{-1}$, it is ion exchange adsorption, and when $E > 8$ kJ mol$^{-1}$, the adsorption is chemical. In this study, $E$ values were calculated to be 7.8567, 8.4515 and 8.7706 kJ mol$^{-1}$ for TB, CV and RB, respectively (Table II). The type of adsorption of TB on the LDAC was of a physisorption nature. In other words, the interaction between TB molecules and LDAC takes place by van der Waals forces. Although the values of $E$ for CV and RB seem to be in the ion exchange range, they are very close to 8 kJ mol$^{-1}$, and it can be stated that the interaction between both CV and RB molecules and the LDAC surface is also by physical adsorption mechanisms.

A comparison of the maximum adsorption capacity of the LDAC with various activated carbons used as cheap adsorbents for TB, CV and RB removal was given in Table III. This comparison demonstrated that the LDAC had a greater adsorption capacity than other adsorbents. Thus, the LDAC can be considered an adsorbent with great potential to remove dyes such as TB, CV and RB from aqueous medium.

TABLE III. Comparison between LDAC and cheap biomass-based activated carbons for TB, CV and RB removal in mg g$^{-1}$

| Activated carbon | TB | CV | RB | Ref. |
|---|---|---|---|---|
| *Garcinia cola* nut shell (CBK1/1) | 189.60 | | | 29 |
| *Garcinia cola* nut shell (CBH2/1 ) | 396.04 | | | 29 |
| Plastic waste polybags (P-ACs) | 16.28 | | | 27 |
| Plastic waste cups (C-ACs) | 115.40 | | | 27 |
| Plastic waste bottles (B-ACs) | 43.93 | | | 27 |
| Coconut tree male flowers (PAAC) | | 60.42 | | 22 |
| Coconut tree male flowers (SAAC) | | 85.84 | | 22 |
| *Millettia thonningii* seed pods-derived | | 7.57 | | 30 |
| Palm petiole-derived | | 209 | | 31 |
| Oak leaves-derived | | 41.15 | | 32 |
| Activated sugar-based carbon (ASC) | | | 123.46 | 28 |
| Earthworm manure-derived | | | 21.60 | 23 |
| Bamboo shoot shell-derived | | | 85.8 | 33 |
| Plaintain peels-derived | | | 84.41 | 34 |
| Cassava slag-derived | | | 105.6 | 35 |
| LDAC | 400 | 212.77 | 344.83 | Present study |

*Adsorption thermodynamics*

Thermodynamic parameters of the adsorption of TB, CV and RB on the LDAC, such as the Gibbs energy ($\Delta G^0$ / kJ mol$^{-1}$), enthalpy ($\Delta H^0$ / kJ mol$^{-1}$) and entropy changes ($\Delta S^0$ / kJ mol$^{-1}$ K$^{-1}$) changes, were calculated using Eqs. (5)–(7) and the van't Hoff plot (Fig. S-7 of the Supplementary material), and the results were shown in Table IV. The negative values of $\Delta G^0$ showed that TB, CV and RB adsorption on the LDAC was spontaneous and feasible (Table IV). The

positive values of $\Delta H^0$ indicated endothermic adsorption. The $\Delta H^0$ values for CV and RB are less than 20 kJ mol$^{-1}$ (Table IV), indicating physical adsorption by van der Waals forces. Although the $\Delta H^0$ value for TB is slightly higher than 20 kJ mol$^{-1}$, it can be said that the interaction between TB and the LDAC occurs physically with electrostatic forces. Moreover, the calculated activation energy and D-R energy values for TB, CV and RB support these thermodynamic results. The increase in randomness and disorder at the dye solution–LDAC interface during the adsorption was designated by positive values of $\Delta S^0$, which is in accordance with the 2nd law of thermodynamics. Similar results for TB, CV and RB adsorption on different activated carbons have been reported by other researchers.[29,31,35]

TABLE IV. The values of thermodynamic parameters (60 ppm, 323 K)

| Dye | $K$ | $\Delta G^0$ / kJ mol$^{-1}$ | $\Delta H^0$ / kJ mol$^{-1}$ | $\Delta S^0$ / kJ mol$^{-1}$ K$^{-1}$ | $R^2$ |
|---|---|---|---|---|---|
| TB | 6.3439 | –4.8845 | 22.9192 | 0.0864 | 0.9987 |
| CV | 3.7657 | –3.5056 | 16.6537 | 0.0627 | 0.9904 |
| RB | 4.7915 | –4.1425 | 17.7545 | 0.0748 | 0.8293 |

*Reusability*

The reusability of the LDAC was evaluated for TB, CV and RB adsorption and desorption, and results were shown in Fig. S-8 of the Supplementary material. 0.1 M HCl solution was used for the desorption studies. After four consecutive adsorption and desorption cycles, the removal efficiencies of TB, CV and RB decreased by 23.5, 19.1 and 15.4 %, respectively. This demonstrated that LDAC could be an economical and effective adsorbent for dye removal.

## CONCLUSIONS

The adsorption behaviours of TB, CV and RB on LDAC were studied, and very good results were achieved. The isotherm studies showed that the adsorption capacity of the LDAC was ranked as TB > RB > CV. The maximal Langmuir adsorption capacity of TB, CV and RB was found as 400, 213 and 345 mg g$^{-1}$, respectively. The kinetic studies implied that the adsorption of TB, CV and RB onto the LDAC fit the PSO kinetics. Besides, the nonlinear forms of the PSO and IDM models had a good agreement with the experimental kinetic data for TB, CV and RB. The boundary layer thicknesses were also evaluated. These values for TB, CV and RB were calculated to be 21.576, 30.383 and 20.840 mg g$^{-1}$, respectively. TB and CV better fit the IDM kinetic model with lower deviation (%) and *RMSE* values compared to RB. The thermodynamic studies showed that the adsorption of TB, CV and RB on the LDAC was spontaneous, feasible and endothermic, with physical adsorption by van der Waals and electrostatic forces.

This study demonstrated that the removal of the dyes with environmentally friendly, cheap, sustainable and high adsorption capacity the LDAC will con-

tribute to environmental and wastewater cleaning, and it may be an alternative to expensive adsorbents.

## SUPPLEMENTARY MATERIAL

Additional data and information are available electronically at the pages of journal website: https://www.shd-pub.org.rs/index.php/JSCS/article/view/12417, or from the corresponding author on request.

## ИЗВОД

## ИСТРАЖИВАЊЕ ПОНАШАЊА АДСОРПЦИЈЕ ТИМОЛ ПЛАВОГ, КРИСТАЛНО ЉУБИЧАСТОГ И РОДАМИНА Б НА АКТИВНОМ УГЉУ ДОБИЈЕНОМ ОД ЛИШАЈА

*[1]Bursa Technical University, Faculty of Engineering and Natural Sciences, Chemical Engineering Department, 16310, Bursa, Turkiye и [2]Van Yüzüncü Yıl University, Faculty of Science, Chemistry Department, 65080, Van, Turkiye*

Пошто се тимол плаво (TB), кристално љубичасто (CV) и родамин Б (RB) често користе у разним индустријама, они узрокују загађење животне средине услед процеса обраде отпадних вода. Ова студија се фокусирала на уклањање TB, CV и RB из водених медија помоћу активног угља добијеног од лишаја (LDAC), и упоређивање њиховог понашања при адсорпцији. Утврђено је да је максимални капацитет адсорпције по Лангмиру за TB, CV и RB 400, 213 и 345 mg $g^{-1}$, редом. Нађено је да уклањање TB, CV и RB износи 86,38, 79,02 и 82,73 %, редом, при истим условима. Експериментални подаци су интерпретирани уобичајено коришћеним кинетичким и изотермним моделима. Израчунате енергије активације, енергија D-R модела, вредности енталпије и процена FT-IR, XRD и SEM/EDX слика снимљених пре и после адсорпције боје показали су да су механизми адсорпције TB, CV и RB на LDAC физички процеси. Кинетички модел псеудо-другог реда боље је описао адсорпционо понашање TB, CV и RB на LDAC. Вредност дебљине граничног слоја за све проучаване боје повећавала се са повећањем почетне концентрације боје и температуре, а CV је такође имао већу вредност дебљине граничног слоја од оне која је нађена код TB и RB.

(Примљено 30. маја, ревидирано 10. августа, прихваћено 20. новембра 2023)

## REFERENCES

1. C. Puri, G. Sumana, *Appl. Clay Sci.* **166** (2018) 102 (https://doi.org/10.1016/j.clay.2018.09.012)
2. M. Sh. Gohr, A. I. Abd-Elhamid, A. A. El-Shanshory, H. M. A. Soliman, *J. Mol. Liq.* **346** (2022) 118227 (https://doi.org/10.1016/j.molliq.2021.118227)
3. S. Kumar (S. Kumar), R. D. Kaushik, L. P. Purohit, *J. Hazard. Mater.* **424** (2022) 127332 (https://doi.org/10.1016/j.jhazmat.2021.127332)
4. P. Naderi, M. Shirani, A. Semnani, A. Goli, *Ecotoxicol. Environ. Saf.* **163** (2018) 372 (https://doi.org/10.1016/j.ecoenv.2018.07.091)
5. M. El Alouani, S. Alehyen, H. El Hadki, H. Saufi, A. Elhalil, O. K. Kabbaj, M. Taibi, *Surfaces Interfaces* **24** (2021) 101136 (https://doi.org/10.1016/j.surfin.2021.101136)
6. M. Sundararajan, V. Sailaja, L. John Kennedy, J. Judith Vijaya, *Ceram. Int.* **43** (2017) 540 (http://doi.org/10.1016/j.ceramint.2016.09.191)
7. A. S. Takabi, M. Shirani, A. Semnani, *Environ. Technol. Innov.* **24** (2021) 101947 (https://doi.org/10.1016/j.eti.2021.101947)

8. G. Sharma, A. Kumar, M. Naushad, A. García-Peñas, A. H. Al-Muhtaseb, A. A. Ghfar, V. Sharma, T. Ahamad, F. J. Stadler, *Carbohydr. Polym.* **202** (2018) 444 (https://doi.org/10.1016/j.carbpol.2018.09.004)
9. S. S. Chan, K. S. Khoo, K. W. Chew, T. C. Ling, P. L. Show, *Bioresour. Technol.* **344** (2022) 126159 (https://doi.org/10.1016/j.biortech.2021.126159)
10. S. Sathiyavimal, S. Vasantharaj, M. Shanmugavel, E. Manikandan, P. Nguyen-Tri, K. Brindhadevi, A. Pugazhendhi, *Prog. Org. Coatings* **148** (2020) 105890 (https://doi.org/10.1016/j.porgcoat.2020.105890)
11. P. V. Nidheesh, R. Gandhimathi, *Desalination* **299** (2012) 1 (https://doi.org/10.1016/j.desal.2012.05.011)
12. A. Muniyasamy, G. Sivaporul, A. Gopinath, R. Lakshmanan, A. Altaee, A. Achary, P. Velayudhaperumal Chellam, *J. Environ. Manage.* **265** (2020) 110397 (https://doi.org/10.1016/j.jenvman.2020.110397)
13. S. Ledakowicz, R. Żyłła, K. Paździor, J. Wrębiak, J. Sójka-Ledakowicz, *Ozone Sci. Eng.* **39** (2017) 357 (https://doi.org/10.1080/01919512.2017.1321980)
14. H. R. Rashidi, N. M. N. Sulaiman, N. A. Hashim, C. R. C. Hassan, M. R. Ramli, *Desalin. Water Treat.* **55** (2015) 86 (https://doi.org/10.1080/19443994.2014.912964)
15. D. A. Gopakumar, V. Arumukhan, R. V. Gelamo, D. Pasquini, L. C. de Morais, S. Rizal, D. Hermawan, A. Nzihou, H. P. . A. Khalil, *Nano-Structures Nano-Objects* **18** (2019) 100268 (https://doi.org/10.1016/j.nanoso.2019.100268)
16. M. R. Gadekar, M. M. Ahammed, *Desalin. Water Treat.* **57** (2016) 26392 (https://doi.org/10.1080/19443994.2016.1165150)
17. H. Zazou, H. Afanga, S. Akhouairi, H. Ouchtak, A. A. Addi, R. A. Akbour, A. Assabbane, J. Douch, A. Elmchaouri, J. Duplay, A. Jada, M. Hamdani, *J. Water Process Eng.* **28** (2019) 214 (https://doi.org/10.1016/j.jwpe.2019.02.006)
18. S. M. Ghoreishi, R. Haghighi, *Chem. Eng. J.* **95** (2003) 163 (https://doi.org/10.1016/S1385-8947(03)00100-1)
19. H. Koyuncu, A. R. Kul, *Surfaces Interfaces* **19** (2020) 100527 (https://doi.org/10.1016/j.surfin.2020.100527)
20. H. Koyuncu, A. R. Kul, *Surfaces Interfaces* **21** (2020) 100653 (https://doi.org/10.1016/j.surfin.2020.100653)
21. E. M. Bakhsh, M. Bilal, M. Ali, J. Ali, A. Wahab, K. Akhtar, T. M. Fagieh, E. Y. Danish, A. M. Asiri, S. B. Khan, *Materials (Basel)* **15** (2022) 1986 (https://doi.org/10.3390/ma15061986)
22. S. Senthilkumaar, P. Kalaamani, C. Subburaam, *J. Hazard. Mater.* **136** (2006) 800 (https://doi.org/10.1016/j.jhazmat.2006.01.045)
23. Z. Wang, D. Shen, F. Shen, C. Wu, S. Gu, *Int. Biodeterior. Biodegrad.* **120** (2017) 104 (https://doi.org/10.1016/j.ibiod.2017.01.026)
24. A. I. Onen, O. N. Maitera,J. Joseph,J. E. E. Ebenso, *Int. J. Electrochem. Sci.* **6** (2011) 2884 (http://www.electrochemsci.org/papers/vol6/6072884.pdf)
25. N. Laskar, U. Kumar, *KSCE J. Civil Eng.* **22** (2018) 2755 (https://doi.org/10.1007/s12205-017-0473-5)
26. L. Z. Lee, M. A. Ahmad Zaini, *Toxin Rev.* **41** (2022) 64 (https://doi.org/10.1080/15569543.2020.1837172)
27. M. Kumari, G. R. Chaudhary, S. Chaudhary, A. Umar, *Chemosphere* **294** (2022) 133692 (https://doi.org/10.1016/j.chemosphere.2022.133692)
28. W. Xiao, Z. N. Garba, S. Sun, I. Lawan, L. Wang, M. Lin, Z. Yuan, *J. Clean. Prod.* **253** (2020) 119989 (https://doi.org/10.1016/j.jclepro.2020.119989)

29. I.-H. T. Kuete, D. R. T. Tchuifon, G. N. Ndifor-Angwafor, A. T. Kamdem, S. G. Anagho, *J. Encapsul. Adsorp. Sci.* **10** (2020) 1 (https://doi.org/10.4236/jeas.2020.101001)
30. E. E. Jasper, V. O. Ajibola, J. C. Onwuka, *Appl. Water Sci.* **10** (2020) 132 (https://doi.org/10.1007/s13201-020-01218-y)
31. H.-O. Chahinez, O. Abdelkader, Y. Leila, H. N. Tran, *Environ. Technol. Innov.* **19** (2020) 100872 (https://doi.org/10.1016/j.eti.2020.100872)
32. M. Sulyman, J. Namieśnik, A. Gierak, *Polish J. Environ. Stud.* **23** (2014) 2223 (https://doi.org/10.15244/pjoes/26764)
33. Y. Hou, G. Huang, J. Li, Q. Yang, S. Huang, J. Cai, *J. Anal. Appl. Pyrolysis* **143** (2019) 104694 (https://doi.org/10.1016/j.jaap.2019.104694)
34. F. A. Adekola, S. B. Ayodele, A. A. Inyinbor, *Chem. Data Collect.* **19** (2019) 100170 (https://doi.org/10.1016/j.cdc.2018.11.012)
35. J. Wu, J. Yang, G. Huang, C. Xu, B. Lin, *J. Clean. Prod.* **251** (2020) 119717 (https://doi.org/10.1016/j.jclepro.2019.119717).

Journal of the Serbian Chemical Society
JSCS@tmf.bg.ac.rs • www.shd.org.rs/JSCS
*J. Serb. Chem. Soc.* *89* (9) S278–S284 (2024) *Supplementary material*

SUPPLEMENTARY MATERIAL TO

# Investigation of the adsorption behaviors of thymol blue, crystal violet, and rhodamine b on lichen-derived activated carbon

HÜLYA KOYUNCU[1]* and ALİ RIZA KUL[2]

[1]*Bursa Technical University, Faculty of Engineering and Natural Sciences, Chemical Engineering Department, 16310, Bursa, Turkiye and* [2]*Van Yüzüncü Yıl University, Faculty of Science, Chemistry Department, 65080, Van, Turkiye*

*J. Serb. Chem. Soc.* *89* (9) (2024) 1211–1226

Table S-I. Some specifications of TB, CV, and RB

| | Thymol Blue | Crystal Violet | Rhodamine B |
|---|---|---|---|
| Molecular structure | 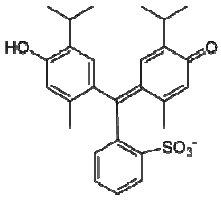 | 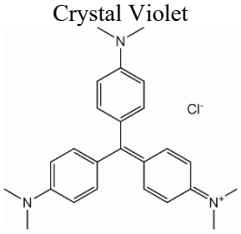 | 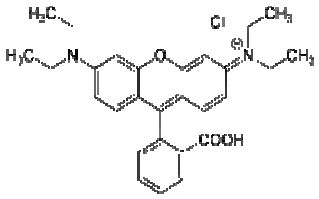 |
| Chemical formula | C27H30O5S | C25H30ClN3 | C28H31ClN2O3 |
| Molecular weight | 466.59 g/mol | 407.99 g/mol | 479.02 g/mol |
| GHS pictograms |  |  |  |

* Corresponding author. E-mail: hulya.koyuncu@btu.edu.tr

(a) (b)

Fig. S-1. a) Lichen *Pseudevernia furfuracea* from Ericek-Bursa; b) lichen-derived activated carbon.

Table S-II. The linearized versions of the PFO, PSO, IDM, Langmuir, Freundlich, and D-R models

| Model Name | Model Equation | Plots axis (y ; x) | Model Parameter |
|---|---|---|---|
| PFO | $\ln(q_e - q_t) = \ln(q_e) - k_1 * t$ | $\ln(q_e - q_t)$ ; $t$ | $q_e$, $q_t$ : (mg $g^{-1}$)<br>$k_1$: ($min^{-1}$) |
| PSO | $\frac{t}{q_t} = \frac{1}{k_2 * q_e^2} + \frac{t}{q_e}$<br>$k_0 = k_2 * q_e^2$ | $\frac{t}{q_t}$ ; $t$ | $k_2$, $k_0$: (g $mg^{-1}$ $min^{-1}$) |
| IDM | $q_t = k_{id} * t^{1/2} + \theta$ | $q_t$ ; $t^{1/2}$ | $k_d$: (mg $g^{-1}$ $min^{-1/2}$)<br>θ: (mg $g^{-1}$) |
| Langmuir | $\frac{1}{q_e} = \frac{1}{K * C_e * q_m} + \frac{1}{q_m}$ | $\frac{1}{q_e}$ ; $\frac{1}{C_e}$ | K : (L $mg^{-1}$)<br>$C_e$: (mg $L^{-1}$)<br>$q_m$: (mg $g^{-1}$) |
| Freundlich | $\ln(q_e) = \ln(k_f) + \frac{1}{n} * \ln(C_e)$ | $\ln(q_e)$ ; $\ln(C_e)$ | $k_f$: (mg $g^{-1}$) |
| D-R | $\ln(q_e) = \ln(q_m) - K' * \varepsilon^2$<br>$\varepsilon = R * T * \ln(1 + 1/C_e)$<br>$E = 1/\sqrt{2 * K'}$ | $\ln(q_e)$ ; $\varepsilon^2$ | $q_m$, $q_e$: (mol $g^{-1}$)<br>ε: Polanyi potential<br>K': (mol$^2$ $kJ^{-2}$)<br>E: (kJ $mol^{-1}$) |

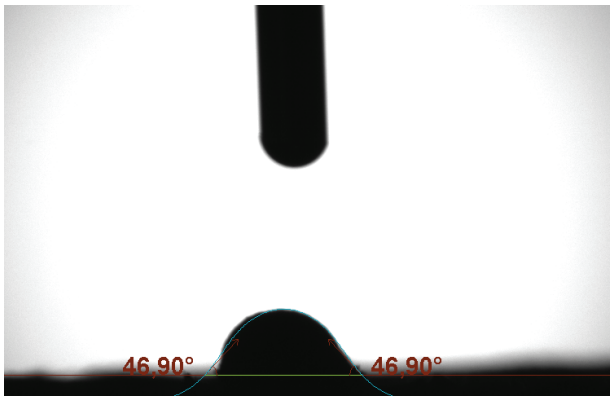


Fig. S-2. Contact angle of the LDAC.

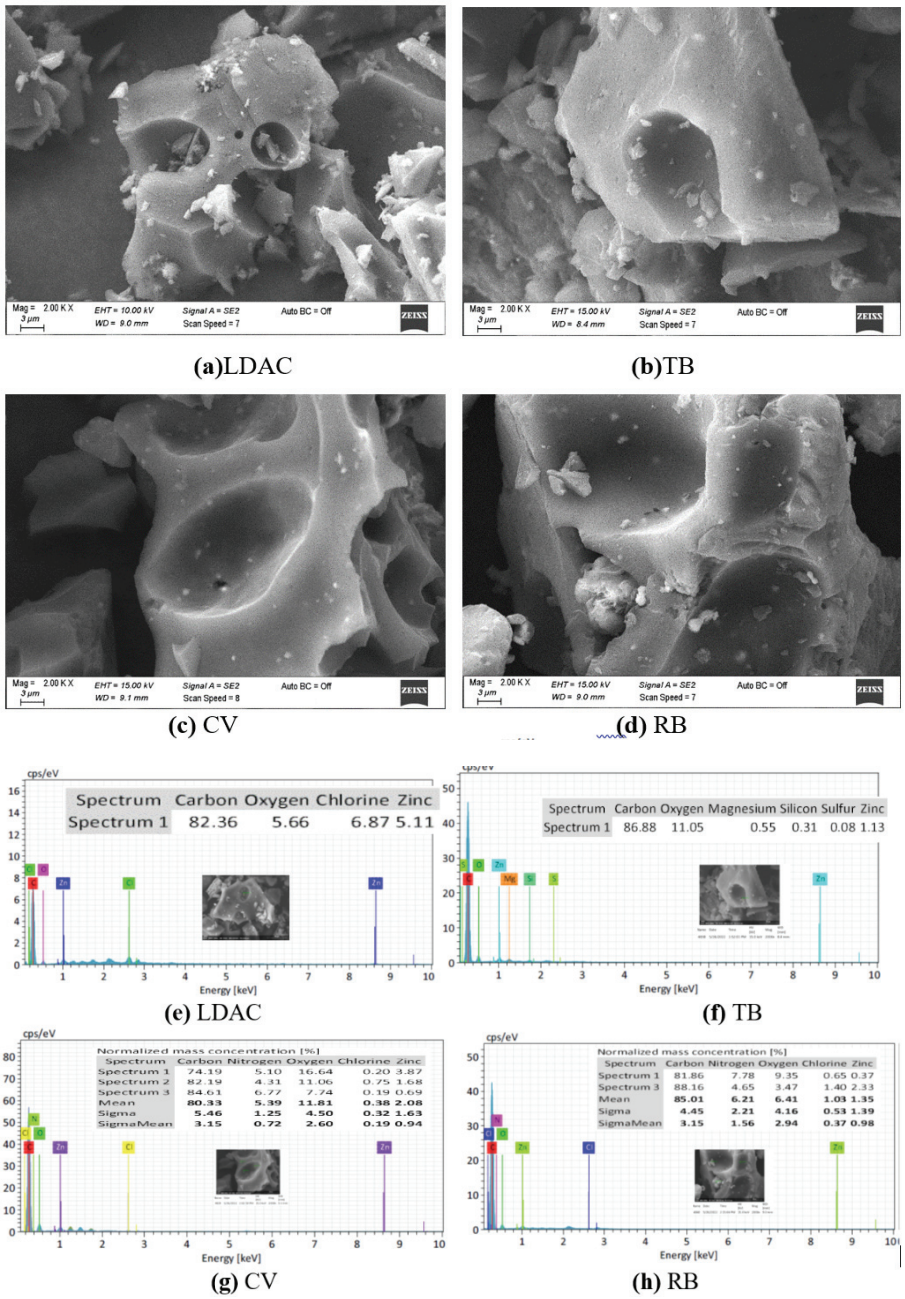


Fig. S-3. SEM photos and EDX results of the LDAC before (a, e) and after TB (b, f), CV (c, g), RB (d, h) loaded.

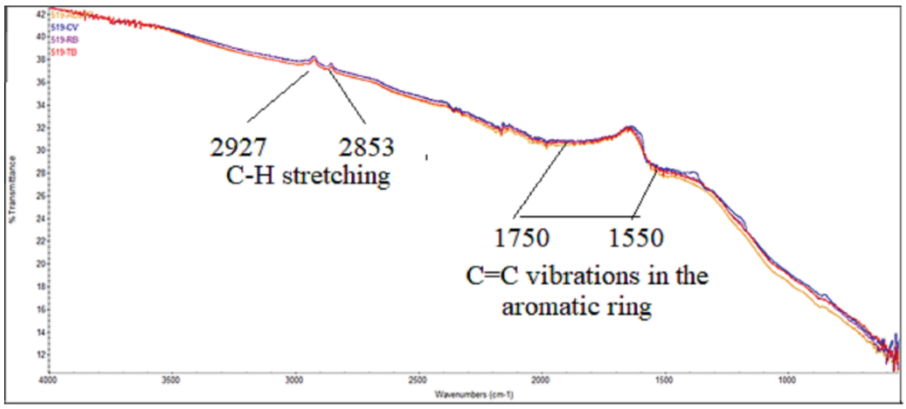


Fig. S-4. FT-IR interferograms of the LDAC before and after TB, CV, and RB loaded.

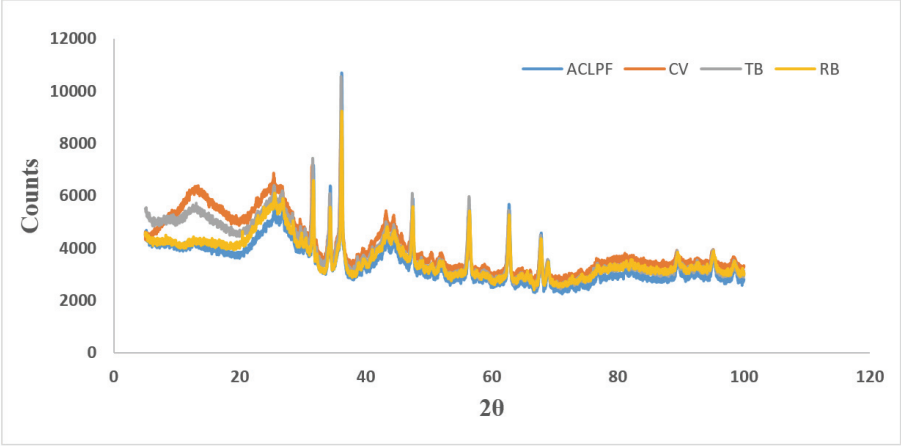


Fig. S-5. XRD patterns of the LDAC before and after TB, CV, and RB adsorptions.

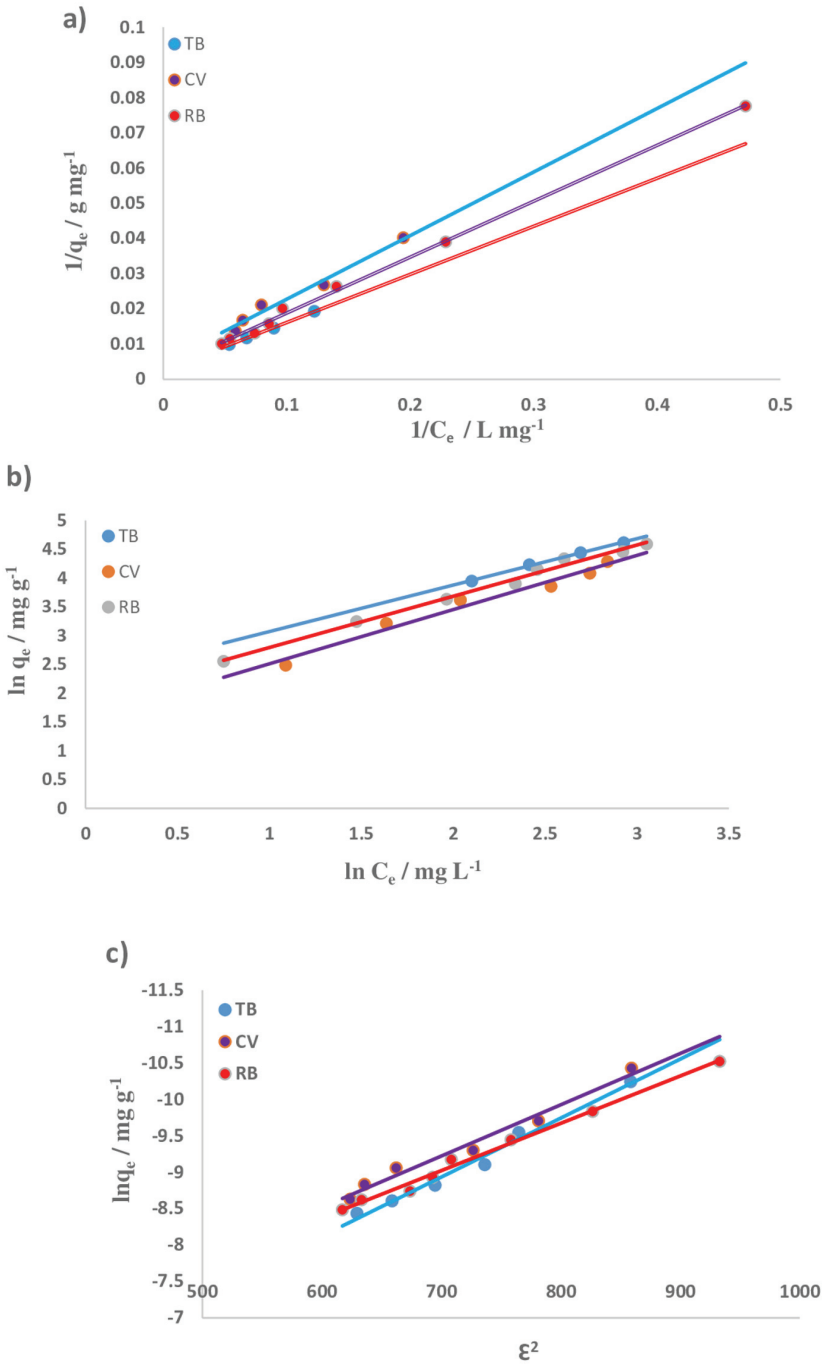


Fig. S-6. a) Langmuir; b) Freundlich; c) D-R isotherms for TB, CV, and RB.

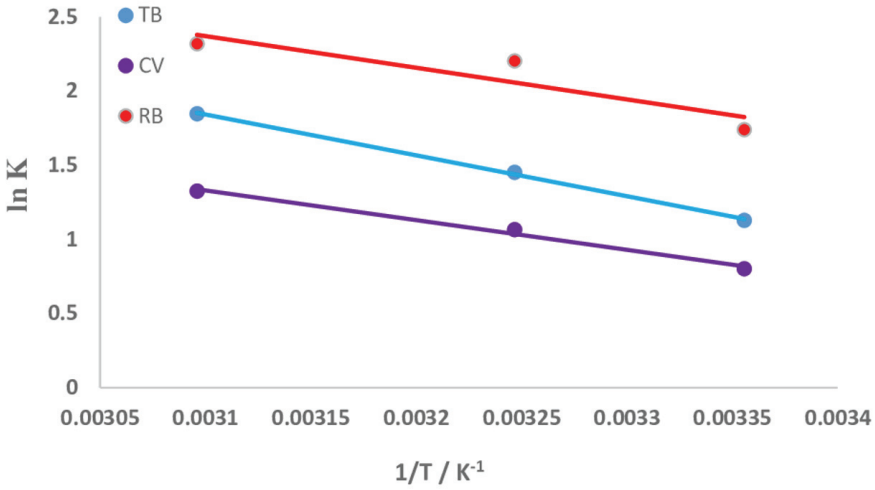


Fig. S-7. The thermodynamic plots for TB, CV, and RB adsorption.

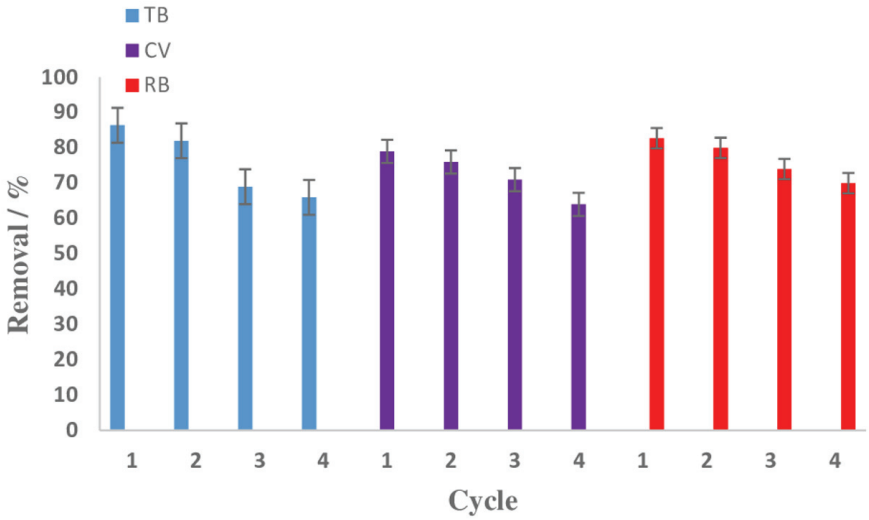


Fig. S-8. The Reusability of the LDAC for TB, CV, and RB adsorption.

Journal of the Serbian Chemical Society
JSCS@tmf.bg.ac.rs • www.shd.org.rs/JSCS
*J. Serb. Chem. Soc.* *89* (9) 1227–1240 (2024)
*JSCS–5783*
*Original scientific paper*
Published 11 September 2024

# Central composite design (CCD) and artificial neural network-based Levenberg–Marquardt algorithm (ANN–LMA) for the extraction of lanasyn black by cloud point extraction

AFAF AMARA-REKKAB[1,2]*

[1]*Institute of Science and Technology, Department of Hydraulics, University Center of Maghnia, Maghnia, Algeria and* [2]*Laboratory of Separation and Purification Technologies, Department of Chemistry - Faculty of Sciences, University of Tlemcen, Box 119, 13000, Algeria*

(Received 20 September, revised 8 November 2023, accepted 3 March 2024)

*Abstract*: The lanasyn black is among the most often used in manufacturing and is challenging to take out during the treatment of wastewaters from textile industry. The cloud point extraction was used for their elimination from an aqueous solution. The multivariable process parameters have been independently optimized using the central composite design and the Levenberg–Marquardt algorithm-based artificial neural network for the highest yield of the extraction of lanasyn black *via* the cloud point extraction. The CCD forecasts the output maximum of 97.01 % under slightly altered process parameters. Still, the ANN–LMA model predicts the extraction yield (99.98 %) using 1.04 g of $KNO_3$, the beginning pH of solution 8.99, the initial content of lanasyn black 24.57 ppm and 0.34 mass % of Triton X-100. With the coefficients of determination of 0.997 and 0.9777, the most recent empirical verification of the model mentioned above predictions using CCD and ANN–LMA is determined to be satisfactory.

*Keywords*: dyes; wastewater; extraction; optimisation; surface methodology; neural models; environment.

## INTRODUCTION

The pollutant levels in wastewater from textile manufacturers are typically high. They include up to 1 g/L of the particles and significant levels of organic contaminants in soluble and colloidal forms. In any case, their colour intensity as a function of dilution is one of the most distinctive indicators of textile industry effluent pollution.[1–4] The colour of wastewater can be mostly attributed to the

* E-mail: amarafaf@yahoo.fr
Dedicated to the memory of Professor Mohamed Amine DIDI, who passed away on January 17, 2023. You will never be forgotten, my dear Professor.
https://doi.org/10.2298/JSC230920022A

widespread use of organic dyes in the textile industry. During the manufacturing, dyes are applied to fibres, textiles and final goods, depending on the business' expertise. Between 10 and 50 % of the pigments used throughout the dying procedure are still present in the technical waste solutions and cleaning water that is produced after cleaning the dyed articles.[5] Because of this, the intensity of colour in wastewaters from textile businesses that use dyes during the production cycle might approach 1:1000. The amount of colouring and the level of dilution in the home and industrial wastewater discharged simultaneously. Using green and sustainable technology necessitates the application of alternative processes that utilise fewer organic solvents.[7]

Until now, numerous methods for removing dyes from aqueous solutions, industrial detritus and polluted water have been reported, including the following: adsorption, electrochemical process, flocculation, membrane filtration, chemical oxidation and biodegradation.[8–10]

Over the past ten years, the cloud point extraction (CPE) is an effective extraction method and has continuously developed.[11,12] CPE has several advantages over conventional pre-treatment methods, including the ease of use, increased efficiency, safety and environmental friendliness.[13] To obtain phase separation from the extraction solution, the solubilisation of the surfactant and cloud point phenomena are used primarily.[14] Typically, the hydrophilic phase of a surfactant expands in water to produce a long, flexible vermiform micelle. As a result, a tiny volume of the surfactant-rich phase might contain a large amount of the analytes that interact with micellar systems. The analytes move to the inside of the micelles and become securely attached to the hydrophobic groups once the concentration of the surfactant exceeds the micelles' critical point, and therefore micelles will form.[15,16] Contrary to the most traditional non-ionic surfactants, Triton X-100 (T100) is a non-ionic surfactant with a distinct structure of the hydrophobic component T100, specifically, features an alkyl-aryl (octyl-phenyl) group as its hydrophobic component instead of an aliphatic tail. It is widely employed in the field of biochemical research as well as in some pharmaceutical formulations and biological system applications.[17]

Clariant of Switzerland manufactures the anionic azo dye lanasyn black M--DL, also known as lanasyn black. The dye is one of the most frequently used in manufacturing and is difficult to eliminate during the effluent treatment.[5]

Our work's objective focuses on removing lanasyn black by the cloud point extraction using the non-ionic extractant T100 and the ionic liquid Aliquat 336. A salting-out technique was implemented, which permits the phase separation of surfactants with high cloud points, including T100, at room temperature. When combining a nonionic salt with an inorganic salt ($KNO_3$), the cloud point of a surfactant solution decreases as the salt concentration increases. The reason for this is because the water molecules surrounding the nonionic surfactant exhibit a

higher degree of the orientation towards the salt anions (such as $NO_3^-$) even under normal room temperature conditions.[18] The influence of function variables was studied using a central composite design and artificial neural network based on Levenberg–Marquardt algorithm. The optimal conditions of the extraction of our dye were determined.

## MATERIAL AND METHODS

### *Materials*

T Complex Textile (Soitex) in Tlemcen, Algeria, sells black lanasyn ($C_{38}H_{32}CrN_8O_{10}S_2$). Triton X-100 is a non-ionic surfactant with an HLB value of 13.5 and a critical micelle concentration (*CMC*) of $3.0\times10^{-4}$ M at 25 °C, was employed in this investigation. $KNO_3$ 99 % came from Merck, used to decrease the point cloud temperature to room temperature. Aldrich is the source of Aliquat 336 (tri-capryl-methyl-ammonium chloride, $CH_3N[(CH_2)_7CH_3]_3Cl$). Sigma–Aldrich manufactures sodium hydroxide and hydrochloric acid. Chemopharma provides the ethanol 96 % needed. To make our solutions, we used distilled water.

### *Batch extraction experiments*

Every alteration done throughout this work is based on the Triton X-100 and added mass of $KNO_3$ cloud point extraction of the organic contaminant black lanasyn (LN). At room temperature and in graduated tubes, from 1.5–4 % of Triton X-100 was added to $Na_2SO_4$ from 0.5–1 g, added to 1mL of Aliquat 336 at 0.3 M dissolved in 5 mL of the mother solution of LN from 10 to 20 ppm and then supplemented up to 10 mL with the same solution. The solution's pH ranged from 2.4–6.82. The solutions are left to stand for 30 min. Then, they were centrifuged at 2000 rpm for 10 min, and UV–Vis measures the diluted phase at the absorption band $\lambda_{max}$ = 570 nm. The various procedures taken throughout LN organic pollutant extraction using cloud point are shown in Fig. 1.

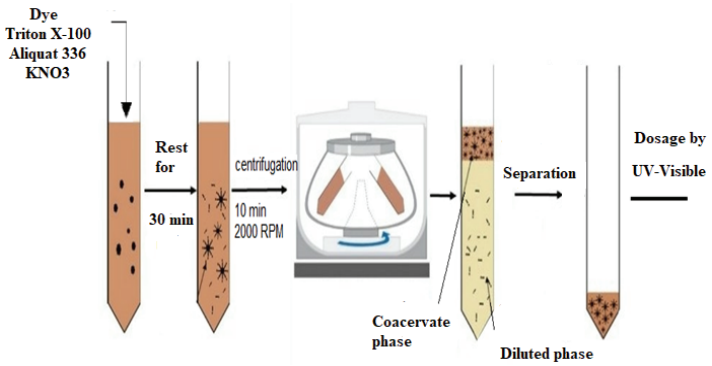


Fig. 1. Schema of the CPE of lanasyn black.

The black lanasyn solutions' UV–Vis absorbance was measured using an SP-UV 200S UV–Vis spectrophotometer. Adwa pH-metre was used to measure pH. The LN removal efficacy (%) was calculated by:[19,20]

$$\text{Removal}(\%) = 100\frac{C_i - C_e}{C_i} \quad (1)$$

where $C_i$ is the initial concentration and $C_e$ is the equilibrium concentration of LN.

*Central composite design*

The central composite design (CCD) is the most frequently employed among all multivariate methods. CCD determines how each component affects how the other factors interact. With the least amount of time and effort, this method establishes the system's ideal circumstances. This approach focuses on achieving several specific objectives, the most crucial of which is to enhance the process by identifying the best input.[21]

In this work, CCD was successfully employed to examine the impact of various variables on the effectiveness of lanasyn black's extraction by the cloud point extraction. Four distinct factors' experimental ranges and levels were selected. Table I lists the mass of $KNO_3$ ($X_1$), Triton X-100 ($X_2$), initial pH of the solution ($X_3$) and initial dye concentration ($X_4$). The following equation was used to calculate the results of 31 experimental runs. The following Equation was used to code the factors:[22–24]

$$x_i = \frac{X_i - X_0}{\Delta X} \tag{2}$$

where $x_i$, $X_i$, $X_0$, and $\Delta X$ are the coded values of the factors, their corresponding real values, the centre point of the real independent variable and the step between the real variables, respectively.

The multi-regression polynomial equation (Eq. (3)) can be used to represent the mathematical representation of relating the independent factor to the outcome:[25–27]

$$y(\%) = A_0 + \sum_{i=1}^{k} A_i X_i + \sum_{i=1}^{k} A_{ii} X_i^2 + \sum_{i=1} \sum_{j=i+1} A_{ij} X_i X_j + \varepsilon \tag{3}$$

As far as they are concerned, $A_0$ denotes the expected response, $A_i$, $A_{ii}$, $A_{ij}$ represents the constant coefficient, and $X_i$, $X_j$ represents the input components in coded values. Finally, it means the overall error. Statistical software Design Expert 13 created the response surface, contour plots and statistical data analysis.

TABLE I. Summary of CCD design

| Level | Experimental factors with their units | | | |
|---|---|---|---|---|
| | Mass of $KNO_3$ ($X_1$) | Triton X-100 ($X_2$) | pH of the solution($X_3$) | Initial dye concentration ($X_4$) |
| –2 | 0.25 | 0.025 | 0.19 | 5 |
| –1 | 0.5 | 0.15 | 2.4 | 10 |
| 0 | 0.75 | 0.275 | 4.61 | 15 |
| 1 | 1 | 0.4 | 6.82 | 20 |
| 2 | 1.25 | 0.525 | 9.03 | 25 |

*Artificial neural network–Levenberg–Marquardt algorithm (ANN–LMA)*

The artificial neural network simulation is a mathematical instrument. It predicts the linear and nonlinear relationships between multiple inputs and outputs in a complex process. Individually, ANN and CCD can be used to optimise the non-linear process parameters of our dye extraction; however, they are highly interdependent on the input parameters. Due to the presence of beams of highly corresponding elements known as neurons, ANN is regarded as more accurate than CCD.[28–30] Input, hidden and output layers are the distinct divisions of multiple neurons that comprise the ANN model. Hidden layers, which can have a single or mul-

tiple architectures, are the operating units that function as the character detectors and introduce nonlinearity into the network. The development of an ANN model is contingent upon multiple phases.[31–33] The phase of learning and the phase of validation. Using previously presented CCD data and the Levenberg–Marquardt feedback algorithm, an ANN model was developed and trained. However, the data points were generated using the second-order polynomial equation of CCD. Fig. 2 shows the simple structure of the current ANN–LMA.

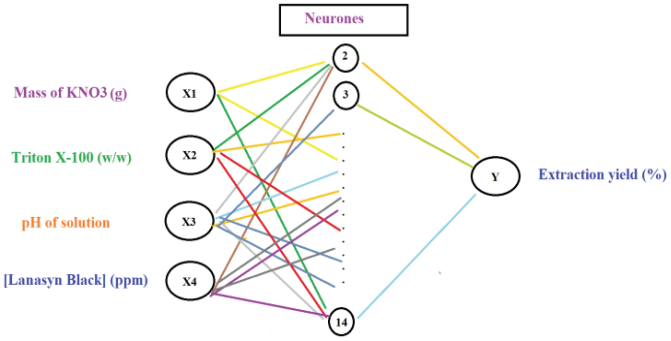


Fig. 2. Proposed modelling by ANN–LMA.

As the error functions, we used the mean absolute error (*MAE*), the mean square error (*MSE*), the root mean squared error (*RMSE*) and the absolute average deviation (*AAD*) to evaluate the performance of the ANN model for predicting the dependent variable. It is determined using the following equations:[28]

$$MAE = \left(\frac{1}{n}\right)\sum_{i=1}^{n}\left|E_{\text{model}} - E_{\text{exp}}\right| \tag{4}$$

$$MSE = \frac{\sum_{i=1}^{n}\left(E_{\text{model}} - E_{\text{exp}}\right)^2}{n} \tag{5}$$

$$ADD(\%) = \frac{100}{\text{n}}\left(\sum_{i=1}^{n}\frac{\left|E_{\text{model}} - E_{\text{exp}}\right|}{E_{\text{exp}}}\right) \tag{6}$$

$$RMSE = \sqrt{\frac{\sum_{i=1}^{n}\left(E_{\text{model}} - E_{\text{exp}}\right)^2}{n}} \tag{7}$$

## RESULTS AND DISCUSSION

### *Statistical results*

According to the combinations selected using central composite modelling, the experimental matrix shown in Table II comprises 31 experiments. Using this approach, we identified the four elements that were evaluated that were the most critical parameters and the synergic interactions.

The five-level matrix generated by CCD and ANN–LMA with the responses obtained experimentally for the extraction of our dye is shown in Table II. It is

clear from the Table II that the extraction yield was obtained around the centre of all parameters. The anion of lanasyn black, negatively charged, reacts in the coacervate phase, Triton X-100 and the ammonium cation of Aliquat 336 form mixed micelles as shown in Fig. 3.[34]

TABLE II. Experimental matrix of experimental data, CCD and ANN–LMA for the extraction of lanasyn black

| Run order | Mass of $KNO_3$ (%) | Triton X-100 (mass %) | pH | Lanasyn black (ppm) | Extraction yield (%) | Predicted value by CCD (%) | Predicted value by ANN (%) |
|---|---|---|---|---|---|---|---|
| 1 | –1 | –1 | –1 | –1 | 88.98 | 86.6054 | 88.8945302 |
| 2 | –1 | 1 | 1 | –1 | 90.22 | 89.2438 | 90.2931885 |
| 3 | 1 | 1 | –1 | 1 | 83.24 | 84.2225 | 84.1005084 |
| 4 | 1 | 1 | –1 | –1 | 91.00 | 89.8971 | 91.2489692 |
| 5 | 1 | –1 | 1 | 1 | 83.60 | 84.1642 | 84.4159927 |
| 6 | 1 | –1 | –1 | –1 | 89.83 | 92.3075 | 90.6289325 |
| 7 | 1 | –1 | 1 | –1 | 82.44 | 81.9387 | 83.89133 |
| 8 | 0 | 0 | 0 | 0 | 96.78 | 97.5114 | 97.7391311 |
| 9 | 2 | 0 | 0 | 0 | 88.26 | 86.6404 | 89.4786037 |
| 10 | 0 | 0 | 0 | 0 | 98.02 | 97.5114 | 97.7391311 |
| 11 | –1 | –1 | 1 | –1 | 82.59 | 82.7492 | 83.2669267 |
| 12 | –1 | 1 | –1 | –1 | 84.66 | 85.2375 | 83.0878711 |
| 13 | –1 | –1 | –1 | 1 | 82.30 | 84.0508 | 84.4210992 |
| 14 | 0 | 0 | 2 | 0 | 93.15 | 93.7221 | 93.9104141 |
| 15 | 1 | –1 | –1 | 1 | 84.91 | 85.1054 | 86.2595135 |
| 16 | –2 | 0 | 0 | 0 | 86.18 | 87.4388 | 87.6001534 |
| 17 | 0 | 0 | 0 | 0 | 98.00 | 97.5114 | 97.7391311 |
| 18 | 0 | 0 | –2 | 0 | 91.59 | 90.6571 | 91.4822843 |
| 19 | 0 | 0 | 0 | 0 | 97.00 | 97.5114 | 97.7391311 |
| 20 | 0 | 2 | 0 | 0 | 82.74 | 83.4954 | 83.0456114 |
| 21 | –1 | 1 | –1 | 1 | 84.49 | 84.2104 | 84.5912063 |
| 22 | 0 | 0 | 0 | 2 | 91.28 | 89.5638 | 91.6904094 |
| 23 | –1 | –1 | 1 | 1 | 89.30 | 89.6221 | 88.7290656 |
| 24 | 1 | 1 | 1 | 1 | 89.55 | 91.1438 | 91.1766252 |
| 25 | 0 | 0 | 0 | 0 | 98.02 | 97.5114 | 97.7391311 |
| 26 | –1 | 1 | 1 | 1 | 98.98 | 97.6442 | 98.3143374 |
| 27 | 0 | –2 | 0 | 0 | 79.00 | 77.8838 | 79.963546 |
| 28 | 1 | 1 | 1 | –1 | 88.00 | 87.3908 | 90.3381571 |
| 29 | 0 | 0 | 0 | 0 | 97.76 | 97.5114 | 97.7391311 |
| 30 | 0 | 0 | 0 | 0 | 97.00 | 97.5114 | 97.7391311 |
| 31 | 0 | 0 | 0 | –2 | 87.01 | 88.3654 | 89.8871532 |

On the basis of these findings, the empirical relationships between the response of CCD and selected variables have been determined:

$$\text{Extraction yield (\%)} = 97.511 - 0.200m(KNO_3) + 1.403\times\text{Triton X-100} + \\ + 0.766\text{pH} + 0.300[\text{LN}] - 2.618m(KNO_3)m(KNO_3) - 4.205\times\text{Triton}$$

$$\text{X-100}\times\text{Triton X-100} - 1.330\text{pH}\times\text{pH} - 2.137[\text{LN}][\text{LN}] - 0.261m(\text{KNO}_3)\times$$
$$\times\text{Triton X-100} - 1.628m(\text{KNO}_3)\text{pH} - 1.162m(\text{KNO}_3)[\text{LN}] + 1.966\times$$
$$\times\text{Triton X-100}\times\text{pH} + 0.382m(\text{Triton X-100})\times[\text{LN}] + 2.357\text{pH}[\text{LN}]$$

To find the significant main and interaction effects of the dye extraction parameters, an ANOVA (Table III) was performed.

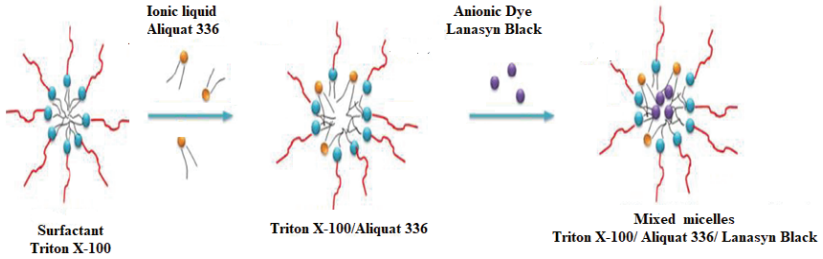


Fig. 3. Lanasyn black dye extraction using combined Triton X-100/Aliquat 336 micelles.

TABLE III. ANOVA for CCD-quadratic model

| Source | Sum of squares | *df* | Mean square | *F*-value | *p*-value | Significance |
|---|---|---|---|---|---|---|
| Model | 706.27 | 14 | 50.45 | 16.50 | < 0.0001 | Significant |
| A-Mass of $KNO_3$ | 0.9560 | 1 | 0.9560 | 0.3128 | 0.5863 | |
| B-Triton X-100 | 47.24 | 1 | 47.24 | 15.45 | 0.0020 | |
| C-pH | 14.09 | 1 | 14.09 | 4.61 | 0.0529 | |
| D-[Lanasyn black] | 2.15 | 1 | 2.15 | 0.7047 | 0.4176 | |
| AB | 1.09 | 1 | 1.09 | 0.3555 | 0.5621 | |
| AC | 42.41 | 1 | 42.41 | 13.88 | 0.0029 | |
| AD | 21.60 | 1 | 21.60 | 7.07 | 0.0209 | |
| BC | 61.82 | 1 | 61.82 | 20.22 | 0.0007 | |
| BD | 2.33 | 1 | 2.33 | 0.7633 | 0.3994 | |
| CD | 88.88 | 1 | 88.88 | 29.08 | 0.0002 | |
| $A^2$ | 146.45 | 1 | 146.45 | 47.91 | < 0.0001 | |
| $B^2$ | 377.68 | 1 | 377.68 | 123.56 | < 0.0001 | |
| $C^2$ | 37.88 | 1 | 37.88 | 12.39 | 0.0042 | |
| $D^2$ | 97.59 | 1 | 97.59 | 31.93 | 0.0001 | |
| Residual | 36.68 | 12 | 3.06 | | | |
| Lack of fit | 35.83 | 10 | 3.58 | 8.38 | 0.1113 | Not significant |
| Pure Error | 0.8552 | 2 | 0.4276 | | | |
| Cor total | 742.95 | 26 | | | | |
| Model | | | $Adeq_{Precision}$ 15.1637 | $R^2$ 95.06 % | $R^2_{(adjust)}$ 89.30 % | $R^2_{(predicted)}$ 71.97 % |

The model *F*-value of 16.50 to $F_{critic}(0.05, 14.12) = 2.65$ indicates that the model is statistically significant. There is only a 0.01 % possibility that this large cloud's *F*-value is caused by noise. *p*-Values less than 0.05 indicate the significant model terms. In this particular instance, Triton X-100, mass of $KNO_3$×pH,

mass of $KNO_3$×[Lanasyn black], Triton X-100×pH, pH×[Lanasyn black], (mass of $KNO_3$)$^2$, (Triton X-100)$^2$, pH$^2$ and [Lanasyn Black]$^2$ are significant model terms. The values exceeding 0.1000 indicate that the model terms are not statistically significant. The lack of fit *F*-value of 8.38 indicates that the lack of fit is not statistically significant in comparison to the pure error (0.05, 10.2) = 19.4. Due to noise, there is an 11.13 % probability that a lack of fit *F*-value will occur in this large cloud. The predicted $R^2$ of 0.7197 corresponds reasonably well to the adjusted $R^2$ of 0.8930, *i.e.*, the difference is less than 0.2. $Adeq_{Precision}$ measures the signal-to-noise ratio. The obtained ratio of 15.164 indicates a sufficient signal. This model can be used to navigate the design space.

*Contour plots and response surfaces*

Fig. 4 is a graphical representation of the correlations between significant, optimal values and the specific output variability by the contour plots and response surface. By the possible point extraction, these images aid in understanding and describing the combined impact of the two variables on lanasyn black extraction.[35] Depending on the contour plot's morphologies, the interaction's significance may be high if the contour plot is elliptical and saddle-shaped, but low if it depicts a circular shape. The maximum response value under the influence of the operational inputs was effectively determined by keeping the remaining pair of factors at their midpoint at the same time.[36]

The elliptical contour diagrams depict the significant impact of interactions between the mass of $KNO_3$×pH, mass of $KNO_3$×[Lanasyn black], Triton X--100×pH, and pH×[Lanasyn black]. The maximum extraction yield was achieved at the centre level of all parameters, suggesting significance.

*Response optimization*

The response optimization was used to optimize the extraction in MINITAB 19.0, and the experiment was run at the specified solution, yielding an extraction rate of 97.87 %, which was extremely close to the predicted value. The mass of $KNO_3$ was 1.07575 g, Triton X-100 was 0.368 mass %, the beginning pH of the solution was 9.03, the initial concentration of black lanasyn was 22.575 ppm, and this combination produced the highest extraction yield.

*ANN–LMA modelling*

Using a feed-forward back propagation network and the Levenberg–Marquardt algorithm, the ANN-GA model was developed. Three data set subdivisions were generated. Each subset contained 80 % of the testing data, 10 % of the validation data, and 10 % of the network training data. It is important to note that these divisions were wholly arbitrary. The inputs and outputs are immutable elements of the ANN's topology (architecture). Moreover, the number of concealed layers and their respective neurons represent a series of variable elements.

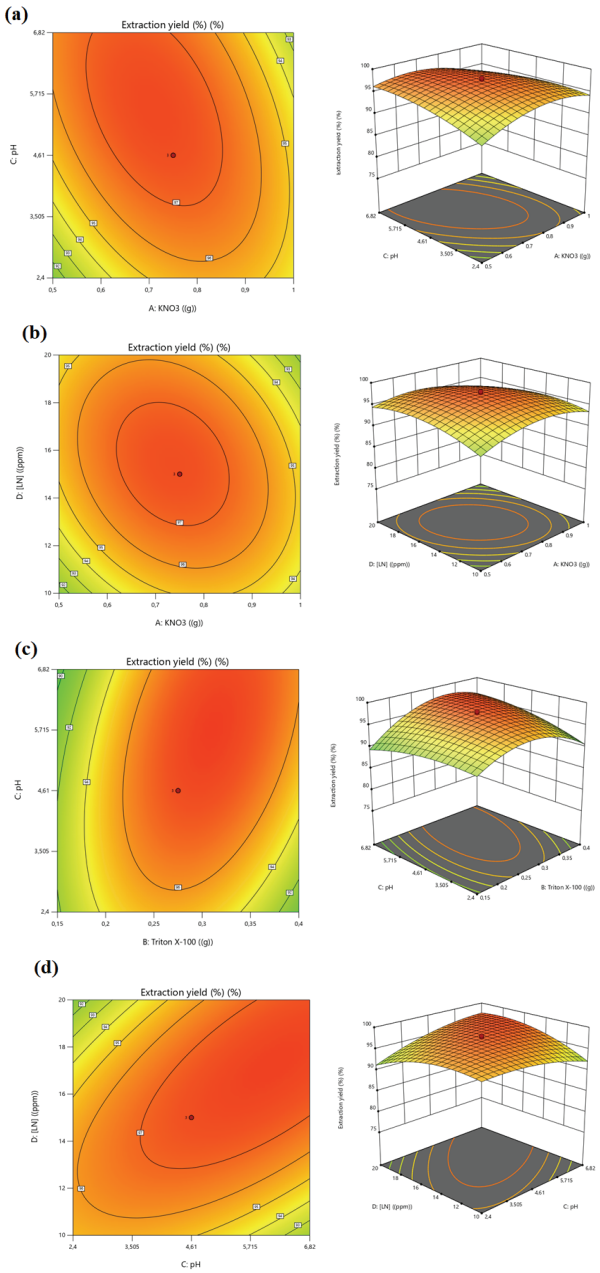


Fig. 4. Contour plots and response surface of the effects: a) mass of $KNO_3$ and initial pH of the solution; b) mass of $KNO_3$ and initial concentration of Lanasyn black; c) Triton X-100 and initial pH of the solution; d) initial pH of the solution and initial concentration of lanasyn black on the extraction of lanasyn black by cloud point extraction.

Fig. 5 shows that the learning converged after 9 periods with the lowest average square error. Thus, during the ANN iterative learning, the model achieved a maximum R-value of 0.987772 (Fig. 6a) and a minimum MSE value of $2.0727 \times 10^{-3}$ (Fig. 6b) at nine epochs for ten neurons in the hidden layer. Therefore, the best 4–10–1 network architecture is used for the process optimization, representing 4 entries in the first layer, 10 hidden neurons, and one upper layer output. The $R^2$ value close to 1 and a low MSE value indicate that the performance of the developed model is satisfactory and corresponds to the experimental extraction values of the LN per point of disruption.

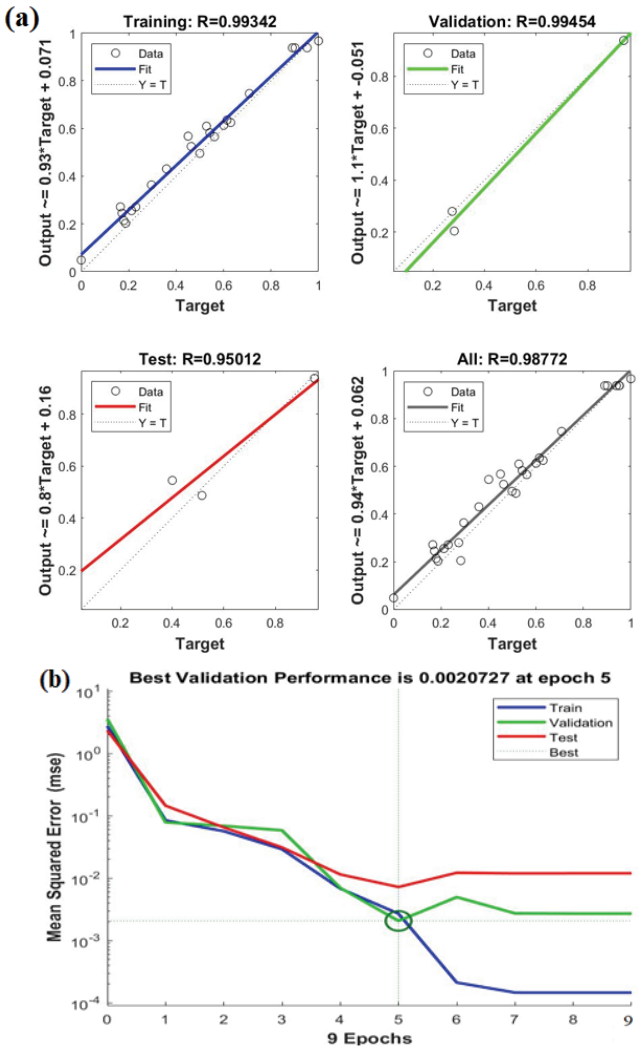


Fig. 5. Regression and performance plots of the ANN–LMA model.

The reliability of the here given model for predicting the maximum output data was confirmed while using the optimal points suggesting the ANN[37] ($KNO_3$ mass: 1.04 g; beginning pH of solution 8.99, initial of Black Lanasyn 24.57 ppm, and 0.34 mass% of Triton X-100). The extraction yield of the experimentally recorded LN was 99.98 % suggesting the suitability and validity of the model. However, the optimums achieved by ANN resulted in an even higher extraction yield than with CCD modelling.[38–41]

*Comparative study between CCD and ANN–LMA*

In order to evaluate the efficacy of the CCD and ANN models, the outputs were compared to the relevant experimental data, Fig. 6.

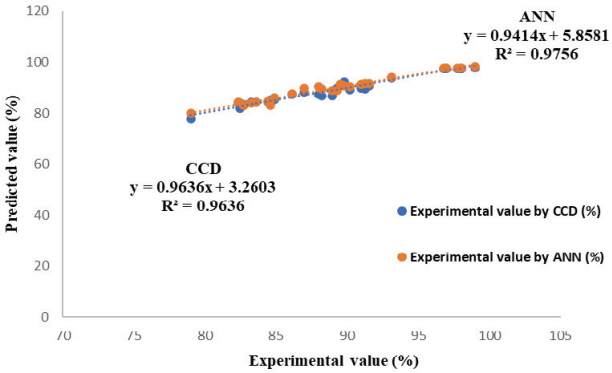


Fig. 6. Comparative parity diagram of experimental and predicted results.

The determination coefficient $R$ = 0.97498 for the CCD model and $R$ = = 0.98772 for the ANN model shows that the values of the model-based predictions are in perfect accordance with the experimental results.

As a result, the proposed models are well-adapted to data and provide stable responses. However, compared to the RSM model, the ANN model has a higher predictive capacity and accuracy based on the experimental results. The $R$ value is closer to 1.0.

In addition to the regression coefficient ($R$), the observed *MAE*, *MSE*, *AAD*, and *RMSE* values for both models were determined to provide a statistical indication of the accuracy of the model predictions. The *MAE*, *MSE*, *AAD* and *RMSE* values for the CCD and ANN models have been calculated and are presented below.

The *MAE* (0.1203), *MSE* (0.4488), *AAD* (0.1363 %) and *RSME* (0.6699) for the CCD model are higher than those (0.0955, 0.2831, 0.1097 and 0.5321 %, respectively) for the ANN model. This means the ANN model offers a higher modelling capacity than the CCD model. This result is similar to several researchers.[42,43]

## CONCLUSION

The lanasyn black was obtained by the textile sector, and is among of the more frequently used in manufacturing. It is difficult to remove during wastewater treatment. Their removal in an aqueous solution was accomplished by the cloud point extraction. For the most significant yield of the extraction of lanasyn black using the cloud point extraction, the multivariable process parameters have been independently optimized using the central composite design (CCD) and artificial neural network–Levenberg–Marquardt algorithm (ANN–LMA). The ANN–LMA model predicts the extraction yield (99.98 %) in the optimal conditions. The most recent experimental validation of the model mentioned above predictions using ANN–LMA and CCD is found to be good, with coefficients of determination of 0.997 and 0.9777, respectively.

## ИЗВОД

## ЦЕНТРАЛНИ КОМПОЗИТНИ ДИЗАЈН (CCD) И LEVENBERG–MARQUARDT АЛГОРИТАМ ЗАСНОВАН НА ВЕШТАЧКОЈ НЕУРОНСКОЈ МРЕЖИ (ANN–LMA) ЗА ИЗДВАЈАЊЕ ЛАНАСИН ЦРНЕ БОЈЕ ЕКСТРАКЦИЈОМ У ТАЧКИ ЗАМУЋЕЊА

AFAF AMARA-REKKAB[1,2]

*[1]Institute of Science and Technology, Department of Hydraulics, University Center of Maghnia, Maghnia, Algeria u [2]Laboratory of Separation and Purification Technologies, Department of Chemistry – Faculty of Sciences, University of Tlemcen, Box 119, 13000, Algeria*

Ланасин црна боја је међу најчешће коришћеним у производњи, нарочито текстилној индустрији, и тешко је уклонити је током третмана отпадних вода. За њену елиминацију у воденом раствору коришћена је екстракција у тачки замућења. Параметри мултиваријантног процеса су независно оптимизовани коришћењем централног композитног дизајна и вештачке неуронске мреже, засноване на Levenberg–Marquardt алгоритму за највећи принос екстракције Ланасин црне боје у тачки замућења. CCD предвиђа излазни максимум од 97,01 %, под благо измењеним параметрима процеса. Ипак, ANN–LMA модел предвиђа принос екстракције од 99,98 %, користећи количину $KNO_3$ од 1,04 g, почетни pH раствора 8,99, почетну вредност ланасин црне боје од 24,57 ppm и 0,34 мас. % Тритона X-100. Са коефицијентима детерминације од 0,997 и 0,9777, одређена је задовољавајућа најновија емпиријска верификација предвиђања модела помоћу CCD и ANN–LMA.

(Примљено 20. септембра, ревидирано 8. новембра 2023, прихваћено 4. марта 2024)

## REFERENCES

1. D. A. Yaseen, M. Scholz, *Int. J. Environ. Sci. Technol.* **16** (2019) 1193 (https://doi.org/10.1007/s13762-018-2130-z)
2. B. K. Nandi, A. Goswami, M. K. Purkait, *Appl. Clay. Sci.* **42** (2009) 583 (https://doi.org/10.1016/j.clay.2008.03.015)
3. I. G. Krasnoborodko, *Destructive wastewater treatment from dyes*, L: Chemistry, 1988
4. M. Ghaedi, H. Hossainian, M. Montazerozohori, A. Shokrollahi, F. Shojaipour, M. Soylak, M. K. Purkait, *Desalination* **281** (2011) 226 (https://doi.org/10.1016/j.desal.2011.07.068)

5. V. Geissen, H. Mol, E. Klumpp, G. Umlauf, M. Nadal, M. D. Ploeg, S. E. A. T. M. van de Zee, C. J. Ritsema, *Int. Soil Water Conserv. Res.* **3** (2015) 57 (https://doi.org/10.1016/j.iswcr.2015.03.002)
6. N. E.Djebbari, A. Amara, A. Didi, M. A. Didi, *Sci. Study Res. Chem. Chem. Eng., Biotech., Food Ind.* **23** (2022) 333 (https://pubs.ub.ro/dwnl.php?id=CSCC6202204V04S01A0005)
7. H. Chandarana, P. Senthil Kumar, M. Srinivasan, M. Anil Kumar, *Chemosphere* **285** (2021) 131480 (https://doi.org/10.1016/j.chemosphere.2021.131480)
8. M. K. Dahri, M. R. R. Kooh, L. B.L. Lim, *Alex. Eng. J.* **54** (2015) 1253 (https://doi.org/10.1016/j.aej.2015.07.005)
9. E. Brillas, E.Mur, R. Sauleda, L. Sanchez, J. Peral, X. Domenech, J. Casado, *Appl. Catal., B* **16** (1998) 31 (https://doi.org/10.1016/S0926-3373(97)00059-3)
10. P. Liang, J. Li, X. Yang, *Microchim Acta* **152** (2005) 47 (https://doi.org/10.1007/s00604-005-0415-7)
11. D. Snigur, E. A. Azooz, O. Zhukovetska, O. Guzenko, W. Mortada, *TrAC, Trends Anal. Chem.* **164** (2023) 117113 (https://doi.org/10.1016/j.trac.2023.117113)
12. R. Halko, I. Hagarová, V. Andruch, *J. Chromatogr., A* **1701**(2023) 464053 (https://doi.org/10.1016/j.chroma.2023.464053)
13. H. S. Ferreira, M. A. Bezerra, S.L.C. Ferreira, *Microchim. Acta* **154** (2006) 163 (https://doi.org/10.1007/s00604-005-0475-8)
14. W. R. Melchert, F. R. P. Rocha, *Rev. Anal. Chem.* **35** (2016) 41 (https://doi.org/10.1515/revac-2015-0022)
15. J. Yongsheng, W. Le, L. Ruihong, W. Haohao, S. Shuhui, C. Mingzhuo, *ACS Omega* **6** (2021) 13508 (https://doi.org/10.1021/acsomega.1c01768)
16. M.N. Jones, *Int. J. Pharm.* **177** (1999) 137 (https://doi.org/10.1016/s0378-5173(98)00345-7)
17. A. Amara-Rekkab, M.A. Didi, *Desalin. Water Treat.* **281** (2022) 186 (https://doi.org/10.5004/dwt.2023.29147)
18. N. Sato, M. Morin, H. Itabashi, *Talanta* **117** (2013) 376 (https://doi.org/10.1016/j.talanta.2013.08.025)
19. A. Asfaram, M. Ghaedi, A. Goudarzi, M. Rajabi, *Dalton Trans.* **44** (2015) 14707 (https://doi.org/10.1039/C5DT01504A)
20. G. Hanrahan, K. Lu, *Crit. Rev. Anal. Chem.* **36** (2006) 141 (https://doi.org/10.1080/10408340600969478)
21. M. Boulahbal, M. A. Malouki, M. Canle, Z. Redouane-Salah, S. Devanesan, M. S. AlSalhi, M. Berkani, *Chemosphere* **306** (2022) 135516 (https://doi.org/10.1016/j.chemosphere.2022.135516)
22. H. Ucbeyiay, *Fuel Process. Technol.* **106** (2013) 1 (https://doi.org/10.1016/j.fuproc.2012.09.020)
23. G. E. B. Box, W.G. Hunter, J.S. Hunter, *Statistics for Experimenters*, 2nd ed., Wiley-Interscience, Hoboken, NJ, 1978
24. T. Mehmood, A. Ahmed, A. Asif, A. M. Sheeraz, M. A. Sandhu, *Food Chem.* **253** (2018) 179 (https://doi.org/10.1016/j.foodchem.2018.01.136)
25. S.I.S. Al-Hawary, K. Azhar, S. A. Sherzod, A.K. Kareem, K. A. Alkhuzai, R. R. M. Parra, A. H. Amini, T. Alawsi, M. Abosaooda, M. Dejaverdi, *Alex. Eng. J.* **74** (2023) 737 (https://doi.org/10.1016/j.aej.2023.05.066)
26. K. Behera, H. Meena, S. Chakraborty, B.C. Meikap, *Int. J. Min. Sci. Technol.* **28** (2018) 621 (https://doi.org/10.1016/j.ijmst.2018.04.014)

27. M. Maleki-Kakelar, A. Aghaeinejad-Meybodi, S. Sanjideh, M. J. Azarhoosh, *Environ. Proc.* **9** (2022) 7 (https://doi.org/10.1007/s40710-022-00564-0)
28. P. Mondal, A. K. Sadhukhan, A. Ganguly, P. Gupta, *3 Biotech* **11** (2021) 28 (https://doi.org/10.1007/s13205-020-02553-2)
29. N. Teslić, N. Bojanić, D. Rakić, A. Takači, Z. Zeković, A. Fišteš, M. Bodroža-Solarov, B. Pavlić, *Chem. Eng. Process.* **143** (2019) 107634 (https://doi.org/10.1016/j.cep.2019.107634)
30. B. Jiang, F. Zhang, Y. Sun, X. Zhou, J. Dong, L. Zhang, *J. Taiwan Inst. Chem. Eng.* **45** (2014) 2217 (https://doi.org/10.1016/j.jtice.2014.03.020)
31. A. Çelekli, H. Bozkurt, F. Geyik, *Bioresour. Technol.* **129** (2013) 396 (https://doi.org/10.1016/j.biortech.2012.11.085)
32. A. Smaali, M. Berkani, F. Merouane, V.T. Le, Y. Vasseghian, N. Rahim, M. Kouachi, *Chemosphere* **266** (2021) 129158 (https://doi.org/10.1016/j.chemosphere.2020.129158)
33. K. Oukebdane, R. Semmoud, M.A. Didi, *Desalin. Water Treat*. **247** (2022) 272 (https://doi.org/10.5004/dwt.2022.28039)
34. M. Berkani, M. Bouhelassa, M. K. Bouchareb, *Arab. J. Chem.* **12** (2019) 3054 (https://doi.org/10.1016/j.arabjc.2015.07.004)
35. D. Bas, I. Boya, *J. Food Eng.* **78** (2007) 836 (https://doi.org/10.1016/j.jfoodeng.2005.11.024)
36. M. Pravitha, M. R. Manikantan, V. Ajesh Kumar, S. Beegum, R. Pandiselvam, *LWT* **146** (2021) 111441 (https://doi.org/10.1016/j.lwt.2021.111441)
37. J. Han, M. Kamber, J. Pei, *Data Mining: Concepts and Techniques*, 3rd ed., Morgan Kaufmann, 2012.
38. E. Bello, T. Ogedengbe, M. Khumbulani, I. Daniyan, *Procedia CIRP* **89** (2020) 59 (https://doi.org/10.1016/j.procir.2020.05.119)
39. R. Pandiselvam, M. R. Manikantan, S. Sunoj, S. Sreejith, S. Beegum, *J. Food Process Eng.* **42** (2019) e12981 (https://doi.org/10.1111/jfpe.12981)
40. S. Youssefi, Z. Emam-Djomeh, S. M. Mousavi, *Drying Technol.* **27** (2009) 910 (https://doi.org/10.1080/07373930902988247)
41. V. Ajesh Kumar, S. Prem Prakash, M. Pravitha, H. Muzaffar, M. Shukadev, V. Prithviraj, V. Deepak Kumar, *Food Pack. Shelf Life* **31** (2022) 100778 (https://doi.org/10.1016/j.fpsl.2021.100778)
42. A. J. Sisi, A. Khataee, M. Fathinia, B. Vahid, Y. Orooji, *J. Mol. Liq.* **316** (2020) 113801 (https://doi.org/10.1016/j.molliq.2020.113801)
43. Z. Jun, C. Leland, S. Dongyi, W. Y. Zhan, *Appl. Energy* **345** (2023) 121373 (https://doi.org/10.1016/j.apenergy.2023.121373).

Journal of the Serbian Chemical Society
JSCS@tmf.bg.ac.rs • www.shd.org.rs/JSCS
*J. Serb. Chem. Soc.* *89* (9) 1241–1253 (2024)
*JSCS–5784*
*Original scientific paper*
Published 11 September 2024

# Introductory concept for teaching chirality – Symmetry of the asymmetric

BRANISLAV Z. KOKIĆ[1]*#, VLADIMIR D. AJDAČIĆ[1#], IGOR M. OPSENICA[2#] and MARIO V. ZLATOVIĆ[2#]

*[1]Innovative centre, Faculty of Chemistry, Belgrade, Ltd., Studentski trg 12–16, 11158 Belgrade, Serbia and [2]University of Belgrade, Faculty of Chemistry, Studentski trg 12–16, 11158 Belgrade, Serbia*

(Received 3 August 2023, revised 11 September 2023, accepted 15 March 2024)

*Abstract*: Chirality is traditionally a problematic subject for undergraduate students at the beginning of learning organic chemistry, yet it is of great importance in life sciences. If the initial introduction of chirality is conducted carelessly, students will face ambiguity through the rest of the course and education every time they come across chirality-related subjects. Although there are numerous methods for overcoming the problems of visualization of chiral molecules in 3D space, the connection of chirality with molecular changes like vibrations and conformations is usually not explained thoroughly. In this work, chirality is introduced on dynamic (real) systems, because students from the start should perceive molecules in their natural state of constant motion and change. Apart from the proposition of the lecture concept, exercises are also included, that employ free and readily available software.

*Keywords*: second-year undergraduate; organic chemistry; stereochemistry, pedagogy.

## INTRODUCTION

Students often have problems with the perception of chirality in bachelor studies.[1] Because of that, great effort has been put into searching for an efficient method for facilitating students' visualization of chirality in 3D space.[2] But molecules are dynamic and the inclusion of molecular changes in chirality principles is essential for understanding real systems. We propose a method for the inclusion of molecular changes in chirality lectures, to complement the well-established concept of chirality introduction in undergraduate courses. It relies on the basic

* Corresponding author. E-mail: kokicb@chem.bg.ac.rs
# Serbian Chemical Society member.
https://doi.org/10.2298/JSC230803032K

knowledge of chemical equilibrium and chemical kinetics, as well as molecular motions and bonding, which is usually taught in general chemistry courses.

Traditionally, chirality is introduced firstly on asymmetric tetrahedral C--atoms. We suggest that dynamicity should be taken into account from the start and the introduction of chirality can be exemplified on the three case studies, describing tetrahedral C-atoms at the end of the lecture. By this approach, atropisomerism can be an integral part of the lecture and it is usually taught afterward or in higher courses.

Also, clips of molecular motions are available for better following of the lecture. Exercises that utilize free and readily available software are also provided.

## CHIRALITY IN DYNAMIC SYSTEMS

Objects that are non-superposable on their mirror image are said to be chiral.[3] Familiarity with mirror reflection from everyday life makes this approach universal for teaching. After this initial introduction of the chirality definition, we propose that students should be familiarized with the fact that enantiomers ($E_1$ and $E_2$) in achiral environment have the same standard enthalpy of formation and standard entropy. However, enantiomers don't have exactly the same amount of energy. It is estimated that the difference in energy between enantiomers for typical chiral molecules is in the order of magnitude $10^{-15}$ kJ/mol.[4] This is the consequence of the phenomenon called parity violation and is caused by the intrinsically chiral nature of the weak nuclear force. But for all practical purposes, it is precise enough to consider that the system that consists solely of $E_1$ molecules has the same energy as the system that consists solely of $E_2$ molecules. Since there are no thermodynamical preferences for one of these states, equilibrium is reached when there is an equal number of enantiomers $E_1$ and $E_2$ in the system (derivation of this statement is provided in the Supplementary material to this paper):

$$E_1 \rightleftharpoons E_2 \tag{1}$$

$$K = \frac{[E_2]}{[E_1]} = 1 \tag{2}$$

$$\Rightarrow [E_1] = [E_2] \tag{3}$$

where $E_1$ and $E_2$ are enantiomers, $[E_1]$ and $[E_2]$ are their concentrations and $K$ is the equilibrium constant for the Eq. (1).

In other words, chiral systems thermodynamically tend to racemize. Chiral molecules will racemize if there is a way for that (molecules can undergo only those changes which energy barrier they can overcome). The speed of racemization is never zero. The question of practical importance is how fast is it happening.[5]

## MOLECULAR CHIRALITY

If we want to consider real molecular systems we have to be aware of their real state, since, after all, we want to determine stereochemical properties of a real molecule and not of its model. Standard drawings with dashed lines help us visualize the molecules and are routinely used in chemistry practice. However, we have to be aware of their limitations.[6] Atoms in a molecule are not static, *i.e.*, bond angles and bond lengths are rapidly changing (literature values for bond lengths and bond angles are average values).[7] Also, there is another change that molecules undergo: rotation about the C–C bond.[7] The importance of the awareness of all molecular motions has been emphasized recently and animations were proposed as a tool for the effective inclusion of these motions in the curriculum.[8] The impact of molecular changes on chirality properties is analyzed through the following case studies.

*Case study #1*

Bromochloromethane is a good example for bond length and bond angle changes because it does not have conformation isomers. Among many structures of bromochloromethane, which are produced by these changes, the ones in which two C–H bonds are not the same length are chiral (Fig. 1, the difference in bond lengths in **3** and **4** is exaggerated for clarity); animation is available at http:// //cherry.chem.bg.ac.rs/handle/123456789/5945. Also, structures that have two different HCCl angles or two different HCBr angles ($\theta$ and $\theta$' in the Fig. 1) are chiral; animation is available at http://cherry.chem.bg.ac.rs/handle/123456789/5946. Simpler – desymmetrization of two hydrogens produces a chiral structure.

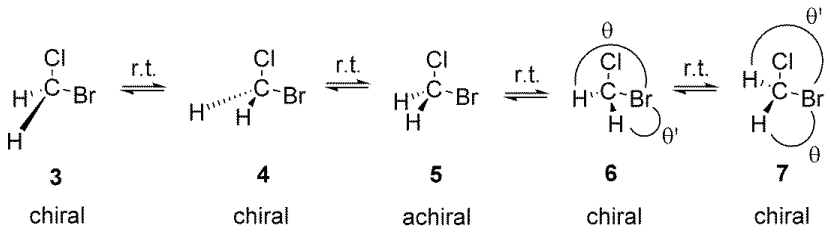


Fig. 1. Macroscopic sample of bromochloromethane contains great number of different molecular structures, which differ in bond angles and bond lengths. All those structures are in dynamic equilibrium. Some of them are chiral.

These "bond length enantiomers" (**3** and **4** in Fig. 1) and "bond angle enantiomers" (**6** and **7** on Fig. 1) are rapidly interconverting and in an achiral environment they are in equilibrium that is a racemic mixture (Eq. (3)). In a system that consists of a great number of bromochloromethane molecules, every chiral structure will have its enantiomer present in the system in the equal amount (Fig. 2).

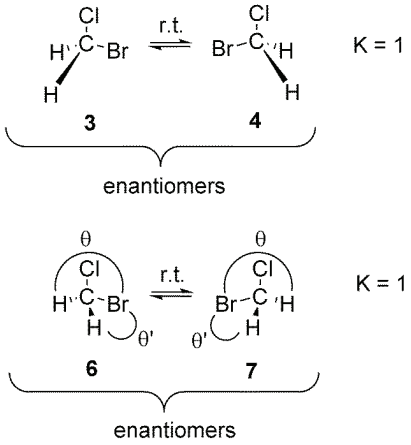


Fig. 2. Every chiral structure of bromochloromethane has its enantiomeric pair present in the system in the equal amount, because the system is in equilibrium.

The reason why we don't call this system – a racemic mixture of bond-length and bond-angle enantiomers is because we cannot separate these enantiomers. They are rapidly interconverting. If we imagine that we somehow separate one type of chiral molecules from the mixture, the moment we put them to ambient conditions they will equilibrate to a racemic system, identical to the one we have separated them from. This resembles the phenomenon of cutting the north pole of the magnet from the south pole – it results in two magnets with north and south poles (Fig. 3).

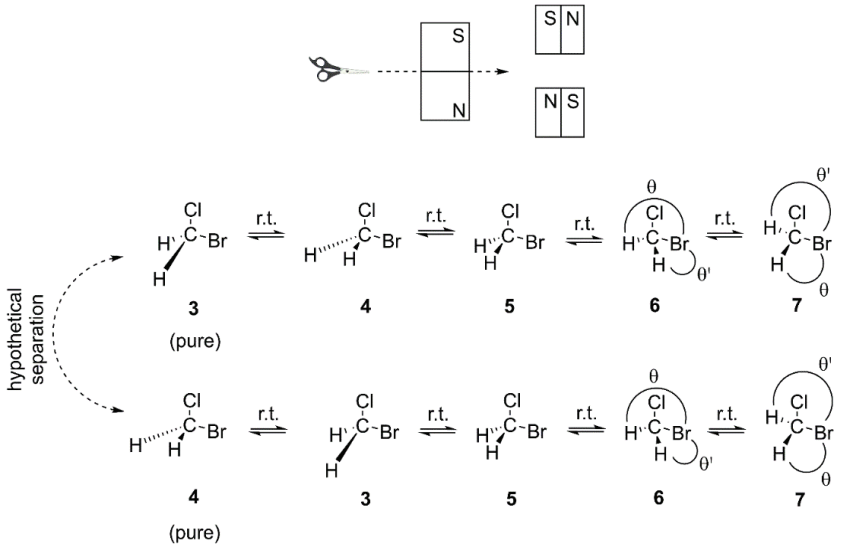


Fig. 2. Analogy between fast racemization and poles of a magnet. Separation will result in two systems, which are identical as the starting one.

Because of that, we call a system consisting of bromochloromethane molecules achiral under ambient conditions, or simpler, we call a bromochloromethane an achiral molecule (Fig. 4).

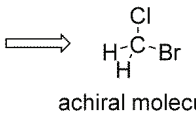


Fig. 4. Bromochloromethane is considered achiral because it does not exhibit chiral properties in contact with other systems and is not considered a racemic mixture because the separation of its chiral constituents is practically impossible.

In the following text, changes in bond angles and bond lengths will be neglected for simplicity, but they are always happening.

In Supplementary material, there is detailed practice on computational prediction of the IR spectrum of any molecule and generation of vibration animations using readily available free software.

*Case study #2*

Let's now consider 1,2-dibromoethane. Besides the mentioned bond angle and bond length changes, rotation about the C–C bond also takes place.[7] The energy required for the full rotation of the C–C bond in this molecule is 42 kJ/mol (10 kcal/mol).[9] This is relatively a small amount of energy and is accessible to molecules on ambient conditions. Every conformation is chiral except two (**8** and **11** in Fig. 5). Every chiral conformation can transform into its enantiomer by rotation about the C–C bond – two examples are depicted in Fig. 5. All conformational enantiomers are equilibrated and the system is achiral (animation is available at http://cherry.chem.bg.ac.rs/handle/123456789/5947). The equilibration is rapid at room temperature (if we somehow manage to isolate a chiral conformer, half of the sample will racemize in just $10^{-6}$ s) and consequently, separation of different chiral conformations is impossible. So we call the system "achiral", rather than "racemic mixture". Simpler, we call a 1,2-dibromoethane an achiral molecule.

The energy barrier for conformational enantiomer equilibration at room temperature depends on the molecular structure. In some cases, the barrier is high and the rotation about the C–C bond requires a significant amount of time and enantiomers are experimentally isolable on ambient conditions. These systems are considered chiral. For example, compound **14** ((*S*)-2,2',3,5',6-pentachloro-1,1'--biphenyl) can transform into its enantiomer (**15**) by simple rotation about C–C bond, but the energy barrier for this process is 184 kJ/mol (44 kcal/mol) in this case (animation is available at http://cherry.chem.bg.ac.rs/handle/123456789/5948). This amount of energy is too high for the equilibration of **14** and **15** at room temperature at a significant rate (half of the sample of pure **14** will racemize in 300 billion years, Fig. 6).[11]

At higher temperatures, molecules have more energy and equilibration is faster (at 300 °C half the sample of pure compound **14** racemizes in half an hour).

But the criterion for calling something "chiral" is based on the practical ability to isolate something at room temperature. Because of that, we consider **14** a chiral compound, in spite of the fact that we can induce its rapid racemization at elevated temperatures. Besides temperature, other factors can accelerate the racemization process. For example: solvents, catalysts, acids, bases, *etc.*

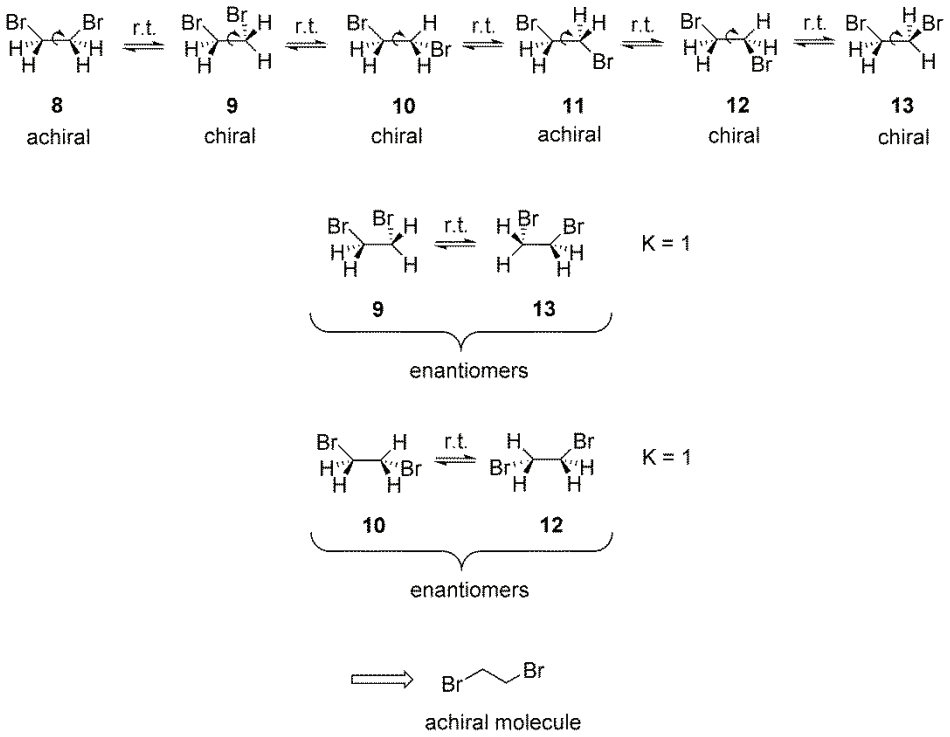


Fig. 5. Conformational changes in the molecules of 1,2-dibromoethane lead to the formation of different chiral structures, which are equilibrated with their enantiomers. Equilibration is fast, so separation of chiral constitutes is practically impossible and 1,2-dibromoethane is considered an achiral molecule.

When the interconversion of conformational enantiomers is rapid at room temperature a similar system is considered achiral, analogous to 1,2-dibromoethane. For example, interconversion of **16** and **17** (3'-isopropyl-2-methyl-1,1'--biphenyl) requires 29 kJ/mol (7 kcal/mol) of energy, so these enantiomers are not isolable at ambient conditions (time needed for the racemization of half of the sample of pure **16** on room temperature is in the order of $10^{-9}$ s) and the compound is considered achiral. The example can be seen in Fig. 7 and animation is available at http://cherry.chem.bg.ac.rs/handle/123456789/5949).[12]

At this point, the introduction of an atropisomerism is consequential from everything mentioned so far, rather than a special case, how it is usually taught.

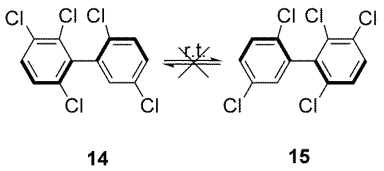


**14** **15**

interconversion of conformational enantiomers is slow

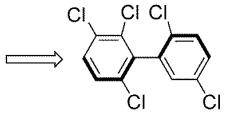


**14**
chiral molecule

Fig. 6. An example of a compound which chiral conformations are not rapidly interconverting. Separation of its chiral constitutes is possible. It is considered chiral.

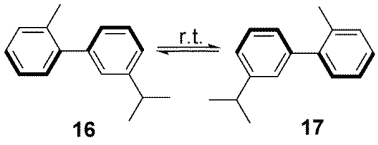


**16** **17**

interconversion of conformational enantiomers is rapid

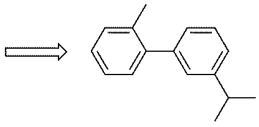

achiral molecule

Fig. 7. An example of a compound which is considered achiral for the same reasons as 1,2-dibromoethane. Fast racemization (conformational equilibration) on ambient conditions makes its chirality unobservable in most experiments.

In Supplementary material are provided tasks in which students need to calculate energy barriers of biphenyls and to propose their configurational stability based on the calculations. The procedure is explained in detail using free readily available software.

Schäfer et al. pointed out that often achiral substance is dominantly composed of chiral structures (because those chiral structures are the most stable form of that compound).[13]

*Case study #3*

Chiral amines that contain an asymmetrically substituted nitrogen atom can racemize by the mechanism that is called pyramidal inversion. For ordinary amines, on average, 29 kJ/mol (7 kcal/mol) is needed for the inversion to take place.[14] So ordinary amines racemize rapidly (half the sample of an ordinary amine racemizes in $10^{-9}$ s) at room temperature and because of that are not considered chiral (Fig. 8).

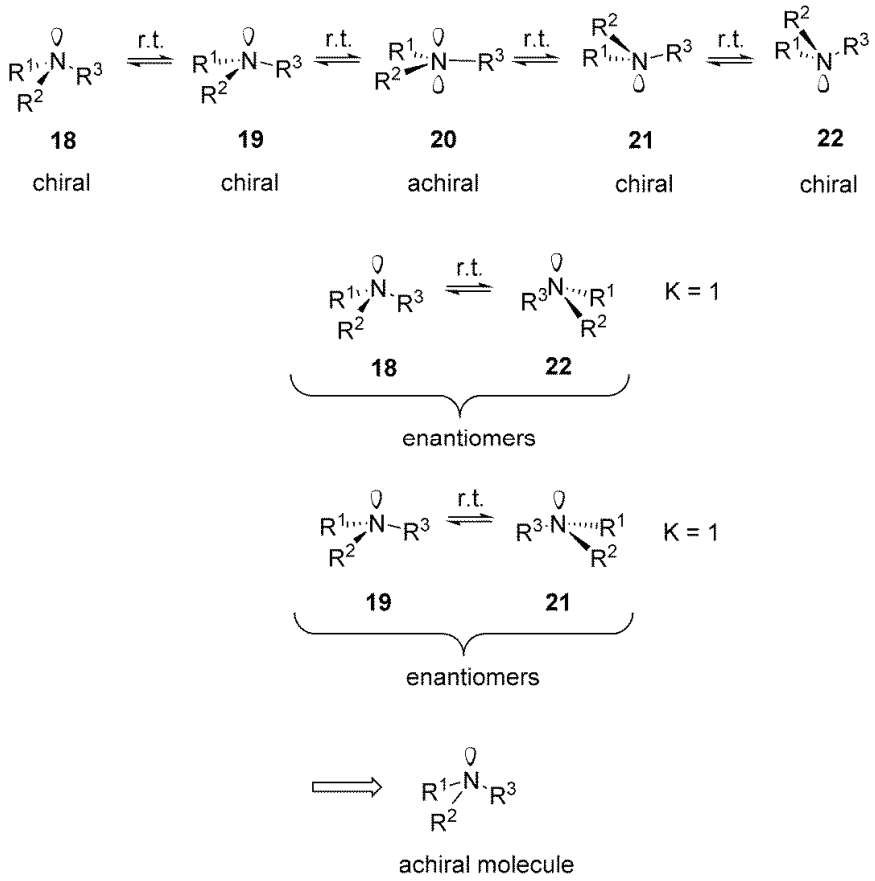


Fig. 8. Although amines racemize by different mechanism, inspection of their chirality follows the same pattern as for the molecules mentioned so far. Fast racemization (equilibration) of chiral structures leads to an achiral system.

For comparison, chiral sulfoxides that contain an asymmetrically substituted sulfur atom are usually configurationally stable at room temperature, but racemize at elevated temperatures.[15] Mechanism for their racemization depends on the structure. Some sulfoxides undergo pyramidal inversion, just like amines. But the energy required for pyramidal inversion at sulfur is much greater: for example, 171 kJ/mol (41 kcal/mol) for methyl phenyl sulfoxide.[16] This amount of energy is relatively high and racemization on ambient temperature for this molecule takes billions of years (half of the sample racemizes in 2 billion years). But, at 214 °C half of the sample will racemize in just one day (Fig. 9).

But methyl phenyl sulfoxide is considered chiral, because enantiomers are isolable at ambient conditions (Fig. 10).

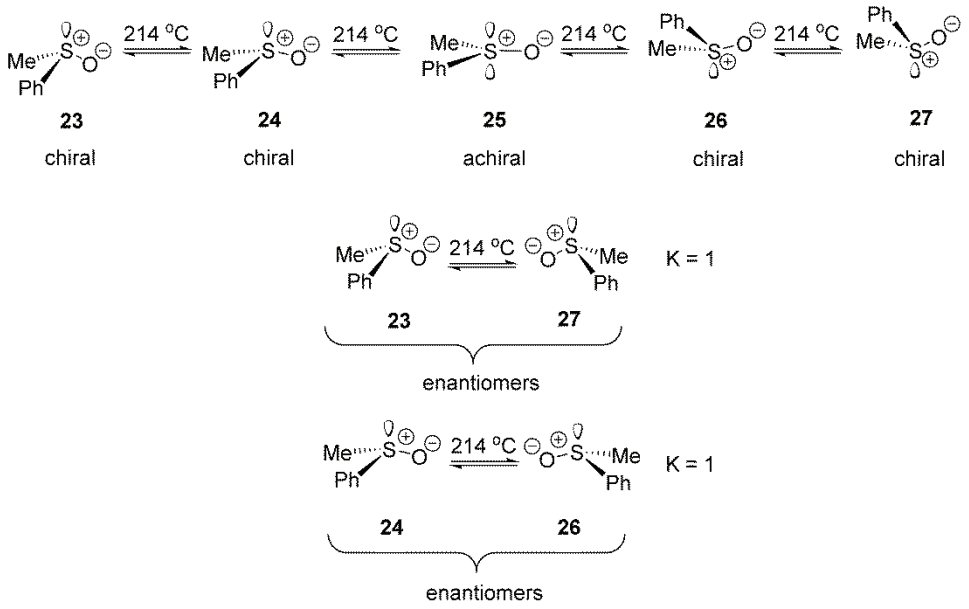


Fig. 9. Pyramidal inversion at sulfur in methyl phenyl sulfoxide requires a high amount of energy. However, at elevated temperatures, it is happening relatively rapidly.

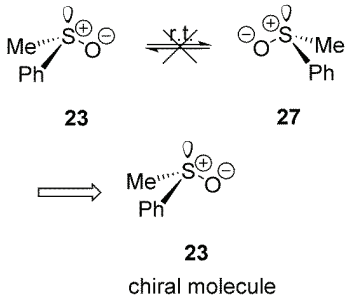


Fig. 10. The analogy between Figs. 8 and 9 is obvious, although sulfoxides are considered chiral because of practical reasons: purification of chemicals in the laboratory is done at room temperature in most cases. At that temperature, sulfoxides are configurationally stable (the rate of racemization is insignificant) and are consequently considered chiral.

Let's analyze *α*-aminoacids. Enantiomerically pure amino acids, like other molecules, thermodynamically strive for racemization and undergo rapid changes in bond lengths, bond angles and conformational changes. However, none of these changes can transform L-aminoacid into D-aminoacid (for the bond angles and bond lengths that are possible in organic compounds, Fig. 11).

To transform a chiral *α*-amino acid (regardless of the bond length, bond angle or conformation) into its enantiomer, we would have to break a sigma bond. However, this process is slow under standard conditions. For most purposes, we can approximate that it does not happen at all. But slow racemization of amino acids is important in investigations of life and is detectable on large time scales or after prolonged heating.[17]

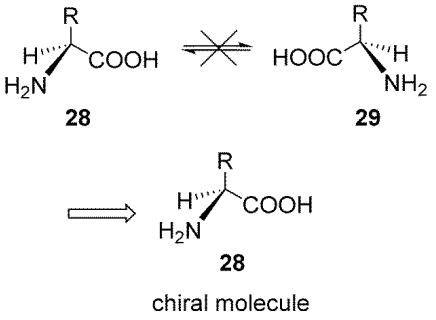


Fig. 11. Amino-acids and most other chiral molecules that contain an asymmetrically substituted carbon atom have a stable chirality. That means they will retain their chirality properties in the solutions under usual conditions. Their racemization must proceed through the breakage of the sigma-bond and that process is slow unless harsh conditions are applied.

It is evident from these examples that theoretical considerations of something that at first seems as fundamental feature of a compound is purely experimental observation of phenomena under a defined set of conditions. The practical use of the word "chiral" can be compared to the use of the word "volatility". We often call compounds volatile or non-volatile, because for practical purposes it is not important whether the substance has a boiling point of 400 or 700 °C. In either case, we can isolate it by chromatography and dry it in a vacuum. But also, it is not relevant if the boiling point is 80 or 130 °C, we will say it is volatile and that it cannot be chromatographed or dried by usual methods if we want to quantify it. Similarly, while working with a substance, it is of no importance whether the racemization time is 5 years or billion years. The only thing that is usually important is that it will not racemize in a significant amount during the experiment. If that is the case, we call it chiral. Likewise, we will not observe any difference between the racemization time of $10^{-6}$ and 1 s, in most experiments, so we describe the chirality features of those substances with the same attribute – achiral. Specification of actual numbers is important if the experiment is focused on that particular phenomenon, or in the transition cases: for example, when the compound has a boiling point of 190 °C, or when half of the sample racemizes in a week at room temperature (which corresponds to the energy barrier of 109 kJ/mol (26 kcal/mol)).

Chemists do not analyze molecular changes and calculate energies for every molecule they work with, to determine its chirality properties, but are rather aware of characteristic structural features that can make a molecule chiral or achiral. Learning those special cases is recommended because students will gain the universal ability to inspect the chirality properties of the largest part of known compounds.[18]

## SUMMARY OF THEORY

Chirality is a fundamental property of an object. Since racemization is a thermodynamically favorable process, it is most practical not to consider the chirality of a molecule as its inherent property, but rather as a feature of a system that

consists of a large number of molecules, under a defined set of conditions. In other words, chirality and associated terminology are based on practical and measurable effects of the system that we consider. Molecular symmetry observed in experiments is actually the averaged structure of non-symmetrical chemical species which constantly change. Detailed discussions on this matter are reported.[19]

## CONCLUSION

The perception of molecules in a dynamic (natural) state, rather than objects that correspond to drawings on paper is essential in life sciences. This work describes a method for the introduction of chirality that leads students to perceive molecules as dynamic entities and to understand the difference between the fundamental and applied descriptions of the word “chiral”. As further aid for teaching, practice and problems (with solutions) that employ readily available free software are provided.

## SUPPLEMENTARY MATERIAL

Additional data and information are available electronically at the pages of journal website: http://www.shd.org.rs/index.php/JSCS/article/view/12526, or from the corresponding author on request.

*Acknowledgements.* Financial support from the Ministry of Science, Technological Development and Innovation of Republic of Serbia, Contract numbers: 451-03-47/2023-01/ /200168, 451-03-47/2023-01/200288. We thank Marija Nenadović, Miloš Jović and Marko Mitić for helpful discussions on the matter.

## ИЗВОД

## КОНЦЕПТ ЗА УВОЂЕЊЕ ПОЈМА ХИРАЛНОСТИ – СИМЕТРИЈА АСИМЕТРИЈЕ

БРАНИСЛАВ З. КОКИЋ[1], ВЛАДИМИР Д. АЈДАЧИЋ,[1], ИГОР М. ОПСЕНИЦА[2] и МАРИО В. ЗЛАТОВИЋ[2]

*[1]Иновациони центар Хемијског факултета у Београду, д.о.о., Студентски трг 12–16, 11158 Београд и [2]Универзитет у Београду – Хемијски факултет, Студентски трг 12–16, 11158 Београд*

Хиралност је педагошки изазовна тема на курсевима органске хемије на основним академским студијама, а изузетно је значајна као феномен јер се јавља практично у свим гранама хемије. Систематично упознавање студената са појмом хиралности је важно због каснијег разумевања сложенијих појава везаних за ову тему. Иако је пријављено мноштво метода које олакшавају визуелизацију тродимензионалних хиралних молекула, молекулске промене као што су вибрације и конформације углавном се не анализирају у контексту хиралности. У овом чланку, хиралност и примена хиралности су објашњене на динамичким (реалним) системима, како би од самог почетка студенти перцепирали молекуле у њиховом природном стању. Осим предлога теоријске наставе на ову тему, предложене су и студентске вежбе на бесплатним и лако доступним софтверима.

(Примљено 3. августа, ревидирано 11. септембра 2023, прихваћено 15. марта 2024)

REFERENCES


1. L. J. Juszczak, *J. Chem. Educ.* **98** (2021) 3384 (https://doi.org/10.1021/acs.jchemed.1c00633)
2. a) A. Alsfouk, *J. Chem. Educ.* **99** (2022) 1900 (https://doi.org/10.1021/acs.jchemed.1c01267); b) C. E. Dickenson, R. A. R. Blackburn, R. G. Britton, *J. Chem. Educ.* **97** (2020) 3714 (https://doi.org/10.1021/acs.jchemed.0c00457); c) M. W. Pelter, M. T. Howell, C. Anderson, A. Sayeed, *J. Chem. Educ.* **97** (2020) 754 (https://doi.org/10.1021/acs.jchemed.9b00934); d) D. M. Silva, C. M. R. Ribeiro, *J. Chem. Educ.* **94** (2017) 1272 (https://doi.org/10.1021/acs.jchemed.7b00219); e) M. Abraham, V. Varghese, H. Tang, *J. Chem. Educ.* **87** (2010) 1425 (https://doi.org/10.1021/ed100497f); f) P. Lloyd-Williams, E. Giralt, *J. Chem. Educ.* **82** (2005), 1031 (https://doi.org/10.1021/ed082p1031)
3. G. P. Moss, *Pure Appl. Chem.* **68** (1996) 2193 (https://doi.org/10.1351/pac199668122193)
4. a) A. Guijarro, M. Yus, *The Origin of Chirality in the Molecules of Life: A Revision from Awareness to the Current Theories and Perspectives of this Unsolved Problem*, The Royal Society of Chemistry, Cambridge, 2009, pp. 31–48 (ISBN: 9780854041565; b) M. Quack, G. Seyfang, G. Wichmann, *Chem. Sci.* **13** (2022) 10598 (https://doi.org/10.1039/D2SC01323A) and references therein
5. C. J. M. Stirling, *J. Chem. Educ.* **51** (1974) 50 (https://doi.org/10.1021/ed051p50)
6. P. Lloyd-Williams, E. Giralt, *J. Chem. Educ.* **80** (2003) 1178 (https://doi.org/10.1021/ed080p1178)
7. D. A. Dougherty, E. V. Anslyn, *Modern Physical Organic Chemistry*, University Science Books, Herndon, VA, 2006 (ISBN: 9781891389313)
8. Y. Zhang, M. Sayama, M. Luo, Y. Lu, D. J. Tantillo, *J. Chem. Educ.* **99** (2022) 2721 (https://doi.org/10.1021/acs.jchemed.2c00443)
9. a) B. M. Wong, M. M. Fadri, S. Raman, *J. Comput. Chem.* **29** (2007) 481 (https://doi.org/10.1002/jcc.20807); b) D. Nori-Shargh, J. E. Boggs, *Struct. Chem.* **22** (2010) 253 (https://doi.org/10.1007/s11224-010-9675-x)
10. a) D. J. Brand, J. Fisher, *J. Chem. Educ.* **64** (1987) 1035 (https://doi.org/10.1021/ed064p1035); b) M. Čepič, *Mol. Cryst. Liq. Cryst.* **475** (2007) 151 (https://doi.org/10.1080/15421400701681141)
11. V. Schurig, S. Reich, *Chirality* **10** (1998) 316 (https://doi.org/10.1002/(SICI)1520-636X(1998)10:4<316::AID-CHIR5>3.0.CO;2-5)
12. A. Mazzanti, L. Lunazzi, M. Minzoni, J. E. Anderson, *J. Org. Chem.* **71** (2006) 5474 (https://doi.org/10.1021/jo060205b)
13. L. Schaefer, C. Van Alsenoy, L. Van Den Enden, *J. Chem. Educ.* **61** (1984) 945 (https://doi.org/10.1021/ed061p945) and references therein
14. J. M. Lehn, in *Dynamic Stereochemistry*, J. E. Baldwin, R. H. Fleming, J. M. Lehn, W. Tochtermann, Eds., Springer, Berlin, 1970, p. 311 (https://doi.org/10.1007/BFb0050820)
15. I. Fernández, N. Khiar, *Chem. Rev.* **103** (2003) 3651 (https://doi.org/10.1021/cr990372u)
16. a) A. Messara, N. Vanthuyne, P. Diter, M. Elhabiri, A. Panossian, G. Hanquet, E. Magnier, F. R. Leroux, *Eur. J. Org. Chem.* **2021** (2021) 5019 (https://doi.org/10.1002/ejoc.202100816) b) H. Marom, P. U. Biedermann, I. Agranat, *Chirality* **19** (2007) 559 (https://doi.org/10.1002/chir.20417)
17. J. L. Bada, *Interdiscip. Sci. Rev.* **7** (1982) 30 (https://doi.org/10.1179/030801882789801304)

18. E. E. Eliel, S. H. Wilen, L. N. Mander, *Stereochemistry of Organic Compounds*, Wiley-Interscience, Hoboken, NJ, 1994, pp. 1119–1190 (ISBN: 9780471016700)
19. a) K. Mislow, P. Bickart, *Isr. J. Chem.* **15** (1976) 1 (https://doi.org/10.1002/ijch.197600002); b) D. F. Mowery, Jr. *J. Chem. Educ.* **46** (1969) 269 (https://doi.org/10.1021/ed046p269).

Journal of the Serbian Chemical Society
JSCS@tmf.bg.ac.rs • www.shd.org.rs/JSCS
*J. Serb. Chem. Soc. 89* (9) S285–S298 (2024) *Supplementary material*

SUPPLEMENTARY MATERIAL TO

# Introductory concept for teaching chirality – Symmetry of the asymmetric

BRANISLAV Z. KOKIĆ[1]*, VLADIMIR D. AJDAČIĆ[1], IGOR M. OPSENICA[2] and MARIO V. ZLATOVIĆ[2]

*[1]Innovative centre, Faculty of Chemistry, Belgrade, Ltd., Studentski trg 12–16, 11158 Belgrade, Serbia and [2]University of Belgrade, Faculty of Chemistry, Studentski trg 12–16, 11158 Belgrade, Serbia*

*J. Serb. Chem. Soc. 89* (9) (2024) 1241–1253

TABLE OF CONTENTS:



* Corresponding author. E-mail: kokicb@chem.bg.ac.rs

## DERIVATION OF EQUATIONS

*Derivation of equation for racemization thermodynamics:*[1]

$$\Delta G^o = \Delta H^o - T\Delta S^o \quad (1)$$

$$\Delta G^o = -RT\ lnK \quad (2)$$

$$\Rightarrow K = e^{-\frac{\Delta H^O - T\Delta S^O}{RT}}, \Delta H^o = 0, \Delta S^o = 0 \quad (3)$$

$$K = 1, foreveryT \quad (4)$$

where $\Delta G^O$ is the standard reaction Gibbs energy, $\Delta H^O$ is the standard reaction enthalpy, $T$ is the temperature, $\Delta S^O$ is the standard reaction entropy and $R$ is the universal gas constant.

*Derivation of an expression for racemization half-times:*

Rate constants for enantiomer interconversions are obtained from the Eyring equation, using $\Delta^{\ddagger}G$ values from cited references and with an approximation $\kappa$=1:

$$k = \frac{\kappa k_B T}{h} e^{-\frac{\Delta^{\ddagger}G}{RT}} \quad (5)$$

where $\kappa$ is the transmission coefficient, $k_B$ is Boltzmann's constant, $T$ is temperature, $h$ is Planck's constant, $\Delta^{\ddagger}G$ is Gibbs free energy of activation and $R$ is the universal gas constant.

Racemization half-times were obtained from kinetic law for the first order reactions approaching equilibrium, $E_1 \rightleftharpoons E_2$, when only $E_1$ is present at the start of the reaction, using calculated (equation 5) rate constants:[2]

$$[E_1] = \frac{k_1 + k_2 e^{-(k_1+k_2)t}}{k_1 + k_2} [E_1]_0 \quad (6)$$

where $[E_1]$ is a concentration of $E_1$, $k_1$ is the rate constant for the direct reaction, $k_2$ is the rate constant for the reverse reaction, $t$ is reaction time and $[E_1]_0$ is the starting concentration of $E_1$.

In the case of enantiomers:

$$k_1 = k_2 = k \quad (7)$$

$$\Rightarrow [E_1] = \frac{1 + e^{-2kt}}{2} [E_1]_0 \quad (8)$$

$$t = \frac{ln\left(\frac{2[E_1]}{[E_1]_0} - 1\right)}{-2k} \quad (9)$$

Half of the sample is racemized when ¼ of $[E_1]_0$ is transformed:

$$\frac{[E_1]}{[E_1]_0} = \frac{3}{4} \quad (10)$$

$$\Rightarrow t_{1/2} = \frac{ln\left(\frac{6}{4} - 1\right)}{-2k} \quad (11)$$

$$t_{1/2} = \frac{ln\left(\frac{1}{2}\right)}{-2k} \quad (12)$$

$$t_{1/2} = \frac{0.347}{k} \quad (13)$$

REFERENCES

1. M. Quack, G. Seyfang, G. Wichmann, *Chem. Sci.* **13** (2022) 10598 (https://doi.org/10.1039/D2SC01323A)
2. P. Atkins, J. Paula, J. Keeler, *Atkins' Physical Chemistry*, 11th ed.; Oxford University Press, Oxford, United Kingdom, 2018; p. 737 (ISBN: 978–0–19–108255–9).

PROBLEMS

*Practice:*

Using quantum mechanical calculations, predict the IR spectrum of bromochloromethane molecule and create animations of all vibrations that correspond to bands visible in the predicted IR spectrum.

*Task 1:*

Using free software Vega ZZ, generate conformational diagrams for the following three biphenyls:

2,2'-dimethyl-1,1'-biphenyl (**A**)

2-tert-butyl-2'-methyl-1,1'-biphenyl (**B**)

2,2'- tert-butyl -1,1'-biphenyl (**C**)

a) All graphs have two maxima with different energies. Does the molecule have to pass through both of these barriers for enantiomer equilibration? Explain.

b) Considering only the lower maximum of generated conformational diagrams, which of these biphenyls could be separated to pure enantiomers on ambient conditions using ordinary laboratory methods? For the energy barrier consider the difference in energy between lower minimum and lower maximum. Energy values in the graphs are in kcal/mol.

c) Explain the trend in energy barrier from **A** to **C**.

*Task 2:*

Compare the most abundant conformations of 1,2-dibromoethane and 1,2-difluoroethane on the basis of chirality properties.

*Task 3:*

Enantiomers don't have exactly the same energy content in an achiral environment. The energy difference is so small that it hasn't been yet detected experimentally. If the difference in Gibbs free energy on 23 °C between enantiomers $E_1$ and $E_2$ is $2.292 \times 10^{-14}$ kJ/mol, calculate the excess of the more stable enantiomer in the system consisting of 1 mol of $E_1$ and $E_2$ in total, in an equilibrium mixture.

SOLUTIONS

*Materials and methods:*

To prepare for practical exercises, the instructor and students have to download and install software for running the simulation. The choice of software is not limited to software recommended here.

For drawing the structures you can use any software that generates standard MOL files. We used Avogadro[1] (Avogadro is an open-source molecular builder and visualization tool; Version 1.20, http://avogadro.cc/(accessed 25.6.2023.)). Some of the software used have integrated tools for drawing molecules (MoCalc2012, Vega ZZ) and can be used as well.

For quantum mechanical calculations, we recommend either Firefly QC package[2], which is partially based on the GAMESS (US)[3] source code.Firefly (Alex A. Granovsky, Firefly version 8, http://classic.chem.msu.su/gran/firefly/index.html (accessed 25.6.2023.)) or NWChem[4] (https://nwchemgit.github.io/ (accessed 25.6.2023.)). Firefly can be made available by sending an e-mail (instructions can be found on the website).

As a graphical user interface for input for QM software, we used MoCalc2012 (https://sourceforge.net/projects/mocalc2012/ (accessed 25.6.2023.)).

For visualization of the IR spectra in the first exercise, we used ChemCraft (Chemcraft - graphical software for visualization of quantum chemistry computations. Version 1.8, build 648. https://www.chemcraftprog.com (accessed 25.6.2023.)), available free of charge for the period of 150 days.

If JSmol is selected as Default Structure Viewer in MoCalc2012 Settings, visualization of IR spectra and isomers can be performed within MoCalc2012.

For conformation simulations, VEGA ZZ is used[5] (http://www.ddl.unimi.it/ (accessed 25.6.2023.)). Energies calculated using this program are more illustrative than accurate. The goal is to provide pedagogical exercise using free software.

*Practice:*

Using Avogadro (or any software that generates standard MOL files (ArgusLab, ChemDraw,...) draw bromchlormethane. Save the structure as a MOL file. Open MoCalc2012 and attach a file for quantum mechanical calculations to the program: Options -> Settings -> On *Main* dialog, next to Firefly, choose the directory where the file for quantum mechanical calculations is.

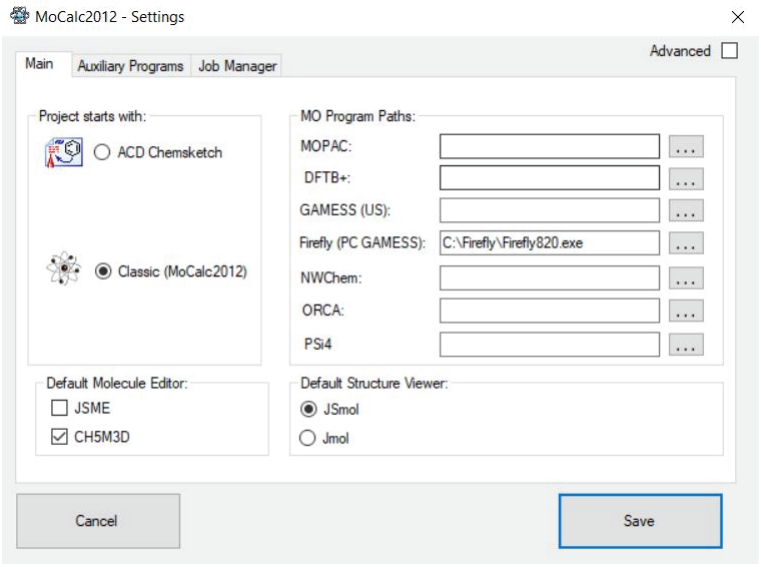


Then click *Save* and choose QM program *Firefly* and open saved structure (Start -> Open Structure File; Ctrl+O). In the first step, we have to optimize geometry of molecule. On drop down menu *Job Type:* select Geometry Optimization, then select *Method* 6-31G* and *DFT-Type* B3LYP. Start optimization by clicking on Run Firefly!

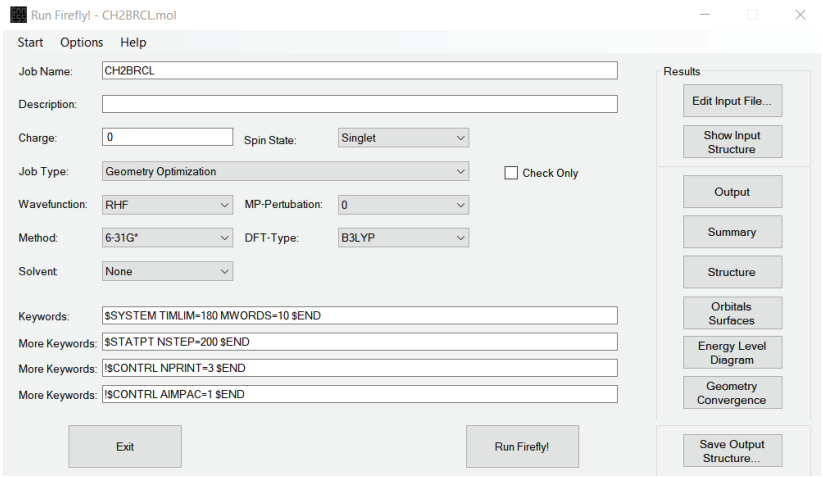


When Firefly finishes optimization, click on *Save Output Structure*... and save optimized molecule. Remember to change name of the molecule. Now open optimized structure and change *Job Type* to IR Spectrum. Leave *Method* and *DFT-Type*. Start calculations. When calculation finishes, you can visualize result.

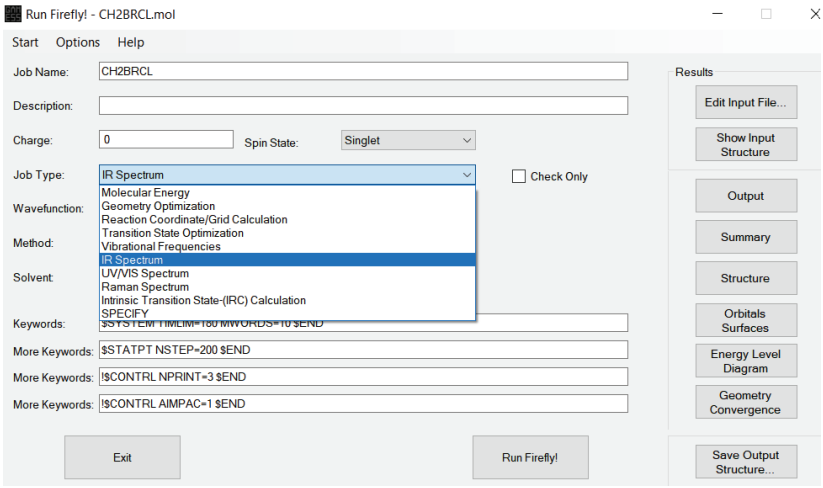


If you use ChemCraft, find a file with a name of optimized structure and extension .gam. Open it and you will see the list of absorptions in $cm^{-1}$. Selecting one of the bands, you can see the appropriate vibration animated. You can enlarge movements by changing *Scale displacement* and/or show vibrational vectors by switching *Show displacement vectors* and *Scaled vectors* on and off.

If you use MoCalc2012, when the calculation finishes, you can click on *IR Spectrum*. You will see absorption bands indicating absorption of specific energy from the spectrum, correlating with a specific vibration. If you click on *Vibrations* and select *Interactive correlation of animated vibrations to bands* you will be able to see spectra on the left, with marked absorption bands (red marks at the upper axis of the spectra), frequency related to the specific absorption (lower left part of the spectra window) and animated molecular vibrations corresponding to selected absorption band. Using the right mouse click on the animation window and selecting *Vibrations* menu, you can change the look and movements on screen.

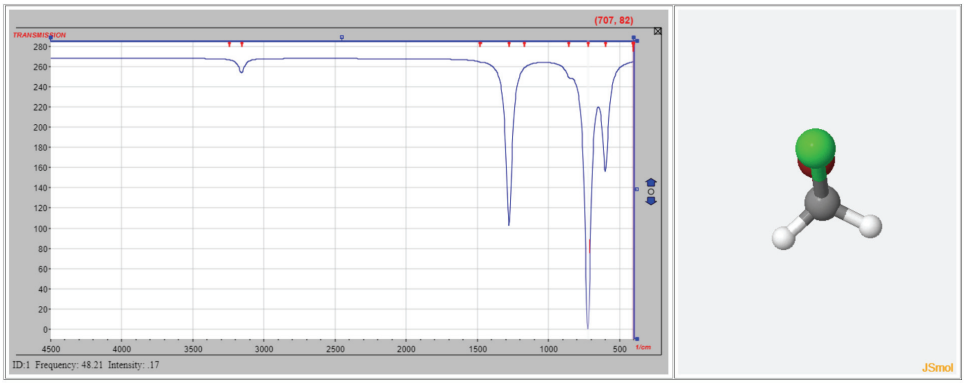

*Task 1:*

Using available tools (Ketcher (Edit -> Ketcher) from Vega ZZ) to draw different 1,1'-biphenyl derivatives from the list.

A - 2,2'-dimethyl-1,1'-biphenyl

B - 2-*tert*-butyl-2'-methyl-1,1'-biphenyl

C - 2,2'- *tert*-butyl -1,1'-biphenyl

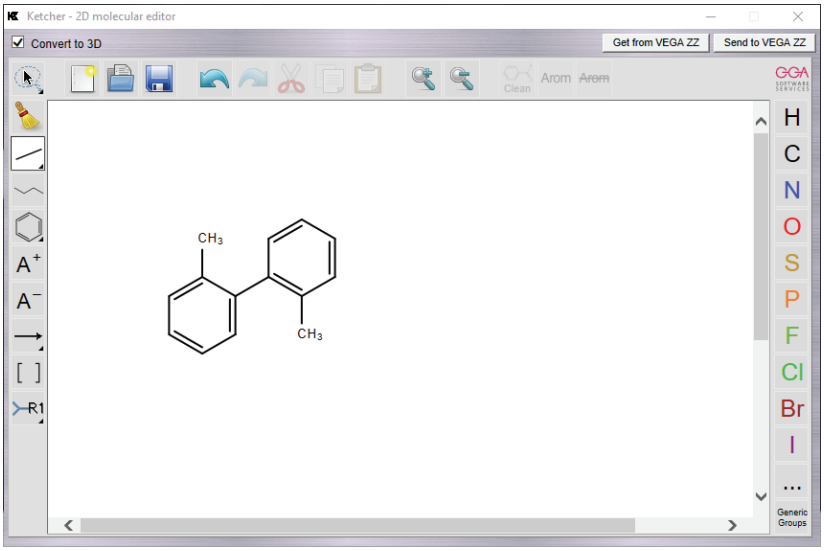


Save them in suitable format (.mol2) or open it directly with Vega ZZ (*Send to VEGA ZZ* option). Every molecule is processed in same way:

After importing/opening molecule in Vega ZZ, run Conformational search (*Calculate -> Ampp -> Conformational search*).

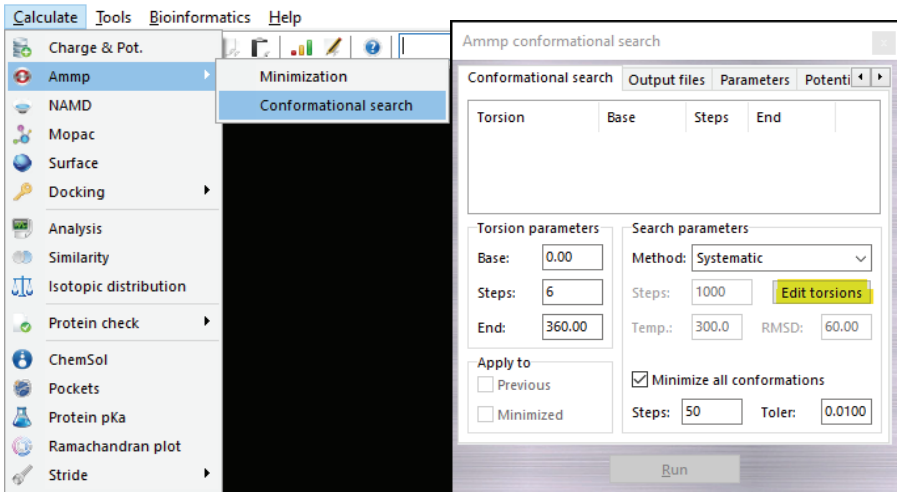

On *Conformational search* dialog, click *Edit torsions* and then select torsion angle.

Torsion angle is selected on *Selection tool*. Click on *Add* and then select atoms in molecule on screen. As a *Torsion angle*, select C2-C1-C1'-C6'.

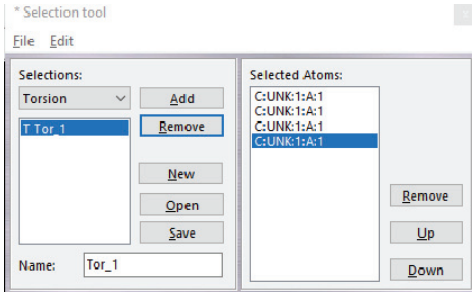


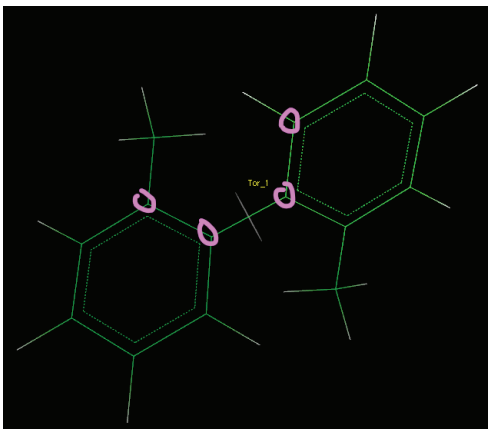


In this program, results can be dependent on the atoms chosen for defining the torsion angle. In the following Scheme 1 are presented ways of defining the torsion angles for **A**, **B** and **C** that we used:

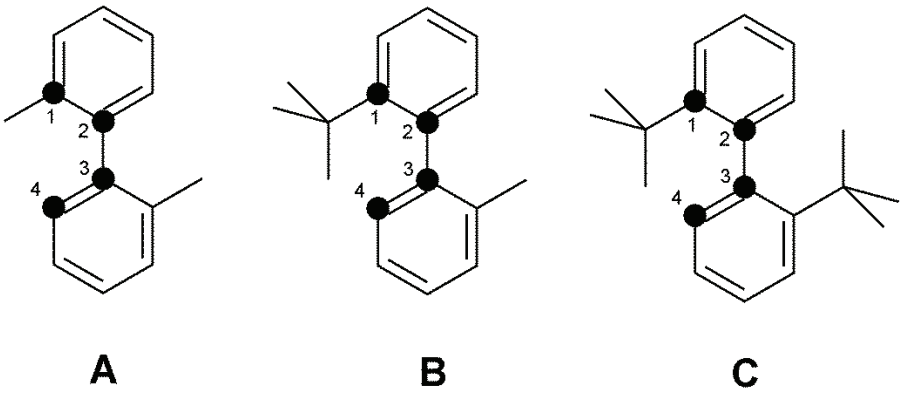


Scheme S-3.

When you selected the torsion angle, click on Steps in dialog window (yellow) and increase steps to 60 (blue). Select *Minimize all conformations* and input 50 steps. After that, on the tab *Output files,* select saving output files you need to disk.

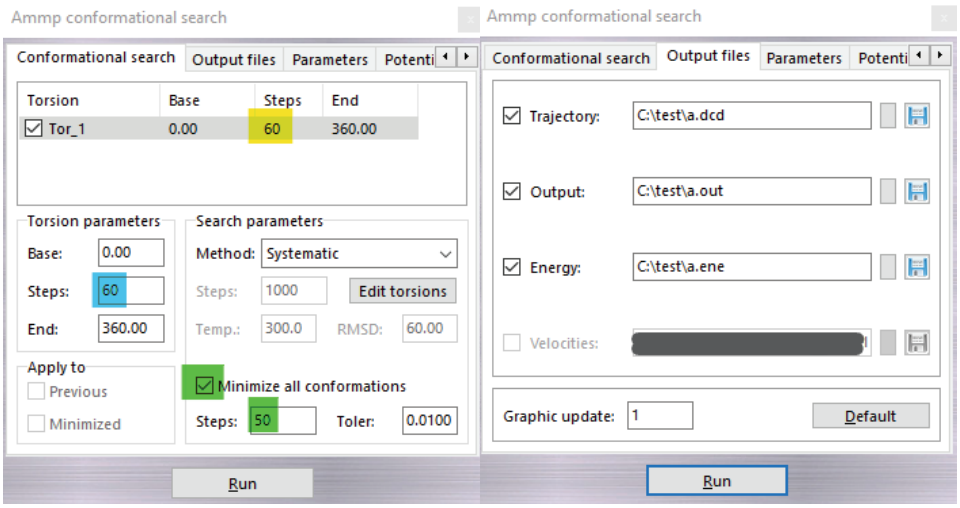


Then click *Run*. Calculations are finished very fast. Now select *Calculate -> Analysis.* Dialog box *Trajectory analysis* pops up. Click on *Open* icon, select .dcd file named as your compound that computer saved. Now you have option to see all conformations and their energies by moving the slider or changing the frame number.

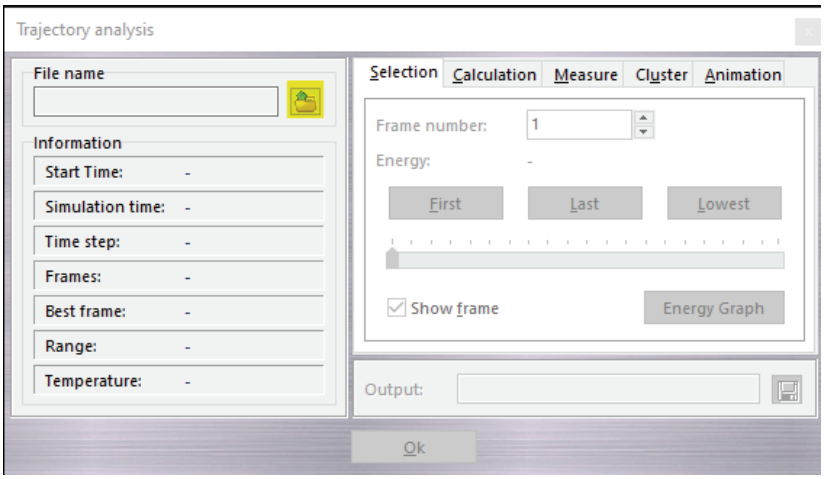

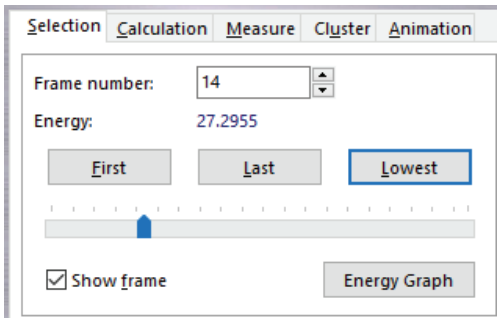


Clicking on Energy Graph, you will have a graphical representation of conformational analysis. If you switch on *Select conformation* (*Edit -> Sel. Conformations or CTRL*+F) your energy graph will be interactive, changing the conformation when you click on line on graphic.

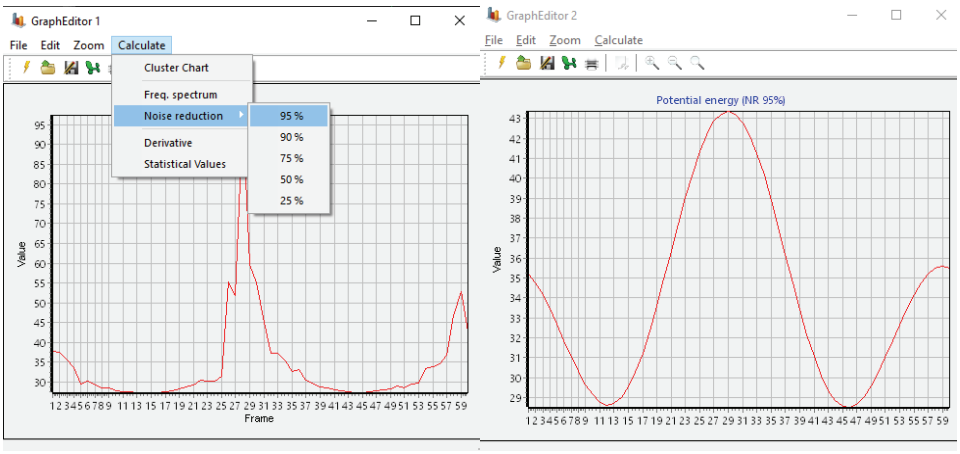


To smooth the graph, select *Calculations -> Noise reduction -> 95%.* Using *File* menu, you can export values to Excel or CSV file. If you want to calculate potential barrier, click on *Calculate -> Statistical Values.*

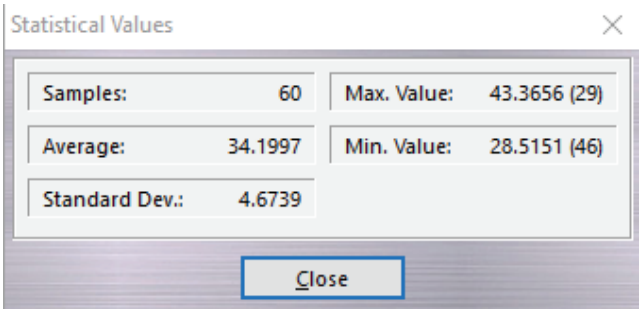


a) Conformational diagrams have two maxima because steric repulsion significantly increases in two conformations during full rotation, because

substituents on the biphenyl moiety get close to each other. These two conformations of **A** are depicted in Scheme 2.

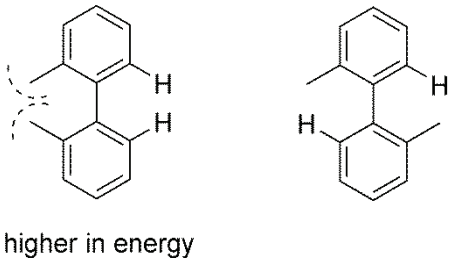


Scheme S-4. The two conformations of 2,2'-dimethyl-1,1'-biphenyl (**A**) that are highest in energy

Enantiomers can interconvert by passing only through one of the barriers (because rotation about the C–C bond can happen in either direction). Interconversion is faster through the barrier of lower energy.

b) Whether a compound can be separated to enantiomers depends on its racemization half-time on the temperature of separation. Formulae for conversion of rotation barrier energy to racemization half-times are provided in Supporting Information 1 (along with their derivation).

**A**: 33.47 kJ/mol (8 kcal/mol)

$$k = \frac{\kappa k_B T}{h} e^{-\frac{\Delta_{\ddagger} G}{RT}} \quad (1)$$

$$\Rightarrow k = 8.4x10^{6} s^{-1} \quad (2)$$

$$t_{1/2} = \frac{0.347}{k} \quad (3)$$

$$t_{1/2} = 4.1x10^{-8} s \quad (4)$$

**B:** 67 kJ/mol (16 kcal/mol)

$$k = 11.2 s^{-1} \quad (5)$$

$$t_{1/2} = 0.031 s \quad (6)$$

**C:** 155 kJ/mol (37 kcal/mol)

$$k = 4.2x10^{-15} s^{-1} \quad (7)$$

$$t_{1/2} = 2.6x10^{6} years \quad (8)$$

Based on this values, it can be concluded that **C** can be isolated as pure enantiomer on ambient conditions, while **A** and **B** cannot.

c) Tert-butyl group is bulkier than methyl group and consequently causes greater steric repulsion with methyl and hydrogen atom, so both of the barriers of

**B** are expected to be higher in energy than in **A**. By analogy, **C** is expected to have greater conformational barriers than **B**.

*Task 2:*

Task 2: The most stable conformer of 1,2-dibromoethane is anti (same as in *n*-butane). It is achiral. The most stable conformer of 1,2-difluoroethane is gauche.[6] This conformation is chiral, so two enantiomeric conformations are a dominant form of 1,2-difluoroethane (Scheme 3).

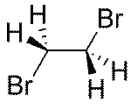

the most stable conformation of 1,2-dibromoethane (achiral)

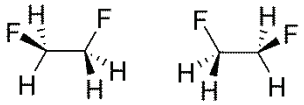

the most stable conformations of 1,2-difluorooethane (chiral)

Scheme S-5. 1,2-Dibromoethane and 1,2-difluoroethane are similar molecules, but a sample of 1,2-dibromoethane is dominantly composed of achiral structures and a sample of 1,2-difluoroethane is dominantly composed of chiral structures.

*Task 3:*[7]

$$E_1 \rightleftharpoons E_2 \quad (9)$$

$$\Delta G° = 2.292 \text{ x } 10^{-14}\, kJ/mol \quad (10)$$

$$\Delta G° = -RT\, ln\, K \quad (11)$$

$$\Rightarrow K = 0.999999999999990316 \quad (12)$$

$$K = \frac{E_2}{E_1} \quad (13)$$

$$0.999999999999990316 = \frac{E_2}{1\text{-}E_2} \quad (14)$$

$$E_2 = 0.499999999999997579\, mol \quad (15)$$

$$E_1 = 1 - E_2 = 0.500000000000002421\, mol \quad (16)$$

Excess of $E_1$:

$$E_1 - E_2 = 4.842 \text{ x } 10^{-15} mol \text{ or } 2.9052 \text{ x } 10^9 \text{ molecules} \quad (17)$$

REFERENCES


1. M. D. Hanwell, D. E. Curtis, D. C. Lonie, T. Vandermeersch, E. Zurek, G. R. Hutchison; *J. Cheminform.* **4** (2012) (https://doi.org/10.1186/1758-2946-4-17)
2. A. A. Granovsky, Firefly version 8, http://classic.chem.msu.su/gran/firefly/index.html (accessed 25.6.2023.)
3. M. W. Schmidt, K. K. Baldridge, J. A. Boatz, S. T. Elbert, M. S. Gordon, J. H. Jensen, S. Koseki, N. Matsunaga, K. A. Nguyen, S. Su, T. L. Windus, M. Dupuis, J.

A. Montgomery, *J. Comput. Chem.* **14** (1993) 1347 (https://doi.org/10.1002/jcc.540141112)
4. E. Aprà, E. J. Bylaska, W. A. de Jong, N. Govind, K. Kowalski, T. P. Straatsma, M. Valiev, H. J. J. van Dam, Y. Alexeev, J. Anchell, V. Anisimov, F. W. Aquino, R. Atta-Fynn, J. Autschbach, N. P. Bauman, J. C. Becca, D. E. Bernholdt, K. Bhaskaran-Nair, S. Bogatko, P. Borowski, J. Boschen, J. Brabec, A. Bruner, E. Cauët, Y. Chen, G. N. Chuev, C. J. Cramer, J. Daily, M. J. O. Deegan, T. H. Dunning Jr., M. Dupuis, K. G. Dyall, G. I. Fann, S. A. Fischer, A. Fonari, H. Früchtl, L. Gagliardi, J. Garza, N. Gawande, S. Ghosh, K. Glaesemann, A. W. Götz, J. Hammond, V. Helms, E. D. Hermes, K. Hirao, S. Hirata, M. Jacquelin, L. Jensen, B. G. Johnson, H. Jónsson, R. A. Kendall, M. Klemm, R. Kobayashi, V. Konkov, S. Krishnamoorthy, M. Krishnan, Z. Lin, R. D. Lins, R. J. Littlefield, A. J. Logsdail, K. Lopata, W. Ma, A. V. Marenich, J. Martin del Campo, D. Mejia-Rodriguez, J. E. Moore, J. M. Mullin, T. Nakajima, D. R. Nascimento, J. A. Nichols, P. J. Nichols, J. Nieplocha, A. Otero-de-la-Roza, B. Palmer, A. Panyala, T. Pirojsirikul, B. Peng, R. Peverati, J. Pittner, L. Pollack, R. M. Richard, P. Sadayappan, G. C. Schatz, W. A. Shelton, D. W. Silverstein, D. M. A. Smith, T. A. Soares, D. Song, M. Swart, H. L. Taylor, G. S. Thomas, V. Tipparaju, D. G. Truhlar, K. Tsemekhman, T. Van Voorhis, Á. Vázquez-Mayagoitia, P. Verma, O. Villa, A. Vishnu, K. D. Vogiatzis, D. Wang, J. H. Weare, M. J. Williamson, T. L. Windus, K. Woliński, A. T. Wong, Q. Wu, C. Yang, Q. Yu, M. Zacharias, Z. Zhang, Y. Zhao, R. J. Harrison, *J. Chem. Phys.* **152** (2020) 184102 (https://doi.org/10.1063/5.0004997)
5. A. Pedretti, A. Mazzolari, S. Gervasoni, L. Fumagalli, G. Vistoli, *Bioinformatics* **37** (2021) 1174 (https://doi.org/10.1093/bioinformatics/btaa774)
6. 1E. E. Eliel, S. H. Wilen, L. N. Mander, *Stereochemistry of Organic Compounds*, Wiley-Interscience, United States, 1994, p. 609 (ISBN: 9780471016700)
7. A. Guijarro, M. Yus, The Origin of Chirality in the Molecules of Life: A Revision from Awareness to the Current Theories and Perspectives of this Unsolved Problem, The Royal Society of Chemistry, Cambridge, UK, 2009, p. 46 (ISBN: 9780854041565).